Polarization transfers in Dissolution Dynamic Nuclear Polarization from the solid-state at high-field to the liquid-state at zero-field

Quentin Stern

To cite this version:

Quentin Stern. Polarization transfers in Dissolution Dynamic Nuclear Polarization from the solid-state at high-field to the liquid-state at zero-field. Theoretical and/or physical chemistry. Université Claude Bernard - Lyon I, 2022. English. NNT : 2022LYO10098 . tel-04238663

HAL Id: tel-04238663
https://theses.hal.science/tel-04238663v1

Submitted on 12 Oct 2023

THESE de DOCTORAT DE L'UNIVERSITE CLAUDE BERNARD LYON 1

Ecole Doctorale N° 206
Ecole Doctorale de Chimie de Lyon

Discipline : Chimie

Soutenue publiquement le 10/11/2022, par :
Quentin Stern

Sur les transferts de polarisation en polarisation nucléaire dynamique par dissolution : de l'état solide à haut champ à l'état liquide à zéro champ

---

Devant le jury composé de :

Han, Songi	Professeure	UCSB	Rapporteure et présidente
Levitt, Malcolm	Professeur	SOTON	Rapporteur
Griffin, Robert	Professeur	MIT	Examinateur
Halse, Meghan	Lecturer	University of York	Examinatrice
Lambert, Simon	Maître de Conférences	UCBL	Examinateur
Schlagnitweit, Judith	Chargée de Recherche	CNRS	Examinatrice
Jannin, Sami	Professeur	UCBL	Directeur de thèse

Polarization Transfers in Dissolution Dynamic Nuclear Polarization from the Solid-State at High-Field to the Liquid-State at Zero-Field

Quentin Stern

17/02/2023

Contents

Abbreviations

AMC	Amplifier multiplier chain
AWG	Arbitrary waveform generator
CE	Cross effect
iCE	Indirect cross effect
CP	Cross polarization
CSA	Chemical shift anisotropy
CW	Continuous wave
DNP	Dynamic nuclear polarization
dDNP	Dissolution dynamic nuclear polarization
EMF	Electromotive force
ESR	Electron saturation resonance
EPR	Electron paramagnetic resonance
FWHM	Full width at half maximum
HypRes	Hyperpolarization resurgence
LOD-ESR	Longitudinally detected-electron saturation resonance
MAS	Magic angle spinning
μw	Microwave
NMR	Nuclear magnetic resonance
NOE	Nuclear Overhauser effect
NV	Nitrogen vacancy
NZ	Non-Zeeman
OE	Overhauser effect
OPM	Optically pumped magnetometer
PANI	Polyaniline

cPANI	Chiral polyaniline
PANI-EB	Polyaniline emeraldine base
PANI-ES	Polyaniline emeraldine salt
PD	Photodiode
PEM	Photoelastic modulator
PHIP	Parahydrogen induced polarization
PRE	Paramagnetic relaxation enhancement
Q-factor	Quality factor
RD	Radiation damping
rf	Radio frequency
SE	Solid effect
SERF	Spin exchange relaxation-free
SNR	Signal-to-noise ratio
TEMPOL	4-hydroxy-2,2,6,6-tetramethylpiperidin-1-oxyl radical
TM	Thermal mixing
ZULF	Zero- to ultra low-field

Abstract

Nuclear magnetic resonance (NMR) is a powerful analytical technique with numerous applications. Yet, NMR is limited by its intrinsic low sensitivity, which owes to the low polarization of nuclear spins at thermal equilibrium. This limitation can be lifted by hyperpolarization methods, which increase the polarization of nuclear spins transiently far above thermal equilibrium. Dissolution dynamic nuclear polarization (dDNP) is one such method, which takes advantage of the higher polarization of unpaired electron spins, yielding nuclear polarization approaching unity. The sample of interest is first hyperpolarized in the solid-state at low temperature and moderate magnetic field and is then dissolved and transferred to the point of use in the liquid-state, reaching signal enhancements of up to five orders of magnitude.

This work explores the spin dynamics at stake in dDNP experiments at various stages along the process, with a particular focus on polarization transfers among spins and the methods to study them. This includes polarization transfers between electron and nuclear spins (DNP mechanisms), between homonuclear spins in the solid-state (spin diffusion), between nuclear spins and their environment (relaxation), and between heteronuclear spins in the liquid-state at zero-field (level anti-crossings). The main contribution of this work is the introduction of the hyperpolarization resurgence experiment (HypRes), which monitors spin diffusion in the near vicinity of electron spins, a mechanism that could previously only be studied indirectly. HypRes should enable a better understanding of this fundamental mechanism of DNP.

Keywords: nuclear magnetic resonance, dissolution dynamic nuclear polarization, spin diffusion, spin physics, zero- to ultra-low field nuclear magnetic resonance, nuclear hyperpolarization, spin polarization transfers, electron paramagnetic resonance.

Résumé

La résonance magnétique nucléaire (RMN) est une technique analytique puissante aux nombreuses applications. Cependant, elle est limitée par sa faible sensibilité intrinsèque, due à la faible polarisation des spins nucléaires à l'équilibre. Cette limitation peut être repoussée par les méthodes d'hyperpolarisation, qui augmentent temporairement la polarisation nucléaire loin de sa valeur d'équilibre. Parmi ces méthodes, la polarisation nucléaire dynamique par dissolution (PNDd) utilise la forte polarisation de spins électroniques non-appariés et atteint des polarisations nucléaires proche de l'unité. L'échantillon est hyperpolarisé à l'état solide à basse température et champ magnétique modéré et est ensuite dissout et transféré au point d'utilisation à l'état liquide, atteignant des augmentations de signal jusqu'à >10'000.

Ce travail est une exploration de la dynamique de spin à l'œuvre au long des expériences de PNDd, avec un accent particulier sur les transferts de polarisation entre spins et les méthodes pour les étudier. Ceci inclut les transferts de polarisation entre spins électroniques et nucléaires (mécanismes PND), entre spins homonucléaires à l'état solide (diffusion de spin), entre les spins nucléaires et leur environnement (relaxation) et entre spins hétéronucléaires à l'état liquide à zéro champ (croisements évités). La contribution principale de ce travail est l'introduction de la méthode de résurgence d'hyperpolarisation (HypRes), qui mesure la diffusion au voisinage des spins électroniques, un mécanisme qui ne pouvait jusque-là être étudié qu'indirectement. Cette méthode devrait permettre une meilleure compréhension de ce mécanisme fondamental de la PND.

Mots-clefs: résonance magnétique nucléaire, polarisation nucléaire dynamique par dissolution, diffusion de spin, physique de spin, résonance magnétique nucléaire à zéro et très bas champ, hyperpolarisation nucléaire, transfert de polarisation de spin, résonance paramagnétique électronique.

Résumé substantiel

La résonance magnétique nucléaire (RMN) est une technique analytique puissante aux nombreuses applications. Cependant, elle est limitée par sa faible sensibilité intrinsèque, due à la faible polarisation des spins nucléaires à l'équilibre. Cette limitation peut être repoussée par les méthodes d'hyperpolarisation, qui augmentent temporairement la polarisation nucléaire loin de sa valeur d'équilibre. Parmi ces méthodes, la polarisation nucléaire dynamique par dissolution (PNDd) utilise la forte polarisation de spins électroniques non-appariés et atteint des polarisations nucléaires proche de l'unité. L'échantillon est hyperpolarisé à l'état solide à basse température et champ magnétique modéré et est ensuite dissout et transféré au point d'utilisation à l'état liquide, atteignant des augmentations de signal jusqu'à $>$10'000. Ce travail est une exploration de la dynamique de spin à l'œuvre au long des expériences de PNDd, avec un accent particulier sur les transferts de polarisation entre spins ainsi que les méthodes pour les étudier et les exploiter.

Le premier chapitre présente le contexte de la résonance magnétique et les deux raisons qui poussent les spectroscopistes à utiliser les plus forts champs magnétiques possibles, la sensibilité et la résolution. Les méthodes d'hyperpolarisation et en particulier la PNDd sont présentées comme alternative pour pallier à la faible sensibilité de la RMN. La RMN à zéro et à très bas champs magnétiques est ensuite présentée comme une méthode permettant l'acquisition de données RMN à haute résolution mais limitée à des mélanges peu complexes. Ce type de RMN a l'avantage de reposer sur une instrumentation bon marché et qui peut est rendue portative.

Dans le deuxième chapitre, les concepts théoriques qui sous-tendent la RMN sont présentés. Ce chapitre ne présente pas de concepts nouveaux en soi mais a vocation de rendre le plus clair possible les bases de la dynamique de spins, en particulier les aspects utiles pour la simulation numérique. Suite à une introduction sur le concept de spin, la représentation quantique de la dynamique de spin basée sur la matrice de densité est dérivée à partir des six postulats de la mécanique quantique, en détaillant les étapes de calcul autant que possible. Ce formalisme est ensuite utilisé pour prédire l'apparence de spectres RMN à haut champ et à zéro champ pour des spins nucléaires couplés par interaction scalaire à l'état liquide, pour des spins nucléaires couplés par interaction dipolaires à l'état solide (pattern de Pake) et pour un spin nucléaire en interaction dipolaire avec un spin électronique. Ce formalisme est aussi utilisé pour expliquer les échanges de polarisation entre spins nucléaires couplés par interaction dipolaire, le phénomène à la base de la diffusion de spin. Finalement, la constante de vitesse de relaxation des spins nucléaires sous l'effet d'un spin électronique dont l'état est fluctuant est dérivée pour des spins à position fixe dans l'espace et couplé par interaction dipolaire.

Le troisième chapitre concerne la PND à l'état solide aux températures de l'hélium liquide (entre 1.2 et 4.2 K) et champ magnétique modéré (7.05 T). La première section détaille les composants du polariseur PNDd utilisé dans ce travail (aimant, cryostat, système radiofréquence, système microonde) et les méthodes pour mesurer la polarisation de spins nucléaires à haut et à bas rapport gyromagnétique à l'état solide. Une méthode innovante et simple pour mesurer l'angle d'une faible impulsion radiofréquence est proposée et utilisée dans le cadre de la mesure de polarisation des spins nucléaires à bas rapport gyromagnétique.

La deuxième section est consacrée à la théorie des quatre mécanismes de la PND à l'état solide pour un échantillon statique. Ces mécanismes décrivent comment la polarisation est transférées des spins électroniques vers les spins nucléaires sous l'effet d'irradiation microonde continue. L'accent est principalement mis sur l'effet croisé et le mélange thermique, les deux mécanismes les plus efficaces en conditions de PNDd et sur les méthodes développées durant ces quinze dernières années pour les simuler.

Les deux sections suivantes présentes des spectres microondes (c'est-à-dire, des graphiques de polarisation ^{1}H sous PND en fonction de la fréquence d'irradiation microonde) pour deux types d'échantillon. Le premier type est un mélange standard de radical TEMPOL (en concentration 50 et 75 mM) dans du "jus de PND" (1:3:6 H_2O:D_2O:glycerol-d_8, v/v/v). Des spectres microondes des deux échantillons enregistrés à quatre températures (1.6, 2.5, 3.0 et 3.8 K) changent de forme avec la température et la quantité de radicaux. Ces résultats suggèrent que le mécanisme dominant pourrait évoluer avec la température. Malgré la banalité de cet échantillon très répandu, il n'est pas clair à ce jour si l'effet croisé ou le mélange thermique y domine la PND. Nos données devraient permettre de tester différents modèles récents d'effet croisé et de mélange thermique et peut-être de déterminer lequel domine dans quelles conditions.

Le deuxième type d'échantillon pour lequel les spectres microondes ont été enregistrés est la polyaniline (PANI), un polymère organique conducteur. Une méthode est proposée pour contrôler la teneur en spin électronique par la protonation partielle de la fonction imine du polymère. Les spectres microondes en fonction de la teneur en radicaux présentent des signatures complexes qui varient avec la teneur en radicaux et suggèrent que plusieurs mécanismes opèrent en même temps. La polarisation ^{1}H la plus haute observée pour les PANI n'est que de 3% tandis qu'elle peut atteindre 90% dans des échantillons standards. L'intérêt des PANI réside ailleurs. Il a en effet été montré que les spins électroniques pouvaient être polarisé par l'application d'un courant électrique dans des PANI chiraux indépendamment de la température. La PND depuis des électrons hyperpolarisés des PANI pourraient donc permettre de polariser des spins nucléaires à des haut niveaux sans avoir recours à la basse température de l'hélium liquide qui est plus en plus rare et coûteux et de surcroit complexe à manipuler.

Les échanges de polarisations entre les spins nucléaires et leur environnement, autrement dit la relaxation nucléaire, sont utilisés dans le quatrième chapitre comme sonde indirect de l'état des spins électroniques. La mesure de propriétés des spins électroniques (temps de relaxation longitudinale, temps d'équilibrage sous l'effet de l'irradiation microonde, polarisation électronique sous l'effet de l'irradiation microonde, forme du spectre électronique) sont des paramètres expérimentaux essentiels pour modéliser la PND. Or, ils sont difficiles à mesurer dans les conditions de PNDd. Bornet *et al.* ont montré que le temps de la relaxation $T_{1\rho}$ des spins ^{1}H pouvaient utilisé pour mesurer indirectement la polarisation électroniques sous l'effet de l'irradiation microonde et la constante de temps de relaxation longitudinal des électrons.

Dans ce chapitre, nous proposons l'utilisation du temps de relaxation transverse T_2^* des spins ^{13}C pour mesurer les propriétés de spin électronique mentionnée plus haut. Des divergences sont observées entre les propriétés électroniques mesurées par le $T_{1\rho}(^1\mathrm{H})$ et le $T_2^*(^{13}\mathrm{C})$. Nous avançons que les propriétés de relaxation ^{1}H sont potentiellement biaisées par la diffusion de spin nucléaire, tandis que les propriétés de relaxation ^{13}C serait plus fiables, ce qui expliquerait les divergences. Cependant, les données présentées ne permettent pas de vérifier ce biais avec certitude.

Les cinquième chapitre présente les contributions les plus innovantes de ce travail et concerne la barrière de diffusion. Les spins nucléaires les plus proches de l'électron sont ceux les plus efficacement polarisés par la PND. Cependant, le gradient de champ magnétique ressenti par ces spins dû à la présence de l'électron fait que leur fréquence de résonance diffère trop fortement de celle de leur voisin pour qu'ils parviennent à échanger leur polarisation. La limite où les spins nucléaires ne parviennent plus à échanger la polarisation est appelée barrière de diffusion. Si l'implication de cette barrière pour la PND est importante, elle n'en reste pas moins difficile à étudier expérimentalement.

Dans ce chapitre, nous introduisons la méthode de résurgence d'hyperpolarisation (HypRes) pour mesurer les transferts de polarisation entre les spins nucléaires invisible proches de l'électrons et ceux, visibles, plus éloignés de l'électron. L'applicabilité de la méthode est démontrée pour la diffusion ^{1}H dans le jus PND dopé au TEMPOL et pour la diffusion ^{13}C dans le [1-^{13}C]-acide pyruvique dopé au radical trityl dans les conditions de PNDd ainsi que pour la diffusion ^{1}H dans un mélange de 2:3 H_2O:glycerol (v/v) dopé au radical ASYMPolPOK en conditions de PND avec rotation à l'angle magique à 100 K et 14.0 T. Dans toutes les conditions étudiées, nos résultats montrent que la diffusion entre spins invisibles et visibles est plus rapide que la relaxation longitudinale des spins visibles.

Pour étudier la diffusion entre les spins les plus proches de l'électron, qui ne peuvent pas être observés directement, une seconde variante de l'expérience HypRes est introduite où les spins invisibles sont manipulés par des impulsions radiofréquence à large bande. Appliquée au jus PND dopé avec 50 mM de TEMPOL, cette expérience démontre que les spins nucléaires jusqu'à 3 Å de l'électron peuvent encore communiquer leur polarisation avec les spins visibles plus rapidement qu'ils ne relaxent à 3.8 K. En d'autres termes, la barrière de diffusion, si elle existe dans cet échantillon et ces conditions, doit être inférieure ou égales à 3 Å.

Dans une troisième variante de l'expérience HypRes, la diffusion de spin nucléaire est mesurée tandis que la polarisation électronique est maintenue par irradiation microonde à une valeur plus faible que la polarisation d'équilibre thermique. Appliquée au jus PND dopé avec 50 mM de TEMPOL, cette expérience démontre que la polarisation électronique a un effet déterminant sur la diffusion de spin nucléaire. Un modèle de diffusion de spin à deux noyaux et un électron où la dynamique de l'électron est traitée de manière semi-classique confirme en théorie le rôle de la polarisation électronique sur la diffusion de spin nucléaire.

La méthode HypRes est versatile et peut être appliquée dans des conditions variées. Elle devrait permettre d'augmenter la compréhension des mécanismes permettant la diffusion de spin nucléaire proche de l'électron pour ensuite optimiser la formulation d'échantillon et les méthodes PND de manière à la rendre plus efficace.

Le dernier chapitre présente des expériences de PND suivies de l'étape où l'échantillon est dissout, transféré vers un deuxième spectromètre et détecté à l'état liquide, c'est-à-dire, des expériences de PNDd. La première section présente les méthodes instrumentales optimisées par notre équipe pour dissoudre, transférer et injecter l'échantillon hyperpolarisé en moins de 2 s, tout en contrôlant le volume de solution injecté. Ce système permet d'obtenir des largeurs de raie ^{13}C inférieures à 1 Hz 2 secondes après injection et des polarisations ^{13}C jusqu'à 50% à l'état liquide. Les méthodes pour quantifiés la polarisation à l'état liquide sont détaillées. Les possibles sources de pertes de polarisation pendant le transfert de l'échantillon hyperpolarisé sont passées en revue et des stratégies pour y pallier en contrôlant le champ magnétique au long du transfert sont proposées. Les performances de cette instrumentation de PNDd en font une plateforme de choix pour les applications de suivi de réactions métaboliques ou de criblage de médicaments.

Dans les deux sections suivantes, la PNDd est combinée avec la RMN à zéro et très bas champs magnétiques dans deux types d'expérience. Dans le premier cas, la dynamique de spin à zéro et très bas champs magnétiques est utilisée pour effectuer un transfert de polarisation des spins ^{1}H vers les spins ^{13}C pendant que la solution hyperpolarisée passe du polariseur de PNDd vers le spectromètre liquide sans l'immobiliser. Cette méthode utilise une inversion adiabatique du champ magnétique qui transfère la polarisation des spins ^{1}H vers les spins ^{13}C, grâce au croisement évité induit par le couplage scalaire entre les hétéronoyaux.

Après avoir présenté la théorie de ces échanges de polarisation par la formule de Landau-Zener et par des simulations numériques, nous appliquons cette méthode à un échantillon un mélange de petites molécules marquées au ^{13}C, dont les spins ^{1}H sont hyperpolarisés par PNDd. Pendant le transfert entre le polariseur et le spectromètre liquide, la solution hyperpolarisée traverse un dispositif réalisant l'inversion de champ magnétique selon un profile maitrisé. La solution est finalement injectée dans un spectromètre RMN de paillasse ou le signal ^{13}C est détecté. Partant d'une polarisation ^{1}H dépassant 50% à l'état solide, des polarisations ^{13}C de 9-12% pour des molécules sont obtenues à l'état liquide. Ceci s'explique par la rapide relaxation ^{1}H dès après la dissolution de l'échantillon.

La faisabilité de la méthode a été démontrée ici pour des molécules à fort couplage-J. Des solutions sont proposées pour étendre la méthode à des molécules à faible couplage-J comme le [1-^{13}C]-pyruvate. Elle pourrait alors permettre d'accélérer la production de métabolites au ^{13}C hyperpolarisé par PNDd dans le contexte d'applications cliniques. En effet, la méthode la plus courante consiste à polariser le ^{13}C directement grâce au radical trityl, ce qui met 1-2 heures. Notre méthode repose sur la PND du ^{1}H qui peut atteindre des polarisations de $> 70\%$ en quelques minutes.

La deuxième expérience couplant PNDd et RMN à zéro champ consiste à hyperpolariser un échantillon par PNDd et le détecter à zéro champ. Les spins ^{1}H ainsi que ^{13}C sont hyperpolarisé par PND avec le radical TEMPOL et l'utilisation de la polarisation croisée. L'échantillon est dissout et transféré au spectromètre RMN à zéro champ où le signal du couplage-J entre les spins ^{1}H et ^{13}C est détecté par magnétométrie optique. Une augmentation de signal de 11'000 par rapport à la méthode classique de prépolarisation dans un aimant de 2 T est obtenue, alors qu'une augmentation de signal de l'ordre de 54'000 est attendue aux vues des polarisations ^{1}H et ^{13}C déterminées dans les mêmes conditions avec une spectromètre RMN de paillasse.

La différence entre l'augmentation de signal obtenue et celle attendue est expliquée par la relaxation paramagnétique dû à l'agent polarisant utilisé pour la PND. Des méthodes utilisant des agents polarisants filtrables sont proposées pour limiter la relaxation paramagnétique. La RMN à zéro champ hyperpolarisée par PNDd est envisagée pour le suivi de réaction catalytique en milieu hétérogène dans des conteneurs métalliques où la RMN standard ne permet pas une haute résolution.

Curriculum vitae

Current positions

- Postdoctoral researcher. in Prof. Sami Jannin's group (HMRlab, CRMN) in Lyon, France (since 2023)
- Member of the AMPERE Bureau as a young member (since 2022)

Education

2018-2022	**Ph.D. of Chemistry** in Prof. Sami Jannin's group (HMRlab, CRMN) in Lyon, France
2017-2018	**Master of Science in Mathematics and Chemistry** at Université de Genève (not completed)
2012-2014	**Master of Science in Molecular and Biological Chemistry** at Ecole Polytechnique Fédérale de Lausanne (EPFL) in 2014. Specializations: Biological Chemistry, Inorganic Chemistry, and Bioanalytical Chemistry. Overall average mark: 5.83/6
2009-2012	**Bachelor in Chemistry** at EPFL in 2012. Overall average mark: 5.68/6. Prix Louis Pelet, awarding the student who obtained the best overall average mark at the Bachelor in Chemistry and Chemical Engineering – (out of 80 students) – Third year of Bachelor: Erasmus at the University of Edinburgh. First publication during this year.

Experience

2018-2021	**Early stage researcher** in the zero- to ultra low-field NMR European innovative training network (ZULF-ITN)
2018-2021	**Representative of the early stage researchers** at the board of the ZULF-ITN European network
2020	**Co-organizer of First international conference on ZULF-NMR** held online during a week: 14 speakers and >100 participants
2018	**Organizer of the first training week of the ZULF-ITN** European network in Lyon, France, gathering 17 people: preparation of the scientific planning, contact with speakers, hotel and restaurant booking and coordination

2015-2017	**Scientific assistant** at Prof. Pascal Boivin's Laboratoire de Sol et substrats (Pedology, HEPIA Lullier)– development of a software in Visual Basic for soil data analysis (Retractometry)
2014	**Scientific assistan**t at Prof. Geoffrey Bodenhausen's Laboratory of Biomolecular Magnetic Resonance (LRMB – EPFL) during three months after the master thesis – Work on DNP enhanced waterLOGSY

Teaching

2018-2021	**Theoretical and practical courses on relaxation in NMR** for the master students of ENS Lyon and UCBL
2018-2021	**Supervisor of 7 master students**
2018-2021	**Author of online tutorials on MATLAB for NMR spectroscopists** (basics of programming in MATLAB, data treatment/model fitting, and simple NMR simulation from scratch), >1600 views
2014-2017	**Teaching assistant for practical works** of Chemistry and substitute at Collège de Genève (high school) for Chemistry classes
2013	**Teaching assistant for the courses of General Chemistry** for engineers at EPFL
2012	**Teacher** in the private school of learning support (Guigoo). Preparation of courses and exercises for groups of medicine students (Organic and General Chemistry)

Music

- Stage and studio musician as singer and bassist
- Singer, co-composer and co-producer of the vocal duet The I-Twins
- Bassist and chorist of the band Najavibes (also performing as backing band)
- Co-founder and co-producer of the label Fruits Records (responsible for logistics, accounts, and contracts)
- Appointed by the Département de l'Instruction Publique du canton de Genève (DIP) to give educative concerts with the band Najavibes for students from 12 to 15 years old in fourteen schools in 2014

Publications

Main contributions

- Stern, Q. *et al.* DNP of conductive organic polymers. *in prep.*
- Stern, Q. *et al.* Rapid ^{1}H→^{13}C hyperpolarization transfer via adiabatic field inversion. *in prep.*
- Picazo-Frutos, R.*, Stern, Q.* *et al.* (2023). Zero- to Ultralow-Field Nuclear Magnetic Resonance Enhanced with Dissolution Dynamic Nuclear Polarization. *Anal. Chem*, **95**(2), 720-729.

- Stern, Q.* & Sheberstov, K. (2022). Simulation of NMR spectra at zero- and ultra-low field from A to Z – a tribute to Prof. Konstantin L'vovich Ivanov. *Magnetic Resonance Discussions, under revision.*

- Chessari, A., Cousin, S. F., Jannin, S., & Stern, Q.* (2022). The role of electron polarization on nuclear spin diffusion. *arXiv* preprint arXiv:2206.14771.

- Stern, Q*., Cousin, S. et al. (2021). Direct observation of hyperpolarization breaking through the spin diffusion barrier. *Science Advances*, **7**(18), eabf5735.

- Elliott, S. J., Stern, Q., *et al.* (2021). Practical dissolution dynamic nuclear polarization. *Progress in Nuclear Magnetic Resonance Spectroscopy*, **126**, 59-100.

Secondary contributions

- Elliott, S. J., Ceillier, M. *et al.* (2022). Simple and Cost-Effective Cross-Polarization Experiments under Dissolution-Dynamic Nuclear Polarization Conditions with a 3D-Printed ^{1}H-^{13}C Background-Free Radiofrequency Coil. *Journal of Magnetic Resonance Open*, 100033.

- Koptyug, I. V., Stern, Q. *et al.* (2022). Frozen water NMR lineshape analysis enables absolute polarization quantification. *Physical Chemistry Chemical Physics*, **24**(10), 5956-5964.

- El Daraï, T., Cousin, S. F. *et al.* (2021). Porous functionalized polymers enable generating and transporting hyperpolarized mixtures of metabolites. *Nature Communications*, **12**(1), 1-9.

- Elliott, S. J., Cala, O. *et al.* (2021). Pulse sequence and sample formulation optimization for dipolar order mediated $^{1}\text{H}\rightarrow{}^{13}\text{C}$ cross-polarization. *Physical Chemistry Chemical Physics*, **23**(15), 9457-9465.

- Elliott, S. J., Stern, Q. *et al.* (2021). Protonation tuned dipolar order mediated $^{1}\text{H}\rightarrow{}^{13}\text{C}$ cross-polarization for dissolution-dynamic nuclear polarization experiments. *Solid State Nuclear Magnetic Resonance*, **116**, 101762.

- Ceillier, M., Cala, O. *et al.* (2021). An automated system for fast transfer and injection of hyperpolarized solutions. *Journal of Magnetic Resonance Open*, **8**, 100017.

- Elliott, S. J., Cala O. *et al.* (2021). Boosting dissolution-dynamic nuclear polarization by multiple-step dipolar order mediated $^{1}\text{H}\rightarrow{}^{13}\text{C}$ cross-polarization. *Journal of Magnetic Resonance Open*, **8**, 100018.

- Elliott, S. J., Stern, Q., & Jannin, S. (2021). Solid-state ^{1}H spin polarimetry by $^{13}\text{CH}_3$ nuclear magnetic resonance. *Magnetic Resonance*, **2**(2), 643-652.

- Elliott, S. J., Cousin, S. F. *et al.* (2020). Dipolar order mediated $^{1}\text{H}\rightarrow{}^{13}\text{C}$ cross-polarization for dissolution-dynamic nuclear polarization. *Magnetic Resonance*, **1**(1), 89-96.

Minor contributions

- Dey, A, Charrier, B. *et al.* (2022). Fine optimization of a dissolution-DNP experimental setting for ^{13}C NMR of metabolic samples. *Magnetic Resonance Discussions*, 1–27.

- Dey, A., Charrier, B. *et al.* (2020). Hyperpolarized NMR metabolomics at natural ^{13}C abundance. *Analytical chemistry*, **92**(22), 14867-14871.

Prior to Ph.D.

- Stern, Q., Milani, J. *et al.* (2015) Hyperpolarized water to study protein-ligand interactions. *Journal of Physical Chemistry Letters*, **6**(9), 1674-1678
- Vuichoud, B., Milani, J. *et al.* (2015) Measuring absolute spin polarization in dissolution-DNP by Spin PolarimetrY Magnetic Resonance (SPY-MR). *Journal of Magnetic Resonance*, **260**, 127-135
- Beveridge, R., Chappuis, Q. *et al.* (2013) Mass spectrometry methods for intrinsically disordered proteins. *Analyst*, **138**(1), 32-42

Conferences

2023	Online talk at the Global NMR discussions. *The surprising consequences of high electron polarization.*
2022	Talk at HyperMix Conference in Nantes, France. *Polarization losses during the sample transfer of dissolution dynamic nuclear polarization experiments: from theory to practice.*
2021	Talk at the Hyp21 in Lyon, France. ^{1}H *detected EPR and other wonders of high electron polarization in dynamic nuclear polarization.*
2020	Online talk at Bruker User's meeting. *Detecting hyperpolarized solutions with a benchtop nuclear magnetic resonance spectrometer.*
	Online talk at Bruker Fourier 80 launch meeting. *Teaching with the Fourier 80.*
	Online talk at the R. G. Griffin and K. O. Tan's ZOOMinars. *Direct observation of dynamic nuclear polarization breaking through the spin diffusion barrier.*
2019	Talk at the Alpine conference in Chamonix, France. *Dynamic Nuclear Polarization Breaking through the spin diffusion barrier.*
2014	Talk at ENC in Boston, USA. *The preparation of hyperpolarized water and its use to enhance water-LOGSY drug screening.*

Acknowledgments

Before anyone else, I would like to express my deepest gratitude to my wife, Alice. I wrote the present manuscript while our son, Jasper, was not even a year old. Alice understood the difficulty of my task and supported me and encouraged me all along the way, despite what she had to take on her shoulders. The three of us lived as a solid team during the whole summer so that I could finish on time. Looking back, I can say it was probably the most intense and difficult endeavor I have ever had. But, thanks to Alice and Jasper, it was a joyful one and I am not only proud of myself but also of the three of us as a team.

Next, I would like to thank Sami Jannin, my supervisor. How to describe in only a few words the quality of our relationship, both on the scientific and human level? During the four years of my Ph.D., Sami has given me increasing freedom and responsibilities together with the support I needed. In this fertile context, I was able to realize my own ideas and make the best use of my creativity, which is my primary fuel. But the most astonishing of Sami's contributions to my Ph.D. was that he often encouraged me to do less. To take it easy. Even to take more holidays. At some point, my level of (self-imposed) stress was so high that I feared for my health. Sami helped me to decrease the pressure by setting more realistic goals. The support he gave me will bear fruits far beyond my Ph.D.; I now have a sense of my limits and what it takes to go past them. I wish to take the next steps always remembering the importance of these limits.

I am grateful to the colleagues with whom I started this long adventure of dDNP. The composition of the team remained steady for several years with Samuel Cousin, Stuart Elliott, Morgan Ceillier, Théo El-Daraï, and Olivier Cala. All of us were more or less newbies in the field of dDNP but we came to a beautiful state of understanding of what we were doing, each of us with complementary skills and areas of expertise. Beyond science, we shared a lot more, including our taste for good food and drinks! Over the years, frictions between team members were inevitable but we overcame them, which made these years enriching on many levels.

I thank Stuart for the friendship we built during those years and which lasts despite the distance. I also owe him a lot for his very frequent proofreading of texts I wrote. Stuart's critical eye on my manuscripts has been a constant source of improvement for my expression in English. In particular, I thank him for reading several chapters of this manuscript.

As I transition from Ph.D. student to postdoc, all the team members that I mentioned above left and were replaced by Chloé Gioiosa, Charlotte Bocquelet, James Tolchard, Sylvie Guibert, Nathan Rougier, and Ewoud Vaneeckhaute. This composition of the team is brand new but I can already feel that we are sailing fast in good spirits! I would like to thank Charlotte for her impeccable honesty, which is the best soil for respectful and fruitful relationships.

I would like to thank the Master's students whom I supervised and who contributed in many ways to the work presented in this dissertation: Laurent Esteffe, Quentin Reynard-Feytis, Ilias El Ouar, Safaa Karchi, Pierre Marmey, Alessandro Chessari, and Guillaume Verhaeghe.

Without an institute and those who keep it standing, there would be no work done. I am grateful to Anne Lesage, David Gajan, Cécile Chamignon, Tanguy Le Marchand, Camille Chabillan, and Guido Pintacuda for their contributions, from directing the institute to refilling the magnets and everything in between. Being not so fond of administrative tasks (to say the least), I was extraordinarily lucky to have my case handled by Maryline Deregnaucourt. Maryline is an award-winning administrator who orders what we need for our research in record time and manages to make us travel through the entire world despite the hurdles of the local administrative jungle. Her contribution is inestimable. I also want to thank all the colleagues in the institute, whom I cannot list here, who made these four years fun, renewed, exciting, surprising, and even confronting.

Part of the work I did required instrumentation development. I want to thank Catherine Jose, Christophe Pages, and Stéphane Hupont, from the prototyping service of ISA. Not only they contributed to my work making it technically feasible but they also taught me a lot about electronics, 3D printing, and machining. I also thank Stéphane Martinez from the workshop of the UCBL who machined an insane amount of pieces that we used over the years. Stéphane is always accommodating and manages to get things ready when we need them, which is obviously fantastic.

Why did I do a Ph.D. in NMR? I think the answer is to be found in the intellectual thrill I experienced during my Master's project in Geoffrey Bodenhausen's team at the EPFL, under Sami's supervision. I am therefore grateful to Geoffrey for exciting a transition in me, which then lead me to where I am now.

Several external collaborators have enriched my work, intellectually or through actual experiments. I would like to thank Frédéric Mentink-Vigier from the MagLab, Arthur Pinon from DTU, Arnab Dey, Patrick Giraudeau, and Jean-Nicolas Dumez from CEISAM, Igor Koptyug and Kostya Ivanov from TOMO, Shimon Vega and Akiva Feintuch from the Weizmann institute, Mohamed Sabba, Christian Bengs, and Malcolm Levitt from the University of Southampton, and Román Picazo-Frutos, James Eills, Kirill Sheberstov, John Blanchard, and Dmitry Budker from HIM. I am also grateful to many members of Bruker Biospin from whom I have learned a lot, in particular Dmitry Eshchenko, Roberto Melzi, and Jim Kempf.

My Ph.D. program was part of the ZULF-ITN, a network involving nine research institutes throughout Europe. I thank Szymon Pustelny and Krystian Sycz for making all this happen and all my fellow early-stage researchers with whom it was so much fun to spend weeks of training in Lyon, Mainz, and York. I also thank Andreas Trabesinger, a member of the network, for his enlightening soft skills courses, for his advice, and for helping Anjusha Vijayakumar-Sreeja, Kirill Sheberstov, and me to organize the First International Conference on ZULF-NMR.

Finally, I would like to thank all my family: Christine, Benoît, Loraine, Camille, Grégoire, and Nadia. You understand me so well and you all supported me in so many ways. From raising me (obviously!) to taking care of Jasper or sharing a beer to help me change my mind, the list of reasons why I owe you, deep or light, is endless.

This project has received funding from the European Union's Horizon 2020 research and innovation program under the Marie Skłodowska-Curie grant agreement No 766402 and the ERC Grant Agreement n$^{\text{o}}$714519/HP4all.

To my grandfather Paul, for his silent inspiration

To my parents Christine and Benoît, for their constant faith in me

To my wife Alice, for her support beyond words

To my son Jasper, for his smiles and shouts

Dearly, Quentin

Chapter 1

Introduction

Nuclear magnetic resonance (NMR) spectroscopy is an analytical method that makes use of the intrinsic magnetic moment of the nucleus of some atoms to gain information on matter. We call this magnetic moment *spin*. Spin is a purely quantum mechanical property whose dynamics are very well understood. This allows NMR spectroscopists to design sophisticated experiments to "ask" equally sophisticated questions to matter, giving rise to a plethora of applications.

The most well-known application of NMR is magnetic resonance imaging (MRI). In the simplest case, MRI is able to measure the density of a nuclear species in 3D, typically with sub-mm resolution. Further than that, it can provide more detailed information such as 3D-resolved relaxation properties, diffusion tensors, and spectroscopic data. Because MRI is non-destructive, non-invasive, and can give access to such rich information, it is used in hospitals as a unique diagnostic tool. But MRI is only the tip of the iceberg of NMR methods: NMR is used routinely by synthetic chemists to analyze the structure of the compounds they produce or to monitor reaction kinetics in real-time; it is used by biological chemists to determine the 3D structures and dynamics of complex proteins containing thousands of atoms or to search for possible drug candidates by detecting the interaction between small molecules and enzymes; it is used by materials scientists to unravel the structure of active-sites of surface catalysts. As varied as it can be, this list is far from exhaustive and every year new methods and applications of NMR are invented.

1.1 The paradigm of high magnetic fields

In typical NMR experiments, a sample containing a large number of spins is immersed in a strong magnetic field. For example, the most common NMR spectrometers operate at a magnetic field $B_0 = 9.4$ T, which is about 200'000 times larger than the Earth's magnetic field. Spins tend to align parallel with the magnetic field (or in some other particular orientations)[1]. One can displace the spins from their equilibrium position by applying radio frequency (rf) pulses perpendicular to the magnetic field direction at the appropriate frequency. The same coil which produces the rf pulse is then used to measure the signal emitted by the spins as they return towards their equilibrium position. The resonance frequency (or precessing frequency) of the spins in a magnetic field B_0 is

$$\omega_0 = -\gamma B_0, \tag{1.1}$$

which is called the Larmor frequency. The constant γ is the gyromagnetic ratio of the spin expressed in rad.s^{-1}.T^{-1}or MHz.T^{-1}. For example, a proton spin (which corresponds to the nucleus of a

---

[1] This simplified representation of spins corresponds to the vector model. A more accurate picture will be given in Chapter 2.

^{1}H atom) has a gyromagnetic ratio of $267.5 \cdot 10^6$ rad.s^{-1}.T^{-1}or 42.58 MHz.T^{-1}, while a ^{13}C spin has gyromagnetic ratio of $67.261 \cdot 10^6$ rad.s^{-1}.T^{-1}or 10.705 MHz.T^{-1}. The Larmor frequencies of ^{1}H or ^{13}C spins at 9.4 T are therefore 400 and 100 MHz, respectively.

Generating a magnetic field as high as 9.4 T is not trivial. It requires the use of superconductivity and hence liquid helium, which implies high running costs. At the time of writing, the high-resolution NMR spectrometer with the world's highest available magnetic field operates at 28.2 T. This magnet is sold for more than 10 million euros, weighs 8 tons, and is more than 4 m high. [1] One can wonder why spectroscopists would want to acquire instruments that are so bulky and expensive. There are two main reasons: sensitivity and resolution. [2] We will now show in detail how the magnetic field strength influences these parameters.

1.1.1 NMR sensitivity

As compared to other forms of spectroscopy, NMR is inherently insensitive. As we will see in more detail in Section 2.2.2, the signal intensities S recorded in NMR experiments are proportional to the nuclear spin polarization P, which corresponds to the degree of alignment of the spins with the magnetic field

$$S \propto P. \tag{1.2}$$

At thermal equilibrium, the polarization of a spin 1/2 is given by Boltzmann's distribution [3]

$$P = \tanh\left(\frac{\hbar\gamma B_0}{2k_bT}\right), \tag{1.3}$$

where $\hbar = 1.05457182 \times 10^{-34}$ m^2.kg.s^{-1} is the reduced Planck constant, $k_B = 1.380649 \times 10^{-23}$ m^2.kg.s^{-2}.K^{-1} is Boltzmann's constant and T is the temperature of the sample. The numerator of the fraction corresponds to the energy released by the spins as they align with the field and is called the Zeeman energy while the denominator corresponds to the thermal energy of the system, which tends to randomize the orientation of the spins. Even at the highest available magnetic fields and temperatures as low as 1 K, the thermal energy greatly exceeds the Zeeman energy. The fraction in the equation above is, therefore, close to 0 and the equation simplifies to

$$P \approx \frac{\hbar\gamma B_0}{2k_bT}, \tag{1.4}$$

which implies that the nuclear polarization is proportional to the magnetic field and the nuclear gyromagnetic ratio and inversely proportional to the temperature. At a field $B_0 = 28.2$ T, i.e., the highest available magnetic field for high-resolution NMR, the polarization of ^{1}H and ^{13}C spins yield the deceiving values of ≈ 97 and ≈ 24 ppm, respectively. Figure 1.1 shows the nuclear polarization for ^{1}H, ^{13}C and ^{15}N spins as a function of the magnetic field at room temperature. The polarization is on the order of 10^{-10} at Earth's magnetic field, on the order of tens to hundreds of ppm at high magnetic field, and only approaches unity, i.e. the theoretical maximum, at unrealistic values of MT (mega Tesla).

The magnetic field strength also influences sensitivity because of Faraday's law of induction. Indeed, the electromotive force (EMF) that the oscillating spins exert on the coil is proportional to their oscillation frequency, [4, 5] which is in turn proportional to the magnetic field strength (see Eq. 1.1). However, at MHz frequency, the penetration of electromagnetic waves in conductors is limited by the skin depth, [4, 5] which causes an attenuation of the induced current proportional to $\sqrt{\omega_0}$. Taken together, the EMF dependence on frequency and the effect of the skin depth result in a signal proportionality to the field strength

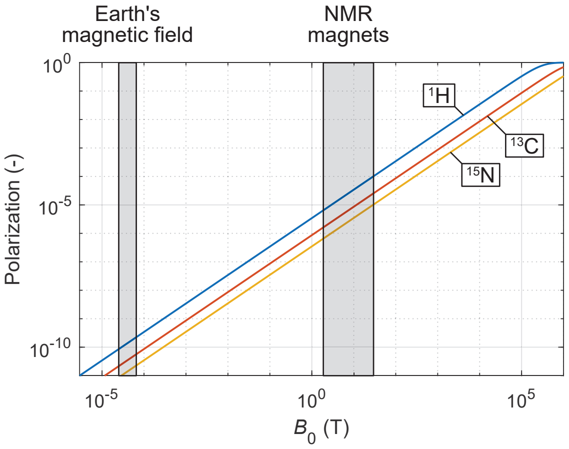

Figure 1.1: Effect of the magnetic field strength on nuclear polarization for three commonly used isotopes at a temperature of 298 K. The grey boxes indicate the span of the Earth's magnetic field and that of NMR magnets, from benchtop spectrometers using permanent magnets to the highest available high-resolution magnet.

$$S \propto \omega_0 \frac{1}{\sqrt{\omega_0}} = \omega_0^{1/2} \propto B_0^{1/2}. \tag{1.5}$$

The NMR signal is therefore proportional to the magnetic field strength because of Boltzmann distribution and proportional to the square root of the magnetic field strength because of the law of induction and the skin depth, yielding

$$S \propto B_0 \cdot B_0^{1/2} = B_0^{3/2}, \tag{1.6}$$

as illustrated in Fig. 1.2A. To overcome the poor sensitivity of NMR, it is common to repeat an experiment many times and add up the resulting signals. As more scans are summed, the signal remains constant while the noise decreases with $\sqrt{n_S}$, where n_S is the number of scans, and so the signal-to-noise ratio (SNR) $R_{S/N}$ increases as

$$R_{S/N} = \frac{n_S S_0}{\sqrt{n_S} N_0} = \sqrt{n_S} \frac{S_0}{N_0}, \tag{1.7}$$

where S_0 and N_0 are the signal and noise intensities of a single measurement, respectively. The number of scans to reach an arbitrary SNR $R_{S/N}$ is thus

$$n_S = \left(\frac{R_{S/N} N_0}{S_0} \right)^2 \tag{1.8}$$

The total experimental time t_{exp} is proportional to the number of scans and because of the relation between the signal and the magnetic field (see Eq. 1.6), we have

$$t_{aq} \propto n_S \propto B_0^{-3}. \tag{1.9}$$

This shows that the time necessary to obtain an arbitrary SNR decreases with the third power of the magnetic field. For example, if a signal is acquired in one time unit at 28.2 T, reaching the same SNR on a benchtop spectrometer operating at 1.88 T will require more than 3000 time units, as depicted in Fig. 1.2B. In other words, increasing the magnetic field strength tremendously diminishes the time necessary to acquire NMR experiments.

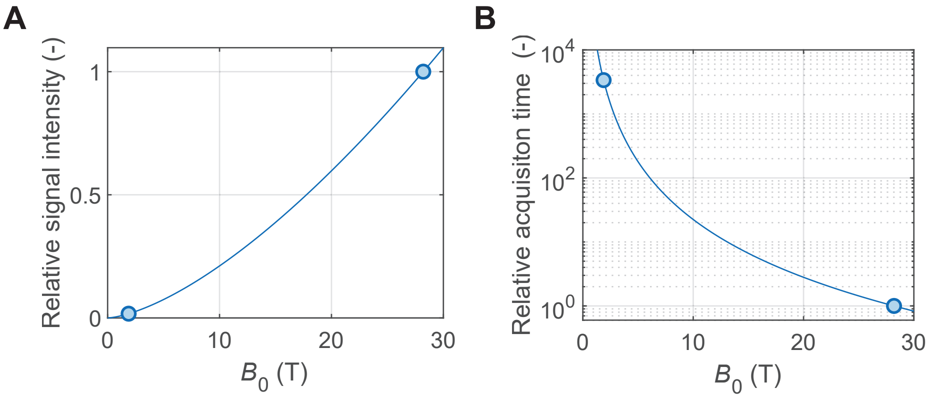

Figure 1.2: **A**. NMR signal intensity relative to that at 28.2 T as a function of the magnetic field strength. **B**. Acquisition time to obtain an arbitrary SNR relative to that at 28.2 T as a function of the magnetic field strength. The colored dots represent the fields of 1.88 and 28.2 T, that is, the magnetic field used in a common benchtop NMR spectrometer and the highest available magnetic field for high-resolution NMR, respectively.

1.1.2 NMR resolution

In addition to improving the sensitivity, increasing the magnetic field also improves the resolution in NMR experiments. For example, let us take a liquid-state sample containing a large number of different species. The spectral features are usually dominated by two factors: the chemical shift of each group of magnetically equivalent spins and the J-coupling between them. Each group of magnetically equivalent spins will have a multiplet centered at chemical shift δ_0 with splitting patterns depending on the J-couplings with the neighboring spins. The chemical shift difference between the groups of equivalent spins gives rise to a frequency difference that is proportional to the magnetic field strength

$$|\Delta\omega| = |\gamma B_0 \left(\delta_{0,1} - \delta_{0,2}\right)|, \tag{1.10}$$

where $\delta_{0,1}$ and $\delta_{0,2}$ are the chemical shifts of two groups of magnetically equivalent spins. On the contrary, J-couplings give rise to splittings which are independent of the magnetic field strength. This implies that increasing the magnetic field strength increases the separation between multiplets and thus decreases potential overlaps between them (this is also true for dipolar and quadrupolar couplings in solid-state NMR). In practice, this allows for better interpretation of the spectra. Fig. 1.3 is an attempt to illustrate this fact. The ^{1}H spectra for the same mix of 12 molecules with equal concentration, with random couplings between -15 and +15 Hz and with random chemical shifts between 1 and 2 ppm were simulated[2] for various magnetic fields (but the same distribution of couplings and chemical shifts). The imaginary sample whose spectrum is simulated here could correspond to a complex mixture of alkanes. As the magnetic field strength is increased, it is clear that the spectral feature becomes sharper and that individual resonances can be identified more easily.

The benefits of increasing the magnetic field strength for the resolution and sensitivity of NMR experiments have motivated the construction of ever stronger magnets. In 2009, the world's first 23.5 T spectrometer was installed at the Centre de Résonance Magnétique Nucléaire à Très Haut

---

[2] All simulations presented in this chapter were performed using home-written MATLAB scripts. This introductory chapter does not give many details on how simulations are performed. More details are given in Chapter 2.

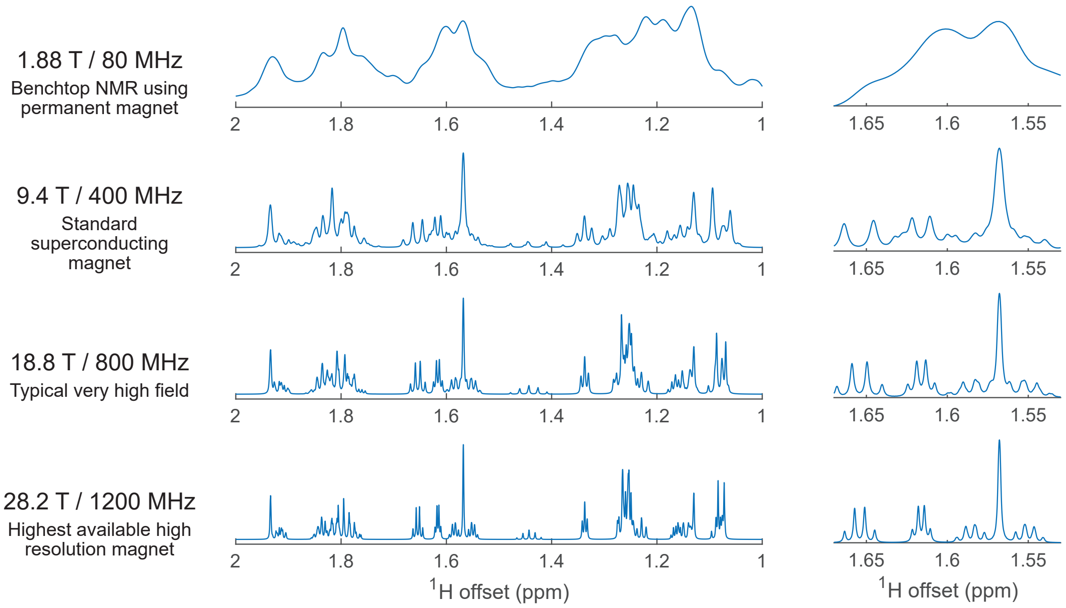

Figure 1.3: Effect of the magnetic field strength on the resolution of high-field NMR illustrated by the simulation of ^{1}H spectra at various magnetic fields for the same mix of 12 molecules, with equal concentration with random couplings between -15 and +15 Hz and with random chemical shifts between 1 and 2 ppm (with spin topology A_3B_2C, A_3B_3, A_2B_2, A_4B, A_3B_2C, A_2B_2...) with a line broadening of 2 Hz. Each spectrum is normalized to the maximum intensity. The spectra on the right are a zoom of those on the left.

Champ (CRMN) at the Université Claude Bernard Lyon 1 in France. This field corresponds to a ^{1}H Larmor frequency of 1 GHz. It took 11 years until the world's first 28.2 T spectrometer was installed at the Centro Risonanze Magnetiche (CERM) at the University of Florence in Italy [1]. This field corresponds to a ^{1}H Larmor frequency of 1.2 GHz. If increasing the magnetic field strength is a strategy that brings obvious benefits, improvements come slowly and result in extraordinarily bulky and expensive instruments.

In the field of medical MRI, common scanners operate at 1.5 and 3 T. Scanners operating at 7 T and higher exist but they are not used routinely for humans. [6] Here, the limitation is not only technical; there are medical risks associated with exposing a patient to extreme magnetic fields. Furthermore, the stronger the magnetic field the higher the specific absorption rate experienced by the patient (i.e. the deposited rf power on their body). Yet, higher magnetic field strengths and hence higher sensitivity would help boost methods like magnetic resonance spectroscopy.

Progress in the sensitivity of NMR spectroscopy can only remain slow and incremental if the approach consists only of increasing the magnetic field strength. For medical MRI, the limit is already reached and so progress cannot be expected from this strategy. However, moving away from the paradigm of high magnetic fields, we will see that the sensitivity of both NMR and MRI can be improved by more than four orders of magnitude without increasing the magnetic field. If one cannot increase the Larmor frequency of the spins without increasing the magnetic field strength, one can transiently increase the nuclear polarization. The enhancement in nuclear polarization translates linearly into an enhancement in signal intensity and hence in SNR and limit of detection. This approach is called hyperpolarization. In particular, this work is focused on a hyperpolarization method called dynamic nuclear polarization (DNP).

1.2 Increased sensitivity using dynamic nuclear polarization

Hyperpolarization methods can be defined as methods to increase transiently the nuclear polarization usually far above Boltzmann equilibrium. There exists a variety of such methods, which make use of very different physics: spin-exchange optical pumping (SEOP) uses direct optical pumping of noble gas atoms; parahydrogen induced polarization (PHIP) uses the spontaneous population of the singlet state of hydrogen gas at low temperature; methods based color-centers in diamonds (like nitrogen-vacancy centers) use optical pumping of electron spins; while DNP uses the intrinsically high polarization of the electron spin.

1.2.1 From the origins of DNP to magic angle spinning DNP

DNP is almost as old as NMR. It was imagined and described in theory by Albert Overhauser in 1953 [7] and confirmed experimentally the same year by Carver and Slichter. [8] DNP consists of transferring the polarization of unpaired electron spins to surrounding nuclear spins *via* microwave (μw) irradiation at (or near) the Larmor frequency of the electron spins. The electron has a large gyromagnetic ratio compared to nuclear spins, corresponding to ≈ 658 times and ≈ 2618 times that of ^{1}H and ^{13}C spins, respectively, and so the electron Boltzmann polarization is correspondingly larger (see Eq. 1.4). Overhauser's idea was to use the conductive electrons in metals to polarize the nuclei. μw irradiation transiently diminishes the net electron polarization. As they return to equilibrium, electron spins polarize nuclear spins by a phenomenon of cross-relaxation mediated by electron mobility (this will be described in more detail in the dedicated Sec. 3.2). This mechanism called the Overhauser effect (OE) after his inventor, can be described in terms of a 1 electron-1 nucleus model. Following Overhauser's invention, DNP was shown to be possible in insulating solids, in particular in crystals doped with paramagnetic transition metals [9] and in amorphous materials [10]. More DNP mechanisms were discovered experimentally and described in theory: [11] the solid effect (SE), [9, 12, 13] which can also be described in terms of 1 nucleus-1 electron model; the cross effect (CE), which is described in terms of a 1-nucleus-2 electron model; [14] and the thermal mixing (TM) which is described in terms of 1 nucleus and many electron spins. [15, 3] Already in 1965, ^{1}H polarizations up to 70% were reported. [13] Until the seventies, the main application of DNP and the main driving force for its development was to create polarized targets in the context of particle physics and high energy physics. [16, 17] Then, in the eighties, DNP stopped receiving as much attention.

Already in 1983, it was shown that DNP was compatible with magic angle spinning (MAS), a method that is necessary to ensure high resolution for solid-state NMR. [18] However, it is in the nineties that the method knew an important revival, thanks to the work of Robert G. Griffin and co-workers. The use of strong μw sources such as gyrotrons enabled to use of MAS-DNP at higher magnetic fields. [19] Then, it was shown that MAS-DNP could be performed on frozen solutions that were compatible with biological substrates. [20, 21]. MAS-DNP thus became a powerful tool for the study of biological samples in the solid-state and this field of research continued continues to expand today. [22]

1.2.2 Hyperpolarized liquid-state NMR using dissolution DNP

MAS-DNP established DNP as a method for enhancing the sensitivity of solid-state NMR. But what about liquid-state NMR? In the early days of DNP, it was recognized that DNP was possible in the liquid-state using the OE. In this case, it is the mobility of the molecules in solution which mediates the electron-nucleus cross-relaxation, thus polarizing the nuclear spins. [23] Liquid-state

OE-DNP has kept being developed since then. [24] However, a methodological breakthrough came with the introduction of dissolution DNP (dDNP); in 2003, Jan-Henrik Ardenkjær-Larsen *et al.* reported an experiment combining solid-state DNP and high-resolution liquid-state NMR. [25] In the original experiment, ^{13}C spins were first polarized in a frozen solution at 3.35 T and 1.2 K, using a stable organic radical as a source of unpaired electron spins. Once ^{13}C polarization on the order of 26% was reached, the solution was dissolved and diluted by hot water directly within the cryostat of the DNP polarizer and rapidly propelled by pressurized He gas into a 9.4 T NMR spectrometer, where the hyperpolarized liquid-state ^{13}C signal was detected. The first reported experiment resulted in a liquid-state signal enhancement of more than 10'000 with respect to a standard experiment at Boltzmann equilibrium as shown in Fig. 1.4. [25] Fig. 1.5 summarizes the steps of a typical dDNP experiment.

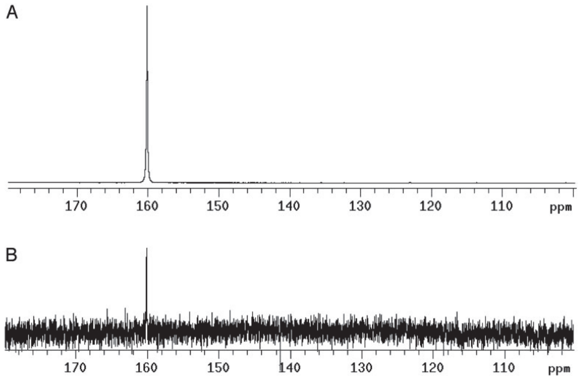

Figure 1.4: Result of the first reported dDNP experiment reproduced with permission from Ref. [25] (Copyright (2003) National Academy of Sciences, U.S.A.). **A**. Single scan detection of natural abundance ^{13}C in urea hyperpolarized by dDNP and detected in the liquid-state at 9.4 T. **B**. Signal averaging of 232'128 scans on the same sample at thermal equilibrium (without DNP).

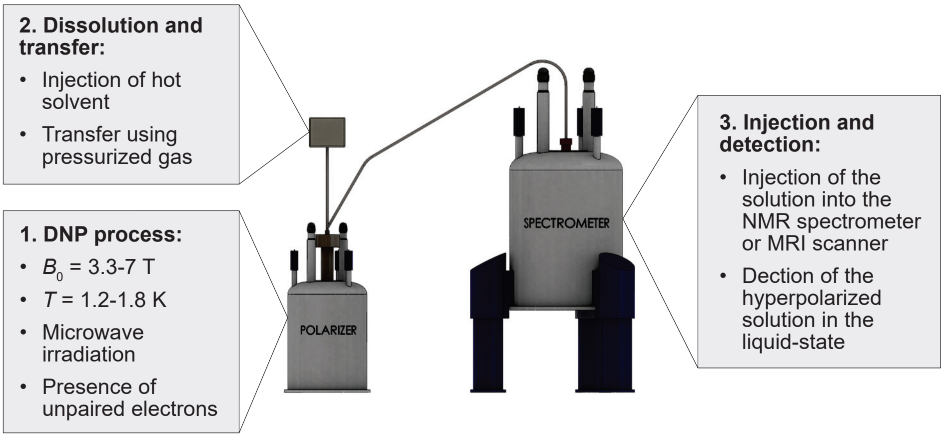

Figure 1.5: Steps of a dDNP experiment in typical operating conditions.

There are several key features to this experiment: first, DNP is performed in conditions where the electron polarization is near unity, as shown in Fig. 1.6, which leads to high nuclear polarization; before the sample escapes the high magnetic field of the polarizer, it is dissolved to avoid strong paramagnetic relaxation in the solid state at low magnetic fields; finally, the sample is diluted by the dissolution solvent which mitigates liquid-state paramagnetic relaxation during the transfer and during detection in the liquid state. These ingredients made dDNP a powerful method for the preparation of hyperpolarized nuclei, in particular for low-γ nuclei, as their relaxation time constants are more forgiving.

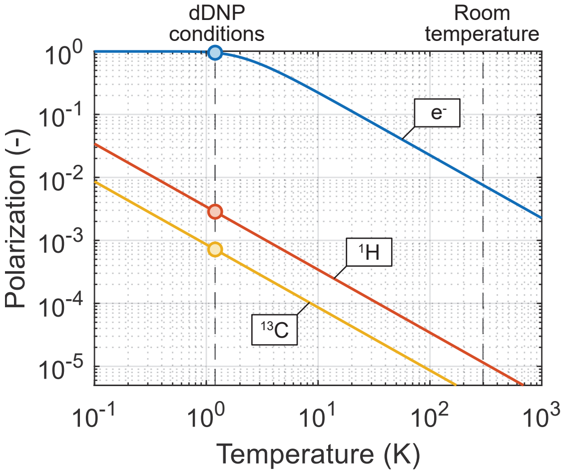

Figure 1.6: Electron spin polarization as a function of temperature at a magnetic field of 3.35 T (i.e. that used for the first reported dDNP experiment), compared with the nuclear spin polarization of ^{1}H and ^{13}C spins.

The great potential of dDNP was revealed when it was used to prepare hyperpolarized metabolites in the context of medical imaging and tumor detection in rats [26, 27] and then in humans. [28] Due to the low natural abundance of ^{13}C and the contrast in polarization, only the hyperpolarized species is visible on ^{13}C MRI images and so the conversion of pyruvate into other metabolites of the Krebs cycle can be monitored as a function of both time and space. The presence of tumor cells is revealed by their rapid uptake of pyruvate and the subsequent conversion into lactate, because of the so-called "Warburg" effect.

The application of dDNP for medical imaging provided a driving force for the development of the method. In parallel, the sensitivity gain offered by dDNP allowed for a number of spectroscopic applications; it was used to push forward the detection limits in drug screening [29, 30, 31, 32] and in metabolomics; [33, 34] it was used to study protein dynamics [35, 36, 37] and to monitor chemical reactions in real-time. [38, 39, 40, 41] In most cases, these applications are based on already existing methodologies of conventional (i.e. non-hyperpolarized) NMR. Yet, the sensitivity boost offered by dDNP pushes the limits of these methods, enabling the observation of processes that would otherwise take too long to be relevant and at lower solute concentrations.

The methodology of dDNP has also been improved in many ways since 2003. Ardenkjaer-Larsen's first experiments were performed at 3.35 T using the radical trityl, which has a narrow electron paramagnetic resonance (EPR) line and is best suited for low-γ nuclei. [25] Higher magnetic fields were later used, typically around 7 T [42, 43] and 9.4 and 10.1 T are also reported [44, 45]. The radical 4-hydroxy-2,2,6,6-tetramethylpiperidin-1-oxyl (TEMPOL) was later used for dDNP to polarize ^{1}H spins [46] and combined with $^1\text{H}\rightarrow^{13}\text{C}$ and $^1\text{H}\rightarrow^{15}\text{N}$ cross-polarization (CP) to polarize low-γ nuclei rapidly and efficiently. [47] μw frequency modulation was used to boost the performance of DNP [48] and μw gating was shown to drastically improve the performance of CP. [49] The use of high-spin lanthanides was shown to boost DNP performance, in particular in the case of DNP with trityl and other narrow EPR line radicals. [50, 51, 52] Magnetic tunnels were developed to mitigate polarization losses at low magnetic fields. [53] Polarizing matrices where the radical molecules are grafted on porous material were developed such that the radical could be filtered out after dissolution. [54] Strategies were also proposed to extend the lifetime of hyperpolarization to several hours such that a hyperpolarized solution could be transported from a point of production to a point of use. [55, 56, 57] Last but not least, the understanding of the processes behind DNP experiments in dDNP conditions has been the subject of constant effort, whether regarding DNP mechanisms [58, 59, 60, 61, 62, 63], hyperpolarized NMR lineshapes [64, 65], electron spin dynamics [66, 67] spin diffusion, i.e., the process of nuclear polarization transport across the sample [68] or the simulation of the overall DNP process under dDNP conditions. [69, 70, 71, 72]

Two decades after its invention, dDNP is accepted as a powerful and versatile tool to hyperpolarize a broad range of molecules to high levels. Yet, dDNP has been actively developed by few groups and a large part of the dDNP playground remains unexplored; a lot of established NMR methods could still benefit from dDNP hyperpolarization. Moreover, some fundamental questions remain unanswered. What is the mechanism for ^{1}H DNP with the TEMPOL, CE or TM? How does nuclear polarization diffuse away from the electron spin? What are the consequences of methyl rotation for DNP mechanisms and spin diffusion? To list only a few examples.

1.2.3 High resolution at zero- to ultra-low field regime

As we saw in the first section, the relation between the resolution of NMR spectra and the magnetic field strength has motivated the construction of NMR magnets operating at ever-increasing fields. However, the other extreme, i.e., the regime where the magnetic field can be considered as absent or only a small perturbation, is also promising.

This regime called zero- to ultra low-field NMR (ZULF) was first investigated in the eighties by A. Pines and co-workers. [73, 74, 75] Typical experiments consisted of shuttling amorphous solid samples from a high-field spectrometer to a region above the NMR magnet where the magnetic field could be switched on and off suddenly (i.e., sufficiently fast to be considered instantaneous). The sample was first thermally prepolarized at high-field and then shuttled to the zero-field chamber. The field was switched off during a variable time t_1 and switched back on. Finally, the sample was brought back into the NMR magnet for detection at high magnetic field. The experiment was repeated varying t_1 and the resulting signal was Fourier transformed with respect to t_1, thus revealing the spectrum of evolution at zero-field. Because the zero-field Hamiltonian only contains the spin-spin interactions, this spectrum solely features spin-spin interactions. What is unique to the zero-field regime, the eigenfrequencies remain the same regardless of the orientation of the molecule. Fig. 1.7 shows the comparison of simulated high-field and zero-field spectra for a pair of dipolar coupled ^{1}H spins separated by 1.6 Å (which corresponds to water in a typical sample of barium chlorate monohydrate) together with the experimental diagrams. The zero-field spectrum of an amorphous sample features the same resolution as that of oriented monocrystals at high-field, instead of a Pake pattern and so it yields more ”concise” spectral features than the high-field equivalent for the same information. The same is true for quadrupolar interactions. [74]

Despite the appealing features of ZULF-NMR, the method did not arouse interest among solid-state NMR experimentalists. This is probably due to the fact that spectra at zero-field get rapidly more complicated, as more complex spin systems are considered. [74] In fact, they get equally complicated as high-field spectra but without the possibility to perform MAS and recover a simpler spectrum. [74] However, ZULF-NMR got more popular after direct detection at ZULF was introduced. The common Faraday induction used at high-field is hopeless at ZULF because the observed frequencies are too low but other detection methods have been proposed: first super-

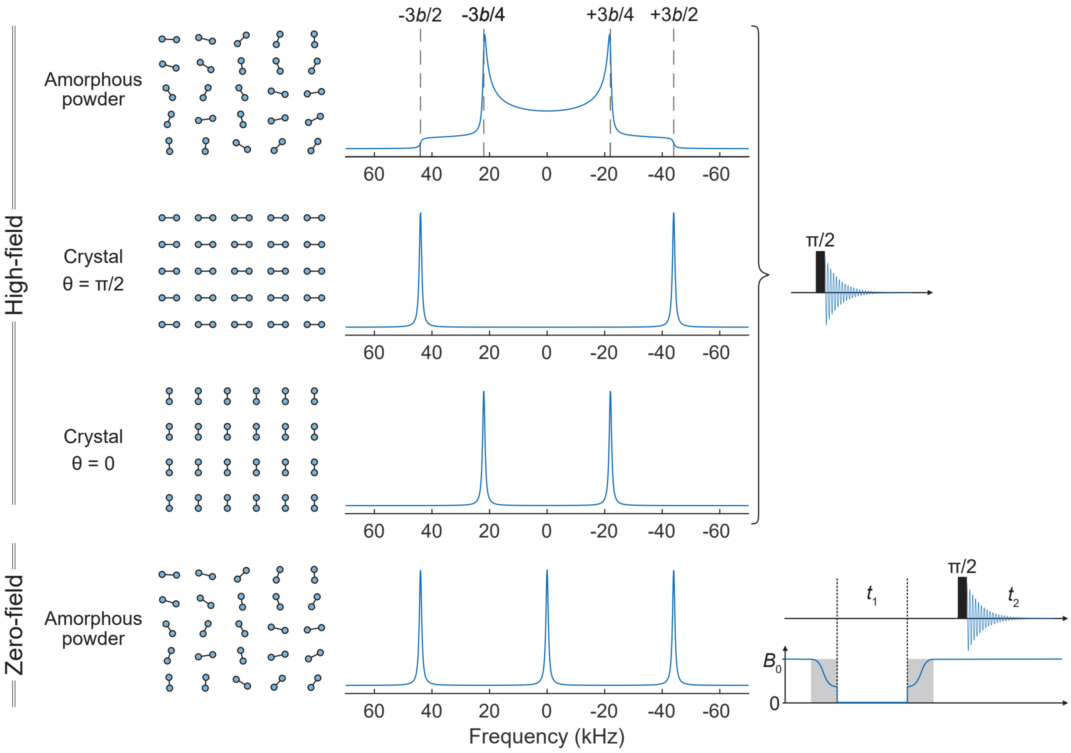

Figure 1.7: Difference between solid-state NMR spectra at high-field and at zero-field. Simulation of spectra for an A_2 pair of ^{1}H spins with an internuclear distance of 1.6 Å, corresponding to a dipole coupling constant of $b = 29.3$ kHz. The high-field experiment is a simple pulse-acquire experiment while the zero-field is a field-cycling experiment with prepolarization and detection at high-field and evolution at zero-field. High-field experiments were simulated for three cases: an amorphous powder and two crystalline samples, with the internuclear vector, either orthogonal or colinear with the magnetic field ($\theta = 0$ or $\pi/2$, respectively). The zero-field experiment was simulated for an amorphous powder. The grey squares on the pulse diagrams of the zero-field experiment indicate the moments where the sample is shuttled up and down. The molecular orientations were averaged over 1000 constant increments of the angle between the molecular vector and the magnetic field, from 0 to π. A line broadening of 1 kHz was applied to the simulated FID prior to Fourier transform.

conducting quantum interference devices (SQUIDs) [76] and then optical pumped magnetometers (OPM) based on rubidium vapor (or other alkali atoms) using the spin exchange relaxation-free (SERF) regime. [77] In particular, SERF-OPMs are well suited for low frequencies up to a few hundreds of Hz. They are cheap (compared with high-field detection devices), sensitive, and can be made portable. [78, 79, 80] Pioneered by D. Budker and coworkers, this detection method was used to detect ZULF signals in the liquid-state. [77, 81, 82] Fig. 1.8A shows a typical modern setup for liquid-state ZULF experiments, using thermal prepolarization in Halbach magnets and detection at ZULF. [81] In the case of isotropic liquids, ZULF spectra are dominated by the J-interaction and so liquid-state ZULF-NMR is often referred to as a J-spectroscopy method. A particularity of liquid-state ZULF-NMR is that it can only detect heteronuclear couplings. In other words, for a molecule to produce a detectable ZULF signal in the liquid-state, it must contain at least two J-coupled spins of different nuclear species. In the simplest case, i.e. an XA spin system like ^{13}C-formate, the spectrum consists of a single line at the J-coupling between the ^{1}H and the ^{13}C spins. Fig. 1.8B shows simulated spectra at high-field, where the J-coupling is only a perturbation with respect to the Zeeman interaction causing a splitting corresponding to the J-coupling; at zero-field, where only the J-coupling is present and causes observable transitions at the J-coupling; and at ultra low-field, where a small bias field of 500 nT perpendicular to the initial magnetization vector splits the zero-field signals. In these simulated ZULF experiments, as was the case for the solid-state experiments, coherences are induced by the sudden transition from the high-field states to the zero-field states.

An important feature of the zero-field regime in the liquid-state is that small molecules exhibit very long coherence time constants, often resulting in experimental signal linewidth on the order of tens of mHz. [83] For a simple XA system as in Fig. 1.8, this can be explained by the fact that the eigenstates at zero-field belong to the singlet-triplet basis even for pairs of heteronuclei and the signal detected in the ZULF experiment is the coherence between the S_0 and T_0 states. [81] As was exploited by M. H. Levitt and coworkers and many others after them, the imbalance between the singlet state and the triplet manifold is immune to internal dipolar relaxation. [84] In simple words, a pair of spins in singlet state do not make each other relax *via* the in-pair dipole-dipole relaxation mechanism, which causes the state to be long-lived (i.e., exceeding T_1). Moreover, the narrow linewidth of ZULF signals is retained even in heterogeneous samples (e.g. solution in porous media or solution containing bubbles). Indeed, the field lines cannot be distorted by changes in magnetic susceptibility, simply because there are no field lines. [85, 86, 87]

If conventional NMR suffers from an inherent low sensitivity, it is even worse in the ZULF regime, first because prepolarization is typically performed in permanent magnets, which are limited to ≈ 2 T; and second, because direct detection at ZULF remains less sensitive that inductive detection at high-field, even for state-of-the-art ZULF detection methods. As a result, ZULF-NMR with thermal prepolarization is commonly limited to neat labeled liquids (with a concentration in the molar range). However, ZULF-NMR can be boosted by hyperpolarization techniques. [88] In recent years, a number of experiments combining PHIP and ZULF-NMR have been reported. [88, 86, 89, 90] The coupling of dDNP with ZULF NMR has been exploited in a single study yet. [91]

So far, ZULF-NMR has mainly been used in fundamental research such as dark matter searches [92] but has also been proposed as a new form of NMR spectroscopy for chemical analysis. [93, 79, 94] The ZULF regime has a strong potential for relaxometry studies of porous media as the low frequencies of the spin states at ZULF make relaxation rates sensitive to slower dynamics, which are typical of porous media. [85, 86, 87] In parallel to signal detection at ZULF, spin dynamics at ZULF are used for the preparation of hyperpolarized metabolites for medical imaging. [89, 95] The ZULF regime was found to be well-suited for the transfer of polarization from parahydrogen to ^{13}C-metabolites. This approach could compete with dDNP because it is much cheaper and more portable. MRI images using ZULF-PHIP have been reported [96, 97] and clinical trials are now close.

We ought to make it clear that ZULF-NMR is unlikely to compete with that of high-field NMR for the study of complex samples containing thousands of atoms, as commonly encountered in biological NMR. Indeed, the absence of chemical shift separation at ZULF causes spectral components to overlap making their interpretation practically impossible. The advantages of ZULF are the portability and low cost of the experimental setups as well as in more fundamental aspects (long coherence time, insensitivity to sample heterogeneity, untruncated spin-spin Hamiltonian), which make it complementary to high-field NMR. ZULF-NMR is a relatively new research field and new applications are emerging.

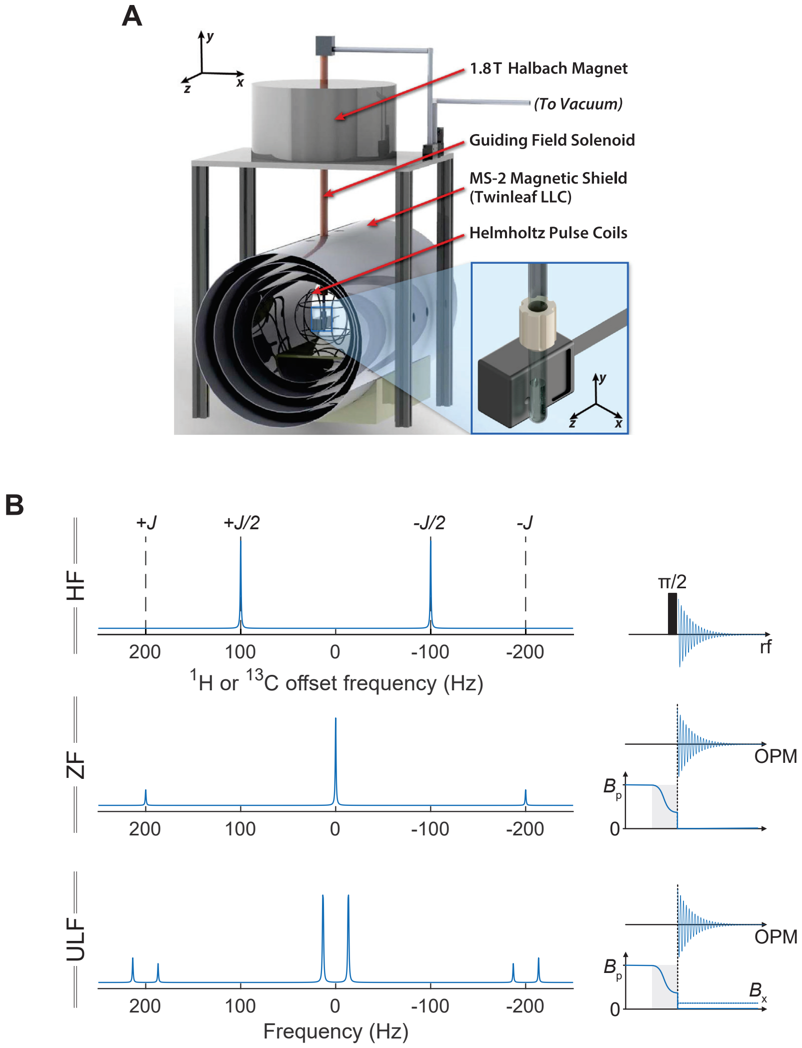

Figure 1.8: **A**. Typical setup for liquid-state ZULF NMR, reproduced with permission from Ref. [80]. The sample is prepolarized in a permanent magnet in Halbach array, shuttled to the zero-field chamber consisting of commercial magnetic shields, and detected using a commercial OPM. **B**. Difference between liquid-state NMR spectra at high-field (HF), zero-field (ZF), and ultra low-field (ULF). Simulation of spectra for an XA pair of ^{1}H and ^{13}C spins with a J-coupling $J = 200$ Hz. The high-field experiment corresponds to ^{1}H as well as ^{13}C detection as it yields the exact same spectrum. The zero-field experiments consist of a sudden transition from high-field to zero-field with initial prepolarization at field B_p. The ultra low-field experiment is the same as that at zero-field except that a small bias field of $B_x = 500$ nT is applied along the x-axis during detection. The grey squares on the pulse diagrams of the ZULF experiments indicate the moments where the sample is shuttled up and down (the simulation neglects the evolution of the system during the shuttling period). A line broadening of 1 Hz was applied to the FID prior to Fourier transform. Note that the axis convention of Panel A (reproduced with permission from Ref. [80]) is different from that used in this work.

1.3 This work and the organization of the dissertation

This work is an exploration of the spin dynamics at stake in dDNP experiments and in hyperpolarized liquid-state NMR at high-field and at ZULF, with a particular focus on polarization transfers among spins and the methods used to study them. Fig. 1.9 gives a schematic representation of the polarization transfers studied in this work.

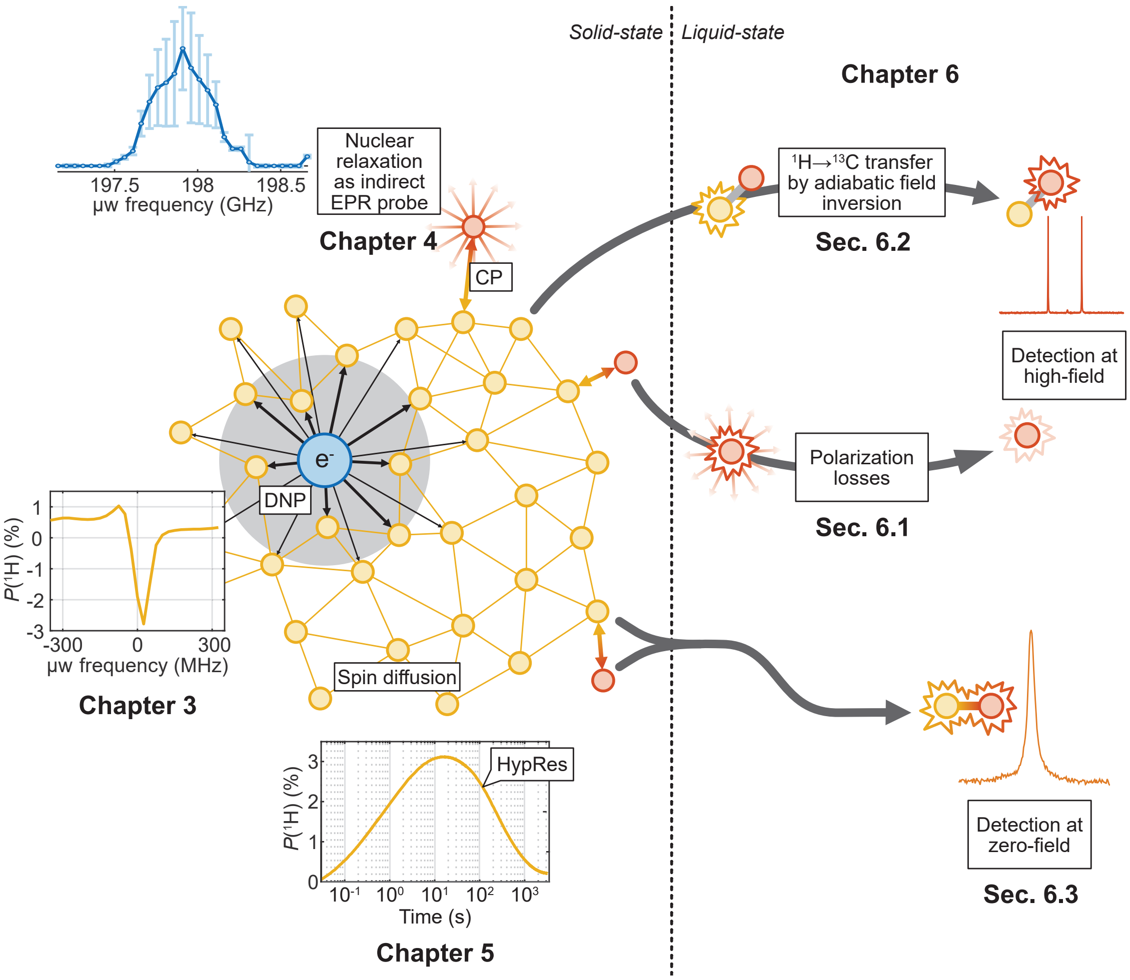

Figure 1.9: Schematic representation of electron and nuclear spins and the polarization transfers between them in dDNP experiments and in hyperpolarized liquid-state NMR at ZULF. The blue circle represents an electron spin (with e$^-$ written in its center) interacting with surrounding ^{1}H spins. The gray circle around the electron spin represents the area within the spin diffusion barrier. Red circles represent ^{13}C spins, which are polarized either by CP in the solid-state or by adiabatic field inversion in the liquid-state.

Before experimental results are presented in Chapters 3-6, the basic concepts of quantum mechanics and spin dynamics are exposed in Chapter 2. After introducing the concept of spin, the postulates of quantum mechanics are presented and used to derive the density matrix formalism for the description of interacting spin ensembles. Relevant interactions for dDNP and liquid-state

NMR at ZULF are then presented and the spectral features they lead to are illustrated by numerical simulations.

Chapter 3 is dedicated to solid-state DNP. The instrumentation and methods used in this work are detailed in the first section. Then, the theory of electron-nucleus polarization transfers under μw irradiation, i.e., DNP mechanisms, is briefly reviewed. The DNP mechanisms are illustrated experimentally in the last two sections of the chapter by μw spectra, which consists of plots of DNP polarization vs. μw irradiation frequency (see example in Fig. 1.9). In Chapter 4, transfers of polarization between nuclear spins and their environment, i.e., relaxation, are used as an indirect probe to measure EPR properties (see example in Fig. 1.9). Chapter 5 is concerned with polarization transfers between homonuclear spins in the vicinity of the electron, i.e., spin diffusion near or through the spin diffusion barrier. The first section reviews the literature on the spin diffusion barrier. Then, the hyperpolarization resurgence (HypRes), a method to study spin diffusion in the vicinity of the electron, is introduced and results recorded in a variety of conditions are presented. Fig. 1.9 shows an example of a HypRes curve, where the polarization of bulk nuclear spins rises due to spin diffusion from hyperpolarized nuclear spins in the vicinity of the electron. The influence of the electron polarization on this process is demonstrated using HypRes and confirmed by a three spin-model.

Chapter 6 presents the liquid-state side of dDNP experiments. The instrumentation and methods of the dissolution experiments performed in this work are detailed in the first section. The sources of polarization losses during dissolution experiments are presented together with strategies to mitigate them. Then, spin dynamics at ZULF are utilized to realize ^{1}H$\rightarrow$^{13}C polarization transfers during the transfer of a hyperpolarized solution from the dDNP polarizer to the liquid-state spectrometer. The method uses an adiabatic magnetic field inversion, during which the J-coupling between ^{1}H and ^{13}C spins creates avoided crossings. Numerical simulations of the transfer are used to optimize the magnetic field inversion profile and the feasibility of the method is demonstrated on model molecules. Fig. 1.9 shows an example of spectrum of ^{13}C spins detected at high-field after hyperpolarization by this method. Finally, results of dDNP hyperpolarized solutions detected using optical magnetometry are presented. Fig. 1.9 shows an example of such hyperpolarized spectrum at ZULF.

Sections presenting experimental results are organized following the same structure as much as possible: the relevant literature is reviewed (unless a preceding section was dedicated to it). The results are presented with minimal interpretation. Finally, the results are discussed and strategies are proposed to improve or understand more thoroughly the results. Each of the experimental chapters (3-6) is concluded with a perspectives section that gives a summary of the results and discusses possible further experiments and future applications of the methods presented in the chapter.

Chapter 2

Quantum Mechanical Framework

As we have seen in the introduction, NMR uses the spin of the nuclei of atoms to gain information on the world. The spin is a purely quantum mechanical object which has no equivalent in the realm of classical physics. More precisely, its origin has no root in classical physics but it can be described and understood to some extent using the theory of angular momentum from classical physics in the framework of quantum mechanics. This chapter aims to present the basis of quantum mechanics and how it is used in the context of NMR. In the first part, we introduce the postulates of quantum mechanics and the related mathematical objects in Hilbert space. We derive the formalism of the density matrix from the postulates and use it to simulate numerically the NMR spectra of simple spin systems at high-field and at ZULF. In the last section, we introduce relevant interactions that the spins are subject to in our experiments and show how they affect the outcome of our experiments.

The section on the postulates of quantum mechanics and the density operator formalism might seem rather long to the expert. I took the opportunity of writing my dissertation to lay the foundations for the next chapters in a way that is as rigorous as possible. The busy and knowledgeable reader might simply jump to the next section.

2.1 Spins as vectors in Hilbert space

2.1.1 The spin

Spin is the name given to the property of angular momentum of some elementary particles such as a proton or an electron. The origin of this property belongs to theoretical and nuclear physics and is beyond the scope of this work. Here, we simply assume that this property is intrinsic to those particles. Not only do we assume that these particles have a spin but we also assume that they are nothing else: their spatial properties or their mass are of no consequence for the experiments we will deal with. This will simplify our description in the next section.

Spin is associated with a quantum number I, which can take positive integer and half-integer values 1/2, 1, 3/2, 2... etc. This work is only concerned with spins with $I = 1/2$. A spin I has an angular momentum $\boldsymbol{I}$, which gives rise to a magnetic moment denoted $\boldsymbol{\mu}$, where the bold font indicates vector quantities. The spin angular momentum and the spin magnetic moment are related to each other by [3, 98]

$$\boldsymbol{\mu} = \gamma \boldsymbol{I}, \tag{2.1}$$

where γ is the gyromagnetic ratio of the spin. The norm of the angular momentum of vector $\boldsymbol{I}$, also called total angular momentum, is given by

$$\|I\| = \sqrt{I(I+1)}\hbar, \tag{2.2}$$

where $\hbar$ is the reduced Planck constant. The vector quantities $\boldsymbol{\mu}$ or $\boldsymbol{I}$ cannot be measured by any physical device; only the projection along a particular axis can be measured at a time. The spin angular momentum projected along a given axis, say the z-axis, may be expressed as a function of integer and half-integer values of $\hbar$.

$$I_z = m_z\hbar, \tag{2.3}$$

where m_z is an integer of half-integer, ranging from $-I$ to $+I$, in integer steps. Because $I = 1/2$ for all the spins considered in this work, the only allowed values of m_z are $+1/2$ and $-1/2$. Therefore, the possible values for the magnetic moment of a spin 1/2 are

$$\mu_z = \pm\gamma\hbar \tag{2.4}$$

Fig. 2.1 gives a visual representation of the magnetic moment projected along the z-axis.

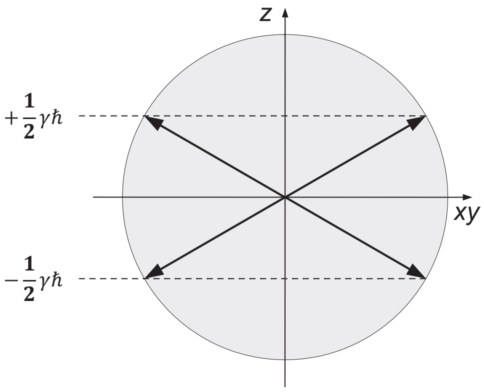

Figure 2.1: Representation of the magnetic moment of a spin 1/2 and its projection along a reference axis.

The potential of a spin interacting with a magnetic field $\boldsymbol{B}$ is given by the laws of electromagnetism

$$E = -\boldsymbol{B}\cdot\boldsymbol{\mu} \tag{2.5}$$

If the magnetic field points along the z-axis and has intensity B_0, then the two possible energy values associated with the angular momentum of the spin along the z-axis are

$$E = \mp\frac{1}{2}\gamma B_0\hbar \tag{2.6}$$

The energy difference between these two states $\gamma B_0\hbar$ is called the Zeeman splitting.

2.1.2 States, measurements, and operators

Quantum mechanics is based on six postulates. We will review them one by one in this section and this will allow us to define the basic mathematical tools that we need to describe NMR experiments. We will use the example of an isolated spin subject to a magnetic field to illustrate the postulates.

The following sections are inspired by and based on Ref [98, 99, 100] as well as on Ilya Kuprov's lecture notes, which are available online at *www.spindynamics.org/*. The only exception is the relation between the description of spins as kets and as density matrices, which I wrote on my own (see below). However, I suppose that similar proofs can probably be found in Mathematics books.

The first postulate can be expressed as:

> **Postulate I:** A quantum mechanical system is fully described by a wave function $|\psi\rangle$. The space of all possible states $|\psi\rangle$ of the system is a complex Hilbert space denoted $\mathbb{H}$. If the system is in state $|\psi\rangle$, the probability to find it in state $|\chi\rangle$ is given by
>
> $$p_{\psi\rightarrow\chi} = |\, \langle\chi|\psi\rangle \,|^2, \tag{2.7}$$
>
> where $\langle\chi|\psi\rangle$ denotes the scalar product on $\mathbb{H}$.

The object $\langle\psi|$ is called a "bra" while $|\psi\rangle$ is called a "ket"; together they form a "braket", which corresponds to the scalar product on $\mathbb{H}$. While the ket represents the state of the system, the bra is the *Hermitian conjugate* of the ket

$$\langle\psi| \overset{\text{def}}{=} (|\psi\rangle)^*, \tag{2.8}$$

a complementary mathematical object which allows us to compute information on the system. Note that, to write Eq. 2.7, we have implicitly assumed that the states were normalized, i.e.,

$$\|\, |\psi\rangle \,\| = |\, \langle\psi|\psi\rangle \,|^2 = 1, \tag{2.9}$$

which will be the case throughout this work.

In general, the wave function is the product of several properties

$$|\psi\rangle = |\psi\rangle_{spin} \otimes |\psi\rangle_{spatial} \otimes ..., \tag{2.10}$$

where $\otimes$ denotes the Kronecker product of the states. If $|\psi\rangle$ lives in the space $\mathbb{H}$, $|\psi\rangle_{spin}$ and $|\psi\rangle_{spatial}$ live in subspaces of $\mathbb{H} = \mathbb{H}_{spin} \otimes \mathbb{H}_{spatial} \otimes ...$ As stated in the introduction of this chapter, we only need to take into account the spin part of the wavefunction to describe all the NMR experiments presented in this work. We will therefore describe all states assuming $|\psi\rangle = |\psi\rangle_{spin}$.

To describe an isolated spin 1/2 subject to an external magnetic field B_0, it is convenient to define two states $|\alpha\rangle$ and $|\beta\rangle$, which correspond to the spin having its angular momentum parallel or antiparallel with respect to B_0, respectively. These states are referred to as at the Zeeman states. Because of Eq. 2.3, Eq. 2.4 and Eq. 2.6, these two states have angular momenta $+\hbar/2$ and $-\hbar/2$, magnetic moments $+\gamma\hbar/2$ and $-\gamma\hbar/2$ and energies $-\gamma B_0\hbar/2$ and $+\gamma B_0\hbar/2$, respectively. As we will see in more detail in the next sections, the states $|\alpha\rangle$ and $|\beta\rangle$ are sufficient to fully describe an isolated spin 1/2, i.e., they form a basis of $\mathbb{H}$, referred to as the Zeeman basis. It implies that all states of an isolated spin can be written as linear combinations of the basis states

$$|\psi\rangle = c_\alpha\, |\alpha\rangle + c_\beta\, |\beta\rangle\,, \tag{2.11}$$

where c_α and c_β are complex coefficients satisfying the normalization condition $|c_\alpha|^2 + |c_\beta|^2 = 1$. More generally, any state of a quantum mechanical system can be written as a linear combination of the basis states

$$|\psi\rangle = \sum_n c_n |n\rangle . \tag{2.12}$$

The matrix representation of quantum mechanics consists of associating the basis states with vectors. In this representation, a state $|\psi\rangle$ is identified with a column vector

$$|\psi\rangle \equiv \begin{pmatrix} c_\alpha \\ \\ c_\beta \end{pmatrix}, \tag{2.13}$$

containing the complex coefficients of Eq. 2.11. The basis states, therefore, take the simple form:

$$\begin{aligned} |\alpha\rangle &\equiv \begin{pmatrix} 1 \\ \\ 0 \end{pmatrix} \\ |\beta\rangle &\equiv \begin{pmatrix} 0 \\ \\ 1 \end{pmatrix} . \end{aligned} \tag{2.14}$$

In the matrix representation, the Hermitian conjugate of the state is the complex transpose of the vector representing the state. Using the first postulate, we find that there is a null probability of finding the system in the $|\beta\rangle$ state if it is initially in $|\alpha\rangle$ and vice versa

$$|\langle\beta|\alpha\rangle|^2 = |\langle\alpha|\beta\rangle|^2 = 0. \tag{2.15}$$

Using the matrix notation, the normalization condition therefore reads

$$|\langle\psi|\psi\rangle|^2 = \begin{pmatrix} c_\alpha^* & c_\beta^* \end{pmatrix} \begin{pmatrix} c_\alpha \\ \\ c_\beta \end{pmatrix} = |\alpha|^2 + |\beta|^2 = 1. \tag{2.16}$$

The second postulate defines the mathematical form of measurable quantities or observables.

Postulate II: Every physical observable A is associated with a Hermitian operator $\hat{A}$ acting on $\mathbb{H}$. The eigenvectors of $\hat{A}$ form a basis $\mathbb{B}$ of $\mathbb{H}$.

Because $\hat{A}$ is Hermitian, its eigenvalues are real. Furthermore, the spectral theorem states that for any Hermitian operator $\hat{A}$, there exists an orthonormal basis of $\mathbb{H}$ formed by eigenvectors $|n\rangle$ of $\hat{A}$. The matrix representation of $\hat{A}$ can therefore be written as

$$\hat{A} = \sum_n a_n |n\rangle \langle n| , \tag{2.17}$$

where the coefficients a_n are the eigenvalues of $\hat{A}$ corresponding to the basis eigenvectors $|n\rangle$. The orthonormality of the $|n\rangle$ states can be written as

$$\langle n|m\rangle = \delta_{nm} = \begin{cases} 1 \text{ if } n = m \\ 0 \text{ otherwise,} \end{cases} \tag{2.18}$$

where δ_{nm} is the Kronecker delta. Because the eigenvectors of $\hat{A}$ form a basis of $\mathbb{H}$, any state $|\psi\rangle$ can be written as a function of the basis states $|n\rangle$ of $\hat{A}$:

$$|\psi\rangle = \sum_n c_n |n\rangle , \tag{2.19}$$

where c_k are normalized complex coefficients, i.e., $|\langle\psi|\psi\rangle|^2 = 1$. The third postulate defines the possible outcome of a measurement of A.

Postulate III: Measuring the observable A can only result in one of the eigenvalues of $\hat{A}$. Because $\hat{A}$ is Hermitian, its eigenvalues are real.

Let us say we want to measure the angular momentum I_z along the z-axis of an isolated spin 1/2. We have seen that the two possible values are $+\hbar/2$ and $-\hbar/2$. By the third postulate, these values are the eigenvalues of $\hat{I}_z$. We, therefore, have the following relations:

$$\begin{aligned} \hat{I}_z |\alpha\rangle &= +\hbar/2 \, |\alpha\rangle \\ \hat{I}_z |\beta\rangle &= -\hbar/2 \, |\beta\rangle \end{aligned} \tag{2.20}$$

The matrix representation for the operator $\hat{I}_z$, which satisfies the above relation is

$$\hat{I}_z = \frac{1}{2}\hbar \begin{pmatrix} +1 & 0 \\ 0 & -1 \end{pmatrix} . \tag{2.21}$$

The matrix representation of the angular momentum operators along two other orthogonal axes are

$$\hat{I}_x = \frac{1}{2}\hbar \begin{pmatrix} 0 & 1 \\ 1 & 0 \end{pmatrix} \tag{2.22}$$

and

$$\hat{I}_y = \frac{i}{2}\hbar \begin{pmatrix} 0 & -1 \\ +1 & 0 \end{pmatrix} , \tag{2.23}$$

which we give without proof.

The fourth postulate gives the probability for measuring a particular eigenvalue.

Postulate IV: For a system in state $|\psi\rangle$, the probability of measuring the eigenvalue a_n of operator $\hat{A}$ is given by

$$p(a_n) = \sum_{k=1}^{g_n} |\langle k|\psi\rangle|^2, \tag{2.24}$$

where g_n is the degeneracy of a_n and the states $|k\rangle$ are the g_n eigenstates associated with a_n. If a_n is non-degenerate, that is, if $g_n = 1$, we have

$$p_{a_n} = |\langle n|\psi\rangle|^2, \tag{2.25}$$

where $|n\rangle$ is the single eigenstate associated with a_n.

Note that we restrict the formulation of the postulates to quantum systems with a discrete spectrum and so we use a discrete summation in the formulation of the fourth postulate.

If a single spin is in state $|\psi\rangle = |\alpha\rangle$, then Eq. 2.25 predicts that we have probabilities $p_\alpha = 1$ and $p_\beta = 0$ to measure angular momenta $+\hbar/2$ and $-\hbar/2$, respectively. Conversely, if a single spin is in state $|\psi\rangle = |\beta\rangle$, then Eq. 2.25 predicts that we have probabilities $p_\alpha = 0$ and $p_\beta = 1$ to measure angular momenta $+\hbar/2$ and $-\hbar/2$, respectively. If the system is in a superposition of states, for example

$$|\psi\rangle = \frac{1}{\sqrt{2}}\left(|\alpha\rangle + |\beta\rangle\right), \tag{2.26}$$

then Eq. 2.25 predicts that there is an equal probability to measure both eigenvalues

$$p_\alpha = p_\beta = \left(\frac{1}{\sqrt{2}}\right)^2 = \frac{1}{2}. \tag{2.27}$$

An important consequence of the fourth postulate is that, if we repeat the same measurement of the observable A on many identical quantum systems (or many times on system prepared equally), then the expectation value of the measurement is

$$\langle\hat{A}\rangle = \sum_n a_n |\langle n|\psi\rangle|^2 = \sum_n \left(\langle n|\psi\rangle\right)^* a_n \langle n|\psi\rangle = \sum_n \langle\psi|n\rangle\, a_n \langle n|\psi\rangle = \langle\psi|\hat{A}|\psi\rangle \tag{2.28}$$

Note that the development we show here is only valid for non-degenerate operators. However, it can be shown that the relation $\langle\hat{A}\rangle = \langle\psi|\hat{A}|\psi\rangle$ holds for any Hermitian operator $\hat{A}$. Furthermore, to obtain this relation, we assumed that $|\psi\rangle$ was expressed in the basis of $\hat{A}$ but the relation holds for any basis $\mathbb{B}$ of $\mathbb{H}$. Indeed, for any $\mathbb{B}$, there exists a unitary operator $\hat{U}$ which takes $\hat{A}$ and $|\psi\rangle$ into the basis $\mathbb{B}$, with the relation

$$|\psi\rangle_{\mathbb{B}} = \hat{U}\,|\psi\rangle_{\mathbb{A}} \tag{2.29}$$

$$\hat{A}_{\mathbb{B}} = \hat{U}\hat{A}_{\mathbb{A}}\hat{U}^{-1} \tag{2.30}$$

where the fact that $\hat{U}$ is unitary implies that its inverse is equal to its complex transpose

$$\hat{U}^{-1} = \hat{U}^*. \tag{2.31}$$

Therefore, because $\langle\psi|_{\mathbb{B}} = \langle\psi|_{\mathbb{A}}\,\hat{U}^{-1}$, we have

$$\langle\psi|_{\mathbb{B}}\,\hat{A}_{\mathbb{B}}\,|\psi\rangle_{\mathbb{B}} = \langle\psi|_{\mathbb{A}}\,\hat{U}^{-1}\hat{U}\hat{A}_{\mathbb{A}}\hat{U}^{-1}\hat{U}\,|\psi\rangle_{\mathbb{A}} = \langle\psi|_{\mathbb{A}}\,\hat{A}_{\mathbb{A}}\,|\psi\rangle_{\mathbb{A}} = \langle\hat{A}\rangle \tag{2.32}$$

For a spin in state $|\alpha\rangle$, the expectation value of the quantity I_z is $\langle\hat{I}_z\rangle = p_\alpha(+\hbar/2)+p_\beta(-\hbar/2) = +\hbar/2$, or using the notation of Eq. 2.28,

$$\langle\hat{I}_z\rangle = \langle\alpha|\hat{I}_z|\alpha\rangle = \begin{pmatrix}1 & 0\end{pmatrix}\hbar\begin{pmatrix}+1/2 & 0\\ 0 & -1/2\end{pmatrix}\begin{pmatrix}1\\0\end{pmatrix} = +\hbar/2 \tag{2.33}$$

Similarly, the angular momentum along the z-axis of the spin in the superposition state of Eq. 2.26 has an expectation value $\langle\hat{I}_z\rangle = p_\alpha(+\hbar/2) + p_\beta(-\hbar/2) = 0$ because both states are equally probable. Using the notation of Eq. 2.28

$$\langle\hat{I}_z\rangle = \langle\psi|\hat{I}_z|\psi\rangle = \frac{1}{\sqrt{2}}\begin{pmatrix}1 & 1\end{pmatrix}\hbar\begin{pmatrix}+1/2 & 0\\ 0 & -1/2\end{pmatrix}\frac{1}{\sqrt{2}}\begin{pmatrix}1\\1\end{pmatrix} = 0 \tag{2.34}$$

In NMR experiments, the recorded signal is the collective effect of many identical spin systems (although we will take special care in Sec. 2.2.2 to describe what is similar and what is different between those many copies). Therefore, the measurement *always* results in an expectation value and does not give access to the state of an individual spin system.

As stated by the fifth postulate, the fact of measuring observable A affects the quantum system.

Postulate V: For a system in state $|\psi\rangle$, immediately after measuring observable A, the system is in $|n\rangle$, where $|n\rangle$ is the state associated with eigenvalue a_n, which resulted from the measurement.

In other words, the fact of measuring A ”projects” the system onto state $|n\rangle$. Mathematically, the projection can be represented using the projector operator $\hat{\mathcal{P}}_n = |n\rangle\langle n|$,

$$|\chi\rangle = \frac{\hat{\mathcal{P}}_n\,|\psi\rangle}{\|\hat{\mathcal{P}}_n\,|\psi\rangle\,\|} \tag{2.35}$$

Contrary to the field of optics, in modern NMR experiments, this postulate has few practical implications, except for single spin detection. In addition to that, the implications it has are very subtle and beyond my understanding.

2.1.3 Time evolution: the Schrödinger equation

This whole section describes the last of the postulates, which defines how the system evolves with time according to the Schrödinger equation.

Postulate VI: The evolution of the system is given by the time-dependent Schrödinger equation:

$$\frac{d}{dt}\left|\psi(t)\right\rangle = -\frac{i}{\hbar}\hat{H}(t)\left|\psi(t)\right\rangle, \tag{2.36}$$

where $\left|\psi\right\rangle(t)$ and $\hat{H}(t)$ are the state of the system and the Hamiltonian operator at time t, respectively. The Hamiltonian is defined as the operator representing the total energy of the system.

The time-dependent Schrödinger equation can be rewritten in a more convenient form using a time propagation operator or propagator. To do so, we calculate the Taylor expansion of the state $\left|\psi(t)\right\rangle$ around time $t = 0$

$$\left|\psi(t)\right\rangle = \left|\psi(0)\right\rangle + t\frac{d}{dt}\left|\psi(0)\right\rangle\Big|_{t=0} + \frac{t^2}{2!}\frac{d^2}{dt^2}\left|\psi(t)\right\rangle\Big|_{t=0} + ... = \sum_{k=0}^{\infty}\frac{t^k}{k!}\frac{d^k}{dt^k}\left|\psi(t)\right\rangle\Big|_{t=0}, \tag{2.37}$$

assuming that the Hamiltonian is constant around $t = 0$. From the time-dependent Schrödinger equation, we have

$$\frac{t^k}{k!}\frac{d^k}{dt^k}\left|\psi(t)\right\rangle = \left(-\frac{i}{\hbar}\hat{H}\right)^k\left|\psi(t)\right\rangle. \tag{2.38}$$

Plugging Eq. 2.38 into Eq. 2.37, we obtain

$$\left|\psi(t)\right\rangle = \sum_{k=0}^{\infty}\frac{t^k}{k!}\left(-\frac{i}{\hbar}\hat{H}\right)^k\left|\psi(0)\right\rangle = \sum_{k=0}^{\infty}\frac{1}{k!}\left(-\frac{it}{\hbar}\hat{H}\right)^k\left|\psi(0)\right\rangle = \exp\left(-\frac{it}{\hbar}\hat{H}\right)\left|\psi(0)\right\rangle, \tag{2.39}$$

where $\exp(\,\cdot\,)$ denotes the matrix exponentiation. We now define the time propagation operator or propagator

$$\hat{U}(0 \to t) = \exp\left(-\frac{it}{\hbar}\hat{H}\right) = \sum_{k=0}^{\infty}\frac{1}{k!}\left(-\frac{it}{\hbar}\hat{H}\right)^k, \tag{2.40}$$

and plug into Eq. 2.40 to get a convenient form for the Schrödinger equation

$$\left|\psi(t)\right\rangle = \hat{U}(0 \to t)\left|\psi(0)\right\rangle, \tag{2.41}$$

which describes the evolution of the system using the time derivative of the state only implicitly.

States which do not evolve under the effect of the Hamiltonian are of particular interest. They are called stationary states. We now show that the set of stationary states corresponds to the eigenstates of the Hamiltonian. In other words, we now show that a state is stationary if and only if it satisfies the time-independent Schrödinger equation

$$\hat{H}\left|\psi\right\rangle = \epsilon\left|\psi\right\rangle, \tag{2.42}$$

where we see from the third postulate that ϵ must be the energy associated with $\left|\psi\right\rangle$. We have said that stationary states are states which do not evolve under the Hamiltonian. More precisely, a stationary state does not evolve apart from a phase factor $e^{i\phi(t)}$

$$|\psi(t)\rangle = e^{i\phi(t)} |\psi(0)\rangle . \tag{2.43}$$

The phase factor will not bring any useful information in the description of our experiments in the experiments we are concerned with. It is a common practice to define a projective Hilbert space $\mathrm{P}\mathbb{H}$, where each subspace of states in $\mathbb{H}$ which differ only by a phase factor are identified to a single point in $\mathrm{P}\mathbb{H}$. We introduce another formulation of the state of the system using the density matrix, which does not depend on the phase factor

$$\hat{\rho} = |\psi\rangle \langle\psi| . \tag{2.44}$$

Note that here we have defined the density matrix for a single spin. We will define it for an ensemble average and we will show how the postulates apply to it in the next section. For now, we only try to understand the consequence of this description of the system on the phase factor and on stationary states. If $|\psi\rangle$ is stationary, there exists $\phi(t)$, such that $|\psi(t)\rangle = e^{i\phi(t)} |\psi(0)\rangle$ which implies that Eq. 2.44 is satisfied for all t because

$$\hat{\rho}(t) = |\psi(t)\rangle \langle\psi(t)| = e^{+i\phi(t)} |\psi(0)\rangle \langle\psi(0)| e^{-i\phi(t)} = |\psi(0)\rangle \langle\psi(0)| = \hat{\rho}(0), \tag{2.45}$$

This shows that the density matrix does not evolve at all for a stationary state, contrary to the case where the spin is described by a ket and time evolution brings a change in the phase factor even for an eigenstate (see Eq. 2.43). The time derivative of the density matrix is obtained from the time-dependent Schrödinger equation

$$\frac{d}{dt}\hat{\rho} = \frac{d}{dt}\left(|\psi\rangle \langle\psi|\right) = \frac{d}{dt}|\psi\rangle \langle\psi| + |\psi\rangle \frac{d}{dt}\langle\psi| = -\frac{i}{\hbar}\hat{H}|\psi\rangle \langle\psi| + |\psi\rangle \langle\psi| \frac{i}{\hbar}\hat{H}^* = -\frac{i}{\hbar}\left(\hat{H}\hat{\rho} - \hat{\rho}\hat{H}\right), \tag{2.46}$$

where we have made use of the fact that the Hamiltonian is Hermitian, i.e., $\hat{H}^* = \hat{H}$. Note that we dropped the time dependence of the states to simplify notation. Introducing the notation of the propagator $[\hat{A}, \hat{B}] = \hat{A}\hat{B} - \hat{B}\hat{A}$, we write Eq. 2.46 as

$$\frac{d}{dt}\hat{\rho} = -\frac{i}{\hbar}[\hat{H}, \hat{\rho}], \tag{2.47}$$

which is known as the Liouville-Von Neumann equation. Now if we assume that the state is stationary, we have

$$\begin{aligned} [\hat{H}, \hat{\rho}] = 0 &\iff \hat{H}|\psi\rangle \langle\psi| = |\psi\rangle \langle\psi| \hat{H} \\ &\iff \hat{H}|\psi\rangle \langle\psi|\psi\rangle = |\psi\rangle \langle\psi| \hat{H} |\psi\rangle \\ &\iff \hat{H}|\psi\rangle = \epsilon |\psi\rangle , \end{aligned} \tag{2.48}$$

where we have made use of the fact that $\langle\psi| \hat{H} |\psi\rangle$ is the expectation value ϵ of $\hat{H}$ and the state is normalized $\langle\psi|\psi\rangle = 1$. We have proved that a state is stationary if and only if it is an eigenstate of the Hamiltonian. A corollary of this result is that the set of stationary states of the system form a basis of the state space $\mathbb{H}$.

We conclude this section on the postulates of quantum mechanics by drawing consequences for the evolution of a single spin subject to a static magnetic field pointing along the z-axis. The Hamiltonian is the operator associated with the total energy of the system and, as we have stated earlier, we only take into account the spin interactions in our description. Therefore, we can write the Hamiltonian as

$$\hat{\boldsymbol{H}} = -\boldsymbol{B}\cdot\hat{\boldsymbol{\mu}} = -B_0\hat{\mu}_z = -B_0\hbar\gamma\hat{I}_z = \hbar\omega_0\hat{I}_z = \hbar\begin{pmatrix} +1/2 & 0 \\ 0 & -1/2 \end{pmatrix}, \tag{2.49}$$

written in the Zeeman basis and where $\omega_0 = -\gamma B_0$ is the Larmor frequency of the spin in magnetic field B_0. $\hat{H}$ is proportional to $\hat{I}_z$, which implies that they share their eigenvectors. Finding the eigenvectors of a diagonal matrix is trivial: they are the basis vectors, $|\alpha\rangle$ and $|\beta\rangle$ in this case and so we have

$$\begin{aligned} \hat{H}\,|\alpha\rangle &= +\hbar\omega_0/2\,|\alpha\rangle \\ \hat{H}\,|\beta\rangle &= -\hbar\omega_0/2\,|\beta\rangle \end{aligned} \tag{2.50}$$

Because of the sixth postulate, the fact that $|\alpha\rangle$ and $|\beta\rangle$ are eigenstates of the Hamiltonian means that they are stationary states of the system. In other words, if the system is in the $|\alpha\rangle$ and $|\beta\rangle$ states at time $t = 0$, it will remain in this state (apart from the phase factor), unless the Hamiltonian changes. This is confirmed by using the propagator

$$\hat{U}(0\to t) = \exp\left(-\frac{it}{\hbar}\hat{H}\right) = \exp\left(-it\begin{pmatrix} +\omega_0/2 & 0 \\ 0 & -\omega_0/2 \end{pmatrix}\right) = \begin{pmatrix} e^{-it\omega_0/2} & 0 \\ 0 & e^{+it\omega_0/2} \end{pmatrix}, \tag{2.51}$$

where we used the fact that the matrix exponential of a diagonal matrix is simply obtained by exponentiating the diagonal elements individually. Therefore,

$$\hat{U}(0\to t)\,|\alpha\rangle = \begin{pmatrix} e^{-it\omega_0/2} & 0 \\ 0 & e^{+it\omega_0/2} \end{pmatrix}\begin{pmatrix} 1 \\ 0 \end{pmatrix} = e^{-it\omega_0/2}\begin{pmatrix} 1 \\ 0 \end{pmatrix} = e^{-it\omega_0/2}\,|\alpha\rangle \tag{2.52}$$

which shows that time propagation does not change $|\alpha\rangle$ apart from the phase factor. The same is true for $|\beta\rangle$. On the contrary, a mixed state $|\psi\rangle = (|\alpha\rangle + |\beta\rangle)/\sqrt{2}$ is not an eigenstate of the Hamiltonian and so it evolves under the effect of the Hamiltonian

$$\hat{U}(0\to t)\,|\psi\rangle = \frac{1}{\sqrt{2}}\begin{pmatrix} e^{-it\omega_0/2} & 0 \\ 0 & e^{+it\omega_0/2} \end{pmatrix}\begin{pmatrix} 1 \\ 1 \end{pmatrix} = \frac{1}{\sqrt{2}}\begin{pmatrix} e^{-it\omega_0/2} \\ e^{+it\omega_0/2} \end{pmatrix} \neq e^{-it\omega_0/2}\,|\psi\rangle\,, \tag{2.53}$$

where we see that the initial state and the state at $t = 0$ do not vary only by a phase factor.

2.2 Spins as density matrices

So far, we have represented the state of the spin system using a wavefunction (or a ket). This approach is often not the most convenient in the context of NMR. As we are going to see in this section, the density matrix that we defined in Eq. 2.44 is a powerful tool for NMR simulation. We will first see show how to extract expectation values from the density matrix and how time propagation is carried out on it. Then, we will show how a large ensemble of uncoupled spins can be described using a density matrix that is nearly identical to that of a single spin. Finally, we will see how coupled spins can be described using the density matrix formalism.

2.2.1 Expectation values and time propagation

The expectation value of operator $\hat{A}$ for density matrix $\hat{\rho}$ is given by

$$\langle \hat{A} \rangle = \mathrm{Tr}\left\{ \hat{A}\hat{\rho} \right\}, \tag{2.54}$$

where the trace operation $\mathrm{Tr}\{\cdot\}$ corresponds to the sum of the diagonal elements. The definition given by Eq. 2.54 is equivalent to that of Eq. 2.28, which we derived in the previous section for the expectation value of the ket. Indeed,

$$\begin{aligned}
\mathrm{Tr}\left\{ \hat{A}\hat{\rho} \right\} &= \mathrm{Tr}\left\{ \sum_{njk} a_n c_k^* c_j \left| n \right\rangle \left\langle n | j \right\rangle \left\langle k \right| \right\} \\
&= \mathrm{Tr}\left\{ \sum_{njk} a_n c_k^* c_j \delta_{nj} \left| n \right\rangle \left\langle k \right| \right\} \\
&= \mathrm{Tr}\left\{ \sum_{nk} a_n c_k^* c_k \left| n \right\rangle \left\langle k \right| \right\} \\
&= \sum_n a_n |c_n|^2 \\
&= \langle \hat{A} \rangle \,,
\end{aligned} \tag{2.55}$$

where we assumed that the operator $\hat{A}$ and the density matrix $\hat{\rho}$ were expressed in terms of the basis states of $\hat{A}$. However, as we did for Eq. 2.28 (see Eq. 2.32), we can show that the expectation value can be computed with Eq. 2.54 as long as $\hat{A}$ and $\hat{\rho}$ are expressed in the same basis, whatever the basis. Using the basis change introduced in Eq. 2.29 and Eq. 2.30, we can write the basis change for the density matrix from basis $\mathbb{A}$ to $\mathbb{B}$ as

$$\hat{\rho}_{\mathbb{B}} = U \hat{\rho}_{\mathbb{A}} U^{-1} \tag{2.56}$$

and therefore we have

$$\begin{aligned}
\mathrm{Tr}\left\{ \hat{A}_{\mathbb{B}} \hat{\rho}_{\mathbb{B}} \right\} &= \mathrm{Tr}\left\{ U \hat{A}_{\mathbb{A}} U^{-1} U \hat{\rho}_{\mathbb{A}} U^{-1} \right\} \\
&= \mathrm{Tr}\left\{ U \hat{A}_{\mathbb{A}} \hat{\rho}_{\mathbb{A}} U^{-1} \right\} \\
&= \mathrm{Tr}\left\{ U^{-1} U \hat{A}_{\mathbb{A}} \hat{\rho}_{\mathbb{A}} \right\} \\
&= \mathrm{Tr}\left\{ \hat{A}_{\mathbb{A}} \hat{\rho}_{\mathbb{A}} \right\},
\end{aligned} \tag{2.57}$$

where we used the fact that $\mathrm{Tr}\{ABC\} = \mathrm{Tr}\{CAB\} = \mathrm{Tr}\{BCA\}$. As an example, the expectation value of $\hat{I}_z$ for $\hat{\rho} = \left| \alpha \right\rangle \left\langle \alpha \right|$ is

$$\begin{aligned}
\langle \hat{I}_z \rangle &= \mathrm{Tr}\left\{ \hat{I}_z \left|\alpha\right\rangle \left\langle\alpha\right| \right\} \\
&= \mathrm{Tr}\left\{ \hat{I}_z \begin{pmatrix} 1 \\ 0 \end{pmatrix} \begin{pmatrix} 1 & 0 \end{pmatrix} \right\} \\
&= \hbar \mathrm{Tr}\left\{ \begin{pmatrix} +1/2 & 0 \\ 0 & -1/2 \end{pmatrix} \begin{pmatrix} 1 & 0 \\ 0 & 0 \end{pmatrix} \right\} \\
&= \hbar \mathrm{Tr}\left\{ \begin{pmatrix} +1/2 & 0 \\ 0 & 0 \end{pmatrix} \right\} \\
&= +\hbar/2.
\end{aligned} \tag{2.58}$$

We now use the expression for the expectation value of the density matrix given by Eq. 2.54 to find an intuitive form of the density matrix, namely the *vector model.* We first express the general state ket of Eq. 2.13 as a density matrix

$$\hat{\rho} = \left|\psi\right\rangle \left\langle\psi\right| = \begin{pmatrix} c_\alpha \\ c_\beta \end{pmatrix} \begin{pmatrix} c_\alpha^* & c_\beta^* \end{pmatrix} = \begin{pmatrix} |c_\alpha|^2 & c_\alpha c_\beta^* \\ c_\alpha^* c_\beta & |c_\beta|^2 \end{pmatrix}, \tag{2.59}$$

where we see that the diagonal contains the population of the $|\alpha\rangle$ and $|\beta\rangle$ states. The four matrix elements of $\hat{\rho}$ can be extracted as the expectation values of the four matrices

$$\mathrm{Tr}\left\{ \left(\frac{\hat{\mathbb{1}}}{2} + \hat{I}_z \right) \hat{\rho} \right\} = \mathrm{Tr}\left\{ \begin{pmatrix} 1 & 0 \\ 0 & 0 \end{pmatrix} \hat{\rho} \right\} = |c_\alpha|^2, \tag{2.60}$$

$$\mathrm{Tr}\left\{ \left(\hat{I}_x - i\hat{I}_y \right) \hat{\rho} \right\} = \mathrm{Tr}\left\{ \begin{pmatrix} 0 & 0 \\ 1 & 0 \end{pmatrix} \hat{\rho} \right\} = c_\alpha^* c_\beta, \tag{2.61}$$

$$\mathrm{Tr}\left\{ \left(\hat{I}_x + i\hat{I}_y \right) \hat{\rho} \right\} = \mathrm{Tr}\left\{ \begin{pmatrix} 0 & 1 \\ 0 & 0 \end{pmatrix} \hat{\rho} \right\} = c_\alpha c_\beta^* \tag{2.62}$$

and

$$\mathrm{Tr}\left\{ \left(\frac{\hat{\mathbb{1}}}{2} - \hat{I}_z \right) \hat{\rho} \right\} = \mathrm{Tr}\left\{ \begin{pmatrix} 0 & 0 \\ 0 & 1 \end{pmatrix} \hat{\rho} \right\} = |c_\beta|^2. \tag{2.63}$$

where $\hat{\mathbb{1}}$ is the identity. We can therefore rewrite the density matrix as

$$
\begin{aligned}
\hat{\rho} &= |c_\alpha|^2 \left(\frac{\hat{\mathbb{1}}}{2} + \hat{I}_z \right) + c_\alpha^* c_\beta \left(\hat{I}_x - i\hat{I}_y \right) + c_\alpha c_\beta^* \left(\hat{I}_x + i\hat{I}_y \right) + |c_\beta|^2 \left(\frac{\hat{\mathbb{1}}}{2} - \hat{I}_z \right) \\
&= (|c_\alpha|^2 + |c_\beta|^2)\frac{\hat{\mathbb{1}}}{2} + (c_\alpha c_\beta^* + c_\alpha^* c_\beta)\hat{I}_x + i(c_\alpha c_\beta^* - c_\alpha^* c_\beta)\hat{I}_y + (|c_\alpha|^2 - |c_\beta|^2)\hat{I}_z \\
&= \frac{\hat{\mathbb{1}}}{2} + P_x\hat{I}_x + P_y\hat{I}_y + P_z\hat{I}_z \\
&= \frac{\hat{\mathbb{1}}}{2} + \boldsymbol{P}\cdot\hat{\boldsymbol{I}},
\end{aligned}
\tag{2.64}
$$

where we have defined

$$
\begin{aligned}
P_x &= 2\mathrm{Re}\{c_\alpha c_\beta^*\} = c_\alpha c_\beta^* + c_\alpha^* c_\beta \\
P_y &= 2\mathrm{Im}\{c_\alpha c_\beta^*\} = i(c_\alpha c_\beta^* - c_\alpha^* c_\beta) \\
P_z &= |c_\alpha|^2 - |c_\beta|^2,
\end{aligned}
\tag{2.65}
$$

and $\boldsymbol{P}$ is a vector containing the individual polarizations. From their definition, we see that P_x, P_y and P_z are real numbers between -1 and $+1$. Furthermore, we find the normalization condition

$$
P_x^2 + P_y^2 + P_z^2 = |c_\alpha|^2 + |c_\beta|^2 = 1. \tag{2.66}
$$

The numbers defined by Eq. 2.65 are called the spin polarization along the x, y, and z-axes; they represent the normalized amount of angular momentum of the spin along the x, y, and z-axes, respectively. The fact that the state of the spin can be described by three real numbers which give its orientation in space allows one to represent the spin using the "vector model". This model identifies the state of the spin with the polarization vector $\boldsymbol{P}$ in 3D space, as depicted in Fig. 2.2. Note that, because of Eq. 2.64, angular momentum operators can be used to describe the state of the system as well as the observables, a fact that may be confusing at first sight.

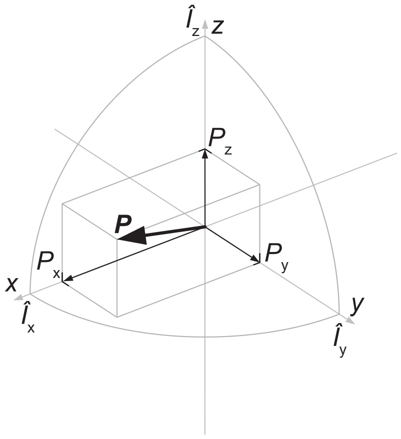

Figure 2.2: Representation of the polarization vector of a spin 1/2 and its projections along the Cartesian axes. The polarization and its projections are colinear with the angular momentum operator and its projections.

The polarization numbers in Eq. 2.65 were introduced as real coefficients that replaced the complex coefficients of the ket vector in the description of the spin. However, beyond this abstraction, polarization is a physical observable and as such, it can only be measured as an expectation value, and not as a single, deterministic value. The expectation value of the spin polarization along axis $k = x, y, z$ can in general be extracted from the density matrix as

$$\langle P_k \rangle = \frac{1}{|I|} \mathrm{Tr} \left\{ \hat{I}_k \hat{\rho} \right\}, \tag{2.67}$$

where I is the spin number, which we accept without proof. [101] This result holds as well in the case of multiple spin systems that we will treat later. In the following discussion, polarization numbers are regarded as abstract coefficients and not as observables.

For a single spin 1/2, it turns out that the vector model is sufficient to describe *completely* the state of the system. Mathematically, this is equivalent to saying that the Hilbert space in which the ket representing the spin lives is isomorphic to the unit sphere in $\mathbb{R}^3$ in which the polarization vector lives. Moreover, the transition probability defined by Eq. 2.7 in the first postulate must be preserved by the isomorphism between the spaces. Let us call the Hilbert space of a single spin and the unit sphere in $\mathbb{R}^3$, $\mathbb{H}_1$ and $\mathbb{H}_2$, respectively. We now prove that $\mathbb{H}_1$ and $\mathbb{H}_2$ are isomorphic (note that I conceived this proof on my own and so it might not be the most direct). We construct an isomorphism that maps each element of $\mathbb{H}_1$ with an element of $\mathbb{H}_2$, and vice versa

$$\begin{gathered} f : \mathbb{H}_1 \to \mathbb{H}_2 \\ \begin{pmatrix} c_\alpha \\ \\ c_\beta \end{pmatrix} \mapsto \begin{pmatrix} P_x = 2\mathrm{Re}\{c_\alpha c_\beta^*\} \\ \\ P_y = 2\mathrm{Im}\{c_\alpha c_\beta^*\} \\ \\ P_z = |c_\alpha|^2 - |c_\beta|^2 \end{pmatrix}, \end{gathered} \tag{2.68}$$

with the inverse

$$\begin{gathered} f^{-1} : \mathbb{H}_2 \to \mathbb{H}_1 \\ \begin{pmatrix} P_x \\ \\ P_y \\ \\ P_z \end{pmatrix} \mapsto \begin{pmatrix} c_\alpha = \cos(\theta/2) \exp(+i\phi/2) \\ \\ c_\beta = \sin(\theta/2) \exp(-i\phi/2) \end{pmatrix}, \end{gathered} \tag{2.69}$$

where θ and ϕ are the angle between z-axis and the polarization vector and the angle between x-axis and the projection of the polarization in the xy-plane, respectively. A little bit of algebra shows that we have $f \circ f^{-1} = f^{-1} \circ f = \mathbb{1}$ and so f is indeed an isomorphism. This also implies that

$$\mathbb{B} = \left\{ \hat{\mathbb{1}}, \hat{I}_x, \hat{I}_y, \hat{I}_z \right\} \tag{2.70}$$

forms a basis of the Hilbert space in which the spin lives.

We now show that the transition probability is preserved by the isomorphism. In $\mathbb{H}_2$, we define the transition probability from state $\hat{\rho}_1$ to state $\hat{\rho}_2$ as

$$p_{1\to 2} = \mathrm{Tr} \left\{ \hat{\rho}_2 \hat{\rho}_1 \right\}, \tag{2.71}$$

which is closely related to the formula for the computation of expectation values from the density matrix in Eq. 2.54. What we now need to show is that this formula using elements of $\mathbb{H}_2$ yields the same result as Eq. 2.7 with elements of $\mathbb{H}_1$. To simplify notations, let us write the coefficients of state $|\psi_1\rangle$ as α_1 and β_1 and those of state $|\psi_2\rangle$ as α_2 and β_2 in $\mathbb{H}_1$ and their image through isomorphism f as x_1, y_1 and z_1 and x_2, y_2 and z_2, respectively. Using Eq. 2.7, we find that the transition probability is

$$\begin{aligned} p_{1\to 2} &= |\langle\psi_2|\psi_1\rangle|^2 \\ &= |\alpha_1\alpha_2^* + \beta_1\beta_2^*|^2 \\ &= (\alpha_1\alpha_2^* + \beta_1\beta_2^*)(\alpha_1^*\alpha_2 + \beta_1^*\beta_2) \\ &= |\alpha_1|^2|\alpha_2|^2 + \alpha_1\beta_1^*\alpha_2^*\beta_2 + \alpha_1^*\beta_1\alpha_2\beta_2^* + |\beta_1|^2|\beta_2|^2. \end{aligned} \tag{2.72}$$

Plugging in the relations of Eq. 2.69, we obtain

$$\begin{aligned} p_{1\to 2} &= \frac{1}{2}\left(1 + \sin(\theta_1)\sin(\theta_2)\cos(\phi_1 - \phi_2) + \cos(\theta_1)\cos(\theta_2)\right) \\ &= \frac{1}{2}\left(1 + x_1x_2 + y_1y_2 + z_1z_2\right). \end{aligned} \tag{2.73}$$

Now if we write the density matrices expressed in $\mathbb{H}_2$ corresponding to kets expressed in $\mathbb{H}_1$ as

$$\hat{\rho}_k = \frac{1}{2}\mathbb{1} + x_k\hat{I}_x + y_k\hat{I}_y + z_k\hat{I}_z, \tag{2.74}$$

where $k = 1, 2$, we can calculate the transition probability using Eq. 2.71

$$\begin{aligned} p_{1\to 2} &= \mathrm{Tr}\left\{\left(\frac{1}{2}\mathbb{1} + x_1\hat{I}_x + y_1\hat{I}_y + z_1\hat{I}_z\right)\left(\frac{1}{2}\mathbb{1} + x_2\hat{I}_x + y_2\hat{I}_y + z_2\hat{I}_z\right)\right\} \\ &= \frac{1}{4}\mathrm{Tr}\left\{\mathbb{1}^2\right\} + x_1x_2\mathrm{Tr}\left\{\hat{I}_x^2\right\} + y_1y_2\mathrm{Tr}\left\{\hat{I}_y^2\right\} + z_1z_2\mathrm{Tr}\left\{\hat{I}_z^2\right\} \\ &= \frac{1}{4}2 + x_1x_2\frac{1}{2} + y_1y_2\frac{1}{2} + z_1z_2\frac{1}{2} \\ &= \frac{1}{2}\left(1 + x_1x_2 + y_1y_2 + z_1z_2\right). \end{aligned} \tag{2.75}$$

To go from the first line to the second, we used the fact that the trace is a linear operation and the trace is 0 for products of orthogonal operators. With that, we have shown that the transition probability between two states expressed in terms of polarization along the Cartesian axes yields the same result as the braket notation. The formulation of the spin dynamics expressed in basis $\mathbb{H}_1$ equipped with the operation defined in Eq. 2.7 is therefore equivalent to that expressed in basis $\mathbb{H}_2$ equipped with the operation defined in Eq. 2.71 and so the representation of a single spin as a vector in 3D space is an appropriate description.

We have translated the state of the system and the computation of the expectation value from the formalism of kets to that of density matrices. What we still need in our toolbox is to translate the time propagation operator into the formalism of the density matrix. This is easily obtained by writing:

$$\begin{aligned} \hat{\rho}(t) &= |\psi(t)\rangle\langle\psi(t)| \\ &= |\psi(t)\rangle\left(|\psi(0)\rangle\right)^* \\ &= \hat{U}|\psi(0)\rangle\left(\hat{U}|\psi(0)\rangle\right)^* \\ &= \hat{U}|\psi(0)\rangle\langle\psi(0)|\hat{U}^{-1} \\ &= \hat{U}\hat{\rho}(0)\hat{U}^{-1}, \end{aligned} \tag{2.76}$$

where we simplified the notation of the propagator

$$\hat{U} = \hat{U}(0 \to t) = \exp\left(-\frac{it}{\hbar}\hat{H}\right). \tag{2.77}$$

Eq. 2.76 is known as the "sandwich formula". We will use it whenever we will describe the time evolution of the system, in particular for numerical calculation.

To simplify the expressions, we can redefine the Hamiltonian as

$$\hat{\mathbb{H}} = \frac{\hat{H}}{\hbar} \tag{2.78}$$

$$\hat{\mathbb{U}}(0 \to t) = \exp\left(-it\hat{\mathbb{H}}\right) = \hat{U}(0 \to t), \tag{2.79}$$

where we see that the time propagator defined using the Hamiltonian of Eq. 2.78 is the same as that of our previous definition; the constant $\hbar$ cancels out in the fraction. This change in the definition of the Hamiltonian does not affect the eigenstates of the Hamiltonian. However, it does affect the eigenvalues. So far, all eigenvalues of the Hamiltonian were proportional to $\hbar$ but dividing the Hamiltonian by $\hbar$ divides the eigenvalues as well. This change is simply a unit change from J to rad.s^{-1}. The eigenvalues of $\hat{I}_z$ are now $+1/2$ and $-1/2$ rather than $+\hbar/2$ and $-\hbar/2$. The Hamiltonian and the energies of the states will be expressed in rad.s^{-1} throughout this work from this point. For simplicity, we will use normal font symbols $\hat{H}$ and $\hat{U}$ to express Hamiltonians and propagators.

The sandwich formula of Eq. 2.76 will be of great use for numerical propagation. However, in some cases, there is a more intuitive way to describe the time evolution of the density matrix, using the commutation relation of the angular momentum operators. The operators $\hat{I}_x$, $\hat{I}_y$ and $\hat{I}_z$ are related by the following cyclic commutation relation

$$\begin{aligned} [\hat{I}_x, \hat{I}_y] &= i\hat{I}_z \\ [\hat{I}_y, \hat{I}_z] &= i\hat{I}_x \\ [\hat{I}_z, \hat{I}_x] &= i\hat{I}_y. \end{aligned} \tag{2.80}$$

Recalling the Liouville-Von Neumann equation (see Eq. 2.47), we see that these commutators define how operators act on each other. For example, if the density matrix at time $t = 0$ is $\hat{\rho}(0) = \hat{I}_z$ and the Hamiltonian can be written as $\hat{H} = \omega_1\hat{I}_y$, where ω_1 is an angular frequency in rad.s^{-1}, then the Liouville-Von Neumann equation tells us that the variation of the density matrix at time $t = 0$ is $d\hat{\rho}/dt = \omega_1\hat{I}_y$. Altogether, the commutation relations form a set of differential equations and the solution for the example that we have given here is

$$\hat{\rho}(t) = \hat{I}_z \cos\omega_1 t + \hat{I}_x \sin\omega_1 t. \tag{2.81}$$

Therefore, $\hat{H} = \omega_1\hat{I}_y$ rotates $\hat{I}_z$ towards $\hat{I}_x$ at frequency ω_1. This example corresponds to the situation where a spin is initially along the z-axis and is rotated around the y-axis by an rf field. This will be treated in more detail in the next section. Note that writing $\hat{\rho}(0) = \hat{I}_z$ does not match the form of the density matrix in Eq. 2.64 because the identity operator $\mathbb{1}/2$ is missing. It is a common practice to drop the identity operator from the density matrix as it does not evolve under the action of any operator (because the identity commutes with all operators).

Whenever a set of three operators features the cyclic commutation relation, this approach will be useful to predict analytically the behavior of the system and hence the expected spectral features both at high-field and at zero-field.

2.2.2 Multiple spin system

We now have the tools to describe the evolution of a single spin under the effect of relevant operators to describe pulse sequence and spin interactions. Yet, NMR experiments do not consist of detecting single spins but rather the collective effect of many spins. Furthermore, spins interact together, which cannot be accounted for, using the tools that we have described so far. This section will present two concepts that we need to describe a complete NMR experiment. First, we will show how the *ensemble average* enables the description of many identical spin systems using a density matrix with the dimension of a single spin. Then, we will show how interacting spins can be described using Kronecker products of operators (whether as an ensemble average or not).

Let us assume that the system consists of a large number of spins that are immersed in a homogeneous magnetic field and do not interact with each other. A brute force approach to the description of such an ensemble would consist of constructing a Hilbert space which would be the Kronecker product of the Hilbert spaces of all individual spins. As the size of the Hilbert space grows with 2^N, where N is the number of spins, the resulting space would be far too large to allow for any calculation, even for the tiniest sample. What we will do instead is to construct the density matrix of the whole system $\hat{\rho}_{tot}$ as the average over an infinite ensemble of spins

$$\begin{aligned}\hat{\rho}_{tot} &= \lim_{N\to\infty} \frac{1}{N}\sum_{n=1}^{N} \hat{\rho}_n \\ &= \frac{\hat{\mathbb{1}}}{2} + \bar{P}_x \hat{I}_x + \bar{P}_y \hat{I}_y + \bar{P}_z \hat{I}_z,\end{aligned} \tag{2.82}$$

where we have defined the average polarization

$$\bar{P}_k = \lim_{N\to\infty} \frac{1}{N}\sum_{n=1}^{N} P_{k,n}, \tag{2.83}$$

where $P_{k,n}$ is the polarization of spin n along axis k. The above equations can be seen as the averaging of the vectors of the individual spins in 3D space. Many NMR experiments start with the spins at thermal equilibrium in a magnetic field aligned with the z-axis. In this case, we know that the average polarization along the z-axis is

$$\bar{P}_z = P_{eq}, \tag{2.84}$$

which is the Boltzmann equilibrium polarization, as defined in Section 1.1.1 (see Eq. 1.3). On the contrary, there is no preferred orientation in the xy-plane and so we have

$$\bar{P}_x = \bar{P}_y = 0. \tag{2.85}$$

In other words, spins can point anywhere in space but the average of all their orientations points towards the z-axis. Fig. 2.3 gives a visual representation of the individual polarization vectors of the spins and their averaged polarization. Plugging Eq. 2.84 and Eq. 2.85 into Eq. 2.82, we obtain the thermal equilibrium density matrix for a single spin 1/2 immersed in a magnetic field along the z-axis

$$\hat{\rho}_{eq} = \frac{\hat{\mathbb{1}}}{2} + P_{eq}\hat{I}_z = \begin{pmatrix} \frac{1+P_{eq}}{2} & 0 \\ 0 & \frac{1-P_{eq}}{2} \end{pmatrix}. \tag{2.86}$$

This density matrix represents a so-called *mixed state* of the system. The norm of the polarization vector associated with this mixed state is P_{eq} (it is obtained using Eq. 2.67), which is not necessarily 1. From expression Eq. 2.69, it is clear that spin states expressed in $\mathbb{H}_1$ and $\mathbb{H}_2$ can only have a polarization vector with unit norm and so mixed states cannot be represented in terms of c_α and c_β coefficients. This is one of the reasons why the density matrix formalism is often more powerful for the description of our experiments.

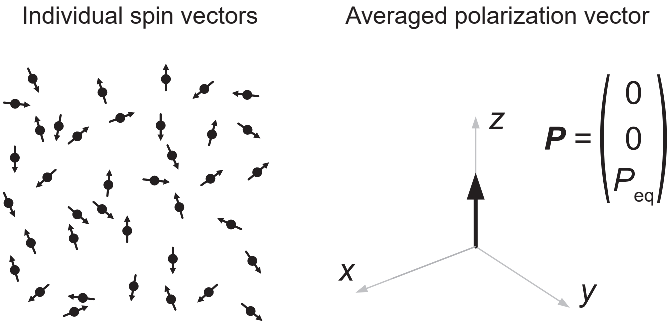

Figure 2.3: Representation of the polarization vector of an ensemble of spins whose average polarization points along the z-axis.

A result from statistical mechanics gives access to a more general expression of the density matrix at thermal equilibrium [98]

$$\hat{\rho}_{eq} = \frac{\exp\left(-\frac{\hbar \hat{H}_0}{k_B T}\right)}{\mathrm{Tr}\left\{\exp\left(-\frac{\hbar \hat{H}_0}{k_B T}\right)\right\}}, \tag{2.87}$$

where k_B and T are Boltzmann's constant and the system temperature, respectively, and the Hamiltonian $\hat{H}_0$ is expressed in rad.s^{-1}. For an ensemble of isolated spins in a magnetic field, the Hamiltonian is $\hat{H}_0 = -\gamma B_0 \hat{I}_z$ and so the equilibrium density matrix is

$$\begin{aligned}\hat{\rho}_{eq} &= \frac{\exp\left(\frac{\hbar\gamma B_0 \hat{I}_z}{k_B T}\right)}{\mathrm{Tr}\left\{\exp\left(\frac{\hbar\gamma B_0 \hat{I}_z}{k_B T}\right)\right\}} \\ &= \frac{1}{\exp\left(+\frac{\hbar\gamma B_0}{2k_B T}\right)+\exp\left(-\frac{\hbar\gamma B_0}{2k_B T}\right)} \begin{pmatrix} \exp\left(+\frac{\hbar\gamma B_0}{2k_B T}\right) & 0 \\ 0 & \exp\left(-\frac{\hbar\gamma B_0}{2k_B T}\right)\end{pmatrix} \\ &= \begin{pmatrix} \frac{1+P_{eq}}{2} & 0 \\ 0 & \frac{1-P_{eq}}{2}\end{pmatrix},\end{aligned} \tag{2.88}$$

where we recovered the result of Eq. 2.86. These two approaches yield the same result but the second is more general.

We now have the necessary tools to describe the most basic NMR experiment. Let us predict the resonance of a ^{1}H-NMR spectrum for a sample of an ensemble of non-interacting spins detected by a simple pulse-acquire experiment at $B_0 = 9.4$ T. The Hamiltonian consists only of the Zeeman term

$$\hat{H}_0 = -\gamma B_0 \hat{I}_z = \omega_0 \hat{I}_z \tag{2.89}$$

where ω_0 is the Larmor frequency of the spins. If the sample has spent enough time in the magnet without being perturbed by any rf pulse, the system is at thermal equilibrium, meaning that it can be represented by the density matrix of Eq. 2.88, with $P_{eq} = 33$ ppm, according to Eq. 1.3. The NMR spectrometer is equipped with coils to act on the spins and detect their oscillating magnetization in the xy-plane also called the transverse plane. The magnetization in the transverse plane is proportional to the expectation value of operators $\hat{I}_x$ and $\hat{I}_y$. Before we apply any pulse, there is no net magnetization in the transverse plane because we have

$$\mathrm{Tr}\left\{\hat{I}_x \hat{\rho}_{eq}\right\} = \mathrm{Tr}\left\{\hat{I}_y \hat{\rho}_{eq}\right\} = 0, \tag{2.90}$$

and there is nothing to be detected. By applying an rf pulse along the y-axis, we can move the spins from the z-axis to the x-axis. If we neglect the evolution under the Zeeman Hamiltonian of the main field B_0 during the pulse for simplicity, the pulse Hamiltonian can be written as

$$\hat{H}_1 = \omega_1 \hat{I}_y, \tag{2.91}$$

where ω_1 is the nutation frequency of the pulse which corresponds to the frequency at which the pulse rotates the spins. From the cyclic commutation relation that we have found earlier, we know that the density matrix evolves under the pulse Hamiltonian as

$$\hat{\rho}(\tau_p) = \frac{\hat{\mathbb{1}}}{2} + P_{eq}\left(\cos(\omega_1 \tau_p)\hat{I}_z + \sin(\omega_1 \tau_p)\hat{I}_x\right), \tag{2.92}$$

where τ_p is the pulse length in seconds. If we choose $\tau_p = \pi/(2\omega_1)$, the density matrix at the end of the pulse is

$$\hat{\rho}_1 = \frac{\hat{\mathbb{1}}}{2} + P_{eq}\hat{I}_x, \tag{2.93}$$

that is, we have chosen the pulse length so as to convert $\hat{I}_z$ completely into $\hat{I}_x$. After the pulse, the system is no longer in a stationary state and so it evolves under the Zeeman Hamiltonian. Again, the cyclic commutation relation gives us the time evolution of the density matrix

$$\hat{\rho}(t) = \frac{\hat{\mathbb{1}}}{2} + P_{eq}\left(\cos(\omega_0 t)\hat{I}_x + \sin(\omega_0 t)\hat{I}_y\right), \tag{2.94}$$

The expectation value of the angular momentum along the x- and y-axes along time is

$$\begin{aligned} \langle \hat{I}_x \rangle &= \mathrm{Tr}\left\{\hat{I}_x \hat{\rho(t)}\right\} = P_{eq}\cos(\omega_0 t)\mathrm{Tr}\left\{\hat{I}_x^2\right\} = \frac{P_{eq}}{2}\cos(\omega_0 t) \\ \langle \hat{I}_y \rangle &= \mathrm{Tr}\left\{\hat{I}_y \hat{\rho(t)}\right\} = P_{eq}\sin(\omega_0 t)\mathrm{Tr}\left\{\hat{I}_y^2\right\} = \frac{P_{eq}}{2}\sin(\omega_0 t). \end{aligned} \tag{2.95}$$

Therefore, the signal recorded by the NMR coil along time in complex notation is

$$S(t) = \langle \hat{I}_x \rangle + i\,\langle \hat{I}_y \rangle = \frac{1}{2}P_{eq}e^{i\omega_0 t}, \tag{2.96}$$

where the phase of the detector was chosen to have a purely real signal at $t = 0$. This shows that, following the rf pulse, the receiver will detect a signal oscillating at the Larmor frequency of the nuclear spin, with an intensity proportional to the initial thermal equilibrium polarization.

Note that we wrote the signal in terms of angular momentum from $-1/2$ to $+1/2$. To express the signal as an oscillating magnetization vector, according to Eq. 2.1, the signal obtained here must be multiplied by $N\gamma\hbar$, where N is the number of spins. Fig. 2.4 shows the evolution of the magnetization vector along the pulse-acquire experiment that we have described here. For this simplest example, we could derive analytically the resulting signal. We will see in the next section how signals can be computed numerically.

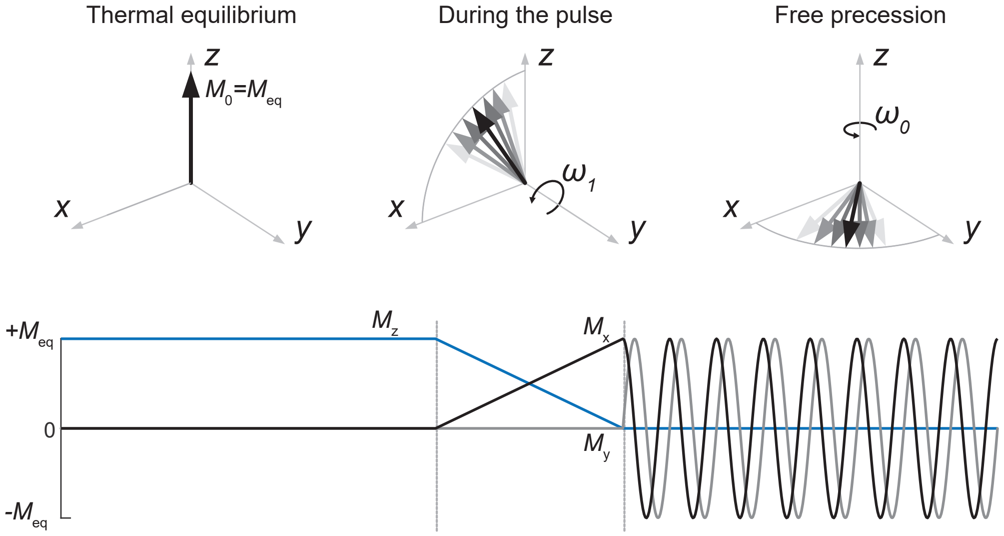

Figure 2.4: Magnetization of an ensemble of spin 1/2 (represented by a black arrow) titled from the thermal equilibrium position to the transverse plane by a $\pi/2$ pulse along the y-axis. The magnetization vector then starts precessing about the z-axis under the Zeeman Hamiltonian.

Let us now turn to the case where the system consists of a large ensemble of a pair of interacting spins. The ensemble average alone is still not able to describe this system. We need to construct operators accounting for each spin separately. This is done by taking the Kronecker product of the single spins with the identity

$$
\begin{aligned}
\hat{I}_{1z} = \hat{I}_z^{2\times2} \otimes \hat{\mathbb{1}}^{2\times2} &= \begin{pmatrix} +1/2 & 0 & 0 & 0 \\ 0 & +1/2 & 0 & 0 \\ 0 & 0 & -1/2 & 0 \\ 0 & 0 & 0 & -1/2 \end{pmatrix} \\
\hat{I}_{2z} = \hat{\mathbb{1}}^{2\times2} \otimes \hat{I}_z^{2\times2} &= \begin{pmatrix} +1/2 & 0 & 0 & 0 \\ 0 & -1/2 & 0 & 0 \\ 0 & 0 & +1/2 & 0 \\ 0 & 0 & 0 & -1/2 \end{pmatrix},
\end{aligned}
\tag{2.97}
$$

where $\hat{I}_{1z}$ and $\hat{I}_{2z}$ are the z-angular momentum operators of spin 1 and 2 in the 2-spin Hilbert space, respectively, while $\hat{I}_z^{2\times2}$ is the operator in the single spin Hilbert space. These operators live in a Hilbert with basis

$$
\mathbb{B}^{2\times2} = \{|\alpha\alpha\rangle, |\alpha\beta\rangle, |\beta\alpha\rangle, |\beta\beta\rangle\}
\tag{2.98}
$$

The same procedure can be applied to compute the angular momentum along the x- and y-axes. The Zeeman Hamiltonian for this pair of spin can be written as

$$
\begin{aligned}
\hat{H}_Z &= \hat{H}_{Z,1}^{2\times2} \otimes \hat{\mathbb{1}}^{2\times2} + \hat{\mathbb{1}}^{2\times2} \otimes \hat{H}_{Z,2}^{2\times2} = \omega_{0,1}\hat{I}_{1z} + \omega_{0,2}\hat{I}_{2z} \\
&= \frac{1}{2}\begin{pmatrix} +\omega_{0,1}+\omega_{0,2} & 0 & 0 & 0 \\ 0 & +\omega_{0,1}-\omega_{0,2} & 0 & 0 \\ 0 & 0 & -\omega_{0,1}+\omega_{0,2} & 0 \\ 0 & 0 & 0 & -\omega_{0,1}-\omega_{0,2} \end{pmatrix},
\end{aligned}
\tag{2.99}
$$

where $\omega_{0,1}$, $\omega_{0,2}$, $\hat{H}_{Z,1}^{2\times2}$ and $\hat{H}_{Z,2}^{2\times2}$ are the Larmor frequencies of spin 1 and 2 and their Zeeman Hamiltonians expressed in single spin Hilbert spaces, respectively. If spin 1 and 2 have polarization P_1 and P_2 at thermal equilibrium, respectively, the density matrix is

$$
\begin{aligned}
\hat{\rho}_{eq} &= \hat{\rho}_1^{2\times2} \otimes \hat{\rho}_2^{2\times2} \\
&= \left(\frac{\hat{\mathbb{1}}}{2} + P_1\hat{I}_z^{2\times2}\right) \otimes \left(\frac{\hat{\mathbb{1}}}{2} + P_2\hat{I}_z^{2\times2}\right) \\
&= \frac{\hat{\mathbb{1}}}{4} + \frac{1}{2}\left(P_1\hat{I}_{1z} + P_2\hat{I}_{2z} + P_1P_2 2\hat{I}_{1z}\hat{I}_{2z}\right)
\end{aligned}
\tag{2.100}
$$

A new term has appeared in the density matrix which is the product of spin 1 and 2: $2\hat{I}_{1z}\hat{I}_{2z}$. Terms associated with two different spins are referred to as "2-spin order". This term is usually neglected in the thermal equilibrium density matrix of NMR experiments without hyperpolarization because the product P_1P_2 is negligible compared to P_1 and P_2. Because the identity commutes with all operators and is responsible for no observable signal, it is often removed from the density matrix. Furthermore, it is often not necessary to consider the exact polarization of the spins but rather the ratio between them and so the thermal equilibrium density matrix is written in many textbooks as

$$\hat{\rho}_{eq} = a\hat{I}_{1z} + b\hat{I}_{2z}, \tag{2.101}$$

where a and b are real numbers. If spin 1 and 2 are homonuclear, a and b are usually chosen to be $a = b = 1$, while if there are different isotopes, they are chosen to respect the ratio between the gyromagnetic ratios so that the density matrix reflects the relative thermal equilibrium polarizations. For example, if spin 1 and 2 are a ^{1}H and a ^{13}C spin, respectively, we may choose $a = 4$ and $b = 1$.

The terms associated with spins 1 and 2 in the Zeeman Hamiltonian (see Eq. 2.99) act on the terms associated with spin 1 and 2 in the density matrix (see Eq. 2.101), respectively. It is easily verified that the angular momentum operators of spin 1 commutes with those of spin 2. Therefore, the cyclic commutation relation and its consequences that we found for $\hat{I}_x$, $\hat{I}_y$ and $\hat{I}_z$ holds for $\hat{I}_{1x}$, $\hat{I}_{1y}$ and $\hat{I}_{1z}$ and for $\hat{I}_{2x}$, $\hat{I}_{2y}$ and $\hat{I}_{2z}$, separately. In other words, what we have understood for the spin within a single-spin Hilbert space holds for each spin within a 2-spin Hilbert space individually. Therefore, a $\pi/2$ pulse acting on spin 1 generates a measurable signal oscillating at $\omega_{0,1}$. This transition is the sum of the two degenerate transitions between $|\beta\alpha\rangle$ and $|\alpha\alpha\rangle$ and between $|\beta\beta\rangle$ and $|\alpha\beta\rangle$, which sums up into a signal resonance. These two transitions are proportional to $a/2$ or $P_1/4$. Because they are degenerate, their intensities sum up to a or $P_1/2$. Similarly, a $\pi/2$ pulse acting on spin 2 generates a measurable signal oscillating at $\omega_{0,2}$ with intensity proportional to b or $P_2/2$.

These analytical results can be compared with numerical simulations, such as those shown as examples in Chapter 1 (see Fig. 1.3, 1.7 and 1.8). We now show how spectra can be simulated for a single spin with Larmor frequency $\omega_{1,0}/2\pi = 10$ Hz and a pair of homonuclear spins with Larmor frequencies $\omega_{1,0}/2\pi = 10$ Hz and $\omega_{2,0}/2\pi = -20$ Hz. Note that these frequencies are defined in the rotating frame, i.e., they represent the difference between the Larmor frequency and the carrier frequency.

Following the discussion above, we use the initial density matrix

$$\hat{\rho}_0 = \hat{I}_z, \tag{2.102}$$

where $\hat{I}_k = \hat{I}_{1k} + \hat{I}_{2k}$ with $k = x, y, z$ in the two-spin case. A non-stationary state is generated by a $\pi/2$ pulse acting on the spins, which is computed using the sandwich formula (see Eq. 2.76) and the propagator of the pulse Hamiltonian (see Eq. 2.91) during the appropriate delay

$$\hat{\rho}_1 = \exp\left(-i\frac{\pi}{2}\hat{I}_y\right)\hat{\rho}_0 \exp\left(+i\frac{\pi}{2}\hat{I}_y\right). \tag{2.103}$$

Free evolution is simulated by propagating the density matrix under $\hat{H}_0 = \omega_{1,0}\hat{I}_1$ or $\hat{H}_0 = \omega_{1,0}\hat{I}_{1z} + \omega_{2,0}\hat{I}_{2z}$ iteratively during the FID and extracting the expectation value of the angular momentum at each time increment. The density matrix for increment $k+1$ is therefore

$$\hat{\rho}_{k+1} = \exp\left(-i\hat{H}_0 dt\right)\hat{\rho}_k \exp\left(+i\hat{H}_0 dt\right), \tag{2.104}$$

where dt is the spectrometer dwell time, i.e., the time between temporal data points. The expectation value of the recorded signal at increment k is

$$\begin{aligned} S_k &= \langle \hat{I}_x \rangle + i \langle \hat{I}_y \rangle \\ &= \mathrm{Tr}\left\{ \hat{I}_x \hat{\rho}_k \right\} + i\mathrm{Tr}\left\{ \hat{I}_y \hat{\rho}_k \right\} \\ &= \mathrm{Tr}\left\{ (\hat{I}_x + i\hat{I}_y)\hat{\rho}_k \right\} \\ &= \mathrm{Tr}\left\{ \hat{I}_+ \hat{\rho}_k \right\}, \end{aligned} \tag{2.105}$$

where we have introduced the shift operator $\hat{I}_\pm = \hat{I}_x \pm i\hat{I}_y$. The resulting time domain signal does not decay because our model does not include relaxation. We, therefore, apply an apodization function

$$S'_k = S_k \exp\left(-\pi \delta\nu_{1/2} t_k\right), \tag{2.106}$$

where $\delta\nu_{1/2}$ is the full width at half maximum (FWHM) of the Fourier transformed signal in Hz and $t_k = (k-1)dt$ is the time since the end of the pulse and a time point of the acquisition. In addition, we apply a second apodization function

$$S'_k = \begin{cases} S_k/2 \text{ if } k = 1 \\ S_k \text{ otherwise,} \end{cases} \tag{2.107}$$

which avoids baseline distortion of the discretized signal. [102, 103] Finally, the signal is Fourier transformed. Fig. 2.5 shows the results of the numerical simulation, which was performed using a home-written MATLAB script, as all the simulations throughout this work.

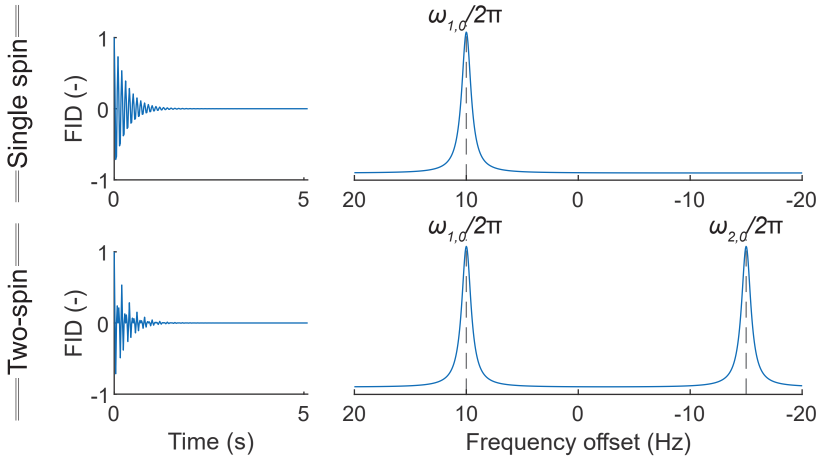

Figure 2.5: Numerical simulation of the spectra for pulse-acquire experiments for a single-spin system and a homonuclear two-spin system (top and bottom, respectively). The plots on the right are the Fourier transform of the plots on the left. Simulation with 256 time increments of 10 ms, Fourier transform after applying $\delta\nu_{1/2} = 1$ Hz of line broadening and zero-filling to 1024 points. For both the FIDs and the spectra, the real part of the signal is displayed.

As can be seen in Fig. 2.5, the numerical simulation features the resonances which we expected from the analytical derivation above. Because the Hamiltonian does not contain any term coupling spins 1 and 2, the spins behave as if the other did not exist (bearing in mind that we neglect relaxation).

2.3 Interactions in NMR and DNP

In this section, we will detail relevant interactions for this work and the related Hamiltonians. We have already mentioned the Zeeman Hamiltonian and the pulse Hamiltonian, which describes spin-field interactions; that of the spin with the static magnetic field B_0 and with the magnetic field component of rf pulses B_1, respectively. We will show how the Zeeman interaction must be slightly corrected to account for the chemical shift. Then we will present three spin-spin interactions:

- The J-coupling is an intramolecular nucleus-nucleus interaction mediated by the electron cloud. It is often referred to as the scalar interaction. J-couplings are relatively weak interactions for NMR, they typically do not exceed a few hundreds of Hz;
- The nucleus-nucleus dipolar interaction D is a through-space interaction between the nuclear spins. It is the quantum mechanical equivalent of the classical dipole-dipole interaction. The nuclear dipolar interaction typically takes values up to tens of kHz;
- The electron-nucleus dipolar interaction A, also referred to as the anisotropic hyperfine interaction, is the same as D but is usually expressed differently in the case of the electron-nucleus interaction. It can take values as high as several MHz.

An important aspect of the interactions is their time dependence: spin-spin interactions have completely different consequences on spectral features whether a molecule is freely tumbling in the liquid-state or static in the solid-state. In particular, dipolar interactions are averaged out by molecular tumbling in isotropic non-viscous liquids. As a consequence, they do not affect the frequency of the nuclear transitions (they cause relaxation but this will not be treated here), which enables the observation of the weak J-coupling interactions. In the solid-state, to the contrary, dipolar interactions give rise to broad spectral features which usually largely exceed J-couplings.

In many situations, terms can be neglected in the Hamiltonians and so different forms can be found in the literature. We will give the most general forms of the Hamiltonians which are necessary for the purpose of this work.

Before we move on to spin-spin interactions, we need to introduce the chemical shift. We have already defined the Zeeman Hamiltonian for a single spin (see Eq. 2.89) as well as for multiple spin systems (see Eq. 2.99). In reality, nuclei are not in vacuum; they are held in molecules and are therefore surrounded by electrons. The presence of these electrons and their movements tend to screen the magnetic field experienced by the nuclei. This effect may be accounted for in the Hamiltonian by including an adimensional shielding factor σ [98]

$$\hat{H}_Z = -\gamma B_0(1-\sigma)\hat{I}_z, \tag{2.108}$$

which can also be expressed in terms of the chemical shift $\delta = -10^6 \cdot \sigma$ in ppm

$$\hat{H}_Z = -\gamma B_0(1+10^{-6}\delta)\hat{I}_z = \omega_0 \hat{I}_z, \tag{2.109}$$

where $\omega_0 = -\gamma B_0(1+10^{-6}\delta)$ is the Larmor frequency of the spin taking the chemical shift into account. The chemical shift is a convenient parameter that does not depend on the magnetic field. Therefore, the resonance (or the multiplets) associated with a spin always appears at the same location of an NMR spectrum expressed in terms of chemical shifts, no matter the magnetic field used for a particular experiment. For ^{1}H and ^{13}C spins, typical values of δ span from 0 to 10 ppm and from 0 to 200 ppm, respectively.

Note that this expression of the chemical shift is only valid for liquids. Indeed, the chemical shift is a rank-1 interaction, which depends on the orientation of the molecule with respect to the static magnetic field B_0. The anisotropic part of the chemical shift is averaged out by molecular motion in liquids leaving only the isotropic part, which is characterized by the constant δ_{iso}. This isotropic part of the interaction is appropriately described by the above equations with $\delta = \delta_{iso}$.

2.3.1 The J-interaction at high-field

The complete form of the tensor representing the J-interaction is given by a 3 by 3 matrix. [104] However, in isotropic liquids, the interaction simplifies to the form [98]

$$\begin{aligned} \hat{H}_J &= 2\pi J_{12} \hat{\boldsymbol{I}}_1 \cdot \hat{\boldsymbol{I}}_2 \\ &= 2\pi J_{12}\left(\hat{I}_{1x}\hat{I}_{2x} + \hat{I}_{1y}\hat{I}_{2y} + \hat{I}_{1z}\hat{I}_{2z}\right) \\ &= \pi J_{12} \begin{pmatrix} +1/2 & 0 & 0 & 0 \\ 0 & -1/2 & +1 & 0 \\ 0 & +1 & -1/2 & 0 \\ 0 & 0 & 0 & +1/2 \end{pmatrix}, \end{aligned} \tag{2.110}$$

where J_{12} is the J-coupling constant between spins 1 and 2, expressed in Hz (and hence the 2π factor to ensure that the Hamiltonian is expressed in rad.s^{-1} which is the convention throughout this work). The diagonal elements show that $\hat{H}_J$ shifts the $|\alpha\alpha\rangle$ and $|\beta\beta\rangle$ states by $+\pi J_{12}/2$ while it shifts the $|\beta\alpha\rangle$ and $|\alpha\beta\rangle$ states by $-\pi J_{12}/2$. Furthermore, the $|\beta\alpha\rangle$ and $|\alpha\beta\rangle$ states are mixed by the off-diagonal terms $+\pi J_{12}$.

Let us assume that a pair of J-coupled spins are subject to a magnetic field B_0. Their Hamiltonian thus consists of the Zeeman and J-interaction $\hat{H}_0 = \hat{H}_Z + \hat{H}_J$, whose complete expression in the $|\alpha\beta\rangle \otimes |\beta\alpha\rangle$ subspace is

$$\hat{H}_0^{|\alpha\beta\rangle\otimes|\beta\alpha\rangle} = \begin{pmatrix} +\Delta/2 - \pi J_{12}/2 & +\pi J_{12} \\ +\pi J_{12} & -\Delta/2 - \pi J_{12}/2 \end{pmatrix}. \tag{2.111}$$

where $\Delta = \omega_{0,1} - \omega_{0,2}$ is the Larmor frequency difference between spin 1 and 2. When the $|\beta\alpha\rangle$ and $|\alpha\beta\rangle$ states are very far in energy, we have $\Delta \gg \pi J_{12}$ and the J-Hamiltonian may be truncated (or secularized) to yield

$$\hat{H}_J \approx \pi J_{12} \begin{pmatrix} +1/2 & 0 & 0 & 0 \\ 0 & -1/2 & 0 & 0 \\ 0 & 0 & -1/2 & 0 \\ 0 & 0 & 0 & +1/2 \end{pmatrix} = 2\pi J_{12}\hat{I}_{1z}\hat{I}_{2z}. \tag{2.112}$$

In this case, the spins are said to be in the *weak coupling regime* or *far from equivalence*, which means that the J-coupling only shifts the energy levels but does not mix them. Hence, the Zeeman states can still be considered to be the eigenstates of the system. This is typically the case for heteronuclei at high-field: for a pair of ^{1}H and ^{13}C spins at 9.4 T, the Larmor frequency difference is $\Delta/2\pi = 300$ MHz while the J-coupling can never be larger than a few hundreds of Hz. Yet, because of the J-coupling, none of the four observable transitions are degenerate. As shown in Fig.

2.6, the two degenerate $\omega_{1,0}$ transitions are split into two transitions separated by $2\pi J_{12}$ and *idem* for the two $\omega_{2,0}$ transitions. The spectrum of spins 1 and 2, therefore, consists of doublets split by $2\pi J_{12}$ and centered at $\omega_{1,0}$ and $\omega_{2,0}$, respectively. Note that in Fig. 2.6 we used the truncated form of the J-Hamiltonian although the frequency difference in Larmor frequency does not greatly exceed the J-coupling. This unphysical situation was chosen as a simple visual argument.

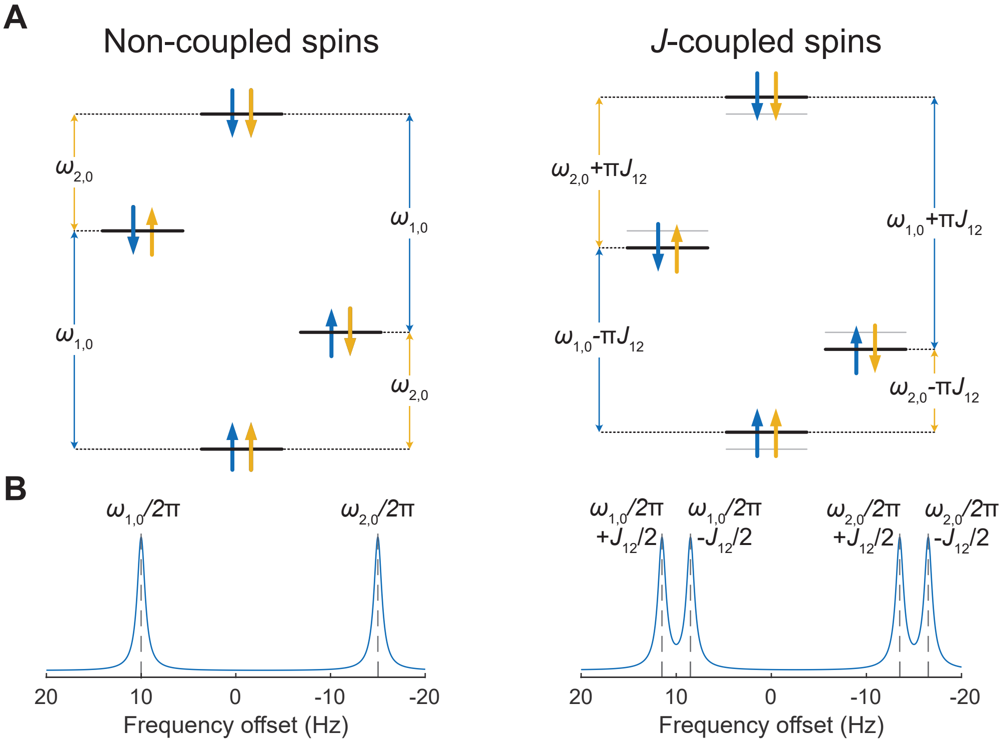

Figure 2.6: **A**. Four-level energy diagrams of a system of two spins 1/2 in the case of non-interacting and J-coupled spins for a positive J-coupling constant. Note that the J-coupling splitting has been greatly exaggerated so that the difference between the non-coupled and coupled diagrams is visible. **B**. Corresponding numerical spectrum simulation using the same parameters as in Fig. 2.5 with $J_{12} = 3$ Hz and the truncated form of J in the coupled case (see Eq. 2.112).

The opposite case is often met in conventional high-field NMR for homonuclear J-coupled spins as their difference in Larmor frequency is only due to the chemical shift and so $\Delta = 10^{-6}(\delta_1 - \delta_2)\omega_0$, where ω_0 is the Larmor frequency of the spin in vacuum. For example, a pair of ^{1}H spins at 1.88 T with a J-coupling of 10 Hz and a chemical shift difference of 0.5 ppm have a frequency difference $\Delta/2\pi \approx 40$ Hz, which is only ≈ 4 times larger than the J-coupling and so the Zeeman states are no longer the exact eigenstates of the system. This gives rise to the so-called "roof effect" where the doublets are no longer symmetric in intensity, as shown in Fig. 2.7. As mentioned above, the absence of roof-effect in the J-coupled spectrum simulated in Fig. 2.6 and Fig. 2.7A is non-physical; it is the result of the secularization of the J-Hamiltonian.

More important for this work is the case of J-coupled heteronuclei at ZULF. The most typical case is the ^{1}H-^{13}C pair of ^{13}C-formate. Despite the large gyromagnetic ratio difference between the two spins, in the absence of magnetic field, there is no Zeeman interaction to differentiate the spins. The eigenstates, in this case, are those of the singlet-triplet basis [81]

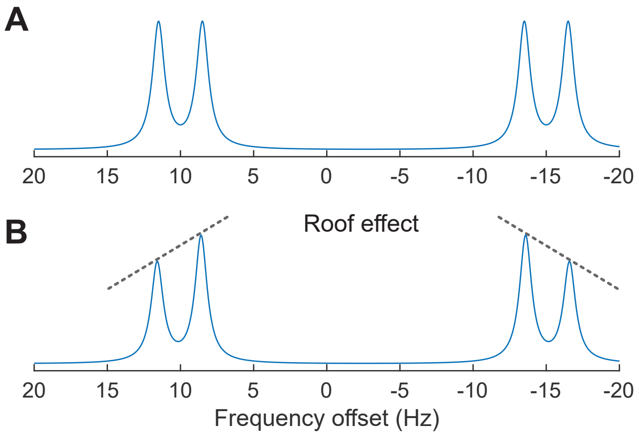

Figure 2.7: Numerical spectrum simulation using the same parameters as in Fig. 2.5 and Fig. 2.6 using the secularized form of J-Hamiltonian (see Eq. 2.112) and the complete form (see Eq. 2.110), respectively.

$$\begin{aligned}|T_+\rangle &= |\alpha\alpha\rangle \\ |T_0\rangle &= \frac{1}{\sqrt{2}}(|\alpha\beta\rangle + |\beta\alpha\rangle) \\ |S_0\rangle &= \frac{1}{\sqrt{2}}(|\alpha\beta\rangle - |\beta\alpha\rangle) \\ |T_-\rangle &= |\beta\beta\rangle\end{aligned} \tag{2.113}$$

The three triplet states $|T_+\rangle$, $|T_0\rangle$ and $|T_-\rangle$ are degenerate with energy

$$\omega_T = \langle T_\pm|\hat{H}_J|T_\pm\rangle = \langle T_0|\hat{H}_J|T_0\rangle = +\pi J_{12}/2, \tag{2.114}$$

while the singlet state $|S_0\rangle$ has energy

$$\omega_S = \langle S_0|\hat{H}_J|S_0\rangle = -3\pi J_{12}/2 \tag{2.115}$$

and so the energy splitting between the singlet state and three degenerate states of the triplet manifold corresponds to the J-coupling, as shown in Fig. 2.8,

$$\omega_T - \omega_S = 2\pi J_{12}. \tag{2.116}$$

2.3.2 The J-interaction at zero-field

While signals at high-field are proportional to nuclear polarization, liquid-state ZULF signals are proportional to the polarization difference between J-coupled heteronuclei. We prove this for the simplest case where a pair of heteronuclei 1 and 2, with J-coupling J_{12}, have initial polarizations P_1 and P_2, respectively, and are initially immersed in a strong magnetic field which is suddenly switched off. We assume that the signal at zero-field is detected by a magnetometer sensitive to fields along the axis of initial polarization of the spins, which we call z. In terms of spin dynamics, this experiment consists of projecting the stationary spin states at high-field onto the zero-field states, i.e., the Zeeman states onto the singlet-triplet states.

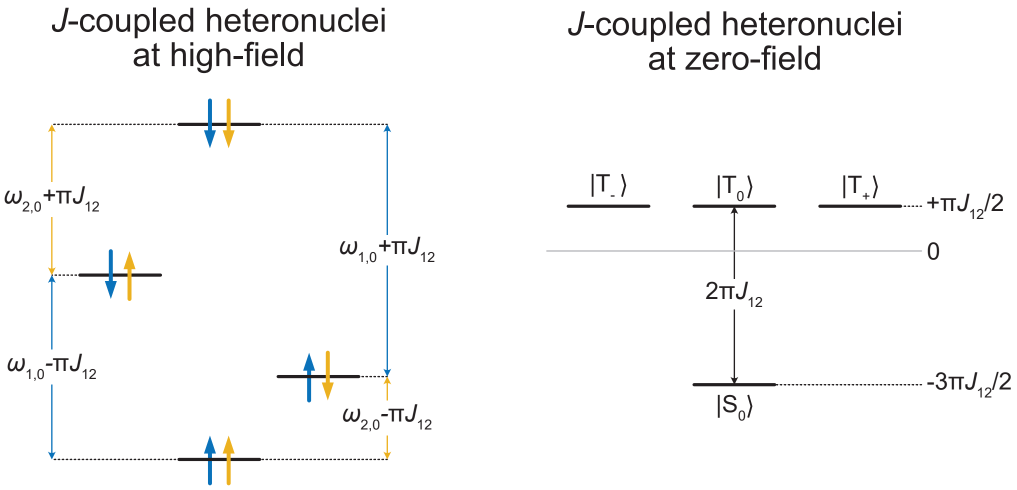

Figure 2.8: Comparison of the energy diagrams for J-coupled heteronuclear spins at high- vs zero-field for a positive J-coupling constant.

We first define a set of two-spin operators to describe the state of the spin pair at zero-field [81, 105]

$$\begin{aligned}\hat{Z}_x &= \hat{I}_{1x}\hat{I}_{2x} + \hat{I}_{1y}\hat{I}_{2y} \\ \hat{Z}_y &= \hat{I}_{1x}\hat{I}_{2y} - \hat{I}_{1y}\hat{I}_{2x} \\ \hat{Z}_z &= \frac{1}{2}\left(\hat{I}_{1z} - \hat{I}_{2z}\right) \\ \hat{D}_z &= \frac{1}{2}\left(\hat{I}_{1z} + \hat{I}_{2z}\right).\end{aligned} \tag{2.117}$$

The reason for choosing this set of operators will soon become evident, because of their commutation relationships. We now rewrite the initial density matrix in terms of these operators. The initial density matrix in the Zeeman basis can be decomposed as

$$\hat{\rho}_0 = p_{\alpha\alpha}\hat{\rho}_{\alpha\alpha} + p_{\alpha\beta}\hat{\rho}_{\alpha\beta} + p_{\beta\alpha}\hat{\rho}_{\beta\alpha} + p_{\beta\beta}\hat{\rho}_{\beta\beta}, \tag{2.118}$$

where $p_{\alpha\alpha}$, $p_{\alpha\beta}$, $p_{\beta\alpha}$ and $p_{\beta\beta}$ are the populations of the Zeeman states related to the nuclear polarization P_I and P_S by

$$\begin{aligned}p_{\alpha\alpha} &= \frac{(1+P_1)(1+P_2)}{4} \\ p_{\alpha\beta} &= \frac{(1+P_1)(1-P_2)}{4} \\ p_{\beta\alpha} &= \frac{(1-P_1)(1+P_2)}{4} \\ p_{\beta\beta} &= \frac{(1-P_1)(1-P_2)}{4},\end{aligned} \tag{2.119}$$

Because $\hat{Z}_z$ can be written as

$$\hat{Z}_z = \frac{1}{2}\left(|T_0\rangle\langle S_0| + |S_0\rangle\langle T_0|\right), \tag{2.120}$$

we can write the elements of the initial density matrix in terms of the operators of Eq. 2.117 as

$$\begin{aligned}\hat{\rho}_{\alpha\alpha} &= \hat{T}_+ \\ \hat{\rho}_{\alpha\beta} &= \left|\alpha\beta\right\rangle\left\langle\alpha\beta\right| = \frac{1}{2}\left(\left|T_0\right\rangle\left\langle T_0\right| + \left|S_0\right\rangle\left\langle S_0\right| + \left|T_0\right\rangle\left\langle S_0\right| + \left|S_0\right\rangle\left\langle T_0\right|\right) \\ &= \frac{1}{2}\left(\hat{T}_0 + \hat{S}_0 + 2\hat{Z}_z\right) \\ \hat{\rho}_{\beta\alpha} &= \left|\beta\alpha\right\rangle\left\langle\beta\alpha\right| = \frac{1}{2}\left(\left|T_0\right\rangle\left\langle T_0\right| + \left|S_0\right\rangle\left\langle S_0\right| - \left|T_0\right\rangle\left\langle S_0\right| - \left|S_0\right\rangle\left\langle T_0\right|\right) \\ &= \frac{1}{2}\left(\hat{T}_0 + \hat{S}_0 - 2\hat{Z}_z\right) \\ \hat{\rho}_{\beta\beta} &= \hat{T}_-\end{aligned} \tag{2.121}$$

and so, plugging Eq. 2.121 into Eq. 2.118, we can write the initial density matrix as

$$\begin{aligned}\hat{\rho}_0 &= p_{\alpha\alpha}\hat{T}_+ + p_{\alpha\beta}\frac{1}{2}\left(\hat{T}_0 + \hat{S}_0 + 2\hat{Z}_z\right) + p_{\beta\alpha}\frac{1}{2}\left(\hat{T}_0 + \hat{S}_0 - 2\hat{Z}_z\right) + p_{\beta\beta}\hat{T}_- \\ &= p_{\alpha\alpha}\hat{T}_+ + \frac{p_{\alpha\beta} + p_{\beta\alpha}}{2}\left(\hat{T}_0 + \hat{S}_0\right) + \left(p_{\alpha\beta} - p_{\beta\alpha}\right)\hat{Z}_z + p_{\beta\beta}\hat{T}_-,\end{aligned} \tag{2.122}$$

where we plug in the relation of Eq. 2.119 to get

$$\hat{\rho}_0 = \frac{(1+P_1)(1+P_2)}{4}\hat{T}_+ + \frac{1-P_1P_2}{4}\left(\hat{T}_0 + \hat{S}_0\right) + \frac{P_1 - P_2}{2}\hat{Z}_z + \frac{(1-P_1)(1-P_2)}{4}\hat{T}_-. \tag{2.123}$$

The Hamiltonian at zero-field only consists of the J-interaction

$$\hat{H}_0 = \hat{H}_J = 2\pi J_{12}\hat{\boldsymbol{I}}\cdot\hat{\boldsymbol{S}} = 2\pi J_{12}\left(\hat{Z}_x + \hat{I}_{1z}\hat{I}_{2z}\right), \tag{2.124}$$

and so we have expressed both the density matrix and the Hamiltonian in terms of the operators of Eq. 2.117. To find the terms which evolve at zero-field, we simplify the Hamiltonian by discarding the terms which commute with the density matrix, yielding

$$\hat{H}_0 = 2\pi J_{12}\hat{Z}_x. \tag{2.125}$$

The choice behind the definition of the set of operators that we have chosen becomes apparent considering the commutation relation

$$\begin{aligned}[\hat{Z}_x, \hat{Z}_z] &= i\hat{Z}_y \\ [\hat{Z}_y, \hat{Z}_x] &= i\hat{Z}_z \\ [\hat{Z}_z, \hat{Z}_y] &= i\hat{Z}_x,\end{aligned} \tag{2.126}$$

where we recognize the cyclic commutation relation, meaning that $\hat{H}_0$ converts $\hat{Z}_z$ into $\hat{Z}_y$ and $\hat{Z}_y$ into $-\hat{Z}_z$ at a frequency $2\pi J_{12}$, while all other terms in the density matrix are stationary. Therefore, the density matrix at time t is

$$\begin{aligned}\hat{\rho}(t) =& \frac{(1+P_1)(1+P_2)}{4}\hat{T}_+ + \frac{(1-P_1)(1-P_2)}{4}\hat{T}_- \\ &+ \frac{P_1 - P_2}{2}\left(\cos\left(2\pi J_{12}t\right)\hat{Z}_z + \sin\left(2\pi J_{12}t\right)\hat{Z}_x\right),\end{aligned} \tag{2.127}$$

where we skipped $\hat{T}_0$ and $\hat{S}_0$ as they give rise to no observable signal. The observable measured by the detector is the magnetization of the sample along the z-axis, which is given by the expectation value of $\hat{M}_z = N\hbar(\gamma_1 \hat{I}_{1z} + \gamma_2 \hat{I}_{2z})$, where N is the number of molecules. We decompose the detected magnetization into an oscillating part

$$\begin{aligned} M_z^{osc}(t) &= \mathrm{Tr}\left\{\hat{M}_z \hat{\rho}^{osc}(t)\right\} \\ &= N\hbar \frac{P_1 - P_2}{2} \left(\gamma_1 \mathrm{Tr}\left\{\hat{I}_{1z}\hat{Z}_z\right\} + \gamma_2 \mathrm{Tr}\left\{\hat{I}_{2z}\hat{Z}_z\right\}\right) \cos(2\pi J_{12} t) \\ &= N\hbar \frac{P_1 - P_2}{4} (\gamma_1 - \gamma_2) \cos(2\pi J_{12} t), \end{aligned} \tag{2.128}$$

and a stationary part

$$\begin{aligned} M_z^{stat} =& \mathrm{Tr}\left\{\hat{M}_z \hat{\rho}^{stat}\right\} \\ =& N\hbar \frac{(1+P_1)(1+P_2)}{4} \left(\gamma_1 \mathrm{Tr}\left\{\hat{I}_{1z}\hat{T}_+\right\} + \gamma_2 \mathrm{Tr}\left\{\hat{I}_{2z}\hat{T}_+\right\}\right) \\ &+ N\hbar \frac{(1-P_1)(1-P_2)}{4} \left(\gamma_1 \mathrm{Tr}\left\{\hat{I}_{1z}\hat{T}_-\right\} + \gamma_2 \mathrm{Tr}\left\{\hat{I}_{2z}\hat{T}_-\right\}\right) \\ =& N\hbar \frac{P_1 + P_2}{4} (\gamma_1 + \gamma_2). \end{aligned} \tag{2.129}$$

We have shown that the zero-field signal is the sum of stationary and non-stationary signals, which are proportional to the sum and the difference between the spin polarizations, respectively, and that the non-stationary signal oscillates at a frequency of $2\pi J_{12}$. Fig. 2.9 shows the numerical simulation for a pair of ^{1}H and ^{13}C spins with a J-coupling of 200 Hz. Because the detected eigenvalue is real, the signal is real and the J-beating is split into positive and negative frequencies.

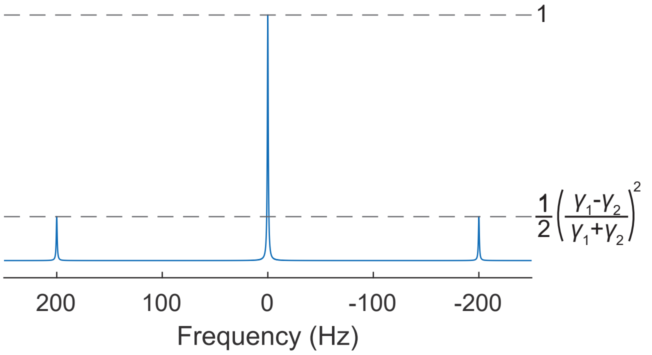

Figure 2.9: Spectrum simulation at zero-field for a pair of ^{1}H and ^{13}C spins with a J-coupling of 200 Hz. Simulation with 256 time increments of 10 ms and 1 Hz of line broadening and zero-filling to 1024 points prior to Fourier transform. The horizontal dashed lines indicate the ratio of the signals expected from the analytical solutions (see Eq. 2.130). The extra factor of 1/2 accounts for the fact the oscillating signal is split into positive and negative components while not for the stationary part.

The intensity of the lines matches the analytical solution. Indeed, since the polarizations are proportional to gyromagnetic ratios ($P_1 \propto \gamma_1$ and $P_2 \propto \gamma_2$), we have

$$\frac{M_z^{osc}(0)}{M_z^{stat}} = \left(\frac{\gamma_1 - \gamma_2}{\gamma_1 + \gamma_2}\right)^2 \tag{2.130}$$

Our analysis has shown that a large fraction of the available nuclear polarization is not converted into a non-stationary state by the simple sudden field drop experiment (see Eq. 2.130), which implies that the spectrum has a large component at zero-frequency. More sophisticated experimental schemes use magnetic field pulses at zero-field to convert the total available polarization into an oscillating signal. [81]

Eq. 2.128 also shows an important point: because the intensity of the observable transition is proportional to the difference between the gyromagnetic ratio of the spins, homonuclear spin systems give rise to no signal. Another interesting consequence of this equation is that pairs of heteronuclei with gyromagnetic ratios of opposite signs are convenient spin systems for liquid-state ZULF. For example, ^{13}C-^{15}N pairs like in cyanide groups are interesting ZULF probes; their gyromagnetic ratio difference is maximized and they exhibit very long coherence times due to the low gyromagnetic ratios.

2.3.3 The nucleus-nucleus dipolar interactions

The nuclear dipole-dipole interaction originates from the classical dipole-dipole interaction. It can be understood as the potential energy associated with the interactions of each magnetic dipole with the magnetic field generated by the other one. This potential energy is given, for two classical point magnetic dipoles $\boldsymbol{\mu}_1$ and $\boldsymbol{\mu}_2$ separated by vector $\boldsymbol{r}$, by [81]

$$E_D = -\frac{\mu_0}{4\pi}\frac{1}{r^3}\left(\frac{3}{r^2}(\boldsymbol{\mu}_1\cdot\boldsymbol{r})(\boldsymbol{\mu}_2\cdot\boldsymbol{r}) - \boldsymbol{\mu}_1\cdot\boldsymbol{\mu}_2\right), \tag{2.131}$$

where r is the Euclidean norm of the vector $\boldsymbol{r}$. The Hamiltonian representing the same interaction between two spins with magnetic moments $\hat{\boldsymbol{\mu}}_1$ and $\hat{\boldsymbol{\mu}}_2$ separated by the vector $\boldsymbol{r}$, derives from the above equation

$$\hat{H}_D = -\frac{\mu_0}{4\pi}\frac{\hbar}{r^3}\left(\frac{3}{r^2}(\hat{\boldsymbol{\mu}}_1\cdot\boldsymbol{r})(\hat{\boldsymbol{\mu}}_2\cdot\boldsymbol{r}) - \hat{\boldsymbol{\mu}}_1\cdot\hat{\boldsymbol{\mu}}_2\right), \tag{2.132}$$

in rad.s^{-1}, where we have assumed that the position of the dipole could be treated classically. It can be expressed in terms of angular momentum operators of spins 1 and 2, using Eq. 2.1

$$\hat{H}_D = b_{12}\left(\frac{3}{r^2}(\hat{\boldsymbol{I}}_1\cdot\boldsymbol{r})(\hat{\boldsymbol{I}}_2\cdot\boldsymbol{r}) - \hat{\boldsymbol{I}}_1\cdot\hat{\boldsymbol{I}}_2\right), \tag{2.133}$$

where we have defined the dipole-dipole constant

$$b_{12} = -\frac{\mu_0}{4\pi}\frac{\hbar\gamma_1\gamma_2}{r^3}. \tag{2.134}$$

This form of the dipolar Hamiltonian is rarely used in NMR. Instead, it is usually expressed using the spherical tensor representation

$$\hat{H}_D = \hat{D}_0 + \hat{D}_{+1} + \hat{D}_{-1} + \hat{D}_{+2} + \hat{D}_{-2}, \tag{2.135}$$

where, choosing the z-axis as the reference axis, we have

$$\begin{aligned}
\hat{D}_0 &= D_0\left(2\hat{I}_{1z}\hat{I}_{2z} - \frac{1}{2}(\hat{I}_{1+}\hat{I}_{2-} + \hat{I}_{1-}\hat{I}_{2+})\right)\\
\hat{D}_{\pm1} &= D_{\pm1}(\hat{I}_{1z}\hat{I}_{2\pm} + \hat{I}_{1\pm}\hat{I}_{2z})\\
\hat{D}_{\pm2} &= D_{\pm2}\hat{I}_{1\pm}\hat{I}_{2\pm},
\end{aligned} \tag{2.136}$$

with the constants

$$
\begin{aligned}
D_0 &= \frac{1-3\cos^2\theta}{2} b_{12} \\
D_{\pm 1} &= \frac{3}{2}\sin\theta\cos\theta e^{\mp i\phi} b_{12} \\
D_{\pm 2} &= \frac{3}{4}\sin^2\theta e^{\mp 2i\phi} b_{12},
\end{aligned}
\tag{2.137}
$$

where θ and ϕ are the polar and azimuthal angles, respectively, between the vector $\boldsymbol{r}$ and the z-axis. The operators of the spherical tensor basis are related to the Cartesian operators by

$$\hat{I}_{k\pm} = \hat{I}_{kx} \pm i\hat{I}_{ky}, \tag{2.138}$$

where $k = 1, 2$. The spatial dependence of the three constants D_0, $D_{\pm 1}$ and $D_{\pm 2}$ is represented in Fig. 2.10.

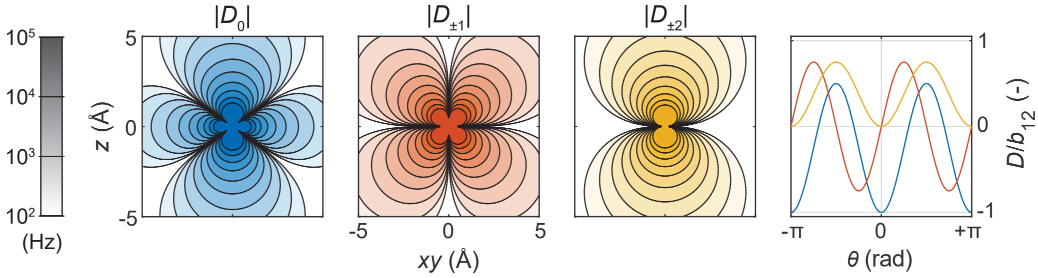

Figure 2.10: Spacial dependence of dipolar interaction for a pair of ^{1}H spins, with one spin located at the origin, expressed in Hz and as absolute values decomposed into spherical harmonics. The right plot shows the angular dependence of the dipolar coupling constants in relative intensity, for $\phi = 0$.

At ZULF, the full form of the dipolar Hamiltonian needs to be taken into account. For a pair of dipolar coupled nuclei at ZULF, spins are in a stationary state when they are colinear. The simulation shown in the Introduction (see Fig. 1.7) shows the case where spins initially polarized along the z-axis are suddenly brought to zero-field, which projects the Zeeman states onto the zero-field states (as was the case for liquid-state zero-field experiments). Therefore, the component of the spin polarization which was initially aligned with the spin-spin vector remains stationary, while the component of the spin polarization which was initially orthogonal with respect to the spin-spin vector starts precessing about it. These two components give rise to the zero-frequency and oscillating components in Fig. 1.7, respectively.

At high-field, some of the terms of the dipolar Hamiltonian can be neglected. To understand which terms can be neglected, the matrix expressions of the terms are instructive. The term $\hat{D}_0$ has a similar structure to the J-coupling Hamiltonian (see Eq. 2.110)

$$\hat{D}_0 = D_0 \begin{pmatrix} +1/2 & 0 & 0 & 0 \\ 0 & -1/2 & 0 & 0 \\ 0 & 0 & -1/2 & 0 \\ 0 & 0 & 0 & +1/2 \end{pmatrix} + D_0 \begin{pmatrix} 0 & 0 & 0 & 0 \\ 0 & 0 & +1/2 & 0 \\ 0 & +1/2 & 0 & 0 \\ 0 & 0 & 0 & 0 \end{pmatrix}, \tag{2.139}$$

The first term shifts the Zemman states without mixing them while the second term mixes the $|\alpha\beta\rangle$ and $|\beta\alpha\rangle$ states. The terms $\hat{D}_{+1}$ and $\hat{D}_{-1}$ mix the $|\alpha\alpha\rangle$ and $|\beta\beta\rangle$ states with the $|\alpha\beta\rangle$ and $|\beta\alpha\rangle$ states

$$\hat{D}_{+1} = D_{+1}\begin{pmatrix} 0 & +1/2 & +1/2 & 0 \\ 0 & 0 & 0 & -1/2 \\ 0 & 0 & 0 & -1/2 \\ 0 & 0 & 0 & 0 \end{pmatrix}, \hat{D}_{-1} = D_{-1}\begin{pmatrix} 0 & 0 & 0 & 0 \\ +1/2 & 0 & 0 & 0 \\ +1/2 & 0 & 0 & 0 \\ 0 & -1/2 & -1/2 & 0 \end{pmatrix}. \tag{2.140}$$

Finally, $\hat{D}_{+2}$ and $\hat{D}_{-2}$ mix the $|\alpha\alpha\rangle$ and $|\beta\beta\rangle$ states with each other

$$\hat{D}_{+2} = D_{+2}\begin{pmatrix} 0 & 0 & 0 & 1 \\ 0 & 0 & 0 & 0 \\ 0 & 0 & 0 & 0 \\ 0 & 0 & 0 & 0 \end{pmatrix}, \hat{D}_{-2} = D_{-2}\begin{pmatrix} 0 & 0 & 0 & 0 \\ 0 & 0 & 0 & 0 \\ 0 & 0 & 0 & 0 \\ 1 & 0 & 0 & 0 \end{pmatrix}. \tag{2.141}$$

If we consider only coherent dynamics and not relaxation, only a few terms are relevant. Because they mix states which are far in energy in the high-field limit, the terms $\hat{D}_{\pm 1}$ and $\hat{D}_{\pm 2}$ are usually neglected. As for $\hat{D}_0$, in the heteronuclear case, the $|\alpha\beta\rangle$ and $|\beta\alpha\rangle$ are far in energy and so the dipolar Hamiltonian reduces to

$$\hat{H}_D^{hetero} \approx D_0 2\hat{I}_{1z}\hat{I}_{2z}. \tag{2.142}$$

In the homonuclear case, the $|\alpha\beta\rangle$ and $|\beta\alpha\rangle$ states are degenerate or nearly degenerate and so the full form of $\hat{D}_0$ has to be taken into account

$$\hat{H}_D^{homo} \approx \hat{D}_0 \tag{2.143}$$

This form of the dipolar Hamiltonian and its truncation in the heteronuclear case have a similar effect to the J-Hamiltonian. However, there are two notable differences. First, the intensity of the interaction is much stronger; second, the interaction is anisotropic, which results in spectra featuring distinctive Pake patterns. Fig. 2.11 shows numerical simulations of spectra for heteronuclear and homonuclear for cases of ^{1}H-^{13}C and ^{1}H-^{1}H pairs, using the Eq. 2.142 and Eq. 2.143, respectively. Due to the dependence of the dipolar coupling constant on the gyromagnetic ratio of the interacting spins, the Pake pattern is broader in the homonuclear case. Furthermore, the characteristic discontinuities of the spectra appear at different multiples of the dipolar coupling constant.

In our DNP experiments, we usually do not observe resolved Pake patterns because common samples are frozen liquids where the distance between the interacting spins is not unique but is rather a distribution. This results in signals being featureless, with lineshape in between Gaussian and Lorentzian.

The mixing of the $|\alpha\beta\rangle$ and $|\beta\alpha\rangle$ states by the homonuclear dipolar Hamiltonian has another important consequence for our experiments. It enables the so-called "spin diffusion" process. This

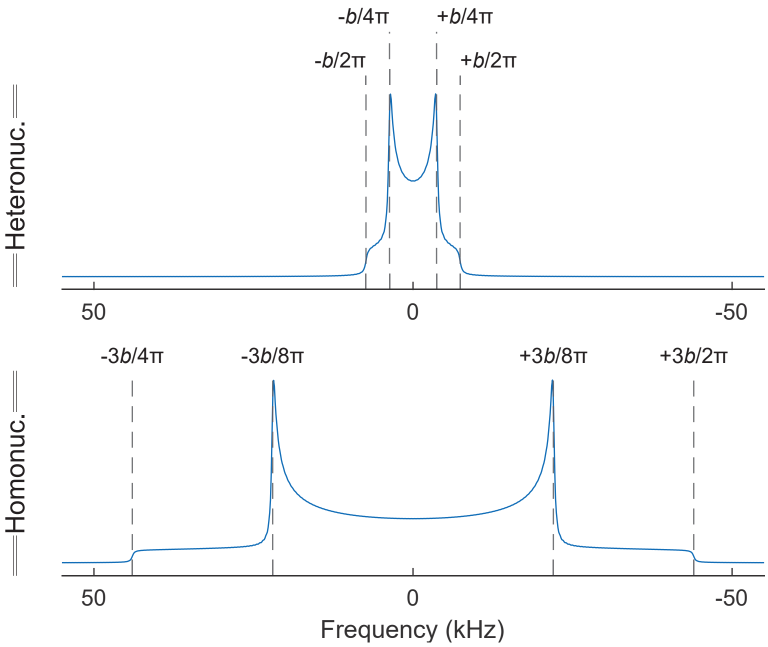

Figure 2.11: Numerical simulation of ^{1}H NMR spectra at high-field for heteronuclear and homonuclear dipolar coupled spins, for ^{1}H-^{13}C and ^{1}H-^{1}H pairs, respectively, separated by 1.6 Å. The initial polarization of the spins was assumed to be 0.001. A $\pi/2$ pulse was simulated on the ^{1}H spins, prior to propagation of the free evolution during 512 time steps of 4 μs. The simulated FID is the expectation value of $\hat{I}_{1+}$ and $\hat{I}_{1+} + \hat{I}_{2+}$ for the hetero and homonuclear cases, respectively. It was averaged over 1000 increments of the angle between the internuclear vector and the magnetic field from 0 to π. A 500 Hz line broadening and zero filling to 2048 points were applied prior to Fourier transform.

process is the spontaneous exchange of polarization between dipolar coupled nuclei with different polarization. For example, let us imagine that two ^{1}H spin with respective polarizations +1 and -1 interact with a dipolar coupling $D_0/2\pi = -20$ kHz. The ket corresponding to this state is the $|\alpha\beta\rangle$ state, which is not an eigenstate of the total Hamiltonian $\hat{H}_0 = \hat{H}_Z + \hat{H}_D^{homo}$. Therefore, the state evolves under $\hat{H}_0$. Fig. 2.12 shows a numerical simulation of the polarization of the two spins along time. The spins exchange their polarization at a rate corresponding to their dipolar coupling. The polarization of each spin was computed using Eq. 2.67.

Here, we have described the exchange of polarization for a pair of isolated spins which do not interact with their surroundings. A real sample like DNP juice consists of a large network of spins connected by dipolar interactions. Each pair of interacting spins exchange polarization in a similar way to that represented by Fig. 2.12, leading to more complicated dynamics. In addition to that, for each pair, the surrounding nuclear (and electronic) spins act as a source of relaxation which damps the oscillation between the states. This will not be treated in detail here but we will come back to this point in the next chapter.

2.3.4 The electron-nucleus dipolar interactions

We now turn to the electron-nucleus interaction, which is usually called the hyperfine interaction or the super-hyperfine interaction when the electron and the nuclear spins are not on the same molecule. When the two spins are on the same molecule, the hyperfine interaction may contain

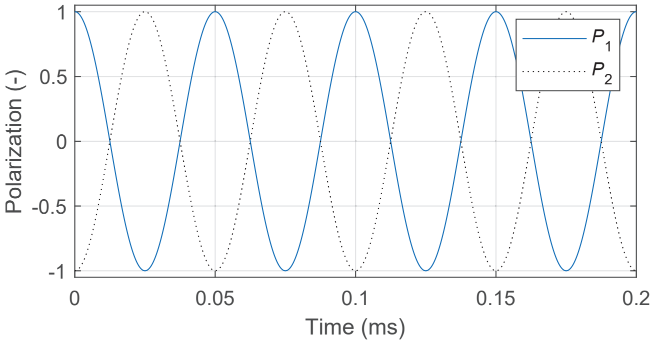

Figure 2.12: Numerical simulation of the polarization along the z-axis for a pair of dipolar coupled spins with a coupling of 20 kHz along time initially in the $|\alpha\beta\rangle$ state. Propagation over 1000 time increment of 0.2 ms.

a contribution of the isotropic hyperfine interaction (or pseudo-contact interaction), which is the electron-nucleus analog of the J-coupling between nuclear spins. We restrict our analysis to the super hyperfine case, which consists only of the anisotropic part or dipolar electron-nucleus interaction. This interaction could be written exactly as the nucleus-nucleus dipolar interaction, simply replacing the gyromagnetic ratio of one nuclear spin with that of the electron spin. However, it is written slightly differently by convention. Calling the electron spin S and the nuclear spin I, it reads [106]

$$\hat{H}_{HFI} = A_{zz}\hat{S}_z\hat{I}_z + A_{z+}\hat{S}_z\hat{I}_- + A_{z-}\hat{S}_z\hat{I}_+, \tag{2.144}$$

where the hyperfine constants are defined as

$$A_{zz} = A_0(1 - 3\cos^2\theta) \tag{2.145}$$

and

$$A_{z\pm} = -3A_0 \cos\theta \sin\theta e^{\pm i\phi}, \tag{2.146}$$

with

$$A_0 = \frac{\mu_0}{4\pi}\frac{\gamma_I\gamma_S}{r_{SI}^3}, \tag{2.147}$$

where r_{SI}, θ, ϕ, γ_I, and γ_S are the distance between the spins, the azimuthal and polar angles between the interspin vector and the magnetic field and the gyromagnetic ratios of the spins, respectively. This definition of the hyperfine interaction only contains terms that correspond to the $\hat{D}_0$ and $\hat{D}_{\pm 1}$ terms of the nucleus-nucleus dipolar Hamiltonian. However, only the terms corresponding to the electron spin being colinear with the magnetic field are taken into account, i.e., all terms containing $\hat{S}_z$. The component of the electron spin in the transverse plane precesses too fast to affect nuclear spin dynamics. The term $A_{zz}\hat{S}_z\hat{I}_z$ is often called the secular part of the dipolar hyperfine interaction because it commutes with the Zeeman Hamiltonian. The remaining terms are often called the pseudo-secular part because they do not commute with the Zeeman Hamiltonian but not "as much" as the other terms that we did not explicit.

The secular part shifts the nuclear levels just as the heteronuclear interaction did. However, in many cases, the electron spin state evolves very rapidly, on a time scale that causes the nuclear spin to experience only an averaged value of the hyperfine interaction. Let us call τ_c the time that the electron spends in a particular state ($|\alpha\rangle$ or $|\beta\rangle$) on average before changing to the other state.

This time constant is called the correlation time constant and represents how long the electron spin state remains correlated with its past state. The hyperfine interaction communicates the state of the electron to the nuclear spin and affects it differently whether the electron spin is in the $|\alpha\rangle$ or $|\beta\rangle$ state (i.e. it shifts its resonance up or down). If τ_c is short compared to the inverse of the hyperfine constant $1/A_{zz}$, the hyperfine interaction is "too slow" to communicate the spin state of the electron to the nucleus and so the nuclear spin experiences an averaged interaction, as we stated above. [107] On the contrary, if the electron spin remains in the same state on a timescale that is large compared to the inverse of the hyperfine constant $1/A_{zz}$, the nuclear spin experiences all the details of the electron spin state. Furthermore, if the electron correlation is long with respect to the NMR detection time scale (i.e., $\tau_c \gg T_2$, where T_2 is the transverse relaxation time constant of the nuclear spin), the state of the electron spin can be considered static all along the NMR detection.

These two limiting cases result in very distinct spectral features of the NMR spectrum. Fig. 2.13 shows the simulated spectra for a ^{1}H spin interacting with an electron spin *via* the secular dipolar hyperfine interaction, for the cases of a static and rapidly fluctuating electron spin state. The distance between the spins is assumed to be 1 nm and the vector connecting them is assumed to be perpendicular to the magnetic field, resulting in $A_{zz}/2\pi \approx 79$ kHz. The simulation was repeated varying the electron polarization from 0 to 1, without including powder averaging so that the spectra are more easily interpreted. To simulate the spectrum in the case of a rapidly fluctuating electron, a tweak was used: the two spin density matrix was computed for a fully polarized electron and the hyperfine interaction was weighted by the actual electron polarization. To avoid this tweak, several approaches are possible. The electron can be treated semi-classically, that is, considering the nuclear spin in a single-spin Hilbert space while the electron acts as a classical field on the nuclear spin. Other approaches belong to the field of paramagnetic NMR and are not discussed here.

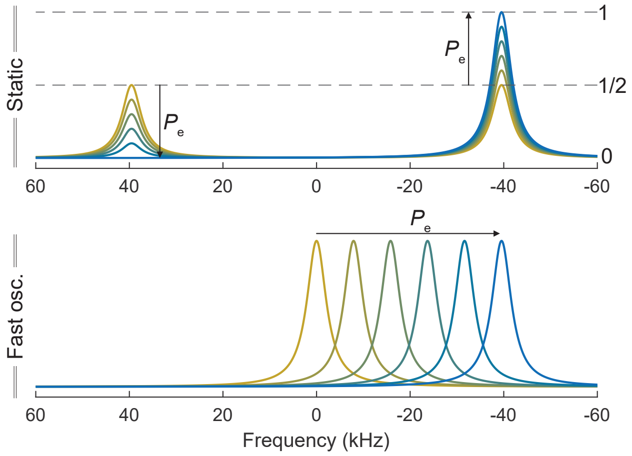

Figure 2.13: Numerical simulation of ^{1}H NMR spectra for a ^{1}H spin interacting with an electron spin with a hyperfine interaction of 79 kHz for the case of an electron with static spin state and with a rapidly fluctuating state. The simulated FID is the expectation value of $\hat{I}_{1+}$ with 512 time increments of 4 μs. A 5 kHz line broadening and zero filling to 2048 points were applied prior to Fourier transform.

In the static case, the NMR signal is split into two. One signal originates from nuclei interacting with an electron in the $|\alpha\rangle$ state while the other originates from nuclei interacting with an electron in the $|\beta\rangle$ state. When the electron polarization is significantly above 0, one state is more populated than the other causing an asymmetry in the doublet. When the electron is fully polarized, only one peak remains and the other completely disappears. In the case where the electron state fluctuates rapidly, the signal is not split but only shifted. This shift, which is proportional to the electron polarization is known as the paramagnetic shift. Conduction electrons in metals cause similar shifts. In this context, this shift is called a "Knight" shift after its discoverer. [107, 98]

As we mentioned in the case of the nucleus-nucleus dipolar interaction, the sample encountered in DNP are frozen solutions where the distance between the spins and the angle between the interspin vector and the magnetic field can take a distribution of values. As a consequence, the hyperfine interaction does not shift or split the signals in our experiment but rather broadens them.

The fluctuation of the electron spin state has another important consequence for nuclear spins: it induces relaxation. We will briefly show how the spin-lattice relaxation rate constant $1/T_1$ is calculated for a nuclear spin interacting through space with an electron spin, in the case where the position of the two spins can be considered fixed in space, using the random fluctuating field model, i.e., assuming that the electron spin state fluctuates without being influenced by the nuclear dynamics. Longitudinal relaxation occurs when the nuclear spin experiences a transverse magnetic field oscillating at its Larmor frequency ω_0. The behavior of the electron spin is stochastic and so it cannot be known exactly. Instead, we describe its state using an autocorrelation function, that we define as

$$g(\tau) = \sum_{m_z} p_{m_z} g_{m_z} = \sum_{m_z} p_{m_z} \left\langle P(0)P(\tau) \right\rangle_{m_z}, \tag{2.148}$$

where P is the polarization of the electron spin along the z-axis and p_{m_z} is the probability for the electron spin to have magnetic quantum number m_z at time $\tau = 0$. The quantity $g_{m_z} = \left\langle P(0)P(\tau) \right\rangle_{m_z}$ is the autocorrelation function for a given initial state of the electron spin (note that m_z determines $P(0)$). Eq. 2.148 is thus a weighted average over the different possible initial states of the electron spin. In the case of a spin 1/2, there are two possible states $|\alpha\rangle$ or $|\beta\rangle$ and their probabilities are $p_\alpha = (1 - \bar{P})/2$ and $p_\beta = (1 + \bar{P})/2$, respectively, where $\bar{P}$ is the average polarization of the electron spin. Along time, the electron spin state will change and go to an unknown state. We assume that stochastic processes (which we do not need to describe in detail for now) will make the autocorrelation function of the electron state tend towards some value P_∞ at rate $1/\tau_c$. It is common to assume that the autocorrelation function is monoexponential, leading to [108]

$$\begin{aligned} g_\alpha(\tau) &= \left\langle P(0)P(\tau) \right\rangle_\alpha = (-1)\left(P_\infty + (-1 - P_\infty)e^{-|\tau/\tau_c|}\right) \\ g_\beta(\tau) &= \left\langle P(0)P(\tau) \right\rangle_\beta = (+1)\left(P_\infty + (+1 - P_\infty)e^{-|\tau/\tau_c|}\right), \end{aligned} \tag{2.149}$$

where τ is the time elapsed since the electron was in the $|\alpha\rangle$ or $|\beta\rangle$ state, in the case of the autocorrelation function $g_\alpha(\tau)$ or $g_\beta(\tau)$, respectively. In both cases, $P(\tau)$ tends towards a value P_∞. Following the definition of Eq. 2.148, the weighed average of the autocorrelation function is

$$\begin{aligned} g(\tau) &= p_\alpha g_\alpha(\tau) + p_\beta g_\beta(\tau) \\ &= \frac{1 - \bar{P}}{2} g_\alpha(\tau) + \frac{1 + \bar{P}}{2} g_\beta(\tau) \\ &= P_\infty^2 + (1 - P_\infty \bar{P})e^{-|\tau/\tau_c|}. \end{aligned} \tag{2.150}$$

Note that to obtain Eq. 2.150, we have only assumed that the autocorrelation function was monoexponential. We have made no assumptions regarding the type of processes causing the state of the electron to fluctuate.

In the absence of μw irradiation, the average polarization $\bar{P}$ is the electron Boltzmann polarization P_{eq} (given by Eq. 1.3) and we assume that relaxation processes make the autocorrelation functions tend towards this same value P_{eq}. Therefore, we can write $\bar{P} = P_\infty = P_{eq}$ leading to

$$g(\tau) = P_{eq}^2 + (1 - P_{eq}^2)e^{-|\tau/\tau_c|}. \tag{2.151}$$

Because we are only concerned with the oscillating component of the electron spin state, we define an unbiased autocorrelation function

$$\begin{aligned} \tilde{g}(\tau) &= g(\tau) - P_{eq}^2 \\ &= (1 - P_{eq}^2)e^{-|\tau/\tau_c|}, \end{aligned} \tag{2.152}$$

that tends towards 0. The probability of finding the electron oscillating at frequency ω is then given by the Fourier transform of this autocorrelation function

$$\begin{aligned} J(\omega) &= \int_{-\infty}^{+\infty} e^{-i\omega} d\omega \tilde{g}(\tau) \\ &= (1 - P_{eq}^2)\frac{2\tau_c}{1 + (\tau_c\omega)^2}. \end{aligned} \tag{2.153}$$

Fig. 2.14 shows the polarization over time $P(\tau)$ used to calculate the autocorrelation function (see Eq. 2.149) and the corresponding spectral densities for an electron spin with a correlation time $\tau_c = 1$ μs, for various equilibrium electron polarizations P_{eq}. When $P_{eq} = 0$, both autocorrelation functions g_α and g_β are equally probable. When the polarization of the electron spin approaches 1, the probability to find the electron out of equilibrium vanishes, leading to a flat spectral density, i.e., the electron spin state no longer fluctuates. In most conditions of NMR experiments, the electron polarization can be considered to be low and so the $1 - P_{eq}^2$ term in the spectral density tends to 1. In dDNP conditions, however, the electron polarization cannot be considered close to 0. In the absence of μw irradiation, we have $P_{eq} = 0.9993$ at 1.2 K and 7.05 T. As we will see this has important consequences for relaxation.

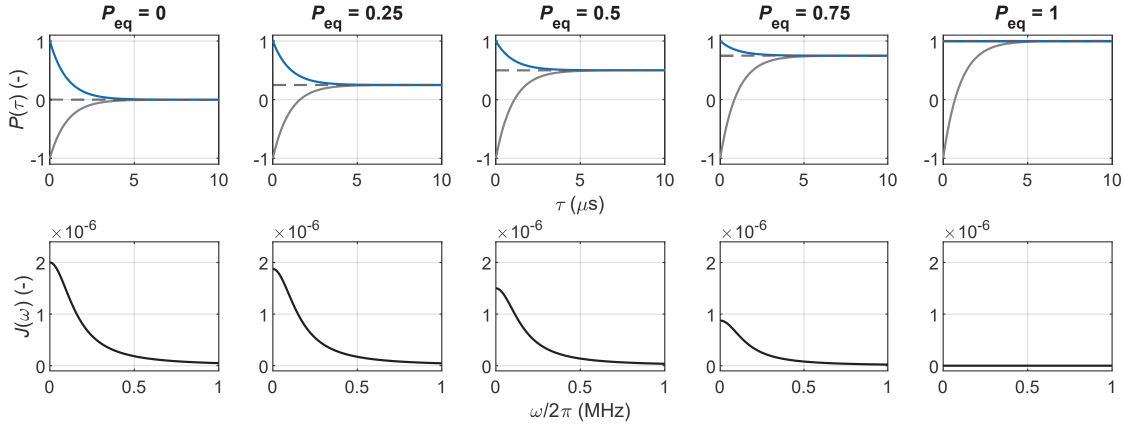

Figure 2.14: Polarization over time $P(\tau)$ used to calculate the autocorrelation function (see Eq. 2.149) and corresponding spectral density functions of the electron spin state for a correlation time constant of 1 μs for various equilibrium polarizations P_{eq}. The blue and gray curves represent the polarization of the electron spin state when in $|\beta\rangle$ or $|\alpha\rangle$ state at time $t = 0$, respectively. The horizontal dashed lines represent the equilibrium polarizations.

We accept without proof that the longitudinal relaxation rate constant according to the random fluctuating field model is given by [98]

$$1/T_1 = W_+ + W_-, \tag{2.154}$$

where W_+ and W_- are the probabilities per unit of time for the nuclear spins to jump between $|\alpha\rangle$ and $|\beta\rangle$ states, given by [98]

$$W_+ = W_- = \frac{1}{2}\left(\langle d_x\rangle^2 + \langle d_y\rangle^2\right) J(\omega_0), \tag{2.155}$$

where $\langle d_x\rangle$ and $\langle d_y\rangle$ are the root mean square of the perturbation along the $x-$ and $y-$axes, respectively, expressed in rad.s^{-1}, and so

$$1/T_1 = \left(\langle d_x\rangle^2 + \langle d_y\rangle^2\right) J(\omega_0). \tag{2.156}$$

In the case we are concerned with, the perturbation is the hyperfine interaction. Among the different terms, only the pseudo-secular part gives rise to a magnetic field component experienced by the nucleus along the $x-$ and $y-$axes. We rewrite the pseudo-secular Hamiltonian to make the perturbation along the $x-$ and $y-$axes explicit. Because we assume that the electron spin state is not affected by the dynamics of the nuclear spin (hypothesis of the random fluctuating field), the electron can be seen as a classical particule generating a magnetic field at the location of the nucleus and so the pseudo-secular Hamiltonian can be expressed in the Hilbert space of the nucleus only

$$\begin{aligned}\hat{H}_{pert} &= S_z(t)\left(A_{z+}\hat{I}_- + A_{z-}\hat{I}_+\right)\\ &= S_z(t)\left(\left(A_{z-} + A_{z+}\right)\hat{I}_x + \left(A_{z-} - A_{z+}\right)\hat{I}_y\right),\end{aligned} \tag{2.157}$$

where $S_z(t)$ is the angular momentum of the electron spin along the z-axis at time t which can take values $+1/2$ and $-1/2$. If we define the system coordinate so that the electron and the nucleus are in the O_{xz}-plan, we have that $A_{z-} + A_{z+} = 2A_{z+}$ while $A_{z-} - A_{z+} = 0$ and so we can conveniently write

$$\hat{H}_{pert} = 2S_z(t)A_{z+}\hat{I}_x. \tag{2.158}$$

The field experienced by the nucleus (expressed in rad.s^{-1}) takes values $+A_{z+}$ or $-A_{z+}$ and so the root mean square of the perturbation is A_{z+}. We have chosen that both the nucleus and the electron are in the O_{xz} plan; in the general case, the magnitude of the perturbation is $|A_{z+}| = |A_{z-}| =: |A_{z\pm}|$. Plugging this result into Eq. 2.156, we get that the paramagnetic relaxation rate is thus [3, 109, 110]

$$\begin{aligned}1/T_{1,para}^{dir} &= |A_{z\pm}|^2 J(\omega_0)\\ &= 2|A_{z\pm}|^2\left(1 - P_{eq}^2\right)\frac{\tau_c}{1 + (\tau_c\omega_0)^2}\\ &= 18\sin^2\theta\cos^2\theta\left(\frac{\mu_0}{4\pi}\right)^2\frac{\hbar^2\gamma_I^2\gamma_S^2}{r^6}(1 - P_{eq}^2)\frac{\tau_c}{1 + (\tau_c\omega_0)^2},\end{aligned} \tag{2.159}$$

where we plugged in the expression of Eq. 2.146 to go from the second to the third line. Note that the rate obtained in Eq. 2.159 is 4× larger than that found in the literature. [3, 109, 110] Despite my efforts, I was not able to find the origin of this discrepancy.

Eq. 2.159 gives the paramagnetic relaxation rate for a nuclear spin interacting with a fluctuating electron spin at fixed positions, taking into account the polarization of the electron spin. We derived it from the autocorrelation function of Eq. 2.150, which implies that it is valid regardless of the mechanism causing the electron spin state to fluctuate, as long as the autocorrelation function is monoexponential. Yet, understanding the mechanism at the origin of the electron spin state fluctuations is necessary to estimate the value of the correlation time constant τ_c (unless it can be determined experimentally). There are two main sources of decorrelation for the spin state of the electron, the interaction of the electron spin with the lattice and with other spins, which are associated with the spin-lattice time constant T_{1S} and electron flip-flop time constant τ_{ff}, respectively. Because relaxation rates are additive, we have [111]

$$\frac{1}{\tau_c} = \frac{1}{T_{1S}} + \frac{1}{\tau_{ff}}, \tag{2.160}$$

Note that the flip-flop time constant is closely related to the electron spin-spin relaxation time constant; they are equal at low electron polarization but differ when the electron polarization approches 1. [112, 113]

In our typical conditions between 1.2 and 4.2 K, at 7 T, and with high radical concentrations between 10 and 50 mM, the time scales of the two processes summed in Eq. 2.160 are separated by many orders of magnitude: the electron spin-lattice relaxation time constant T_{1S} is in the range 10–100 ms [49] (see Chapter 4), while the electron flip-flop time constnat τ_{ff} is in the range 1–10 μs. [113]) Hence, the contribution of electron spin-lattice relaxation to the decorrelation of the electron spin state can safely be neglected. The flip-flop rate, i.e., the rate at which two spins exchange polarization due to their dipolar interaction, is of the order of their dipolar coupling constant (Fig. 2.12 gives a visual example of flip-flops in the case of nuclear spins). One can therefore write

$$\frac{1}{\tau_c} \approx \frac{1}{\tau_{ff}} \approx \frac{D_{SS}}{2\pi}, \tag{2.161}$$

where D_{SS} is the dipolar coupling constant between the electron spin for which τ_c is calculated and its nearest neighboring electron spin.

As pointed out by Abragam and Goldman, [3] the simple picture we are giving here is flawed. Indeed, in the limit $1/\tau_c \approx 1/\tau_{ff}$, Eq. 2.159 predicts a rate that if faster than that measured experimentally. The reason for this discrepancy is that electron-electron interactions, if they are indeed a source of decorrelation for the electron spin state, do not exchange polarization with the lattice (as spin-lattice relaxation does). Eq. 2.159 therefore gives the rate of the exchange of energy between the nuclear Zeeman reservoir and the electron-electron dipolar reservoir; the acquired energy of the latter reservoir must then be transmitted to the lattice in a second step. If the nuclear Zeeman energy is small (which is often not the case in dDNP conditions), the first step may be limiting and so Eq. 2.159 is correct. On the contrary, if the second step is limiting, the nuclear spin-lattice relaxation rate is not given by Eq. 2.159. A more precise description of nuclear relaxation by coupled electron spins requires using thermal mixing theory, [3] which will not be presented here.

With a radical concentration of 50 mM, the distance between electron spin neighbors is the nm range and so the dipolar interactions between them is in the MHz range, leading to correlation time on the μs timescale, which implies that $(\tau_c\omega_0)^2 \gg 1$. This simplifies the rate of Eq. 2.159 to

$$\begin{aligned} 1/T_{1,para}^{dir} &\approx 18 \sin^2\theta \cos^2\theta \left(\frac{\mu_0}{4\pi}\right)^2 \frac{\hbar^2\gamma_I^2\gamma_S^2}{r^6} \frac{1-P_{eq}^2}{\tau_c\omega_0^2} \\ &= 18 \sin^2\theta \cos^2\theta \left(\frac{\mu_0}{4\pi}\right)^2 \frac{\hbar^2\gamma_S^2}{r^6} \frac{1-P_{eq}^2}{\tau_c B_0^2}. \end{aligned} \tag{2.162}$$

There are several points to be noted in Eq. 2.162:

- First, the relaxation rate diminishes quadratically with the magnetic field;

- It depends on the inverse sixth power of the distance between the nuclear and the electron spins, meaning that it fades off very rapidly. As we will see in the next chapter, paramagnetic relaxation can still affect remote nuclei indirectly *via* spin diffusion. This gives rise to an observed bulk relaxation rate which differs from the individual direct paramagnetic relaxation rate of the spins;

- The rate is proportional to $1 - P_{eq}^2$ and so it vanishes if the electron polarization goes to unity. This holds for other relaxation rates such as the nuclear spin-spin relaxation rate in the laboratory and in the rotating frame $1/T_{2,para}$ and $1/T_{1\rho}$, respectively;

- It is inversely proportional to the correlation time. Increasing the electron concentration decreases the correlation time and, in turn, it contributes to decreasing the nuclear relaxation rate. However, increasing the electron concentration also decreases the distance between nuclei and the average closest electron, which increases the nuclear relaxation to the sixth power. Therefore, increasing the electron concentration strongly increases paramagnetic relaxation;

- Finally, the rate we have derived is counter-intuitively independent of the nuclear gyromagnetic ratio. Indeed, increasing the gyromagnetic ratio increases the Larmor frequency. As the frequency increases, the spectral density of the electron oscillation at the nuclear Larmor frequency decreases with γ_I^2 (in the limit $(\tau_c \omega_0)^2 \gg 1$), which cancels out with the same term in the numerator. However, the observed bulk relaxation rate may still be limited by the ability of the nuclear spins to share their polarization (spin diffusion), which would make the observed relaxation rate dependent on the gyromagnetic ratio even if the direct paramagnetic relaxation rate is independent of the nuclear gyromagnetic ratio.

The hyperfine interactions make the nuclear spins relax towards Boltzmann equilibrium but of course, it also allows them to be polarized by DNP. This feature is central to this work and will be treated in the next chapter.

Chapter 3

Solid-state DNP

This chapter gives an overview of the methods used in solid-state DNP in dDNP conditions. We start by presenting the hardware for low-temperature DNP and the methods to quantify accurately the polarization of high- and low-γ nuclei. The theory of DNP mechanisms is reviewed focusing mostly on the aspects which are relevant to our experimental conditions. We then show μw spectra (i.e., plots of polarization under DNP vs μw irradiation frequency) for two types of samples; first, for common samples of DNP juice (H_2O:D_2O:glycerol-d_8 1:3:6 v/v/v) doped with TEMPOL radical and second for conductive polymers of polyaniline (PANI). The results are analyzed in light of the theory presented in the dedicated section.

3.1 Instrumentation and methods

This section presents the instrumentation for low-temperature that was used throughout this work. First, the magnet and the cryostat are described and the processes to reach low temperatures are presented. Then, the instrumentation for rf pulses and continuous wave (CW) μw irradiation is described, and the performance of the system is discussed. Finally, we show how to quantify the polarization of hyperpolarized signals in the solid-state in the case of high and low-gamma nuclei (^{1}H and ^{13}C, respectively).

3.1.1 Low temperature and high magnetic field: the cryostat and the magnet

All experiments presented in this work were performed on the AlphaPolarizer, a Bruker dDNP polarizer functional model. Its design is based on an ultra-shielded wide-bore Bruker Ascend magnet generating a magnetic field of 7.05 T, corresponding to ^{1}H and ^{13}C Larmor frequencies of 300 and 75 MHz, respectively. Like common NMR magnets, this magnet uses a superconducting coil immersed in liquid helium at a temperature of 4.2 K. The insulation of the helium reservoir is realized by high vacuum and an extra reservoir of liquid nitrogen at 77 K. Such a system requires that the liquid nitrogen and the liquid helium are refilled every week and every two to three months, respectively.

The bore of the magnet accommodates a cryostat, which we often referred to as the variable temperature insert (VTI, see Fig. 3.1A). This piece of equipment is the core of the DNP apparatus. It allows the operator to control the entry of liquid helium from an external transport Dewar and to pump on the liquid helium bath inside the VTI so as to reach temperatures down to ≈ 1.15 K. It is equipped with liquid helium sensors to monitor the height of the helium bath and temperatures, and pressure sensors. It is connected to several pumps to control the entry of liquid helium and decrease its pressure as well as to ensure the insulation of the cryostat (Pumps 1, 2, and 3 on Fig. 3.1 respectively). It contains electronically-controlled valves to a helium gas line to set a positive overpressure in the interior of the system with respect to the exterior when the system needs to be opened (e.g., to insert a sample or to connect the system to the liquid helium transport Dewar) and hence prevent any contamination of the VTI by air or moisture. Finally, the cryostat accommodates a DNP probe, which is connected to rf and μw channels for NMR and DNP operations (which will be detailed in Sec. 3.1.2).

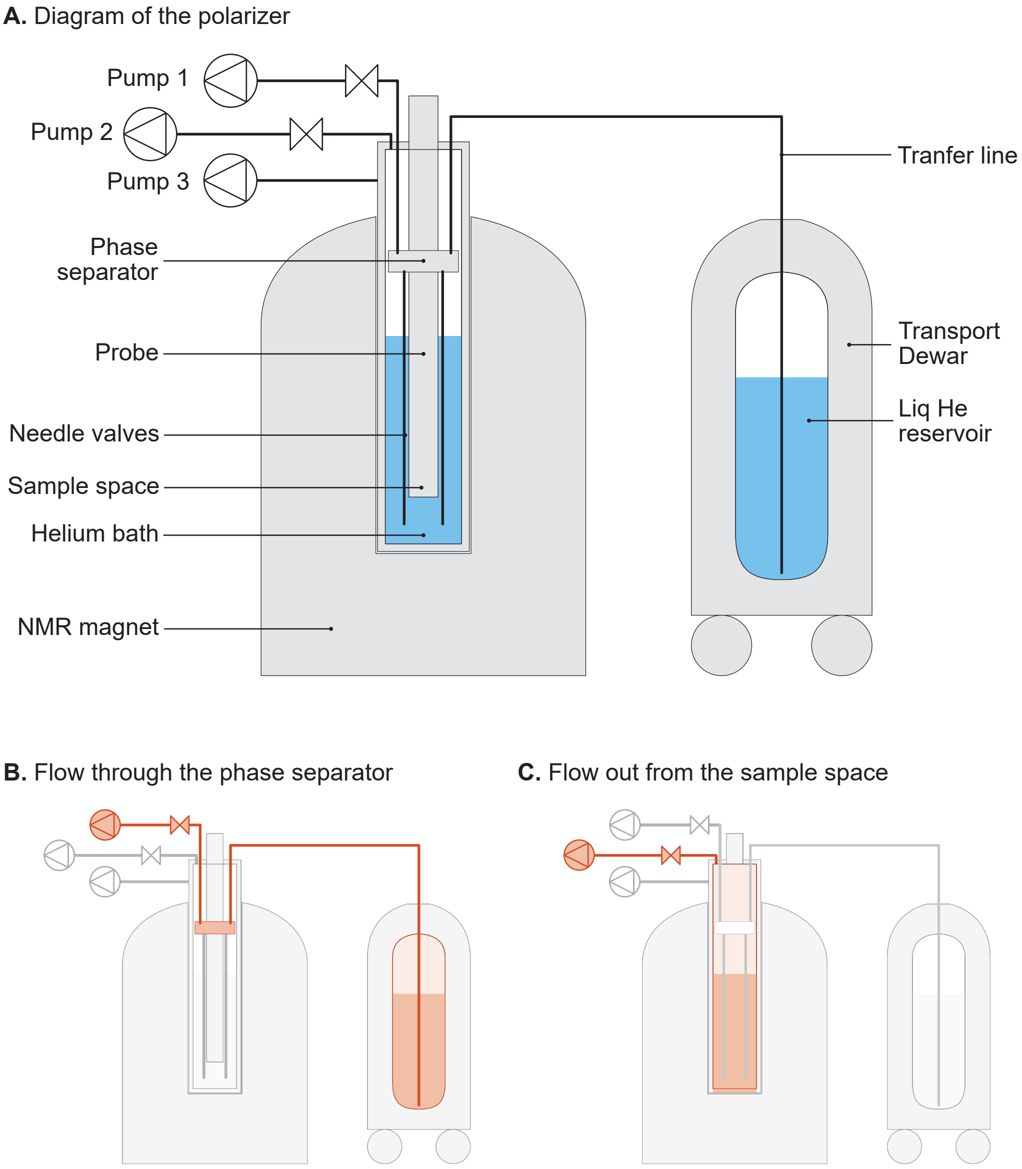

Figure 3.1: **A**. Diagram of the polarizer detailing the components of the cryostat. **B-C**. Helium flow path to bring helium inside the cryostat through the phase separator and to pump on the sample space, respectively.

In typical operations, a transport Dewar of 100 L of liquid helium is connected to the system *via* a vacuum-insulated transfer line. The helium which flows through the transfer line enters the system in the phase separator, a donut-shaped piece of porous copper near the top of the cryostat (the donut shape is meant to allow the probe to go through). The phase separator is also connected to a membrane pump *via* a flow controller and to the sample space (i.e., the interior of the cryostat) *via* a pair of electronically-controlled needle valves. When the needle valves are closed, the phase separator is not connected to the sample space and the helium which flows from the Dewar to the membrane pump cools down the phase separator, and the radiation shields of the cryostat which are thermally connected to the phase separator (Pump 1 in Fig. 3.1A). This flow path is shown in Fig. 3.1B. When the needle valves are opened, the phase separator is connected to the sample space and so liquid helium can flow from the Dewar to the sample space *via* the phase separator. To ensure this flow, a powerful dry pump controlled with a butterfly valve maintains the pressure of the sample space at a chosen value below atmospheric pressure (Pump 2 in Fig. 3.1A).

To cool down the cryostat from room temperature to liquid helium temperature, our typical procedure consists of maintaining the pressure of the cryostat at 700 mbar (thanks to the Roots pump and the butterfly valve) with the needle valves opened while pumping on the phase separator with the membrane pump at maximal capacity (resulting in a gas flow through the membrane pump between 3 and 10 liters of room temperature helium gas per minute). As cold helium goes through the phase separator and the needle valves, the system slowly cools down within ≈ 6 hours. This procedure consumes ≈ 10 L of liquid helium. Once the phase separator has reached ≈ 4.2 K, liquid helium (instead of cold helium gas) starts flowing through the needle valves and accumulating in the sample space. The fraction of liquid that has gone to the gas phase during the transfer from the Dewar to the phase separator is evacuated by the membrane pump while the fraction which evaporates within the sample space is evacuated by the Roots pump. Once the liquid helium level has raised to a designated liquid helium sensor, the system automatically closes the needle valves and keeps on maintaining the pressure of the sample space at 700 mbar. Refilling the whole cryostat typically takes a few minutes once the system is cold. If the cryostat is filled with liquid helium until the top (just below the phase separator), the system can be operated without liquid helium refills for 6 to 8 hours, depending on the operating pressure. The connection between the helium bath and the Roots pump is shown in Fig. 3.1C. The spaces depicted by the diagrams of Fig. 3.1B and C are connected solely by the needle valves.

The temperature of the liquid helium bath depends on the equilibrium pressure of the sample space imposed by the Roots pump and the butterfly valve. At equilibrium, the temperature of the bath is given by the boiling point of liquid helium. At atmospheric pressure, the boiling point of helium is ≈ 4.2 K. At 700 mbar, the boiling point is 3.85 K. The lowest pressure that the Roots pump is able to reach in our system is 0.58 mbar, corresponding to a helium boiling point of 1.15 K. To reach this pressure and temperature, the system is first filled with liquid helium at 700 mbar and 3.85 K and only then it is pumped down to < 1 mbar. As pressure decreases, liquid helium evaporates and the bath temperature decreases from 3.85 K to < 1.2 K. During this process, helium goes through the so-called "lambda point", at ≈ 2.17 K. The lambda point is the temperature below which liquid helium becomes superfluidic. As the liquid helium approaches the lambda point, the heat capacity of helium increases, which implies that the decrease in temperature costs more helium than at higher temperatures. Crossing the lambda point is thus a costly process. Once the temperature is below the lambda point and as temperature decreases further, the heat capacity of helium tends towards 0 and so evaporating more helium to further decrease the temperature becomes less and less efficient. Other DNP setups with better insulations are able to decrease the temperature to around 1.0 K but not much lower, because of the low heat capacity of liquid helium at this temperature.

The cryostat of our dDNP setup consumes ≈ 100 L for a week of operation, including the cool-down from room temperature on the first day of the week. When I started my Ph.D., the price of liquid helium was around 8 euros/L and so a week of operation cost 800 euros. The price of helium has been steadily increasing since then. It has now reached $\approx$ 30 euros/L and continues to increase. With a current operating cost of 3000 euros per week, dDNP experiments become more and more expensive using this type of cryostat, referred to as a “wet cryostat”. [114, 115] However, alternatives exist. In particular, some systems use helium recirculation and the same helium bath for the superconducting coil and for the sample space. [44, 45] If the precise temperature control is more difficult on such systems than on wet cryostat, they have the great advantage of much lower running costs.

3.1.2 Electromagnetic fields: rf pulses and μw irradiation

High-field NMR systems use pickup coils to manipulate the spins and record the signals they produce. The current design of our polarizer allows us to pulse on and detect two different nuclei at a time using orthogonal Helmholtz coil pairs, which are inductively coupled to the circuitry of the NMR console through external tuning and matching boxes. The coils produce an rf field orthogonal to the static magnetic field B_0. The magnetic component of the rf field is what interacts with the spins. The maximum of this magnetic component, called B_1, is used to characterize the performance of the coil. The field B_1 field is related to the nutation frequency of the pulses produced by the coil by

$$\omega_1 = \gamma B_1, \tag{3.1}$$

where γ is the gyromagnetic ratio of the nuclear spins for which the coil is tuned. The nutation angle of a pulse with length τ and nutation frequency ω_1 is

$$\theta = \omega_1 \tau. \tag{3.2}$$

If the coil has a nutation frequency of $\omega/2\pi = 25$ kHz, the pulse length to perform a $\pi/2$ angle is 10 μs. Our coils typically have nutation frequencies of 30-60 kHz for ^{1}H spins and 20-30 kHz for ^{13}C spins. One of the key requirements of our coils is that they are able to sustain pulses of such nutation frequencies during ms in order to perform efficient spin-lock pulses during cross-polarization (CP i.e., polarization transfers from ^{1}H to ^{13}C spins in the solid-state). Performing such pulses in liquid helium is challenging because of arcing due to the low striking voltage in liquid helium. Repeated arcing may damage the capacitors of the probe and hence hamper the performance of the coil. The design of our coils has proved to be efficient to perform CP. [47, 49, 116, 117, 118, 119, 120, 121] However, the coils tend to break down and need frequent repair. [120, 121]

As will be detailed in Sec. 3.1.3 and 3.1.4, the quantification of nuclear polarization under DNP requires comparing the NMR signal obtained under DNP with that at thermal equilibrium. Depending on the probe design, support material might be required to hold the coils. The presence of this material within the sensitive area of the coil may result in a strong background signal adding up to the signal of interest. In addition to that, the sample cup may bring further background signal. At the beginning of my Ph.D., we used to build coils with a KelF tube as support. The intensity of the background signal was comparable to that of the signal of interest at thermal equilibrium at 3.8 K (for 100 μl of DNP juice with 3 M of a ^{13}C-labeled analyte) both for ^{1}H and ^{13}C NMR detection. As consequence, in order to record a thermal equilibrium signal, one had to record the background signal (i.e., the signal in the absence of sample) and subtract it from the signal recorded with the sample. During the course of my Ph.D., we introduced a design of background free coil, which we presented in this Ref [120] (see Fig. 3.2). This design decreased the background signal originating from the coil to 0 both for ^{1}H and ^{13}C NMR detection. However, the sample cup still produces a ^{13}C background corresponding to $\approx$ 8% of a sample of 100 μl of DNP juice with 3 M of a ^{13}C-labeled analyte. In the case of ^{1}H detection, the overall background of the coil and sample cup was found to be negligible, a very convenient feature making experiments more reliable and faster.

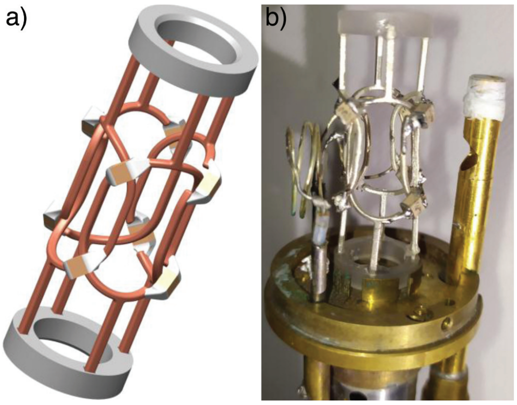

Figure 3.2: Design of the ^{1}H-^{13}C background free coil, reproduced with permission from Ref. [120]. **A**. 3D model of the coils. **B**. Photograph of the probe bottom (upside down), including the coils, the inductive loops, and the μw guide.

The DNP probe contains rf channels to manipulate the nuclear spins as well as a waveguide to channel μw until the sample and excite EPR transitions. Our polarizer uses a solid-state μw source consisting of a synthesizer and an amplifier-multiplier chain (AMC), both by Virginia Diodes Inc. (VDI). The synthesizer produces μw at a computed-controlled frequency around 12.3 GHz and at a fixed power, which we measured to be $\approx$ 60 mW. The synthesizer output is attenuated to $\approx$ 6 mW before the μw are fed into the AMC, which multiplies the μw frequency by precisely 16 to a value around 198 GHz and amplifies the power to $\approx$ 118 mW. The connection between the synthesizer and the AMC is made by an rf cable; once the frequency has been multiplied by the AMC, the wavelength becomes too short for efficient transmission through an rf cable. Therefore, a waveguide consisting of stainless steel is used instead (see Fig. 3.3).

Our setup enables to control five parameters related to μw:

- The irradiation central frequency, typically between 197.9 and 198.7 GHz after multiplication stages
- The bandwidth of frequency modulation around the central frequency, typically on the order of 100 to 200 MHz after multiplication stages
- The frequency of the modulation, typically 500 Hz
- The gating (i.e., the on/off state) of the irradiation
- The output power of the AMC from 0 to 118 to 130 mW after multiplication and amplification (the maximum available power depends on the central frequency).

The polarizer is controlled by the computer through a JAVA interface called the AlphaController. The three parameters related to μw frequency are controlled by the AlphaController and communicated to the synthesizer by the JAC, a Linux-based processor in the DNP cabinet. The AMC output power is also controlled by the AlphaController; it is communicated by the JAC to the AMC *via* a MOXA digital-to-analog converter as a voltage from 0 to 5 V (corresponding to maximum and 0 power, respectively). Finally, the gating is controlled by the pulse sequences

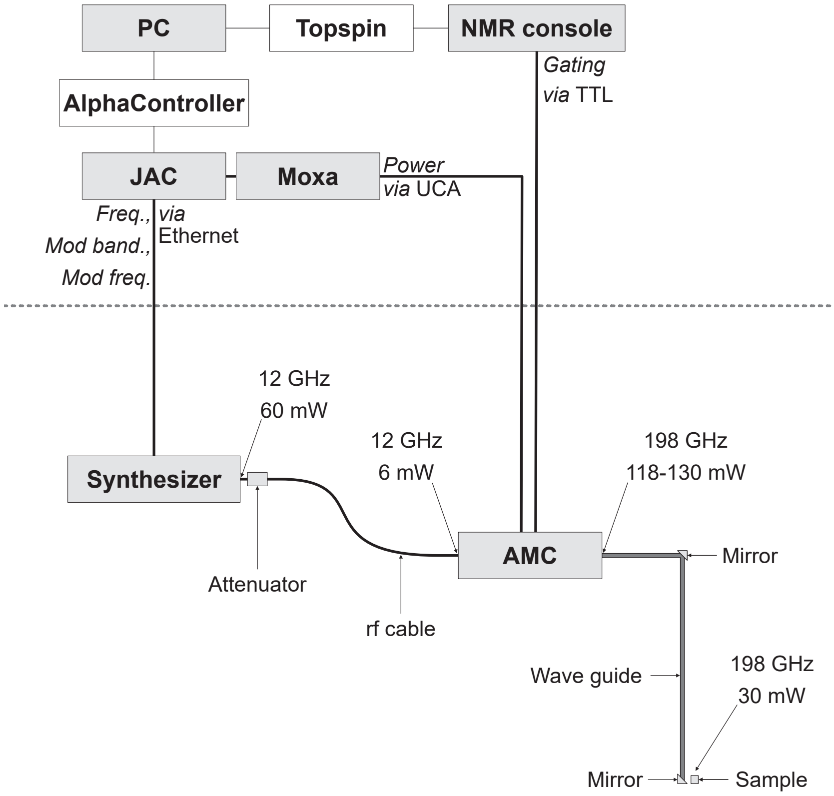

Figure 3.3: Setup of the μw source from the synthesizer to the sample space. The values of the μw power and frequency are given for several stages of transmission. Powers are approximate values, which were measured using different means depending on the stage. The top part of the diagram shows the communication between the control computer and the hardware components *via* two different softwares, Topspin and AlphaController.

in Bruker's software Topspin as a TTL voltage. The fact that the gating is controlled through the pulse sequences allows one to synchronize μw with NMR pulses, a feature that was shown to increase the performance of CP. [49]

In its original design, the setup was not equipped with the control of the μw power. We modified the AlphareController software so that it could control the power by applying a voltage to the dedicated port of the AMC (UCA line in Fig. 3.3). We further added a "task scheduler" to the AlphaController. This feature allows the user to define a list of time-resolved tasks (with $\approx$ 1 s resolution), such as refilling liquid helium into the cryostat and setting the temperature and the μw parameters. This feature was used in a number of experiments presented in this work, in particular to program fine μw spectra overnight (see in Sec. 3.3.2).

The μw power can be measured at several stages of the transmission using different methods. At stages where the frequency is of 12 GHz, the power may be measured using a simple hand-held powermeter (in this case a commercial Agilent device). Once the frequency is in the hundreds of GHz range, a more sophisticated device is used (in this case, a bolometer VDI Erickson PM5B). At the final stage (i.e., in the sample space), it is impossible to connect a powermeter and so one can only measure the deposited μw power indirectly by monitoring the change in pressure upon switching on irradiation. The change in pressure is then compared with that under the effect of a resistive heater. Fig. 3.4 shows an example with four replicates, where the change in pressure in the sample space was recorded upon switching on irradiation.

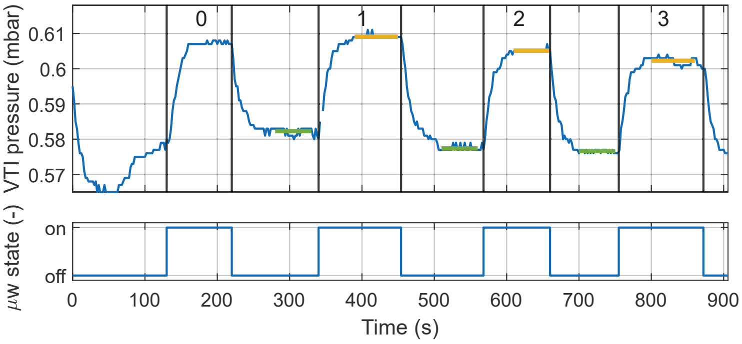

Figure 3.4: Example of measurement of the μw power deposited in the VTI realized by monitoring the change of pressure upon switching on μw irradiation in the helium bath at ≈ 1.16 K. The green and yellow horizontal lines represent the base pressure and the pressure under μw irradiation, respectively, for the three consecutive measurements. In this case, the pressure difference was found to be 0.027 ± 0.001 mbar, corresponding to a deposited power of 14.2 ± 0.5 mW.

One of the reasons why I learned to measure the μw power deposited onto the sample is that it makes it possible to measure the transmission of the μw while operating the system. This happened to be useful on several occasions where we believed that the AMC was damaged. Indeed, the AMC is a very sensitive device and it broke down two times during the four years that I spent in the team. Such events represent an important limiting factor since the repair of the AMC can take up to several months, during which no DNP experiments can be performed.

3.1.3 Polarization quantification for high-γ nuclei

Fig. 3.5 shows a typical example of ^{1}H polarization building up under DNP, together with the diagram of the pulse sequence used to acquire it, i.e., a saturation recovery-type experiment. This section shows how the NMR signal of hyperpolarized species is measured in the solid-state and how it is used to compute the spin polarization under DNP to obtain results as in Fig. 3.5, in the case of high-γ nuclei. We first show how the build-up of a hyperpolarized signal is monitored using small angle pulses. Then, we show how thermal equilibrium reference signals are recorded and how background signals are removed. Finally, we briefly explain how radiation damping (RD) might bias polarization quantification.

Common high-field spectrometers yield signals which are not expressed in meaningful units. In order to convert the signal intensity of a DNP-enhanced signal into a polarization value, one has to record a signal in conditions where the polarization is known, i.e., at thermal equilibrium, and compare the signal intensities. As we have seen in the previous chapter, NMR signals are proportional to nuclear spin polarization (see Eq. 2.96). Therefore, the polarization under DNP can be obtained as

$$P_{DNP} = \frac{I_{DNP}}{I_{TH}} P_{Th} \tag{3.3}$$

where I_{DNP}, I_{TH} and P_{Th} are the signal integrals under DNP and at thermal equilibrium and the thermal equilibrium polarization given by Boltzmann's equation (see Eq. 1.3), respectively. We now describe how to measure I_{DNP} and then I_{TH}.

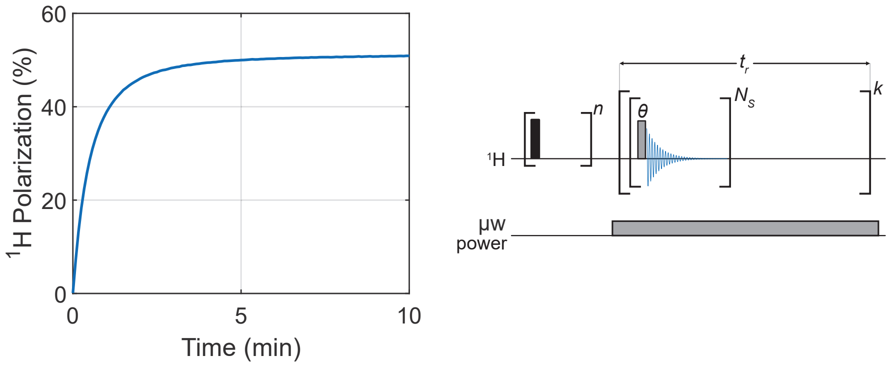

Figure 3.5: Example of an experimental DNP build-up curve of 100 μL of DNP juice doped with 50 mM TEMPOL, recorded at 1.6 K in our polarizer using small angle pulses with $\theta = 0.1°$ for detection where each point is the sum of $N_S = 64$ transients with a repetition time $t_r = 5$ s, after a saturation with typically $n = 30$ $\pi/2$ pulses.

In our operating conditions, ^{1}H DNP is so sensitive but at the same time so slow that we record the experiment in a slightly unusual way, compared to common NMR techniques. Instead of repeating a saturation-recovery experiment varying the delay between saturating the spins and detecting their signal with a $\pi/2$ pulse, we perform a single experiment where we monitor the signal building up along time using small angle pulses. We mentioned the concept of pulse angle at the beginning of this chapter (see Eq. 3.2). Small angle pulses are pulses where the pulse length τ and the nutation frequency ω_1 are chosen so that the pulse converts only a fraction of the longitudinal magnetization into transverse magnetization. In other words, it borrows a fraction of the magnetization to get an "image" of the longitudinal magnetization, while leaving most of it unaffected. If the state of the spin system can be represented as $\hat{\rho}(t) = P(t)\hat{I}_z$, where $P(t)$ is the polarization of the spins at time t (see Eq. 2.93 and 2.101), a pulse with angle θ converts the system into

$$\begin{aligned} \hat{\rho}_1 &= P(t) \exp\{+\theta \hat{I}_y\} \hat{I}_z \exp\{-\theta \hat{I}_y\} \\ &= P(t) \left(\cos\theta \hat{I}_z + \sin\theta \hat{I}_x \right), \end{aligned} \tag{3.4}$$

where we used the cyclic commutation relations defined in the previous chapter (see Eq. 2.80) to go to the second line. The same commutation relations show that the term $\hat{I}_z$ will remain stationary under the Zeeman Hamiltonian while $\hat{I}_x$ will start evolving giving rise to an observable signal proportional to $P(t)\sin\theta$.

In practice, we choose the pulse angle so that the signal does not saturate the receiver when the system is at maximum polarization. In the case of ^{1}H detection, we usually choose the pulse angle as small as $\theta = 0.1°$, and, for each time point t, we sum the signal of $N_S = 64$ transients. The summed signal is then proportional to $N_S P(t) \sin\theta$, while the polarization remaining along the z-axis after the detection block is $P(t)\cos^{N_S}\theta \approx 0.99990$, meaning that the perturbation caused by the measurement is completely negligible. Note that assuming that the sum of the signal is proportional to the number of pulses N_S is only valid if $\cos^{N_S}\theta \approx 1$, which is the case here. The general case is important for the detection of low-γ nuclei and will be treated below.

The thermal equilibrium spectrum (needed to get the reference integral I_{Th}) is usually recorded keeping as many parameters constant as possible, with respect to the hyperpolarized experiment. However, The SNR of the thermal equilibrium signal might be improved by increasing the receiver gain R_G. In some cases, one might as well modify the number of scans N_S. To account for this difference in acquisition parameters, one needs to normalize the integrals before computing the polarization using Eq. 3.3. The normalization may be written as

$$I^n = \frac{I}{N_S R_G}, \tag{3.5}$$

where I is the non-normalized integral, both for the thermal equilibrium and the hyperpolarized signals. We usually do not modify the pulse angle from one experiment to another to avoid introducing a bias associated with the uncertainty of the pulse angle. On the contrary, we often do not record the thermal equilibrium at the same temperature as that where we perform DNP experiments. Indeed, we usually perform DNP experiments at the lowest available temperature to maximize DNP performance, i.e., below 2 K. A this temperature, electron polarization is close to 1 and so because of Eq. 2.159, paramagnetic relaxation becomes prohibitively slow. In such conditions, recording a thermal equilibrium signal would take several hours, even for ^{1}H spins. Therefore, we rather record the thermal equilibrium signal at 3.8 K, where the ^{1}H bulk T_1 is on the order of 1 min. Assuming that the quality factor (Q-factor) of the probe is not affected by temperature, Eq. 3.3 remains valid even if I_{DNP} and I_{Th} are recorded at different temperatures. The Boltzmann polarization of ^{1}H spins at 3.8 K and 7.05 T is 0.19%.

Depending on the probe construction, a background signal may be present in addition to that originating from the sample. While this signal is negligible for the hyperpolarized case, it might be significant for the thermal equilibrium case. Fig. 3.6 shows the thermal equilibrium signal of 100 μl of DNP juice acquired at 3.8 K using $\theta = 0.1°$, $N_S = 64$ and $R_G = 16$, in the case of a standard coil and a background free coil (A and B, respectively). [120] In the case of the standard coil, the signal originating from the coil support (i.e., the background) is nearly as intense as that of the sample itself (which is obtained by taking the difference between the total thermal equilibrium signal and the background signal). In the case of the background free coil, the ^{1}H background signal does not come out of the noise using the same acquisition parameters as for the thermal equilibrium signal (not shown). [120] This convenient feature of the background free coil allows one to record the ^{1}H polarization more rapidly and removes a potential source of error.

To compute the thermal equilibrium reference integral, one can average the signal integrals acquired once the signal has plateaued. The standard deviation of the values over which the signal is averaged can be used as the error on the reference integral. If we average the integral of the thermal signals over the last 50 detection blocks (corresponding to 250 s of detection), we get a relative error of 0.4% for both Fig. 3.5A and 3.5B (despite the fact that the two measurements were performed with different probes). The polarization under DNP shown in Fig. 3.5 was measured during the same experimental run as the thermal equilibrium of Fig. 3.6B. Because the uncertainty on the integral of the hyperpolarized signal is negligible compared to that of the thermal equilibrium signal, the uncertainty on the polarization value can be considered to be dominated by that on the thermal equilibrium. Under this assumption, the maximum polarization on Fig. 3.5 is $51.5\% \pm 0.2\%$. This value has a rather low error. However, there is a strong systematic error caused by radiation damping (RD). In reality, we expect polarization on the order of $70 - 80\%$ for this sample in these conditions. [121]

RD is the result of the coupling of the nuclear spins with the detection coil. At low magnetization, this coupling is negligible but at high magnetization the coupling act as a pulse. [122, 123] This pseudo-pulse is in antiphase with respect to the transverse magnetization and its intensity is proportional to the transverse magnetization. The consequences of RD on NMR experiments are complex and numerous. [123] In the context of our solid-state DNP experiments with small angle detection, the consequence of RD is only to effectively shorten or lengthen the nuclear T_2^*, under positive and negative DNP, respectively. Fig. 3.7A shows a visual representation of the effect of RD on an FID. The FID in the absence of RD is assumed to have a Gaussian decay

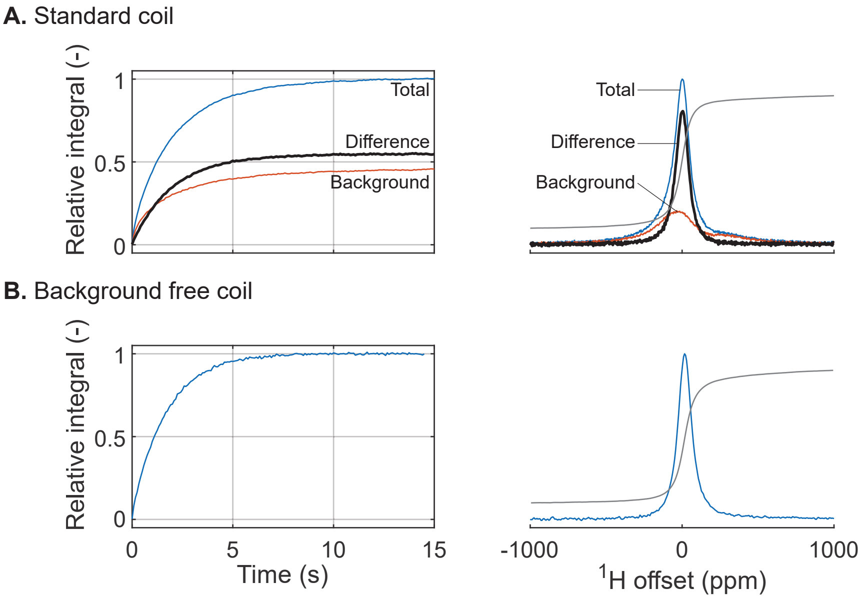

Figure 3.6: **A-B**. Signal processing for the thermal equilibrium of 100 μl of DNP juice at 3.8 K in the case of standard and background-free coils, respectively. The gray lines on the spectra represent the signal integral.

envelope $f(t)$. For positive DNP, the effect of RD is simulated by $f(t)\exp(-t/\tau_{RD})$, where τ_{RD} is a constant related to the intensity of RD, while for negative DNP, the effect of RD is simulated by $f(t)\exp(+t/\tau_{RD})$. Although this is a rough simulation, it is sufficient for our purpose of giving a visual representation of RD.

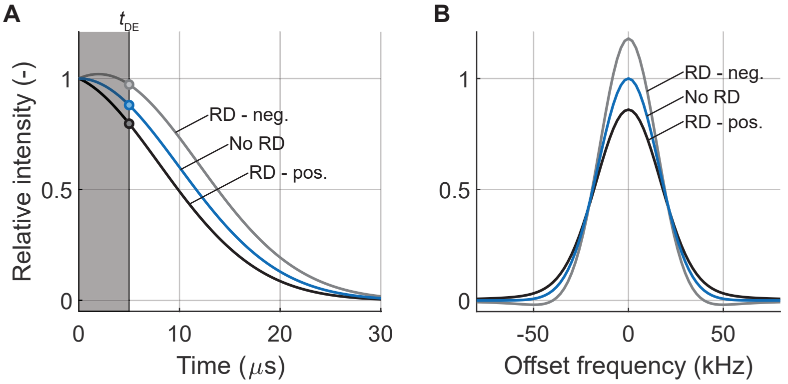

Figure 3.7: **A-B**. Schematic representation of the effect of RD on the FID and the NMR spectrum, respectively. The dots on the curves of Panel A represent the signal intensity at the end of the dead time t_{DE}, that is, the first recorded point of the FID.

The signal integral after Fourier transform is proportional to the first point of the FID. Since there is a dead time τ_{DE} between the pulse and the start of the acquisition, the first point of the FID and hence the signal integral are not conserved when RD is significant. As depicted in Fig. 3.7A, in presence of significant RD, the intensity of the first point of the FID diminishes and increases, for positive and negative DNP, which leads to an underestimation and overestimation of the signal integral, respectively. Fig. 3.7B shows the Fourier transform of the FIDs of Fig. 3.7A; the change in effective T_2^* due to RD broadens and sharpens the NMR signal, in the case of positive and negative DNP, respectively.

If it is difficult to compensate for RD in the polarization quantification, the fact that it affects the signal linewidth at least gives an indication that the effect is present. Since the RD time constant τ_{RD} is proportional to the Q-factor of the coil, [123] the better the Q-factor and the more biased the polarization quantification. As an example, Fig. 3.8A shows ^{1}H DNP curves of 100 μl of DNP juice doped with 50 mM TEMPOL under positive and negative DNP. The polarization reaches unphysical values beyond unity in the case of negative DNP. Fig. 3.8B shows that the FWHM nearly doubles for positive DNP and becomes nearly negligible compared to the initial FWHM, in the case of positive and negative DNP, respectively.

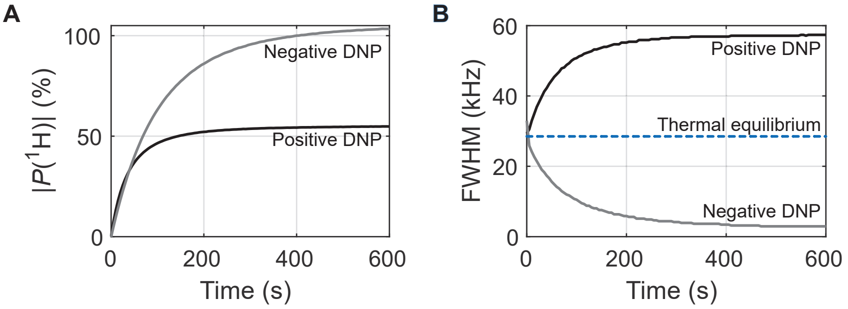

Figure 3.8: **A-B**. Absolute polarization and FWHM, respectively, for 100 μl of DNP juice doped with 50 mM TEMPOL under positive and negative DNP.

The intensity of RD can be diminished by diminishing artificially the Q-factor of the coil (by increasing its resistance of the rf circuit) or by detuning the coil. If RD is entirely canceled, the FWHM should be the same for positive and negative DNP. When such procedures are used, the ^{1}H polarization in DNP juice doped with 50 mM TEMPOL is found to be typically above 70%.

3.1.4 Polarization quantification for low-γ nuclei

The quantification of the polarization in the solid-state requires some extra care in the case of low-γ nuclei, such as ^{13}C. Indeed, the sensitivity being much lower than for ^{1}H, one has to use pulses with a larger angle and so the depletion of magnetization caused by the pulses cannot be considered negligible, as we did previously for ^{1}H. Yet, one needs to average several scans in order to obtain a thermal equilibrium reference signal with sufficient SNR. In our typical procedures, we choose the pulse angle for ^{13}C spins to be 5°. After a train of 64 pulses with angle, only $\cos(5°) \approx 0.78 \ll 1$ of the original magnetization is left. This implies that each of the 64 scans is acquired with a slightly different initial state and that the summed signal is not linear with the number of scans. We now derive a precise formula to account for this effect.

Let us assume that the system has longitudinal magnetization M_0. After a single pulse with angle θ, the magnetization left along the z-axis is $\cos(\theta) M_0$, while that in the transverse plane is $\sin(\theta) M_0$ (see Eq. 3.4). Before the k^{th} pulse, the magnetization left along the z-axis is

$$M_k^z = \cos(\theta)^{k-1} M_0 \tag{3.6}$$

and so the k^{th} pulse brings magnetization

$$M_k^{xy} = \sin(\theta)\cos(\theta)^{k-1} M_0, \tag{3.7}$$

into the transverse plane. For a train of N_S pulses, the total magnetization recorded in the transverse plane is

$$M_{tot}^{xy} = \sin(\theta) M_0 \sum_{k=1}^{N_S} \cos(\theta)^{k-1}. \tag{3.8}$$

Because of the following identity

$$\sum_{i=1}^{N} a^{i-1} = \frac{a^N - 1}{a - 1}, \tag{3.9}$$

we can conveniently rewrite Eq. 3.8 without the sum operation as

$$M_{tot}^{xy} = \sin(\theta) M_0 \frac{\cos(\theta)^{N_S} - 1}{\cos(\theta) - 1}. \tag{3.10}$$

For consistency, we can verify that the signal is proportional to the number of scans when the pulse angle tends toward 0, by calculating the limit

$$\begin{aligned} \lim_{\theta \to 0} \frac{\cos(\theta)^{N_S} - 1}{\cos(\theta) - 1} &= \lim_{\theta \to 0} \frac{\left(1 - \frac{1}{2}\theta^2 + o(\theta^4)\right)^{N_S} - 1}{1 - \frac{1}{2}\theta^2 + o(\theta^4) - 1} \\ &= \lim_{\theta \to 0} \frac{1 - \frac{N_S}{2}\theta^2 + o(\theta^4) - 1}{-\frac{1}{2}\theta^2 + o(\theta^4)} \\ &= \lim_{\theta \to 0} \frac{N_S + o(\theta^2)}{1 + o(\theta^2)} \\ &= N_S, \end{aligned} \tag{3.11}$$

and so we find that the signal is linear with the number of scans

$$\lim_{\theta \to 0} M_{tot}^{xy} = N_S \sin(\theta) M_0, \tag{3.12}$$

as expected.

Eq. 3.10 allows us to normalize a signal by the number of summed scans, even if the pulse angle is not negligible, using

$$I^n = \frac{I}{R_G} \frac{\cos(\theta) - 1}{\cos(\theta)^{N_S} - 1}. \tag{3.13}$$

For example, if we detect a signal with 64 scans and a pulse angle of 5°, the normalization factor for the number of scans given by Eq. 3.13 is $\approx 56.9 \neq 64$ (with $R_G = 1$). As we will see with an experimental case, using a large number of scans allows us to conveniently record thermal equilibria of low-γ nuclei with high SNR. If we do use a high number of scans, this numerical example shows the importance of taking the depletion of magnetization by the pulses into account.

The correction given by Eq. 3.10 requires that the pulse angle is precisely determined. The usual approach to the determination of the pulse angle consists of performing a nutation experiment at a given pulse power to get the pulse length for a $\pi/2$ pulse and then calculating the power necessary to perform a small angle pulse. However, it is also possible to measure the pulse angle with great precision by recording the magnetization depletion due to the pulses. We came up with a simple experimental scheme to measure the pulse angle which consists of polarizing the spins by DNP until they produce a decent SNR; then, their signal is detected with a series of detection blocks with N_S scans. [120, 121] If the B_1 field of the coil is homogeneous, the intensity of the signal decays monoexponentially with the detection blocks. Indeed, the signal recorded in the i_{th} detection block is

$$M^{xy}_{tot,i} = \cos(\theta)^{N_S(i-1)} \sin(\theta) M_0 \frac{\cos(\theta)^{N_S} - 1}{\cos(\theta) - 1}. \tag{3.14}$$

Normalizing the signal with respect to the first detection block, we get

$$\frac{M^{xy}_{tot,i}}{M^{xy}_{tot,1}} = \cos(\theta)^{N_S(i-1)}, \tag{3.15}$$

which is a monoexponential decay. Fig. 3.9 shows examples of pulse angle measurements for a typical DNP sample, where the decay is fitted with Eq. 3.15. The residuals of the fit are not randomly dispersed around 0. This is probably the result of a slight inhomogeneity of the B_1 field. Nonetheless, the measured angles have relative fit errors below 0.2%.

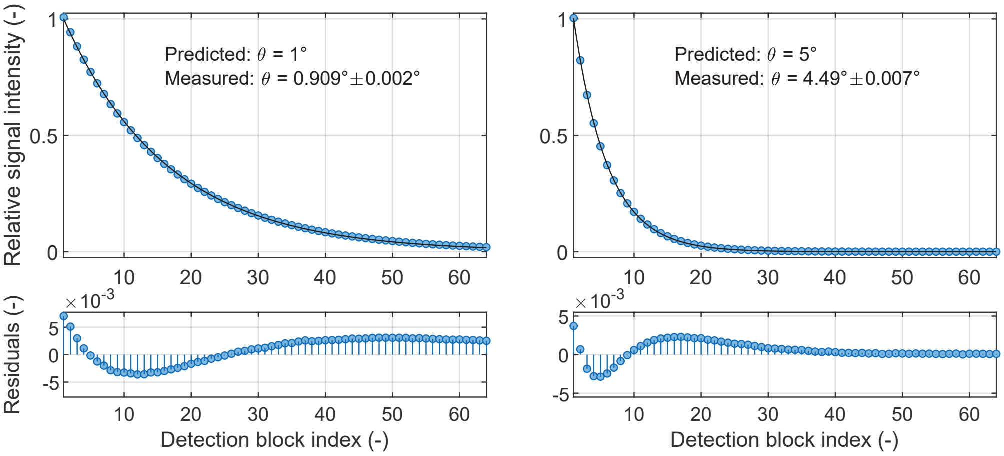

Figure 3.9: Fit of the signal decay under the magnetization depletion by small angle pulses for predicted angles of 1° and 5° on a sample of 3 M [1-^{13}C]-acetate and 50 mM TEMPOL in DNP juice at 1.2 K, using Eq. 3.15. Prior to detecting the decay, the ^{13}C spins were hyperpolarized by multi-contact CP to reach high SNR. Each point is the sum of $N_S = 256$ and 64 transients in the case of 1° and 5° pulses, respectively.

Fig. 3.10 presents a comparison of the angle predicted by Topspin's built-in function with that measured using our method. The predicted and measured angles are well correlated but the measured angle is 13% smaller than the prediction. This tends to show that the $\pi/2$ reference pulse used to predict the pulse angles had a significant bias. Fig. 3.10B shows the nutation experiments which were used to determine the reference $\pi/2$ pulse length for a power of 60 W. The reference pulse length was chosen to be 7.75 μs, by visual inspection of the maximum of the nutation curve. With our method, we found a reference $\pi/2$ pulse of $7.75/a \approx 8.87$ μs, where $a \approx 0.87$ is the slope of the solid line on Fig. 3.10. As can be seen in Fig. 3.10B (dashed vertical line), this value seems to be beyond the position of the maximum on the nutation curve.

The reason why we want to measure the pulse angle with high accuracy is to correct for the signal depletion during a train of detection pulses. The predicted pulse angle is significantly different from the measured angle. Choosing the direct measurement of the angle rather than Topspin's prediction seems more reliable because it is precisely based on the depletion of the signal, which is

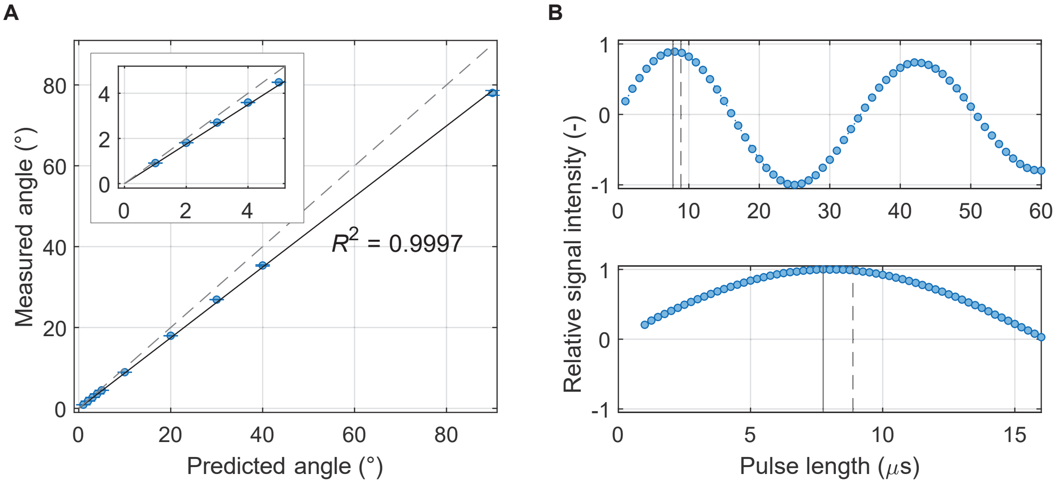

Figure 3.10: **A**. Correlation of measured and predicted pulse angles. Two examples of measurements are shown in Fig. 3.9. **B**. Nutation experiments at 60 W on the same sample. The solid and dashed vertical lines represent the pulse length that was chosen at reference for the $\pi/2$ pulse and the length which is obtained by correcting the reference using the result of Panel A.

what we are trying to account for. We will therefore use it for the polarization quantification for low-γ nuclei.

Having measured the pulse angle, we can record the thermal equilibrium signal of ^{13}C spins. Contrary to the case of ^{1}H spins, the build-up towards thermal equilibrium cannot be monitored with a high temporal resolution because the pulses would retrieve too much polarization. Our strategy thus consists of monitoring the build-up very roughly, typically with trains of $N_S = 2-4$ pulses and a repetition rate t_r = 20 min and, once the spins have reached thermal equilibrium, record their signal with the best SNR possible, i.e., with a higher number of scans. Because the build-up is only roughly monitored, one needs to have prior knowledge of the ^{13}C relaxation time constant. This can be obtained by polarizing the spins by multiple-contact CP and monitoring the decay of polarization. At 3.8 K and 7.05 T, the T_1 of ^{13}C spins in DNP juice with 50 mM TEMPOL is of the order of 20 min. Because we do not record the thermal equilibrium build-up with a high temporal resolution, we use a relaxation delay of 2 h, which is chosen higher than the usual $5T_1$ value as a precaution (for example if the radicals are partially degraded and the T_1 is longer than assumed). Fig. 3.11 shows an example of such a measurement.

3.2 Theory of DNP mechanisms

DNP mechanisms describe the first step of the DNP process, namely how the polarization of electron spins is transferred to nuclear spins through the hyperfine interaction *via* μw irradiation. There are four distinct DNP mechanisms that can mediate this transfer: solid effect (SE), cross effect (CE), Overhauser effect (OE), and thermal mixing (TM). In this section, we briefly review the theory behind DNP mechanisms.

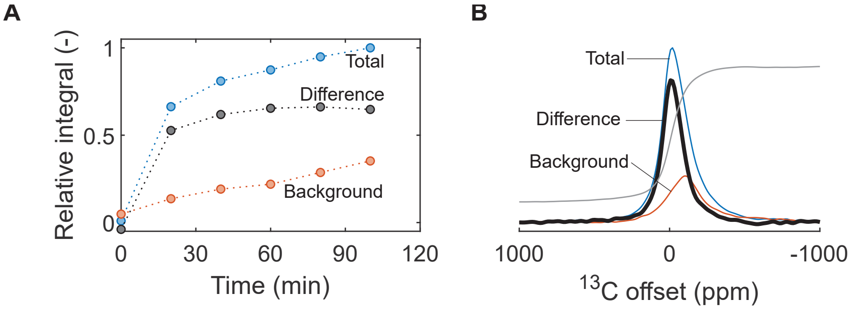

Figure 3.11: **A-B.** Signal monitoring and processing for the ^{13}C thermal equilibrium signal of 100 μl of DNP juice with 50 mM TEMPOL and 3 M [1-^{13}C]-sodium acetate at 3.8 K using a background free coil (the residual background originates from the sample cup). The thermal equilibrium signal is monitored with detection blocks with $N_S = 4$ every 20 min in A. Once it has reached thermal equilibrium, the signal is detected with SNR with a single acquisition block with $N_S = 64$ in B. The process is repeated with and without sample in the sample cup (signals labeled 'Total' and 'Background', respectively). The gray line on the spectrum represents the signal integral.

3.2.1 Solid effect and Overhauser effect

SE and OE can be explained in terms of a 1 electron-1 nucleus model, as depicted in Fig. 3.12, for the case of a spin 1/2 with positive gyromagnetic ratio such as ^{1}H and ^{13}C spins, where ω_{0S} and ω_{0I} are the Larmor frequency of electron spin S and nuclear spin I, respectively.

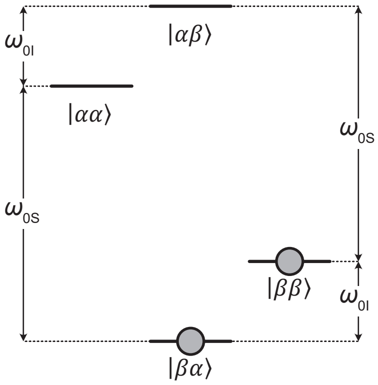

Figure 3.12: Schematic representation of the four levels of a 1 electron-1 nucleus spin system. The gray dots represent the populations at thermal equilibrium (i.e., without DNP), in conditions where the electron spin is fully polarized and the nucleus has polarization $P_\mathrm{I} \approx 0$.

SE is the most straightforward mechanism. It consists of pumping mixed EPR-NMR transitions, either zero-quantum (ZQ) or double-quantum (DQ), ω_ZQ and ω_DQ, respectively, as depicted in Fig. 3.13 A and B. μw pumping at $\omega_{\mu w} = \omega_\mathrm{DQ}$ tends to equilibrate the populations of the $|\alpha\alpha\rangle$ and $|\beta\beta\rangle$ states. After electronic relaxation from $|\alpha\alpha\rangle$ to $|\beta\alpha\rangle$, a new cycle can take place. This process accumulates population of $|\beta\alpha\rangle$, which translates into positive nuclear polarization. To the contrary, μw pumping at $\omega_{\mu w} = \omega_\mathrm{ZQ}$ tends to equilibrate the populations of the $|\beta\alpha\rangle$ and $|\alpha\beta\rangle$ states, while electronic relaxation brings the population from $|\alpha\beta\rangle$ to $|\beta\beta\rangle$. This process accumulates population of $|\beta\beta\rangle$, which translates into negative nuclear polarization.

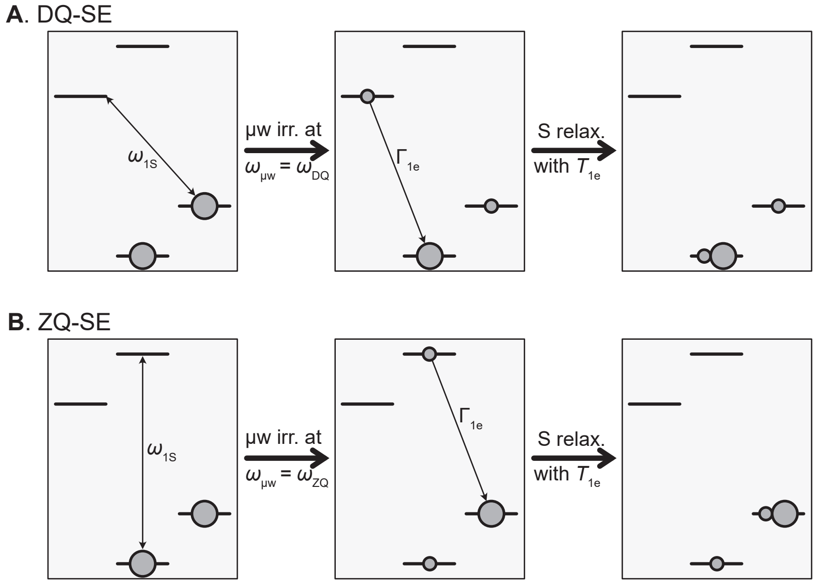

Figure 3.13: **A-B.** Steps of the SE-DNP mechanism for the DQ and ZQ transitions, respectively. Γ_{1e} is the rate of electron spin-lattice relaxation.

The old literature often refers to ZQ and DQ as “forbidden transitions”. [124] However, later authors prefer referring to them as “second order transitions”. [101] Whatever the name they are given, these transitions have low probability because they do not respect the selection rule of $\Delta(m_\mathrm{S}+m_\mathrm{I}) = \pm 1$, where m_S and m_I are the spin quantum number of the electron and the nucleus, respectively, if a second order perturbation is not taken into account. [124] As a consequence, SE-DNP is often limited by the transition probability induced by the μw field which is given, for a field of strength ω_1S at frequency $\omega_{\mu w}$, by [101]

$$\Gamma_\mathrm{SE} = \frac{\pi}{8}\frac{|A_{z+}|^2\omega_\mathrm{1S}^2}{\omega_\mathrm{0I}^2} h(\omega_\mathrm{0S} - \omega_{\mu w} \pm \omega_\mathrm{0I}), \tag{3.16}$$

where A_{z+} and $h(\omega)$ are the pseudosecular hyperfine interaction (see Eq. 2.146) and the homogeneous lineshape of the electron resonance, respectively, with the resonance condition

$$\omega_{\mu w} = \omega_\mathrm{0S} \pm \omega_\mathrm{0I}. \tag{3.17}$$

The sign in front of ω_0I depends on whether Γ is calculated for the DQ or ZQ transitions. If the width of lineshape $h(\omega)$ is small compared to the nuclear Larmor frequency, the matching conditions for DQ and ZQ cannot be attained at the same time. This results into well-resolved positive and negative peaks on the μw spectrum appearing at lower and higher frequencies, respectively, as shown in Fig. 3.14. Eq. 3.17 implies that these two peaks on the μw spectrum as separated by twice the Larmor frequency of the nucleus

$$|\omega_{DQ} - \omega_{ZQ}| = 2\omega_\mathrm{0I}, \tag{3.18}$$

which gives a clear signature of SE on μw spectra.

Eq. 3.16 shows that SE transitions are proportional to the 6^{th} power of the inverse of the distance between the nucleus and the electron r, since $|A_{z+}|$ is proportional to r^{-3}. As a consequence, the efficiency of SE-DNP decays rapidly as the distance between the electron and the

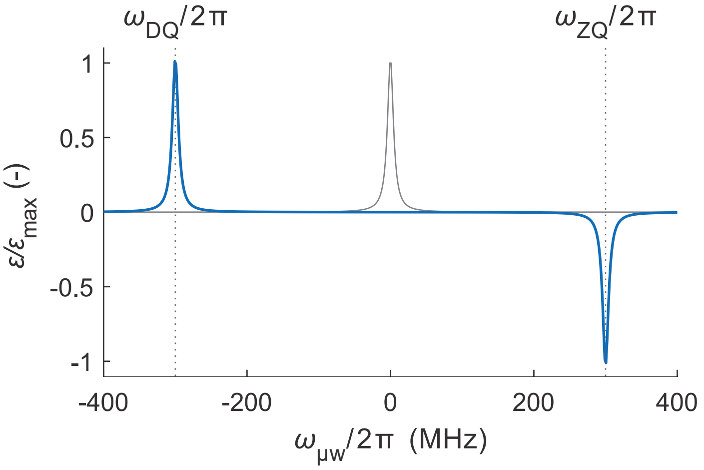

Figure 3.14: Simulated μw spectrum (in blue) for a ^{1}H spin polarized under SE-DNP at 7.05 T, corresponding to a nuclear Larmor frequency of 300 MHz. The EPR spectrum is shown in light gray, assuming a Lorentzian lineshape $h(\omega)$ with an FWHM $\delta_{1/2} = 10$ MHz. the dotted vertical lines indicate the frequencies of the ZQ and DQ transitions. The frequency axis is shifted so that $\omega_{0\mathrm{S}} = 0$.

nucleus increases (as for all DNP mechanisms). Furthermore, SE-DNP decays quadratically when the static magnetic field B_0 increases as it is proportional to $\omega_{0\mathrm{I}}^{-2}$, which makes SE-DNP more efficient as lower magnetic fields.

The OE can also be rationalized in terms of a 1 electron-1 nucleus spin system, as depicted in Fig. 3.12. In this case, the μw frequency is set on resonance with the single-quantum EPR transition [125]

$$\omega_{\mu w} = \omega_{0\mathrm{S}}. \tag{3.19}$$

For nuclei to be polarized by OE-DNP, one of the cross-relaxation rates Γ_{ZQ} or Γ_{DQ} has to dominate over the other as well as over the electron spin-lattice relaxation rate R_{1e} and the nuclear spin-lattice relaxation rate R_{1n} (or at least compete with these rates). [126, 125] Fig. 3.15 shows a schematic representation of the process. μw first equilibrates all populations. If Γ_{DQ} dominates over Γ_{ZQ}, $|\alpha\alpha\rangle$ gets depleted while $|\beta\beta\rangle$ gets more populated. Following electronic relaxation, a net excess of $|\beta\beta\rangle$ is created, resulting in negative nuclear polarization. To the contrary, if Γ_{ZQ} dominates over Γ_{DQ}, $|\alpha\beta\rangle$ gets depleted while $|\beta\alpha\rangle$ gets more populated. Following electronic relaxation, a net excess of $|\beta\alpha\rangle$ is created, resulting in positive nuclear polarization.

OE is often limited by the efficiency of the DQ and ZQ cross-relaxation transitions. Owing to the field dependence of the Γ_{ZQ} and Γ_{DQ} rates, OE has a more complex field dependence than SE. In the liquid-state, it can be independent of magnetic field strength for low field strength, while it can decrease with B_0^{-2} at higher magnetic fields. [126] In the solid-state under MAS, it was shown to increase with B_0. [127] In all cases, Γ_{ZQ} and Γ_{DQ} are only non-zero if the electron-nucleus hyperfine interaction has non-zero probability to fluctuate at frequencies $\omega_{0\mathrm{S}} - \omega_{0\mathrm{I}}$ and $\omega_{0\mathrm{S}} + \omega_{0\mathrm{I}}$. Such fluctuations are often met in conductive metals due to the motion of electrons [7] and in liquids due to translational and rotational diffusion. [126] However, OE-DNP was observed in insulating solids both under MAS at 100 K [127, 128] and under dDNP conditions at 1.2 K. [129] In the case of the radical BDPA, the necessary fluctuations of the hyperfine interactions were proposed to be the result of electron motion within the π-conjugated system of the radical.

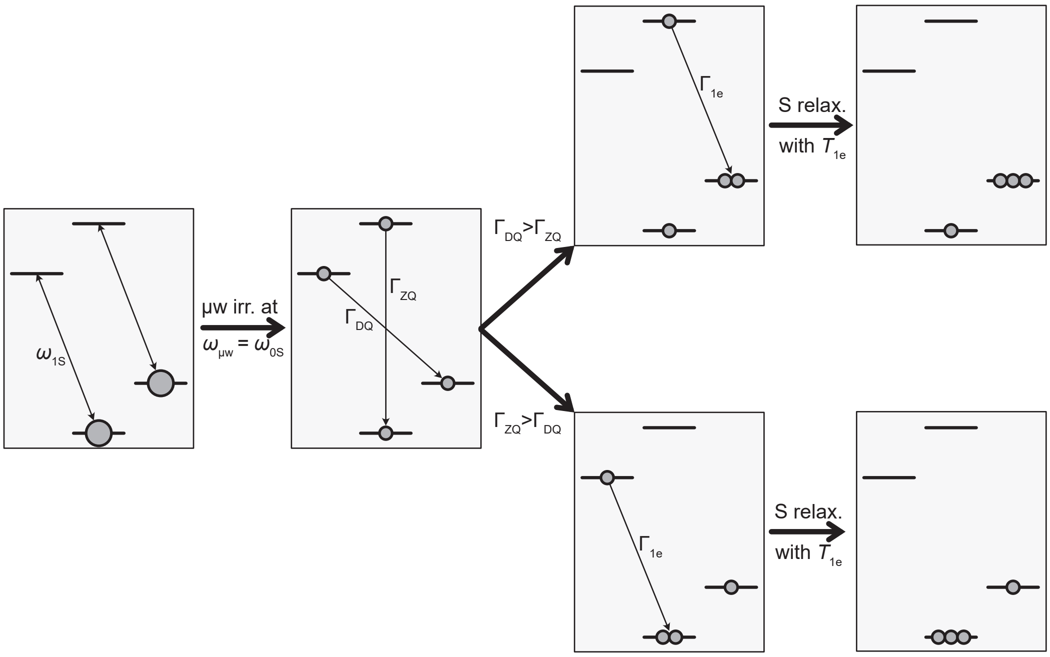

Figure 3.15: Schematic representation of the steps of OE-DNP. Γ_{1e}, Γ_{ZQ} and Γ_{DQ} are the rate of electron spin-lattice relaxation and of ZQ and DQ electron-nucleus cross-relaxation, respectively.

[130, 131] Methyl rotation has also recently been shown to provide the necessary fluctuations of the hyperfine interaction. [128]

3.2.2 Cross effect and indirect cross effect

As for OE, the μw frequency $\omega_{\mu w}$ for CE is not set on a mixed EPR-NMR transition but rather on an allowed single quantum (SQ) EPR transition, and a cross-relaxation mechanism subsequently polarizes the nucleus. However, contrary to the case of OE, $\omega_{\mu w}$ is set slightly off-resonance with respect to the center of the EPR transition. CE can be rationalized in terms of a 2 electron-1 nucleus model where the difference between the Larmor frequencies $\omega_{0\mathrm{S1}}$ and $\omega_{0\mathrm{S2}}$ of electrons spins S1 and S2, respectively, is equal to the nuclear Larmor frequency $\omega_{0\mathrm{I}}$

$$|\omega_{0\mathrm{I}}| = |\omega_{0\mathrm{S1}} - \omega_{0\mathrm{S2}}|, \tag{3.20}$$

as depicted in Fig. 3.16A. If the μw frequency is set to the Larmor frequency of S1

$$\omega_{\mu w} = \omega_{0\mathrm{S1}}, \tag{3.21}$$

μw irradiation tends to equalize the populations of the SQ transition of S1 but not of S2.

As depicted in Fig. 3.16B, this results in a situation where an energy conservative triple spin flip Γ_{SSI} can take place, provided at least one electron interacts with the nucleus and the two electrons interact with one another. [11, 58] Following electronic spin-lattice relaxation from $|\beta\alpha\alpha\rangle$ to $|\beta\beta\alpha\rangle$, a new cycle can start, accumulating population of nuclear $|\alpha\rangle$ state and hence building up positive nuclear polarization. If the μw frequency is set to $\omega_{\mu w} = \omega_{0\mathrm{S2}}$, one finds that negative nuclear polarization is created following the same logic as that of Fig. 3.16B. For this simple three-spin model, positive and negative extrema are therefore expected at $\omega_{0\mathrm{S1}}$ and $\omega_{0\mathrm{S2}}$, respectively, on the

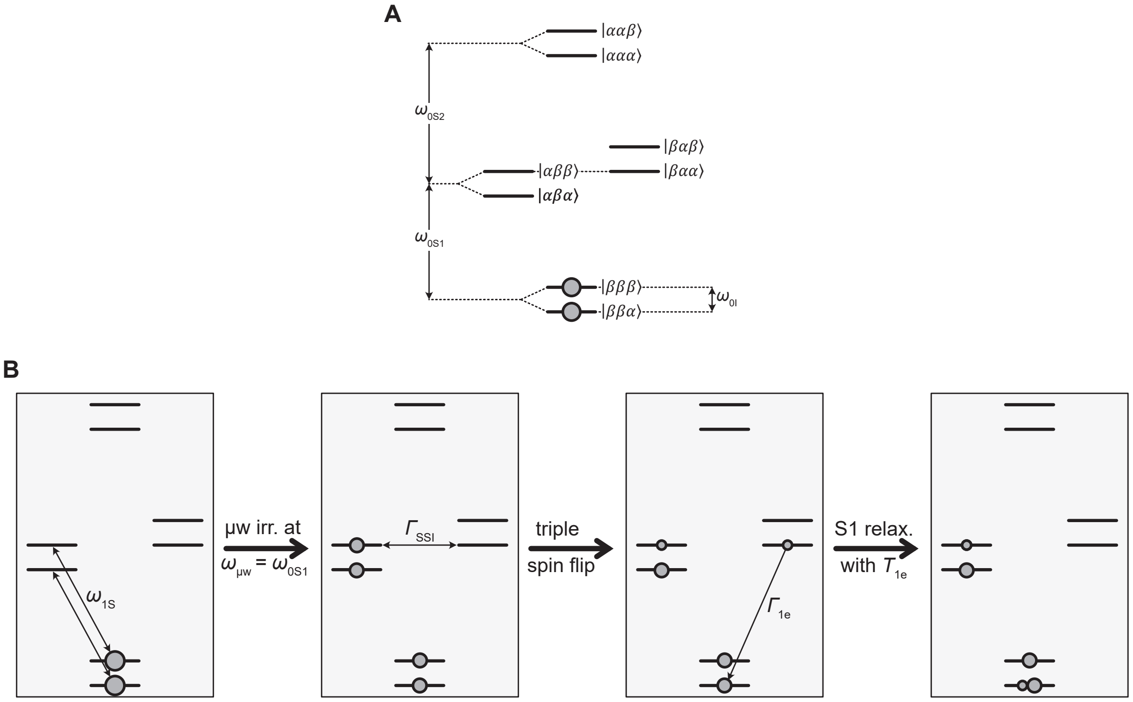

Figure 3.16: **A.** Eight energy levels of a 2 electron-1 nucleus spin system used to describe the CE, where the electrons are assumed to be fully polarized while the nucleus has polarization $P_{\mathrm{I}} \approx 0$. Because of the matching condition of Eq. 3.20, the $|\alpha\beta\beta\rangle$ and $|\beta\alpha\alpha\rangle$ states are degenerate. **B.** Schematic representation of the steps of CE-DNP. Γ_{SSI} is the triple spin-flip rate connecting the $|\alpha\beta\beta\rangle$ and $|\beta\alpha\alpha\rangle$ states.

μw spectrum. Because of Eq. 3.20, these extrema are expected to be separated by the nuclear Larmor frequency ω_{I}.

In general, the polarization of the electron spins is not initially 1 and saturation may not lower the polarization of the saturated spin down to 0. If P_{S1} and P_{S2} are the polarizations of S1 and S2 at equilibrium under μw irradiation, the highest achievable nuclear polarization is [132, 58, 133, 134]

$$P_{\mathrm{I}} = \frac{P_{\mathrm{S2}} - P_{\mathrm{S1}}}{1 - P_{\mathrm{S1}} P_{\mathrm{S2}}}. \tag{3.22}$$

as long nuclear spin-lattice relaxation may be neglected.

One may wonder how the very restrictive matching condition of Eq. 3.20 may be fulfilled. We may distinguish two different approaches: that of MAS-DNP and that of static DNP. In the former case, the picture is more complicated than that of Fig. 3.16 because the energy levels evolve along the rotation of the sample. [135] Therefore, the three spins have a higher probability to be found at the matching condition at some angle along the rotor rotation, than in a fixed position. Without going into the details, we note that highly sophisticated strategies have been devised to maximize the efficiency of the process, such as biradical polarizing agents, where two radicals are chemically tethered together. Typical biradicals include pairs of nitroxides [136, 137] or a nitroxide with a trityl derivative. [138, 139] A number of parameters have been identified as key to improving MAS-DNP enhancement using biradicals: the distance and angle between the electron spins, their respective T_{1e} and their exchange and dipolar interactions, among others.

The influence of these parameters has been studied in great detail using quantum mechanical simulations [135, 136, 140, 141, 142, 143] and experimental data, which guides the design of ever more efficient biradicals. [136]

We now describe how CE behaves under static DNP. In this case, biradicals would hardly be efficient polarizing agents as only a small fraction of them would satisfy the matching condition of Eq. 3.20 and so monoradicals are commonly used. To ensure sufficient e-e interactions and hence a high triple spin-flip rate Γ_{SSI}, relatively high radical concentrations of up to 25-50 mM are typically used [121] (while typical MAS-DNP sample use typical radical concentrations of 10-20 mM). This results in a large network of interacting electrons. Using a radical with an EPR line that is broader than the nuclear Larmor frequency, there are radicals with a distribution of frequencies and a distribution of coupling with the neighboring electron and so the matching condition of Eq. 3.20 may be fulfilled, at least for some of the radicals. For this reason, nitroxide radicals such as TEMPO and TEMPOL are typically used for DNP of ^{1}H and ^{19}F spins and ^{13}C based radicals such as trityl and BDPA for low-γ nuclei.

The situation we are trying to describe gets more complicated than a simple case such as SE, because we now have to treat many electrons and nuclei at the same time. However, the problem may be treated in fairly simple terms using Kundu *et al.*'s model of indirect cross effect (iCE). [132, 133, 134] Fig. 3.17A shows a simulation of the EPR spectrum of TEMPOL at 7.05 T performed using the EasySpin package. The spectral features are dominated by the inhomogeneous broadening due to two anisotropic interactions, namely the hyperfine interaction with the ^{14}N spin and the electron g-tensor. In the CE picture, μw irradiation is assumed to "burn a hole" in the EPR spectrum as represented in Fig. 3.17B. For simplicity, we assumed that the hole has a Gaussian profile with an FWHM $\delta_{1/2} = 150$ MHz

$$P_{\mathrm{S}}(\omega) = P_{\mathrm{S},eq}\left(1 - \exp\left(-\left(\frac{\omega - \omega_{\mu w}}{\sigma}\right)^{2}\right)\right), \tag{3.23}$$

where $P_{\mathrm{S},eq}$ and $\sigma = \delta_{1/2}/(2\sqrt{2\log 2})$ are the electron spin polarization at Boltzmann equilibrium and the standard deviation of the Gaussian saturation envelope, respectively. In reality, hole burning is the result of three competing processes: μw irradiation tends to lower the polarization of the electron spins with a frequency close to $\omega_{\mu w}$; spectral diffusion tends to spread the effect of saturation across the EPR spectrum *via* e-e dipolar interactions; spin-lattice relaxation tends to bring the electron polarization back towards Boltzmann polarization. [133, 134] This model is referred to as the electron spectral diffusion model (eSD) in Ref. [133, 134]. For simplicity and for the sake of the argument, we may assume that the result of all these processes is a hole with a Gaussian profile as that of Eq. 3.23.

The iCE model infers the nuclear polarization from the saturated EPR lineshape, by averaging the nuclear polarization obtained by Eq. 3.22 overall electron pairs satisfying the CE matching condition (see Eq. 3.20). If the EPR spectra is chopped into N bins with index k, such pairs of electrons have frequencies $\omega_{\mathrm{S}k}$ and $\omega_{\mathrm{S}k} + \omega_{\mathrm{I}}$. The average nuclear polarization resulting from iCE may be computed as [132]

$$P_{\mathrm{I}} = \frac{1}{f}\sum_{k}^{N} h(\omega_{\mathrm{S}k} + \omega_{\mathrm{I}})h(\omega_{\mathrm{S}k})\frac{P_{\mathrm{S}}(\omega_{\mathrm{S}k} + \omega_{\mathrm{I}}) - P_{\mathrm{S}}(\omega_{\mathrm{S}k})}{1 - P_{\mathrm{S}}(\omega_{\mathrm{S}k} + \omega_{\mathrm{I}})P_{\mathrm{S}}(\omega_{\mathrm{S}k})}, \tag{3.24}$$

with a normalization factor

$$f = \sum_{k}^{N} h(\omega_{\mathrm{S}k} + \omega_{\mathrm{I}})h(\omega_{\mathrm{S}k}), \tag{3.25}$$

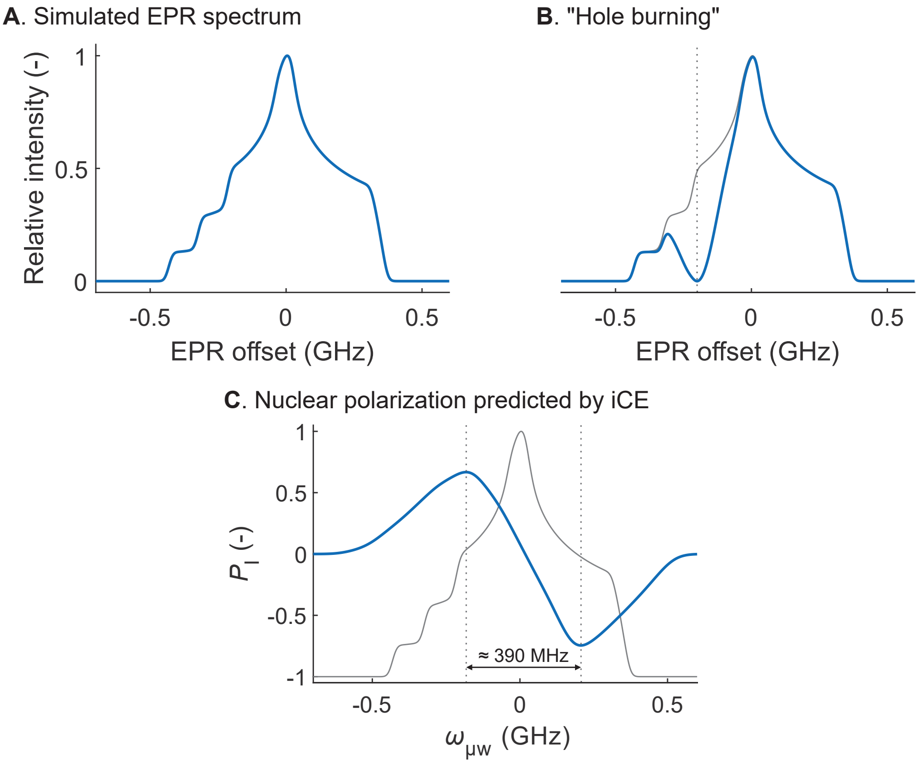

Figure 3.17: **A.** EasySpin simulation of the EPR spectrum of TEMPOL at 7.05 T with a Lorentzian broadening of 25 MHz using hyperfine coupling parameters $A_{xx} = 19.8$ MHz, $A_{yy} = 22.1$ MHz and $A_{zz} = 108$ MHz and g-tensor parameters $g_{xx} = 2.00908$, $g_{yy} = 2.00554$ and $g_{zz} = 2.00233$ from Ref. [144]. **B.** Simulation of a hole burning by μw irradiation centered at -0.2 GHz and with a Gaussian profile with a width of FWHM $\delta_{1/2} = 150$ MHz MHz. The blue and light gray lines represent the EPR spectrum before and after the hole burning, respectively. The dotted vertical line indicates the μw frequency. **C.** Simulated μw spectrum obtained using the iCE model in blue, assuming a Boltzmann electron polarization $P_{\mathrm{S},eq} = 0.99$. The simulated EPR spectrum is shown for comparison in light gray.

where $h(\omega)$ and $P_{\mathrm{S}}(\omega)$ are the number of electrons with frequency ω and their polarization, respectively. This CE mechanism is indirect in the sense that it predicts that nuclei are polarized even if they interact with electron pairs that were not directly affected by μw irradiation but indirectly *via* spectral diffusion. Fig. 3.17C shows the expected DNP spectrum expressed in terms of nuclear polarization as a function of the μw irradiation frequency $\omega_{\mu w}$, assuming that the electron polarization is given by Eq. 3.23 with $P_{\mathrm{S},eq} = 0.99$. Contrary to the case of SE (see Fig. 3.14), the positive and negative lobes overlap. They are separated by ≈ 390 MHz, which is larger than the value $\omega_{\mathrm{I}} = 300$ MHz predicted by the simple three spin-model, owing to the complex and broad EPR lineshape.

3.2.3 Spin temperature and thermal mixing

The picture of CE and iCE that we have presented here assumed that μw burnt a hole in the EPR line, i.e., the electron polarization was lowered for electrons with a frequency sufficiently near $\omega_{\mu w}$. However, in the case where electrons interact strongly, fast spectral diffusion allows electron spins to rearrange in the configuration with the highest entropy under μw irradiation. In this case, the electron polarization along the EPR line is given by [145, 146]

$$P_{\mathrm{S}}(\omega) = \tanh\left(\alpha\omega_{\mu w} + \beta\left(\omega - \omega_{\mu w}\right)\right). \tag{3.26}$$

where α and β are the inverse temperatures of the Zeeman electron reservoir and of the electron non-Zeeman (NZ) reservoir, respectively, related to the spin temperatures T_α and T_β by

$$\alpha = \frac{\hbar}{k_b T_\alpha} \text{ and } \beta = \frac{\hbar}{k_b T_\beta}. \tag{3.27}$$

This situation corresponds to TM-DNP where, instead of burning a hole, μw irradiation establishes a homogeneous spin temperature within the NZ electron reservoir. In the absence of μw irradiation, $T_\alpha = T_\beta = T_L$, where T_L is the lattice temperature. When μw irradiation is switched on, a flow of energy from the NZ to the Zeeman reservoirs causes T_α to increase and T_β to decrease, ideally towards $+\infty$ and 0, respectively. [145, 146] Fig. 3.18A shows the electron polarization distribution along the EPR line according to Eq. 3.26 assuming $\omega_{\mu w} = -0.2$ GHz and $T_\alpha = +\infty$ (or $\alpha = 0$) for several values of T_β. Fig. 3.18B shows the corresponding EPR spectra, with characteristic negatively polarized electrons. Note that, in a given set of experimental conditions, $\alpha = 0$ would result in a unique value of β. Varying the intensity of μw irradiation, one might obtain different values of β but for corresponding finite values of α. The curves in Fig. 3.18 could therefore not be realistically obtained simply by varying the μw power but they are shown here to illustrate the effect of the NZ electron reservoir spin temperature on the EPR line.

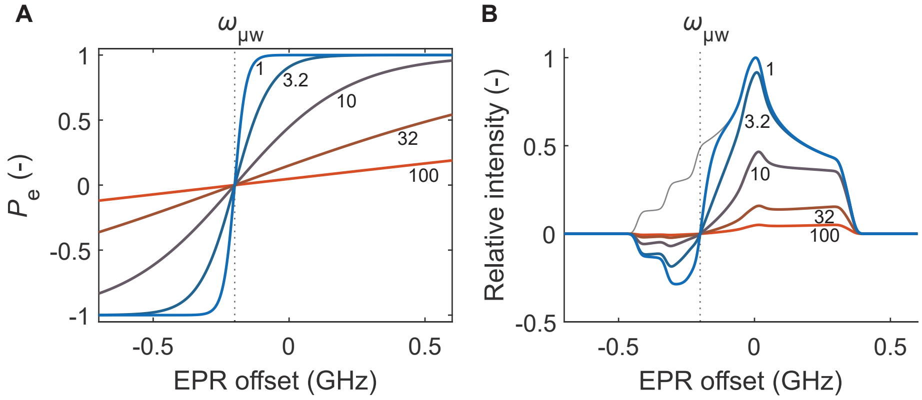

Figure 3.18: **A-B.** Electron polarization along the EPR line for $\alpha = 0$ and various values of β shown next to curves as spin temperature T_β in mK and corresponding EPR spectra, respectively. The unperturbed simulated EPR spectrum is shown for comparison in light gray on Panel B.

Considering Eq. 3.22, the presence of both positively and negatively polarized electrons on the spectra of Fig. 3.18B is advantageous compared to those under hole burning conditions (see spectra in Fig. 3.17), as it increases the electron polarization difference $P(\omega + \omega_{\mathrm{I}}) - P(\omega)$, which translates into higher nuclear polarization under DNP. This represents a major advantage of TM over CE. In fact, the nuclear polarization under TM-DNP is trivially given by the spin temperature of the NZ electron reservoir. Indeed, if $P_{\mathrm{I}}(\omega)$ is the polarization of the nuclear spins interacting with an electron spin with frequency ω, writing $\kappa = \alpha\omega_{\mu w} + \beta\left(\omega - \omega_{\mu w}\right)$, we have

$$\begin{aligned} P_{\mathrm{I}}(\omega) &= \frac{P_{\mathrm{S}}(\omega+\omega_{\mathrm{I}}) - P_{\mathrm{S}}(\omega)}{1 - P_{\mathrm{S}}(\omega+\omega_{\mathrm{I}})P_{\mathrm{S}}(\omega)} \\ &= \frac{\tanh(\kappa+\beta\omega_{\mathrm{I}}) - \tanh(\kappa)}{1 - \tanh(\kappa+\beta\omega_{\mathrm{I}})\tanh(\kappa)} \\ &= \tanh(\beta\omega_{\mathrm{I}}), \end{aligned} \tag{3.28}$$

where we used a common identity of the hyperbolic tangent to go from the second to the third line. Therefore, P_{I} does not depend on ω under TM-DNP and so averaging $P_{\mathrm{I}}(\omega)$ over the EPR line using Eq. 3.24 results into averaging a constant value. The reason behind this fact is that when the electron NZ reservoir has a homogeneous spin temperature, the polarization gradient along the EPR line is constant. [146]

The shape of the μw spectrum under TM-DNP is therefore determined by the inverse spin temperature of NZ reservoir β which is obtained under μw irradiation at frequency $\omega_{\mu w}$. We will not go into the details of how this is calculated but we note that the spectral features of the μw spectra in TM conditions are very similar to that under CE (see Fig. 3.17C), namely, overlapping positive and negative lobes. [146] As a consequence, it is not straightforward to determine experimentally which of the two mechanisms dominates in given conditions.

In summary, according to the description that we have given of CE and TM, the main difference between these two mechanisms is that μw irradiation burns a hole in the EPR spectrum in the former case, while it establishes a homogeneous spin temperature within the electron NZ reservoir in the latter case. Furthermore, all electrons are positively polarized in the former case while there might exist both positively and negatively polarized electron spins in the latter case. In both cases, the nuclear polarization under DNP can be inferred from the steady state EPR spectrum under partial saturation. Whether CE or TM is active depends on the strength of the e-e dipolar interactions. [133].

Wenckebach recently showed analytically that CE and TM were two limits of a more general mechanism. [58] He calculated the triple spin-flip rate Γ_{SSI} for a 2 electron-1 nucleus system

$$\Gamma_{\mathrm{SSI}} = \frac{\pi}{8}\frac{|A_{z+}|^2 D_0^2}{\omega_{0\mathrm{I}}^2}\delta(\omega_{0\mathrm{I}} - \omega_J), \tag{3.29}$$

where D_0, $A_{z,\pm}$, $\omega_{0\mathrm{I}}$ and ω_J are the e-e dipolar interaction strength (see Eq. 2.137), the hyperfine interaction strength between one electron and the nucleus (see Eq. 2.146), the nuclear Larmor frequency and a quantity related to the relative strength of the e-e interaction and the difference Larmor frequencies of the electrons, given by

$$\omega_J = \sqrt{(\omega_{0\mathrm{S2}} - \omega_{0\mathrm{S1}})^2 + D_0^2}, \tag{3.30}$$

respectively. Whether the triple spin flip occurs under CE or TM depends on the dominating term in ω_J. If $(\omega_{0\mathrm{S2}} - \omega_{0\mathrm{S1}})^2$ dominates, then $\omega_J \approx |\omega_{0\mathrm{S2}} - \omega_{0\mathrm{S1}}|$ and so Γ_{SSI} is only non-zero for

$$|\omega_{0\mathrm{S2}} - \omega_{0\mathrm{S1}}| = |\omega_{0\mathrm{I}}|, \tag{3.31}$$

which corresponds to the matching condition of CE. To the contrary, if D_0^2 dominates, then $\omega_J \approx |D_0|$ and so Γ_{SSI} is only non-zero for

$$|D_0| = |\omega_{0\mathrm{I}}|, \tag{3.32}$$

which corresponds to the matching condition of TM. Using statistical thermodynamics tools, Wenckebach then extended his results to an infinite number of spins. [59] In a random distribution of molecules in a frozen solution, the minimum distance between two electron spins plays a particularly important role as it sets a maximum value to D_0 and thus determines if TM-DNP is probable. [60, 106]

It is interesting to compare the triple spin-flip rate of TM and CE $\Gamma_{\rm SSI}$ (see Eq. 3.29) to the flip-flop rate of SE $\Gamma_{\rm SE}$ (see Eq. 3.16). Apart from the matching conditions, the only difference is that the former is proportional to D_0^2 while the latter is proportional to $\omega_{\rm 1S}^2$. D_0^2 can be controlled by the sample design while $\omega_{\rm 1S}^2$ is limited by the power of the μw source.

3.3 DNP on common samples

In this section, we present DNP results on common samples of DNP juice doped with TEMPOL radical. We first demonstrate the effect of radical doping on ^{1}H spins at thermal equilibrium at 3.8 K. Then, we present an experimental approach used to determine the DNP mechanisms at play in given experimental conditions. This approach consists of recording the nuclear polarization under DNP (or the DNP enhancement) as a function of the μw irradiation frequency $\omega_{\mu w}$, which results in a "μw spectrum", also called "DNP spectrum" or "μw sweep profile". We present detailed μw spectra for DNP juice doped with 50 and 75 mM at various temperatures.

3.3.1 DNP juice doping

Most experiments presented in this work were performed on samples based on DNP juice, i.e., a mixture of water, heavy water, and deuterated glycerol in a ratio of 1:3:6 (v/v/v). In this section, we show how the thermal equilibrium ^{1}H signal of DNP juice is affected by the presence of TEMPOL molecules at 7.05 T and at 3.8 K.

Fig. 3.19 shows thermal equilibrium signals recorded at 3.8 K in DNP juice doped with TEMPOL with concentrations between 10 and 100 mM. Qualitatively, one can observe two effects of the presence of radicals: the higher the radical concentration, the faster the relaxation towards Boltzmann equilibrium, and the broader the NMR line.

To extract quantitative information out of the thermal equilibrium build-up curves, they were fitted with a stretched exponential function

$$I(t) = I_\infty \left(1 - \exp\left(-\left(\frac{t}{T_1}\right)^\beta\right)\right), \tag{3.33}$$

where I_∞, T_1 and β are the signal intensity at infinite time, the relaxation time constant, and the stretch coefficient between 0 and 1, respectively. When the stretch coefficient tends towards 1, Eq. 3.33 tends towards a monoexponential. We use a stretched exponential rather than a monoexponential when the dynamics of the system are not dominated by a single mechanism, resulting in a distribution of relaxation time constants. The average relaxation time constant is given by

$$T_{1,\rm av} = \frac{T_1}{\beta}\Gamma\left(\frac{1}{\beta}\right) \tag{3.34}$$

where Γ is the gamma function. If $\sigma(x)$ is the standard deviation of x, the error on $T_{1,\rm av}$ is calculated as

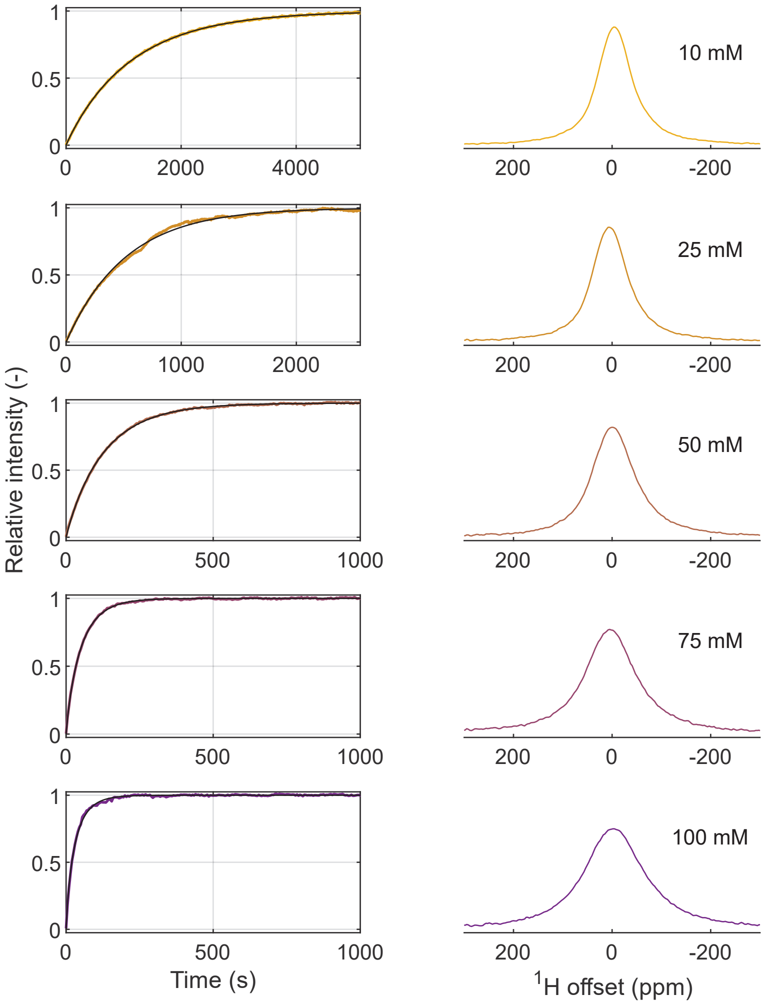

Figure 3.19: Evolution of the ^{1}H thermal equilibrium signal of DNP juice at 3.8 K with increasing TEMPOL concentration from 10 to 100 mM. The signal was recorded by summing 64 scans with 0.1° pulses. Colored and black lines correspond to experimental data and stretched exponential fits (see Eq. 3.33), respectively. The spectra on the right correspond to the last spectrum of each build-up. The concentration of TEMPOL radical is indicated next to the spectra.

$$\begin{aligned}\sigma(T_{1,\mathrm{av}}) &= T_{1,\mathrm{av}}\sqrt{\frac{\sigma(T/\beta)}{(T/\beta)^2}+\frac{\sigma\left(\Gamma(1/\beta)\right)}{\Gamma(1/\beta)^2}} \\ &= T_{1,\mathrm{av}}\sqrt{\frac{\beta}{T}\sqrt{\frac{\sigma(T)}{T^2}+\frac{\sigma(\beta)}{\beta^2}}+\frac{\sigma\left(\Gamma(1/\beta)\right)}{\Gamma(1/\beta)^2}}\end{aligned} \tag{3.35}$$

using common rules of propagation of uncertainty. For simplicity, the error on $\Gamma(x)$ is calculated as

$$\sigma\left(\Gamma(x)\right) = \frac{1}{2}\left(\left|\Gamma\left(x\right) - \Gamma\left(x - \sigma\left(x\right)\right)\right| + \left|\Gamma\left(x\right) - \Gamma\left(x + \sigma\left(x\right)\right)\right|\right), \tag{3.36}$$

yielding

$$\sigma\left(\Gamma(1/\beta)\right) = \frac{1}{2}\left(\left|\Gamma\left(1/\beta\right) - \Gamma\left(\frac{\beta - \sigma(\beta)}{\beta^2}\right)\right| + \left|\Gamma\left(1/\beta\right) - \Gamma\left(\frac{\beta + \sigma(\beta)}{\beta^2}\right)\right|\right). \tag{3.37}$$

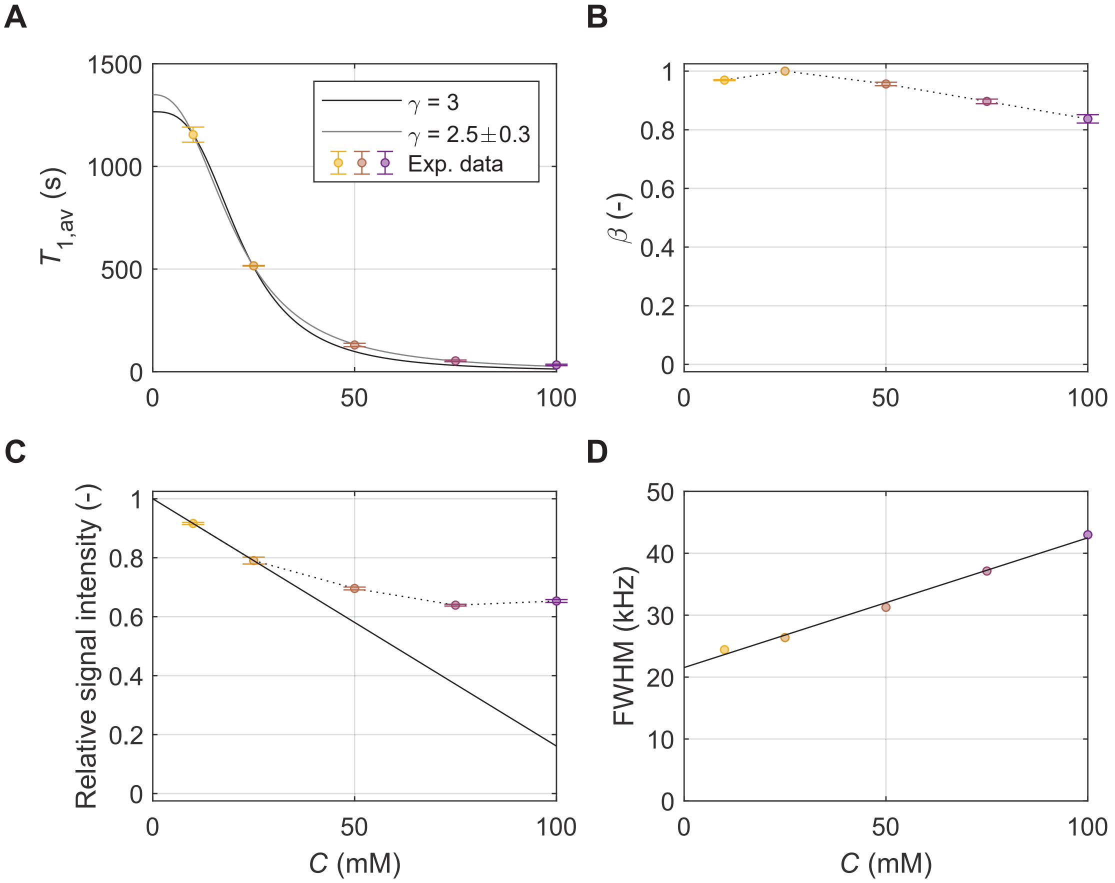

Figure 3.20: **A.** Average spin-lattice relaxation time constant of DNP juice as a function of radical concentration at 3.8 K shown as colored dots, obtained by fitting Eq. 3.33 to the data of Fig. 3.19 (converted from T_1 to $T_{1,av}$ using Eq. 3.34). The black and gray lines correspond to the model of Eq. 3.42 and Eq. 3.42 with $\gamma = 3$ and with γ left as a free parameter, respectively. **B-C.** β coefficient and intensity at $t \to \infty$, respectively, obtained from the same fit as on Panel A. The black line on Panel C is a linear regression of the first two points of the curve. **D.** FWMH of the thermal equilibrium signal as a function of radical concentration, obtained using Topspin's build-in function *hwcal*. The colored dots and the black line are the experimental data points and the linear regression, respectively.

The results of the fits are summarized in Fig. 3.20. The average relaxation time constant spreads over orders of magnitude as the radical concentration is increased from 10 to 100 mM of

TEMPOL (see Fig. 3.20A). A rough fit function can be obtained assuming that the relaxation consists of a diamagnetic term $T_{1,dia}$ which does not depend on the radical concentration, and a paramagnetic term $T_{1,para}$ which depends on the radical concentration C

$$\frac{1}{T_1} = \frac{1}{T_{1,dia}} + \frac{1}{T_{1,para}}. \tag{3.38}$$

In the previous chapter, we have derived an expression for the paramagnetic relaxation rate constant (see Eq. 2.159). Dropping all variables which do not depend on the radical concentration, we get

$$\frac{1}{T_{1,para}} \propto \frac{1}{r^6}\frac{1}{\tau_c}. \tag{3.39}$$

This relaxation rate is valid for a nucleus interacting with an electron spin but does not take spin diffusion into account. In reality, bulk relaxation is the sum of two processes: the direct relaxation caused by the electron and spin diffusion which communicates the effect of the electron spin to the bulk. Assuming in first approximation that nuclear spin diffusion is independent of radical concentration and that the bulk relaxation is not limited by spin diffusion, we get that the distance between a nucleus and the closest electron is simply $\propto 1/C^{1/3}$ and so $1/r^6 \propto C^2$. This assumption corresponds to Jeffries' model of "spheres-of-influence", which will be described in Chapter 5. [147, 13, 148] Furthermore, we assume that the inverse of the correlation time of the electron spin state is proportional to the electron-electron dipolar interaction D_{ee}. The dipolar interaction is proportional to the inverse cube of the distance between the electron spins r_{ee}, which is, in turn, proportional to the radical concentration (see Eq. 2.161)

$$\frac{1}{\tau_c} \propto D_{ee} \propto \frac{1}{r_{ee}^3} \propto C. \tag{3.40}$$

Plugging these two assumptions into Eq. 3.39, we get

$$\frac{1}{T_{1,para}} \propto C^2 C = C^3 \tag{3.41}$$

and hence an expression for the total relaxation time constant

$$T_{1,av} = \left(a + bC^3\right)^{-1} \tag{3.42}$$

This function was fitted to the data of Fig. 3.20A. This very simple model is in clear disagreement at high radical concentration (note that if the function is fitted to the rate constant instead of to the time constants, then the model is in disagreement with the rates at low radical concentration). This is not surprising since the β coefficient is significantly different from 1 for most radical concentrations and is not constant over the range of radical concentrations (see Fig. 3.20B). A possible explanation is that the observed relaxation is limited by the relaxing power of the electron spins at low radical concentration (causing $\beta \approx 1$) and, as the radical concentration is increased, the electron spins are able to relax the nuclei more efficiently, on a time scale which becomes comparable to that of spin diffusion (causing $\beta \ll 1$). In addition, a fit function where the exponent γ is let free

$$T_{1,av} = \left(a + bC^{\gamma}\right)^{-1} \tag{3.43}$$

is shown in light gray. Fitting this functions leads to $\gamma = 2.5 \pm 0.3$.

The signal intensity extrapolated to $t \to \infty$ as a function of the radical concentration is shown on Fig. 3.20C. Increasing the radical concentration causes an important signal loss, an effect known as bleaching. [149] The bleaching is the result of the decrease in the transverse relaxation time T_2 of the nucleus under the influence of the electron spin fluctuations. When the nuclear T_2 becomes comparable to the spectrometer dead time (delay between the pulse and the acquisition), the nuclei stop contributing to the measured NMR signal. Increasing the radical concentration decreases the distance between a nucleus and the closest electron spin and hence increases the bleaching. Furthermore, paramagnetic interaction with the radical may cause the frequency of the nuclei to be shifted outside the detection range of the NMR coil (see Sec. 5.2.3). Assuming that, at low radical concentration, the signal is proportional to the concentration, the signal intensity at the two lowest concentrations was fitted with a straight line, shown in black in Fig. 3.20C and the curve was rescaled so that the linear regression intercepts the y-axis at 1.

Fig. 3.20 shows the FWMH of the ^{1}H thermal equilibrium signal as a function of radical concentration, obtained using Topspin's build-in function *hwcal*. The data points are reasonably well fitted by a straight line (in black). This suggests that the primary source of broadening is the increased paramagnetic shift of the nuclei, which is proportional to the radical concentration. Another possible source of broadening of the NMR signal would be a decrease in nuclear spin-spin relaxation time constant T_2^* upon increasing radical concentration. However, this mechanism would have a more complex dependence on radical concentration.

3.3.2 μw spectra of DNP juice

We now show μw spectra for DNP juice doped with 50 and 75 mM TEMPOL and 500 mM [1-^{13}C]-acetate at 7.05 T and at 1.6, 2.9, 3.0, and 3.8 K. By recording precise μw spectra as a function of temperature and radical concentration, we aim at building a data set to test models such as Kundu *et al.*'s iCE model [133] and Jannin *et al.*'s extended spin temperature model. [146] This project was originally a collaboration with Prof. S. Vega, who sadly passed away in 2021. I would like to dedicate this work on DNP mechanisms to his memory.

DNP in these conditions is known to be more efficient when the μw frequency is modulated around the central frequency. [48] However, frequency modulation modifies the appearance of the μw spectrum, acting as a moving average. Therefore, we chose to use a fixed μw frequency for all experiments. For each μw frequency, the DNP build-up was recorded in a time-resolved manner until the DNP plateau (see example in Fig. 3.21). Without frequency modulation, DNP is slow if a TEMPOL concentration of 25 mM is used, [48] which motivated our choice to work with radical concentrations of 50 and 75 mM. DNP build-ups were recorded for both samples, at each temperature and at 29 μw frequencies between 197'160 and 198'660 MHz in steps of 50 MHz. Each build-up was launched as a single pseudo-2D experiment *via* Topspin's spooler. The list of μw frequencies was generated by a MATLAB script together with the associated start time of the buildup experiments and fed to the task scheduler of the AlphaController (see Fig. 3.3), so that it would change the μw frequency during the saturation block at the start of each build-up experiment. This allowed us to run such experiments overnight.

Fig. 3.21 shows an example of raw results of the DNP spectrum for 50 mM TEMPOL at 1.6 K, consisting of a series of DNP build-up curves (shown as colored lines). This particular μw spectrum was recorded in ≈ 8.5 hours and was the longest of the data set. Each DNP build-up is fitted with a stretched exponential function of the form of Eq. 3.33 (shown as black lines in Fig. 3.21).

Fig. 3.22A-B show the polarization at the end of each build-up (i.e., the maximum recorded polarization) for both samples and each temperature, as colored dots. The colored lines are spline interpolations of the data points. The polarization at the end of the build-up corresponds to the polarization at DNP equilibrium (i.e., when $t \to \infty$) to a very good approximation, at least near the center of the μw spectrum. However, on the edges (for offset frequencies above +300 and below -300 MHz), the DNP build-up time gets exceedingly large and so the maximum measured

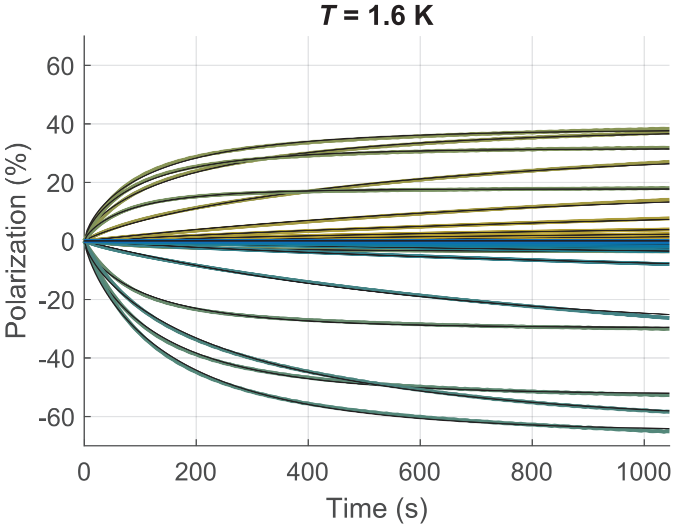

Figure 3.21: Raw results of the μw spectrum for 50 mM TEMPOL in DNP juice at 1.6 K, consisting of a series of DNP build-up curves for various μw frequencies. The measured polarization along time is fitted with a stretched exponential curve (see Eq. 3.33), represented by colored and black curves, respectively.

polarization might be slightly lower than the polarization at equilibrium. We chose to display the maximum polarization rather than the extrapolated polarization at equilibrium because the latter is noisier and introduces a bias, which complicates the interpretation.

Both for the sample with 50 and 75 mM TEMPOL, the maximum absolute DNP polarization is higher for negative DNP than for positive DNP. This is at least partially due to RD, which leads to an underestimation and an overestimation of positive and negative polarizations, respectively. [121] In addition, it is possible that negative DNP is fundamentally more efficient than positive DNP. [146] The best polarization values are obtained, as expected, for the lowest temperature. For the sample with 50 mM, the best positive and negative polarization are $P_{\mathrm{DNP}}^{\mathrm{max+}} \approx 38\%$ and $P_{\mathrm{DNP}}^{\mathrm{max\text{-}}} \approx -65\%$, respectively. For the sample with 75 mM, the best positive and negative polarization are $P_{\mathrm{DNP}}^{\mathrm{max+}} \approx 34\%$ and $P_{\mathrm{DNP}}^{\mathrm{max\text{-}}} \approx -58\%$, respectively. To verify whether negative DNP is indeed more efficient than positive DNP in our conditions, the μw spectra were also recorded indirectly through the ^{13}C spins by performing a single CP detection at the end of the ^{1}H DNP build-up. The ^{13}C signal under negative DNP is $\approx 20\%$ larger than that under positive DNP, confirming that negative DNP is more efficient.

The obtained polarization values are surprising since we commonly expect polarization on the order of $> 70\%$ for a sample of 50 mM TEMPOL in these conditions. [121, 68] This is unfortunately likely due to an improper thermal equilibrium quantification. This causes the absolute values of polarization to be biased.

Fig. 3.22C-D and E-F show the fitted stretched coefficient β and the average relaxation rate constants $R_{\mathrm{DNP,av}}$, respectively. The DNP rate increases with temperature and is faster near the center of the μw spectrum. This is expected since, as the μw frequency gets further from the DNP optimum, the build-up rate gets closer and closer to $R_1 \ll R_{\mathrm{DNP}}$. Interestingly, in all cases, the rates feature a dip near the center of the spectrum, which we cannot rationalize for the time being.

The stretched coefficient gets closer to 1 on the edges of the μw spectra, indicating that the build-ups get closer to a monoexponential. A possible explanation is that two processes are competing. The two competing processes could be triple spin flips and spin diffusion from nuclear spins

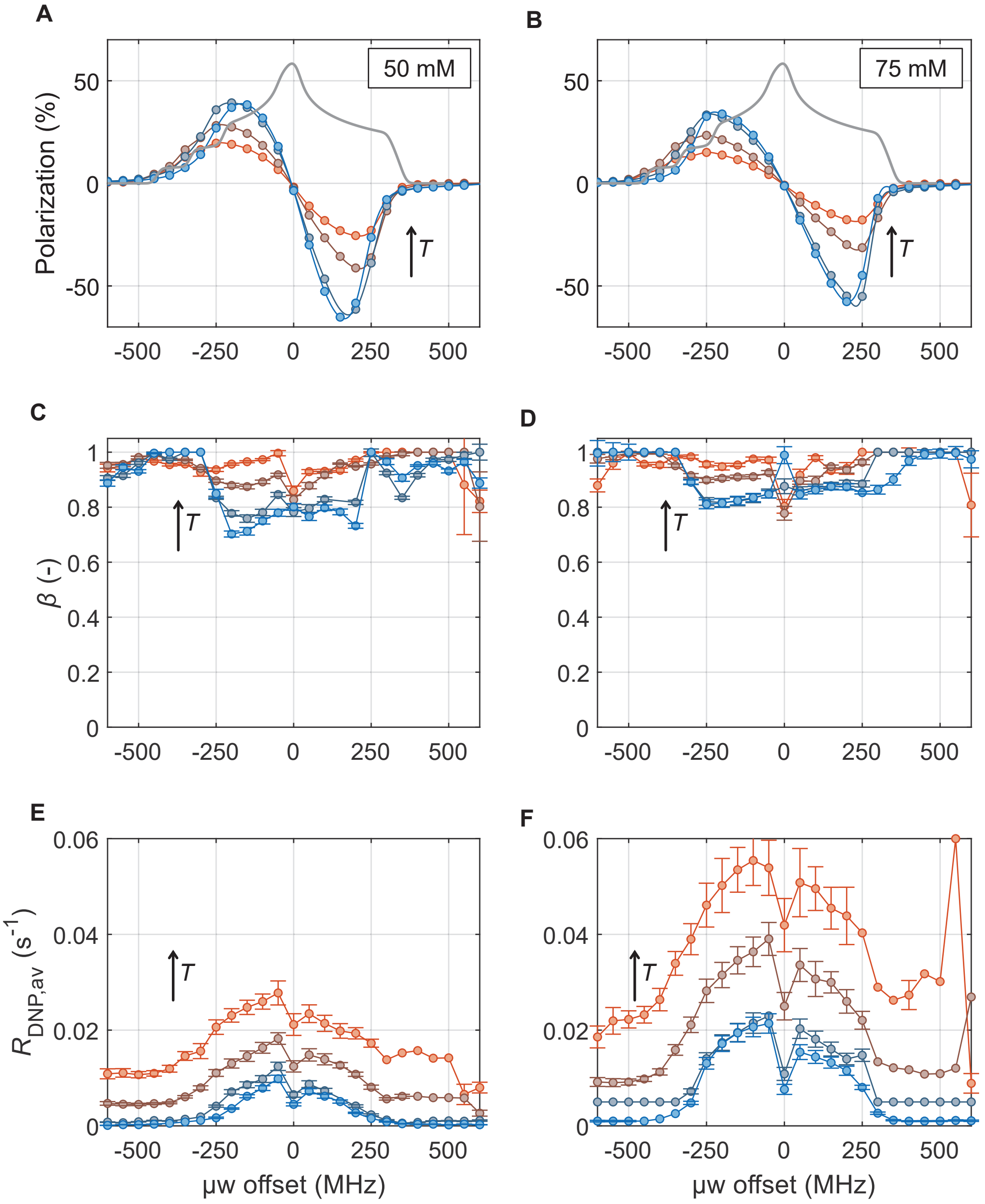

Figure 3.22: **A-B.** μw spectra at 1.6, 2.9, 3.0, and 3.8 K for DNP juice doped with 50 and 75 mM TEMPOL, respectively. The maximum recorded polarization is shown as colored points together with a spline interpolation (colored lines). The simulated spectrum of TEMPOL is shown for comparison as a gray line, using the same simulation parameters as in Fig. 3.17. **C-D.** Corresponding fitted values of β coefficient **E-F.** Corresponding values of $R_{\mathrm{DNP,av}}$ obtained from the fitted values using Eq. 3.34.

near the electron spin to those further away. It will be shown in Chapter 5 that spin diffusion is quenched at high electron polarization and therefore at lower temperature and in the absence of μw irradiation. Similarly, the triple spin-flip rate gets quenched at high electron polarization and therefore at lower temperature and in the absence of μw irradiation. [101, 67] The fact that the β coefficient is nearly flat at 3.8 K could indicate that one of these mechanisms is dominating and one is limiting. On the contrary, at 1.6 K, the lower β coefficient near the center of the μw spectrum could indicate that the spin diffusion rate and the triple spin-flip rate are on the same order of magnitude while one of them takes over on the edges.

3.3.3 The effect of temperature and radical concentration

Fig. 3.23A-B shows the optimum μw frequencies for positive and negative DNP (indicated by ω_+ and ω_-, respectively) and the difference $\Delta\omega$ between them, respectively, as a function of temperature. The positions of the extrema were computed from the spline interpolation in Fig. 3.22A-B. $\Delta\omega$ is larger for the sample with 75 mM TEMPOL than that with 50 mM ($\approx$ 1.3 larger at 1.6 K). Moreover, it increases with temperature and is larger than the nuclear Larmor frequency (shown as a horizontal dashed line) in all cases.

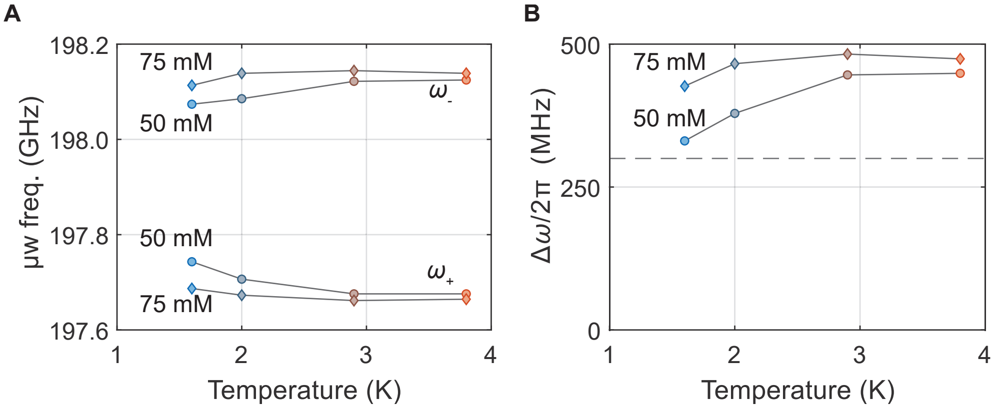

Figure 3.23: **A.** Optimal frequency for negative and positive DNP as a function of temperature, computed from the spline interpolation in Fig. 3.22A-B. **B.** Difference between the optima shown in Panel A. The ^{1}H Larmor frequency is shown as a horizontal dashed line.

The larger values of $\Delta\omega$ for the sample with 75 mM (see Fig. 3.23B) are probably the result of stronger spectral diffusion, which spreads the saturation from further on the edges of the EPR line. If efficient spectral diffusion is a necessary condition for TM-DNP, CE-DNP is not insensitive to spectral diffusion either, because the shape of the hole burnt by μw irradiation depends on the interplay between the strength and frequency of the μw, the efficiency of spectral diffusion and electron spin-lattice relaxation (see Sec. 3.2.2). Therefore, the fact that the DNP mechanism at play in our sample is sensitive to the efficiency of spectral diffusion is not in itself a proof that this mechanism is TM rather than CE (or iCE).

From Wenckebach's Eq. 3.29, we know that CE takes place when there exist electron spins whose difference in frequencies matches the nuclear Larmor frequency $|\omega_{0\mathrm{S}2} - \omega_{0\mathrm{S}1}| = |\omega_\mathrm{I}|$, while TM takes place when there exist electron spins whose mutual dipolar interaction matches the nuclear Larmor frequency $|D_0| = |\omega_\mathrm{I}|$. [60, 106] The change in radical concentration does not affect the electron frequencies $\omega_{0\mathrm{S}k}$ and so it does not affect the probability of finding electron spins fulfilling the CE matching conditions. On the contrary, the change in radical concentration changes the values of D_0 between electron spins. In a sample of 50 mM, the distance between an electron and its nearest neighbor is on average $\approx \Gamma(4/3)(4\pi N_A C/3)^{-1/3} \approx 1.8$ nm, [150] where Γ, N_A and C are the gamma function, the Avogadro number, and the electron spin concentration, respectively. At this distance, D_0 is on the order of ≈ 9 MHz $\ll \omega_\mathrm{I}$. Therefore, most electron spins do not have sufficient dipolar couplings with their neighbors to fulfill the TM matching conditions and so increasing the electron concentration increases the probability to find electron spins fulfilling the TM matching condition. [60]

Finally, we note that $\Delta\omega$ is strongly affected by temperature, especially for the sample with 50 mM TEMPOL. If TM were indeed the mechanism operating at the lowest temperature, a tempting explanation for increasing efficiency of TM at lower temperatures would be the following. The lower the temperature, the longer T_{1e} which allows spectral diffusion to spread the effect of μw across the entire EPR line more efficiently hence establishing a homogeneous spin temperature in the NZ electron reservoir. This in turn would give more favorable conditions for TM-DNP.

Kundu *et al.* found that iCE gave a satisfactory account of DNP on similar samples to ours between 10 and 40 K at 3.34 T. [132] Jannin *et al.* found that the extended spin temperature model gave a satisfactory account of DNP at 1.2 K and at magnetic fields of 3.35 and 5 T but they did not study the temperature dependence of the DNP mechanisms. [146] Analyzing our data at 7.05 T using both models might possibly reveal a cross-over from TM to CE as temperature increases.

3.4 DNP on conductive polymers

The previous section presented DNP results on very common samples for DNP experiments, namely DNP juice doped with TEMPOL. We now turn to a more unusual sample of PANI, an organic conductive polymer that has been known for more than 150 years and has been extensively studied since the seventies. [151] Following Overhauser's original idea of performing DNP on conductive metals, [7, 8] it seems natural to try DNP on conductive polymers. Our interest in PANI in particular comes from recent discoveries that unpaired electrons in chiral PANI (cPANI) can be polarized by flowing an electric current through the polymer, [152] an effect known as current induced spin selectivity (CISS). [153] DNP on cPANI could potentially reach high nuclear polarization relying on high electron polarization achieved by a preceding hyperpolarization step by CISS rather than by Boltzmann equilibrium at high magnetic field and low temperature. This would therefore alleviate the need for liquid helium. Furthermore, PANI can be prepared to be highly porous, [154, 155] which would allow one to polarize arbitrary solutions within the pore of the material, as has already been exploited for a number of polarizing matrices. [54, 57, 156]

In this section, we present a proof of principle that DNP is possible in PANI polymers at 1.6 K and 7.05 T. We first show a method to control the unpaired electron spin concentration in PANI starting from commercially available products, by immersion of PANI (as a powder) in an acid solution followed by lyophilization. Then, we characterized in detail the temperature dependence of the signal intensity and of the spin-lattice relaxation rate of ^{1}H spins in one of the samples. We found that the thermal equilibrium signal intensity does not follow the expected $1/T$ trend of Boltzmann's law, where T is the temperature. We also found very fast relaxation with $T_1 \approx 40$ s at 1.6 K (while the T_1 of ^{1}H spins in DNP juice with 50 mM TEMPOL is on the order of an hour). Both these facts can be attributed to the motion of conduction electrons. Finally, we present μw spectra at various electron concentrations at 1.6 K. If we only found relatively low ^{1}H polarization of $\approx 3\%$, our results show a surprisingly complex behavior of PANI under DNP. At the lowest radical concentration, the μw spectra exhibit a narrow absorption-like pattern in the center of the spectrum, reminiscent of recently reported cases. [157, 158, 159] As the radical concentration is increased, the negative lobe of the absorption-like pattern increases until it reaches a negative desorption-like pattern. TM and OE are speculated to be responsible for this behavior, although the details of their interplay remain unclear. In addition, a weak SE is observed at low radical concentration.

The results presented in this section are unpublished.

3.4.1 Tuning the radical concentration

There exist several forms of PANI. We will be concerned with two of them, the emeraldine base and salt, (PANI-EB and PANI-ES, respectively), as shown in Fig. 3.24. Both are commercially available at various molecular weights. In principle, PANI-EB contains no unpaired electrons, while PANI-ES contains two unpaired electrons per repeat unit. PANI-EB can be converted into PANI-ES by protonating the two imine groups present in each unit. The additions of the two protons allow the unit to rearrange into a more favorable aromatic electronic configuration. As can be seen from the structure in Fig. 3.24B, all four amine positions of PANI-ES are equivalent. Furthermore, they are connected by π-conjugation through benzene rings and amine groups. The unpaired electrons can therefore move from one position to the next by mesomery, which is at the origin of the conductivity of PANI-ES. This is verified experimentally by the fact that the conductivity of PANI increases upon conversion from EB to ES. [151, 160]

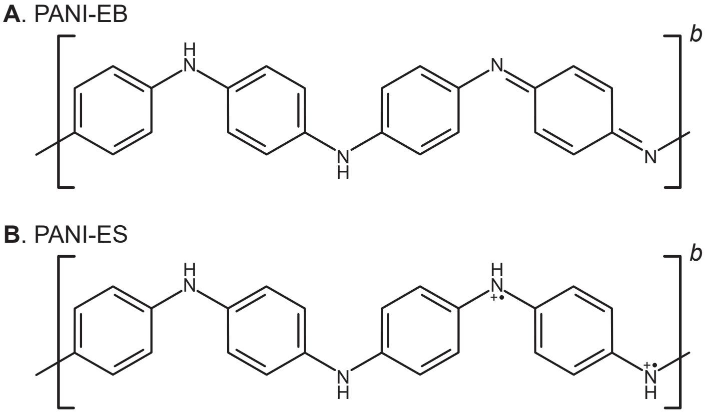

Figure 3.24: **A-B.** Chemical structures of the repeat units of the polymers PANI-EB and PANI-ES, respectively.

We prepared eleven samples of PANI with various expected levels of conversion from PANI-EB to PANI-ES. We used a protocol inspired by Ref. [160] which consisted of immersing $m_{EB} = 100$ mg of commercial PANI-EB into $V = 7$ mL of a solution of HCl in D_2O with a chosen pH. In order to reach the desired level of conversion

$$\chi = \frac{n_{ES}}{n_{EB} + n_{ES}}, \tag{3.44}$$

where n_{EB} and n_{ES} are the number of moles of PANI-EB and PANI-ES, respectively, the solution of HCl was prepared so as to contain

$$n_{HCl} = 2\chi n_{EB} = 2\chi \frac{m_{EB}}{M_W} \tag{3.45}$$

moles of HCl, where $M_W = 362.46$ g.mol^{-1} is the molecular weight of a single unit of PANI-EB. A stock solution of HCl in D_2O with pH = 1 was prepared and mixed with pure D_2O in the appropriate ratio to reach the desired values of χ from 0 to 1. The calculated final pH of the solution prior to adding the powder ranged between 2.10 and 1.11 for $\chi = 0.1$ and 1.0, respectively. For $\chi = 0$, the solution was immersed in pure D_2O.

The powders were left in the acidic solution for two days to allow the protons to migrate inside the polymer and were subsequently lyophilized in liquid nitrogen under vacuum at 10^{-2} mbar. Spin counting by X-band EPR was performed on the powders at room temperature by Guillaume

Verhaeghe (a Master student in our group) and my colleague Théo El Daraï. The results are shown in Fig. 3.25A. The radical concentration increases from ≈ 20 to ≈ 320 μmol.g^{-1} for $\chi = 0$ to $\chi = 1$, respectively. The maximum concentration is about an order of magnitude lower than expected. On the contrary, a null radical concentration was expected for $\chi = 0$. The presence of electron spins in the sample with $\chi = 0$ observed by EPR was confirmed by DNP measurements (see below). It can be attributed to the imperfect drying of the powder, which would cause moisture to protonate the imine groups to a small extent.

Fig. 3.25B and C show the behavior of the ^{1}H spins in PANI at 1.6 K and 7.05 T as a function of the radical concentration determined by EPR. The average ^{1}H relaxation rate of PANI increases with χ as well as the FWHM of the signal, which is the result of increasing electron-nucleus interactions.

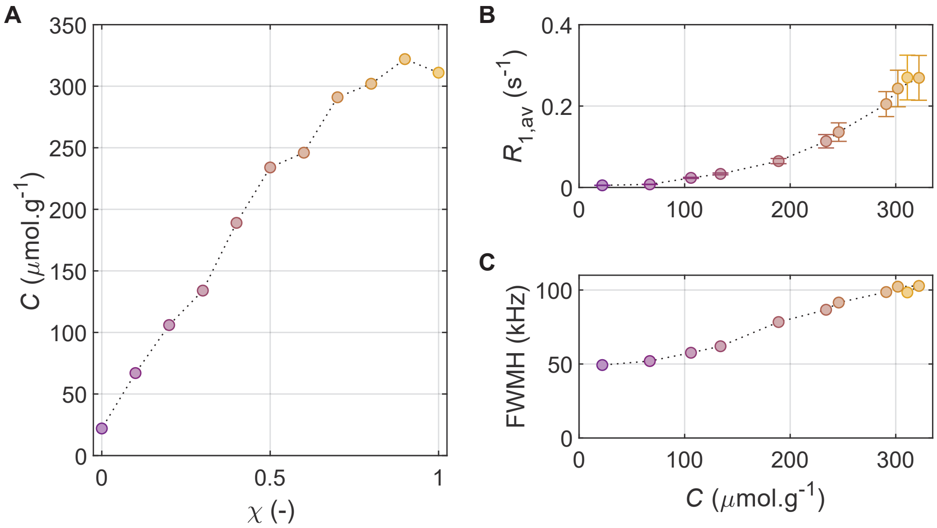

Figure 3.25: **A.** Electron spin concentration of PANI samples as a function of the protonation ratio χ, determined by X-band EPR at room temperature. **B-C.** Average relaxation rate obtained by fitting a stretched exponential (see Eq. 3.33) to the ^{1}H thermal equilibrium build-ups and FWHM of the ^{1}H signal of the same samples at thermal equilibrium at 1.6 K, respectively, as a function of the electron spin concentration shown in Panel A.

3.4.2 Unusual behavior at thermal equilibrium

Working with PANI samples, we noticed that the probe resonance frequency was moving significantly from sample to sample, much more than we usually observe on common samples. This made us suspect that conduction electrons in PANI could absorb rf waves and affect the Q-factor of the coil and in turn the signal intensity. We asked ourselves whether this could be temperature-dependent. One of our usual assumptions is that the signal intensity at thermal equilibrium is proportional to $1/T$, where T is the temperature. This assumption allows us to quantify polarization by recording a thermal equilibrium signal at a higher temperature than that where we perform DNP, i.e., 1.2-1.6 K (see Sec. 3.1.3 and 3.1.4). The reason for this choice is that thermal relaxation in DNP juice is prohibitively slow below 2 K.

In order to verify whether this holds for PANI, we recorded the Q-factor of the coil and the thermal equilibrium signal for the sample with $\chi = 0.2$ at nineteen temperatures between 1.6 and 4.3 K. We did not find a significant change in the Q-factor (not shown). The signal build-ups are shown in Fig. 3.26A. They were fitted with a stretched exponential function (see Eq. 3.33). As shown in Fig. 3.26B, the signal intensity increases monotonically but does not correlate with $1/T$.

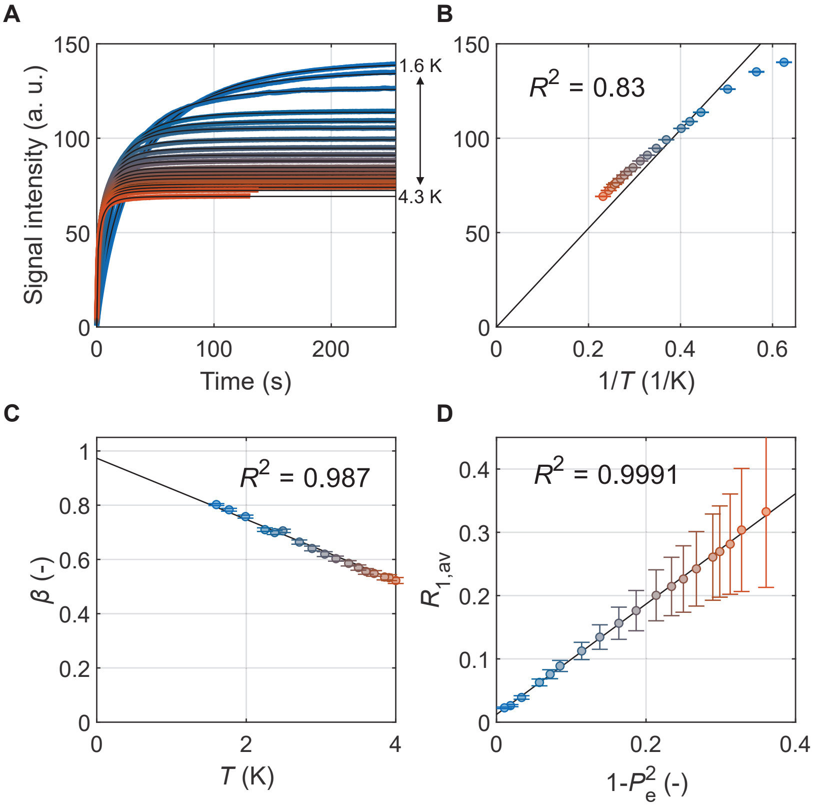

Figure 3.26: **A.** ^{1}H thermal equilibrium build-ups for 28.3 mg of PANI with $\chi = 0.2$ at 7.05 T between 1.6 and 4.3 K recorded with 1° pulses. The colored and black curves represent the experimental signal intensity over time and stretched exponential fit (see Eq. 3.33), respectively. **B.** Fitted thermal equilibrium signal intensity obtained from Panel A showed as colored dots as a function of $1/T$. The black line is a linear regression of the points (forced to go through 0). **C-D.** Fitted β coefficient and average relaxation rate (obtained from the fit using Eq. 3.34) as a function of temperature, respectively. The colored dots are the values obtained from Panel A and black lines are linear regressions with free y-intercept.

The relaxation parameters β and $R_{1,\mathrm{av}}$ show interesting correlations with temperature. We found empirically that the β coefficient correlate linearly with temperature (see Fig. 3.26C) and that the extrapolated value at $T = 0$ K is $\beta \approx 0.97 \pm 0.02$, very close to 1. A β coefficient different from 1 is the sign of the coexistence of distinct mechanisms contributing to relaxation with comparable rates or with a distribution of such rates. The fact that $\beta \to 1$ when $T \to 0$ indicates that relaxation tends to be limited by a single mechanism as temperature decreases, or at least towards a single rate.

We also found a correlation between the average relaxation rate $R_{1,\mathrm{av}}$ (obtained from the stretched exponential fit using Eq. 3.34) with $1 - P_e^2$, where P_e is the Boltzmann polarization of the electron. As will be detailed in Sec. 4.1, this correlation is expected to hold if the relaxation rate has the form

$$R_1 = R_{1,a} + (1 - P_e^2)R_{1,b}^0, \tag{3.46}$$

where the first and second terms are relaxation rates that do not and do depend on the electron polarization, respectively. The perfect fit of Eq. 3.46 to the measured relaxation rate shows that $R_{1,a}$ does not depend on the polarization of the electron and on temperature. We found $R_{1,a} \approx 0.012 \pm 0.003$ s^{-1} and $R^0_{1,b} \approx 0.87 \pm 0.01$ s^{-1}, while in DNP juice doped with 50 mM TEMPOL, we found $R_{1,a} < 10^{-4}$ s^{-1} and $R^0_{1,b} \approx 0.0076 \pm 0.0007$ s^{-1}. The PANI sample with $\chi = 0.2$ has a radical concentration on the order of ≈ 100 μmol.g^{-1}, which is about twice the concentration of a sample with 50 mM TEMPOL.

The fact that both $R_{1,a}$ and $R^0_{1,b}$ are two orders of magnitude higher in PANI with $\chi = 0.2$ than in DNP juice with 50 mM TEMPOL gives a clear indication that the mobility of the electron spins plays a role in nuclear relaxation in PANI. In DNP juice doped with TEMPOL, $R_{1,a}$ is a term representing diamagnetic relaxation (i.e., it is electron-independent). Indeed, because TEMPOL electron spins are fixed in space in DNP juice, they can only make nuclei relax by flip-flops [161] and the corresponding term bears the $1 - P_e^2$ dependence. [48] The fact that $R_{1,a}$ in PANI is two orders of magnitude higher than in DNP juice with 50 mM TEMPOL suggests that the translational motion of the electron spins causes nuclear relaxation. [162, 163] In turn, the fact that $R_{1,a}$ is found to be temperature-independent implies that temperature does not influence the electron mobility and hence the conductivity in PANI, which is consistent with the Q-factor of the probe being independent of temperature.

As for $R^0_{1,b}$, it is also found to be two orders of magnitude higher in PANI. The difference in electron concentration can hardly explain such a stark difference. Both in PANI and TEMPOL doped DNP juice, electron flip-flops are expected to cause nuclear relaxation with a $1 - P_e^2$ dependence. However, an important difference in the case of PANI, is that the motion of the electron potentially allows it to relax nuclear spins *via* flip-flops on a much wider spatial range than if they were fixed as in insulating solids. The role of nuclear spin diffusion in relaying electron-induced relaxation would therefore be weaker in PANI than in DNP juice.

3.4.3 μw spectra on PANI

We recorded μw spectra for all eleven samples at 1.6 K and 7.05 T with a separation of 25 MHz between μw frequencies, using a procedure similar to that presented in Sec. 3.3.2. Again, we did not use frequency modulation. However, we chose to record the full μw in a single pseudo-2D experiment (which should perhaps be called a pseudo-pseudo-3D experiment). This ensures easier synchronization of the μw frequency and the NMR experiment, controlled separately by the AlphaController and TopSpin, respectively. Because of the fast relaxation in PANI, the longest μw spectrum could be recorded in ≈ 3.3 hours for 40 μw frequencies as compared to ≈ 8.5 hours for 29 frequencies for DNP juice with 50 mM TEMPOL. Based on the observation that the ^{1}H signal of PANI is not linear with $1/T$ and that ^{1}H relaxation is so fast, we chose to record thermal equilibrium signals at the same temperature as that of DNP experiments, i.e., 1.6 K, in order not to introduce a biais in the polarization quantification. Contrary to the case of DNP juice, this is affordable since the relaxation of PANI are high even at low radical concentration and low temperatures.

Fig. 3.27 shows the resulting μw spectra for $0 \leq \chi \leq 0.8$, expressed in terms of maximum recorded polarization (and not in terms of extrapolated polarization for $t \to \infty$) as a function of the μw frequency offset with respect to 197'630 MHz. The spectra for $\chi > 0.8$ are not shown because they are flat (as that for $\chi = 0.8$). The horizontal dashed line corresponds to the Boltzmann equilibrium polarization of ^{1}H spins at 1.6 K, $P_{eq} \approx 0.45\%$.

For samples with $0.2 \leq \chi \leq 0.3$, peaks of ZQ-SE and DQ-SE are clearly visible at $+300$ and -300 MHz, respectively, although weak. A stronger narrow pattern is present at the center of the μw spectra for $0 \leq \chi \leq 0.7$. As χ increases and, hence, as the radical concentration and the conductivity of the polymer increases, this spectral pattern evolves smoothly from an absorption-

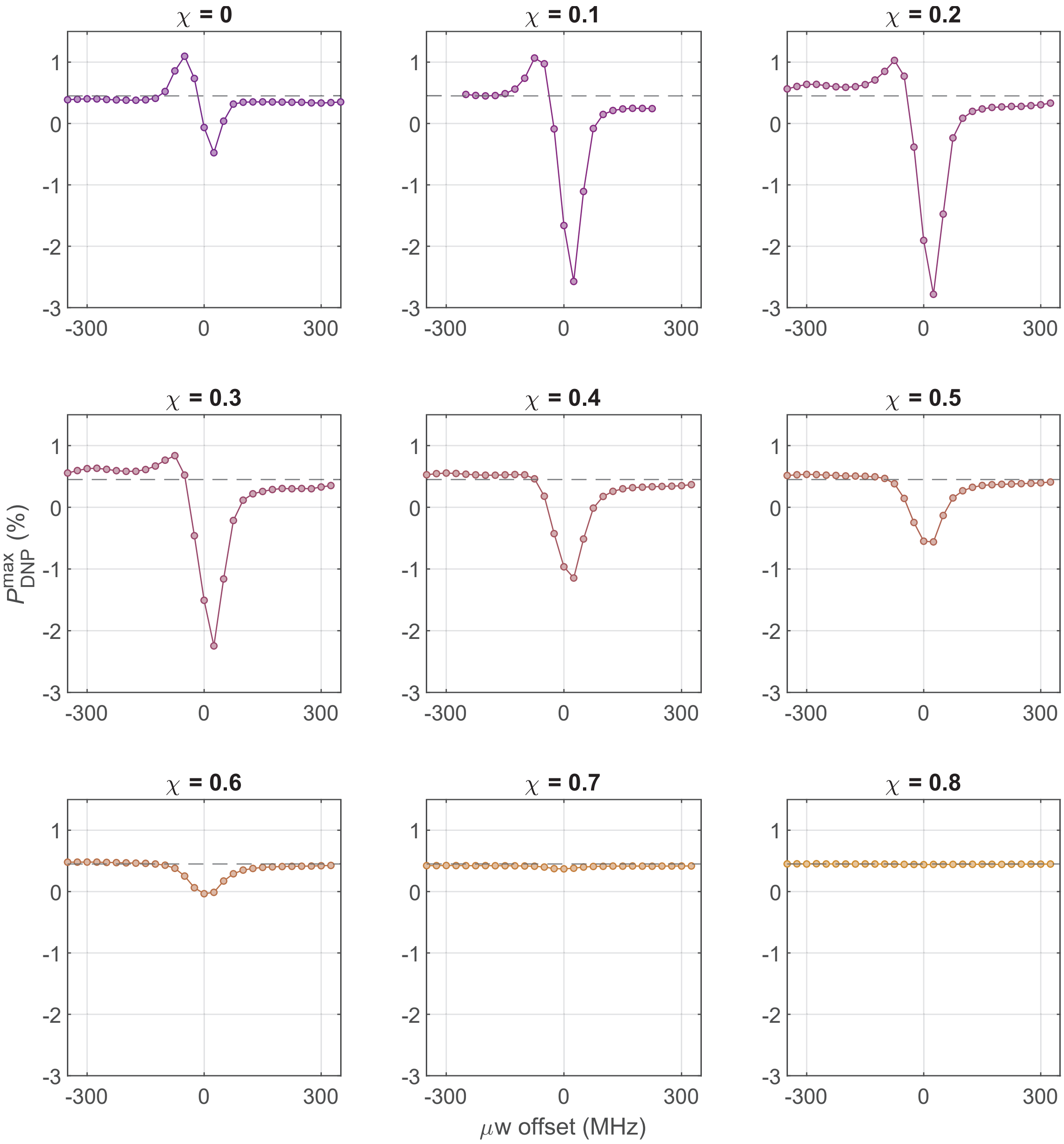

Figure 3.27: μw spectra for PANI with various values of expected conversion χ from EB to ES, for $\approx$ 30 mg of sample at 1.6 K. The horizontal dashed line corresponds to the Boltzmann equilibrium polarization of ^{1}H spins $P_{eq} \approx 0.45\%$.

like signal with a lower frequency positive lobe and higher frequency negative lobe separated by $\approx$ 100 MHz to a negative dispersion-like peak with a width of $\approx$ 125 MHz. Along the transition from one pattern to the other, the negative lobe increases while the positive lobe decreases until the dispersion-like peak is reached.

The best performing sample, i.e., that with $\chi = 0.2$, was investigated in further detail. A broader μw spectrum was recorded to verify that it does decay towards the thermal equilibrium polarization on the edges. Fig. 3.28A shows that the μw spectrum does reach the ^{1}H Boltzmann polarization for offset frequencies larger than ±400 MHz. The build-ups for all frequencies were fitted with a stretched exponential model (see Eq. 3.33). The average time and rate constants obtained from the fitted parameters using Eq. 3.34 and the fitted β coefficient are shown in Fig. 3.28B-D, respectively.

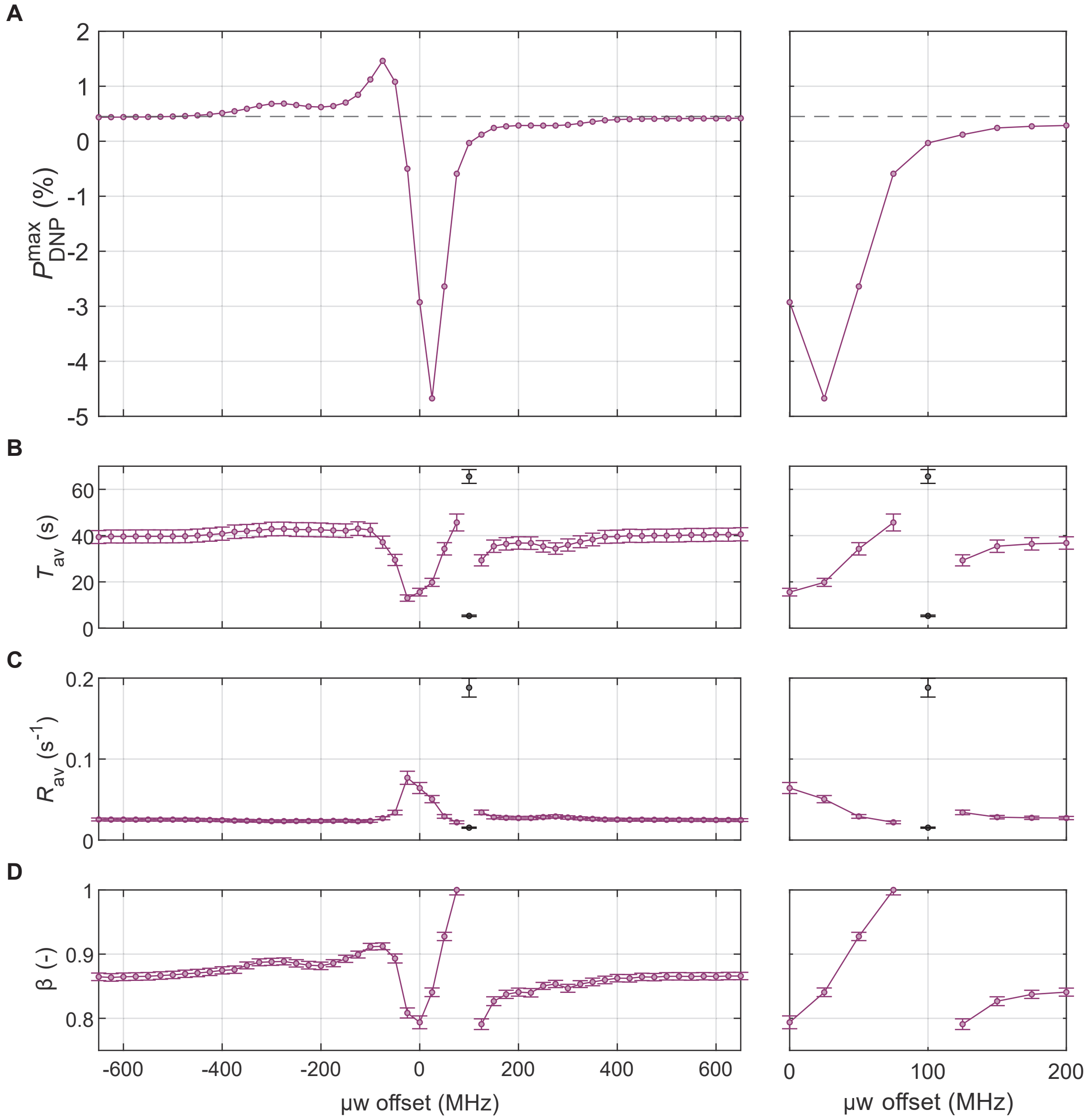

Figure 3.28: **A.** μw spectrum of PANI with $\chi = 0.2$ on a broad range of μw frequencies. **B-C.** Average build-up time and rate constant T_{av} and R_{av}, respectively, obtained from the stretched exponential fit of the build-ups using Eq. 3.34. **D.** Stretched coefficient obtained by fitting the build-ups with a stretched exponential model. The build-up with μw frequency +100 MHz could not be fitted with a stretched exponential (see Fig. 3.29) and was fitted with a biexponential function instead (see Eq. 3.47 and Fig. 3.29). The fitted values of the biexponential model are shown as black dots on Panel B and C.

The build-up with a μw frequency of +100 MHz exhibits a very different behavior compared to others. As can be seen in Fig. 3.29, in this case, the polarization goes first positive on a short time scale and negative on a slower time scale. This particular curve could obviously not be fitted with a single stretched exponential. Instead, it was fitted with a biexponential function of the form

$$P(t) = P_\infty + (P_+ - P_\infty)\exp\left(-\frac{t}{T_{fast}}\right) - P_+\exp\left(-\frac{t}{T_{slow}}\right), \tag{3.47}$$

where P_∞, P_+, T_{fast} and T_{slow} are the polarization when $t \to \infty$, the polarization of the positive maximum and a fast and a slow relaxation time constant, respectively. The model curve is shown as a black line on Fig. 3.29 and the fitted time and rate constants are shown as black dots in Fig. 3.28B-C, respectively. The time and rate constant as a function of μw irradiation frequency feature a discontinuity at +100 MHz. The slow time and rate constants obtained by the biexponential fit seem to be in the continuity of the curve at increasing frequencies while the fast time and rate constants seem to be in the continuity of the curve at decreasing frequencies.

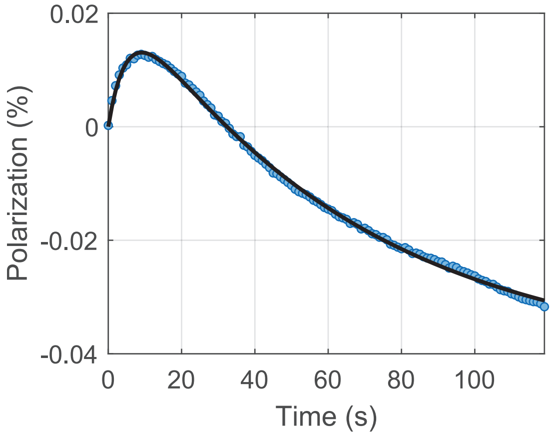

Figure 3.29: Polarization build-up of PANI with $\chi = 0.2$ under DNP with μw irradiation at 167'730 MHz (corresponding to an offset frequency of +100 MHz with respect to the reference frequency). The blue dots and the black line correspond to experimental data points and a biexponential model (see Eq. 3.47), respectively.

One may notice that the polarization on the μw spectra for PANI with $\chi = 0.2$ shown in Fig. 3.27 is higher than that in Fig. 3.28A. In the former case, the maximum absolute polarization is at $\approx -2.8\%$, while it is of $\approx -4.7\%$. The experiments were performed on samples from the same batch on different days. For the time being, it is unclear whether this difference is real or it is the result of experimental mistakes.

3.4.4 DNP mechanisms in PANI

If the signal enhancement observed in PANI with μw irradiation at +300 MHz and −300 MHz can be attributed to SE without doubt, the features at the center of the spectrum are much more difficult to explain. TM and OE are two possible mechanisms that could explain these features. [158, 157, 127, 128, 129]

The detailed analysis of the sample with $\chi = 0.2$ gives a strong hint that two distinct mechanisms operate simultaneously in PANI. Indeed, Fig. 3.29 suggests that one mechanism brings the polarization towards a positive value on a short timescale while a second mechanism pulls the polarization towards a greater negative value on a slower timescale. Note that the experiment of

Fig. 3.29 was recorded immediately after an experiment with negative DNP. The positive polarization observed in the beginning of the curve of Fig. 3.29 can therefore not be attributed to spin diffusion from negatively polarized hyperfine shifted spins (Chapter 5 is dedicated to the study of this effect).

The results of thermal relaxation in Sec. 3.4.2 give evidence that the mobility of the electrons plays a strong role in nuclear relaxation in PANI. This relaxation mechanism is related to OE; after all, the difference between OE-DNP and spin-lattice relaxation by mobile electrons is that the population of the electron-nuclear spin states under OE-DNP is modified by μw irradiation but the relaxation pathways are the same. A notable difference between OE-DNP in conductive solids and TM-DNP is that the former relies on electron mobility to modulate the hyperfine interaction, while the latter relies on electron flip-flops. The two mechanisms can occur simultaneously, albeit with different matching conditions and possibly different rates.

The efficiency of OE in PANI can be expected to depend on the protonation level χ. Indeed, electron mobility in PANI is known to increase with χ [160] and electron mobility is the mechanism at the origin of OE in conductive solids. OE-DNP usually gives rise to positive enhancement with a dispersion-like pattern at the center of the μw spectrum. Here, the dispersion-like pattern appears for high values of χ and hence for high electron mobility, which would be reasonable for OE but it is negative, which would be unusual for OE.

Increasing radical concentration commonly increases the e-e interaction strength and hence the efficiency of TM (see Sec. 3.2.3, in particular Eq. 3.29). In this regard, PANI represents a special case. When χ is small, the polymer contains mainly imines and few amines (see Fig. 3.24). Because the electrons can only freely move along amines, they are trapped as well-defined pairs located in between imines. As χ increases, the number of amines increases while the number of imines diminishes, allowing electrons to move more and more freely along the polymer, and they are no longer located as well-defined pairs. Therefore, at increasing radical concentrations, a larger number of electrons can interact but strong e-e interactions are already present even at the lowest radical concentration, providing appropriate conditions for TM.

The spectral feature of the μw spectrum for $\chi = 0$, namely an absorption-line peak, was reported by several authors recently. [158, 159] In particular, Equbal *et al.* found that this feature increases with e-e interactions for ^{1}H static DNP at 7 T and 20 K using trityl radical and postulated that TM was the mechanism at play. [158] Li *et al.* showed using numerical simulation in a model system of three electrons and one nucleus that this pattern would occur for a specific distribution of e-e couplings (5, 15, and 350 MHz) and T_{1e} values (1 μs, 5 μs, and 8 ms). [157] As discussed above, even in PANI with $\chi = 0$, strong e-e coupling are expected, which could make TM-DNP possible and explain the observed pattern. However, a distribution of T_{1e} values such as that in Li *et al.*'s simulation would be very surprising in the case of PANI and so the mechanism they simulated, at least with these values, is unlikely to explain our observations.

The interpretation of the μw spectra alone does not allow us to draw definitive conclusions regarding the DNP mechanisms operating in PANI. Simulating PANI chains by quantum chemical methods could be of interest to calculate electron-electron interactions, electron-nucleus interactions, and electron mobility. This could then be used to simulate DNP mechanisms and get deeper insights into the DNP in PANI.

3.5 Perspectives

We have presented instrumentation for DNP experimentation where most steps of the process are computer-controlled and can be automatized; refills of liquid He and the temperature of the He bath are controlled by a dedicated user interface and can be programmed with a time resolution of ≈ 2 s. μw parameters related to the frequency and relative power are controlled by the same interface with the same time resolution. The on/off status of the μw source (i.e., μw gating) is controlled by the NMR pulse sequence *via* TTL pulses, with a time resolution of hundreds of μs. The steps which require manual intervention and which still cannot be automatized are sample insertion and probe tunning.

The automation of the process has several advantages. First, it allows the operator to perform repeatable processes with known He consumption and duration. This helps minimizing the He consumption, which becomes more and more important due to the increasing price of liquid He. Second, it permits overnight operation for long experiments such as μw spectra where the μw frequency needs to be changed experiment after experiment. The time of use of the instrument is therefore increased. Furthermore, because the instrument needs to be kept cold from one day of operation to the next, performing overnight experiments also represents a better use of liquid He.

The fact that the μw frequency and relative power can only be controlled with a time resolution of ≈ 2 s makes it appropriate for recording μw spectra. However, it represents a limitation for the experiments of NMR detected EPR that will be presented in the next chapter (see Chapter 4). The same time resolution at that of the μw gating (i.e., on the order of hundreds of μs) by controlling the μw source with *via* a LabView interface receiving TTL pulses from the NMR pulse sequence.

μw spectra for DNP juice doped with 50 and 75 mM TEMPOL were recorded at four temperatures between 1.6 and 3.8 K. The DNP performance is found to increase when temperature decreases as expected but the polarization extrema are below expectations probably due to an improper quantification of the thermal equilibrium. However, this only brings a bias on the scaling of the y-axis of the μw spectra. The frequency separation between the positive and negative DNP optima was shown to increase with temperature and to be larger for the sample with 75 mM TEMPOL, indicating a possible crossover of the DNP mechanism with temperature. These data provide a promising basis for testing different DNP models such as TM and iCE. Yet, a crucial piece of information to test the models is the spin-lattice relaxation time of the electron spins T_{1e} at the temperatures where the μw spectra are recorded.

Understanding the mechanisms at stake in our conditions of field and temperature is of great interest to further improve DNP performance. When the radical concentration in DNP juice is increased, the strength of the interactions between electrons increases which should affect DNP mechanisms. However, this also increases the number of electrons per radical and possibly the intensity of paramagnetic relaxation. If we can find a suitable model to explain our data, it should be possible to predict the optimal electron-electron interaction strength and guide the design of sample architectures to reach this optimum. An optimum was perhaps already reached in the case of HYPSO 5 samples, [54] in which the ^{1}H polarization at 1.2 K and 6.7 T approaches unity. In these samples, the radicals are not homogeneously distributed since they are grafted on the surface of the pores of a mesoporous solid.

PANI polymers were introduced as a new substrate for DNP. μw spectra were recorded 1.6 K as a function of the radical content and a surprising richness of DNP mechanisms was found. The spectra feature vanishingly small SE on the edges and a stronger pattern at the center of spectra. This pattern evolves from absorption-like to dispersion-like as radical concentration increases. If the absorption-like pattern is reminiscent of recently reported cases, [157, 158, 159] the crossover from absorption to dispersion is more surprising. Finally, the analysis of the individual build-up curves in the μw spectra revealed that, for some μw frequencies, two mechanisms were operating at the same time pulling the ^{1}H polarization towards different values near the center of the spectrum.

If only modest polarization of $\approx 3\%$ were obtained, the interest of PANI polymers is that electron spins can be polarized above Boltzmann equilibrium independently of temperature using CISS in cPANI. In the past years, a lot of effort has been put into nitrogen-vacancy (NV) doped diamonds as a source of hyperpolarization at room temperature. Indeed, electron spins in negatively charged NV centers can be polarized by LASER illumination and the polarization can be transferred to surrounding ^{13}C spins by DNP at low-field. However, it remains challenging to transfer the ^{13}C polarization to target molecules outside the diamonds. In the case of PANI, ^{1}H spins are polarized and so their polarization can be transferred more easily by spin diffusion to a host solution (possibly frozen at liquid nitrogen temperatures). Furthermore, the architecture of the polymer can be controlled to make PANI a solid porous powder.

Finally, we note that, due to the extraordinarily high relaxation rate of ^{1}H spins in PANI even in conditions where the electron polarization approaches unity, porous PANI polymers could be used as filterable relaxing agents for brute force hyperpolarization. [164, 165] The method consists of bringing a sample to mK temperatures in a moderate magnetic field and letting it relax to the high Boltzmann equilibrium polarization of nuclear spins in these conditions. However, the main limitation of the method is the relaxation time of nuclear spins in these conditions which can exceed days. [164] Adding paramagnetic dopants in the form of a standard polarizing agent does not help as static electrons relax nuclear spins *via* electron spin flip-flops, which are quenched in these conditions. If the electrons in PANI remain mobile even at mK temperatures, they could provide the relaxation source necessary for efficient brute force hyperpolarization. We note that Khutsishvili proposed this idea for the case of conductive metals as early as 1955 [166] but mentioned that the method would be limited to nuclear spins *in* the metal. PANI polymers would be ideal in this regard, as they can be made porous to host a solution to be polarized and ^{1}H spins can be used to relay polarization. [57, 154, 155]

Chapter 4

NMR detected EPR

The understanding of DNP mechanisms requires the knowledge of EPR properties such as the electron spin-lattice relaxation time T_{1e}, the spin-spin relaxation time $T_{2,e}$, the EPR lineshape, and the EPR lineshape under DNP. The most powerful approach for the measurement of such properties is pulsed EPR. [167, 158, 157] However, pulsed EPR under dDNP conditions, i.e., at fields $3.3 < B_0 < 7$ T and temperature $T < 2$ K, is challenging. To the best of my knowledge, reported pulsed EPR instruments at fields $3.3 < B_0 < 7$ do not operate at temperatures below $T \approx 4$ K. [167, 168, 169, 70]

Alternatives exist which require simpler hardware but only provide information comparable to that offered by CW-EPR. One such example is longitudinally detected electron saturation resonance (LOD-ESR). [170, 48, 51, 114] Implementing LOD-ESR in a running dDNP polarizer merely requires adding coils of wire sensitive to magnetic fields along the main magnetic field B_0, usually above and below the sample to allow μw to reach the sample, and some electronics to gate the μw and record the electrical signal in the coil. LOD-ESR is typically used to measure T_{1e} and CW-type EPR spectra. Another approach is indirect EPR detection *via* NMR properties, which uses μw gating but does not require any further hardware modification as compared to standard dDNP instrumentation (at least in the simplest form of the experiment). An example of this approach is the measurement of T_{1e} by monitoring the displacement of an NMR signal after switching off μw irradiation. [171, 172] The shift of the NMR signal is proportional to the dipolar field generated by the electron spins, which is in turn proportional to the electron polarization. The return of the electron polarization towards equilibrium after switching off μw irradiation can therefore be monitored *via* the shift of the NMR line. Another approach consists of measuring NMR relaxation properties which are sensitive to electron polarization. We have seen that nuclear paramagnetic spin-lattice relaxation $1/T_{1,para}$ was proportional to $1 - P_e^2$, where P_e is the polarization of the electron (see Eq. 2.159). The same is true for relaxation in the transverse plane. Bornet *et al.* have exploited the ^{1}H relaxation rate in the rotating frame $1/T_{1\rho}$ to measure EPR properties in DNP juice doped with 50 mM TEMPOL at 1.2 K and 6.7 T. [49] They found $T_{1e} \approx 48 \pm 1$ ms and an electron polarization under μw irradiation of 48%. Recently, Guarin *et al.* showed that the ^{1}H spin-spin relaxation rate $1/T_1^*(^2\text{H})$ was strongly affected by the change in electron polarization upon switching on and off μw irradiation in various samples at 6.7 T and between 1.2 and 4 K. [67]

In this chapter, we introduce the use of the spin-spin relaxation rate of ^{13}C spins $1/T_2^*(^{13}\text{C})$ to measure EPR properties. We first discuss the theory behind the use of NMR relaxation properties as indirect EPR probes. We then use $1/T_2^*(^{13}\text{C})$ to measure the electron spin polarization as a function of μw power as well as T_{1e} and $T_{e,sat}$ time constants at 1.2 K (where $T_{e,sat}$ is the time constant of the equilibration of the electron polarization upon switching on μw irradiation). Furthermore, similarly to Bornet *et al*, we use $1/T_\rho(^1\text{H})$ to measure T_{1e}. However, we base our analysis on a simpler approach that does not require the simulation of spin diffusion by finite element methods. We measure T_{1e} at various temperatures between 1.6 and 3.8 K and, surprisingly, we find that it increases with temperature. We also present the use of $1/T_\rho(^1\mathrm{H})$ to record a rudimentary EPR spectrum of TEMPOL at 1.6 K. Finally, we discuss the difference between ^{13}C and ^{1}H relaxation properties as indirect probes for EPR properties.

4.1 The choice of the autocorrelation function

The idea that underlies NMR detected EPR is to use an NMR quantity that is sensitive to the electron polarization as a reporter of the latter. The strategy introduced by Bornet *et al.* which we were inspired by consists of measuring NMR relaxation rates in conditions where the electron polarization is known, that is, in the absence of μw irradiation, where the electron polarization is given by Boltzmann's law (see Eq. 1.3). The relaxation rate is measured at various temperatures and hence at various electron polarizations. Based on a suitable model relating the relaxation rate to the electron polarization, a calibration curve is obtained, which can then be used to infer the electron polarization in circumstances where it is perturbed by μw irradiation. EPR quantities such as T_{1e} and even a full EPR spectrum can be obtained in this way. An underlying assumption of this approach is that the only parameter affecting signicantly the NMR relaxation rate in all conditions of measurement is the electron polarization and that the relation between the electron polarization and the NMR relaxation rate is known.

In this section, we discuss the relation between NMR relaxation rates and electron polarization, as different expressions can be found in the literature. [49, 67] The basic assumption is that a relaxation rate has the form

$$R_k = R_{k,para} + R_{k,dia}, \tag{4.1}$$

where $R_{k,para}$ and $R_{k,dia}$ are paramagnetic and diamagnetic relaxation rates (i.e., due to electron dependent and independent mechanisms, respectively), with

$$R_{k,para} = R^0_{k,para}(1 - \bar{P}P_\infty), \tag{4.2}$$

where $R^0_{k,para}$ is the relaxation rate constant at null electron polarization, which depends on the type of relaxation (spin-lattice, spin-spin, etc). $\bar{P}$ and P_∞ are the average electron polarization and the polarization towards which the autocorrelation of the electron spins state tends, respectively. It is because paramagnetic relaxation rates $R_{k,para}$ depend on the average electron polarization $\bar{P}$ that NMR relaxation can be used to detect EPR properties indirectly.

We presented the construction of the autocorrelation of the electron spin state which leads to this term $1 - \bar{P}P_\infty$ in Sec. 2.3.4 (see Eq. 2.150). In that section, we stated that, in the absence of μw irradiation, we have $\bar{P} = P_\infty = P_{eq}$, where P_{eq} is the Boltzmann equilibrium polarization of the electron spin as defined in Eq. 1.3, leading to

$$R_{k,para} = R^0_{k,para}(1 - P^2_{eq}). \tag{4.3}$$

But what happens once we switch on μw irradiation? Bornet *et al.* used the expression [49]

$$R_{k,para} = R^0_{k,para}(1 - P_{eq}P_{\mu w}), \tag{4.4}$$

where P_{eq} and $P_{\mu w}$ are the electron polarization at Boltzmann equilibrium and the average electron polarization under μw irradiation. To the contrary, Guarin *et al.* based their analysis on the expression [67]

$$R_{k,para} = R^0_{k,para}(1 - P^2_{\mu w}). \tag{4.5}$$

However, none of them explained the choice behind one or the other autocorrelation function, which in turn leads to one or the other expression of the relaxation rate. We now try to understand the mechanisms which could rationalize these expressions. Let us first remember that $\bar{P} = p_\beta - p_\alpha$ was used in the construction of the autocorrelation function of Eq. 2.150 assuming that p_β and p_α were the probabilities to find the electron in the β and α states at any time $\tau = 0$, respectively. Therefore, there is no doubt that $\bar{P}$ corresponds to the average polarization of the electron spin under μw irradiation $P_{\mu w}$ (or the electron Boltzmann polarization P_{eq} in the absence of μw irradiation).

The more subtle question is what is P_∞. P_∞ was used in the construction of Eq. 4.2 as the polarization towards which the autocorrelation function tends. Therefore, the value of P_∞ depends on the mechanism which makes the electron state leave its state (or decorrelate from its state). Let us assume for the sake of the argument that electron spins are far apart and do not interact significantly with each other. Let us assume in addition, that μw irradiation is weak and so electron flips are primarily due to spin-lattice relaxation. In other words, before the electron spin state is disturbed by electron-electron interactions or by μw irradiation, spin-lattice relaxation takes the autocorrelation towards P_∞. In this case, it is natural to assume that the autocorrelation functions tends towards $P_\infty = P_{eq}$ with correlation time constant $\tau_c = T_{1e}$. These assumptions lead to Bornet *et al.*'s expression Eq. 4.4.

On the contrary, let us now know assume that electron flips are dominated by electron-electron dipolar interactions and so $T_{2,e} \ll T_{1e}$. In this case, there is no reason to assume that electron-electron flip-flops would make the autocorrelation tend towards P_{eq}; it should rather tend towards $P_\infty = P_{\mu w}$ with correlation time constant $\tau_c = T_{2,e}$, leading to Guarin *et al.*'s expression Eq. 4.5.

The second of these two mechanisms is of course more appropriate both in Bornet *et al.* and Guarin *et al.*'s cases as well as in ours. Indeed, all three cases are concerned with TM-DNP where electron-electron interactions are required to dominate over electron spin-lattice relaxation so that a spin temperature can establish within the electron-electron non-Zeeman reservoir. It is possible that another explanation that may justify Eq. 4.4 did not occur to us. Yet, in light of the above argument, we will use Eq. 4.5 in the following analysis. Furthermore, because both in the absence of and under μw irradiation, our argument leads us to the conclusion $\bar{P} = P_\infty$, for simplicity, we will write the relaxation rate as

$$R_{k,para} = R^0_{k,para}(1 - P_e^2), \tag{4.6}$$

where P_e is the electron polarization, either in the absence of or under μw irradiation.

4.2 EPR properties *via* $R_2^*(^{13}\mathrm{C})$

In the present case, we use the ^{13}C spin-spin relaxation rate $R_2^*(^{13}\mathrm{C})$ to infer the electron polarization P_e under μw irradiation as a function of the μw power. We further use this approach to measure T_{1e} and $T_{sat,e}$ (i.e., the time constant of the equilibration of the electron polarization upon switching on μw irradiation). Assuming that the rate is given by

$$R_2^* = R^*_{2,dia} + R^{0*}_{2,para}(1 - P_e^2), \tag{4.7}$$

we first determine $R^*_{2,dia}$ and $R^{0*}_{2,para}$ experimentally by measuring R_2^* in the absence of μw irradiation at various temperature between 1.2 and 4.2 K and therefore at various known Boltzmann equilibrium electron polarizations P_{eq}. This is done using the pulse sequence shown in Fig. 4.1A. We assume that $R^*_{2,dia}$ does not depend on temperature. Second, the electron polarization under μw irradiation is determined by measuring R_2^* with the pulse sequence shown on Fig. 4.1B and using the previously determined values of $R^*_{2,dia}$ and $R^{0*}_{2,para}$ and the relation

$$P_e = \sqrt{1 - \frac{R_2^* - R_{2,dia}^*}{R_{2,para}^{0*}}}, \tag{4.8}$$

which follows from Eq. 4.7. As a comparison, Bornet *et al.*'s expression (see Eq. 4.4) leads to

$$P_{\mu w} = \frac{1}{P_{eq}} \left(1 - \frac{R_2^* - R_{2,dia}^*}{R_{2,para}^{0*}} \right). \tag{4.9}$$

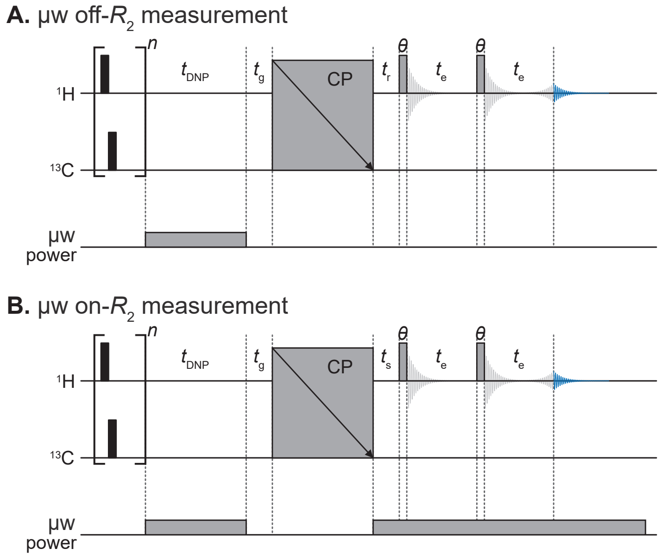

Figure 4.1: **A-B.** Pulse sequence diagrams for the measurement of the $R_2^*(^{13}\mathrm{C})$ in the absence of and under μw irradiation, respectively. After a train of saturation pulses, ^{1}H spins are polarized by DNP during t_{DNP}; delay t_g allows electron spins to return to Boltzmann equilibrium before the ^{1}H polarization is transferred to ^{13}C spins by a CP block; In A, after resting delay t_r, the ^{13}C signal is measured by a solid echo with pulses of angle θ with a variable echo time t_e. In B, μw irradiation is switched back on after the CP block. Delay t_s allows the electron polarization to reach dynamic equilibrium before the echo is performed. The FID represented in blue corresponds to that recorded by the spectrometer and Fourier transformed.

4.2.1 Determination of $R_{2,dia}^*$ and $R_{2,para}^{0*}$

We measured the $R_2^*(^{13}\mathrm{C})$ of the $\approx$ 270 mM natural abundance ^{13}C of a sample of DNP juice doped with 50 mM TEMPOL at twelve temperatures between 1.18 and 4.26 K using μw gating, using the pulse sequence of Fig. 4.1A. The echo times t_e were determined in a variable delay list with exponentially increasing delays. The echos were measured using pulse angles $\theta = 40°$. The results are shown in Fig. 4.2A. A monoexponential decay function

$$I(t_e) = I_0 \exp\left(-\frac{t_e}{T_2^*} \right) \tag{4.10}$$

was fitted to the signal intensity as a function of t_e. Note that the maximum delay for all measurements was $t_e = 10$ ms but is not visible on the plots of Fig. 4.2A.

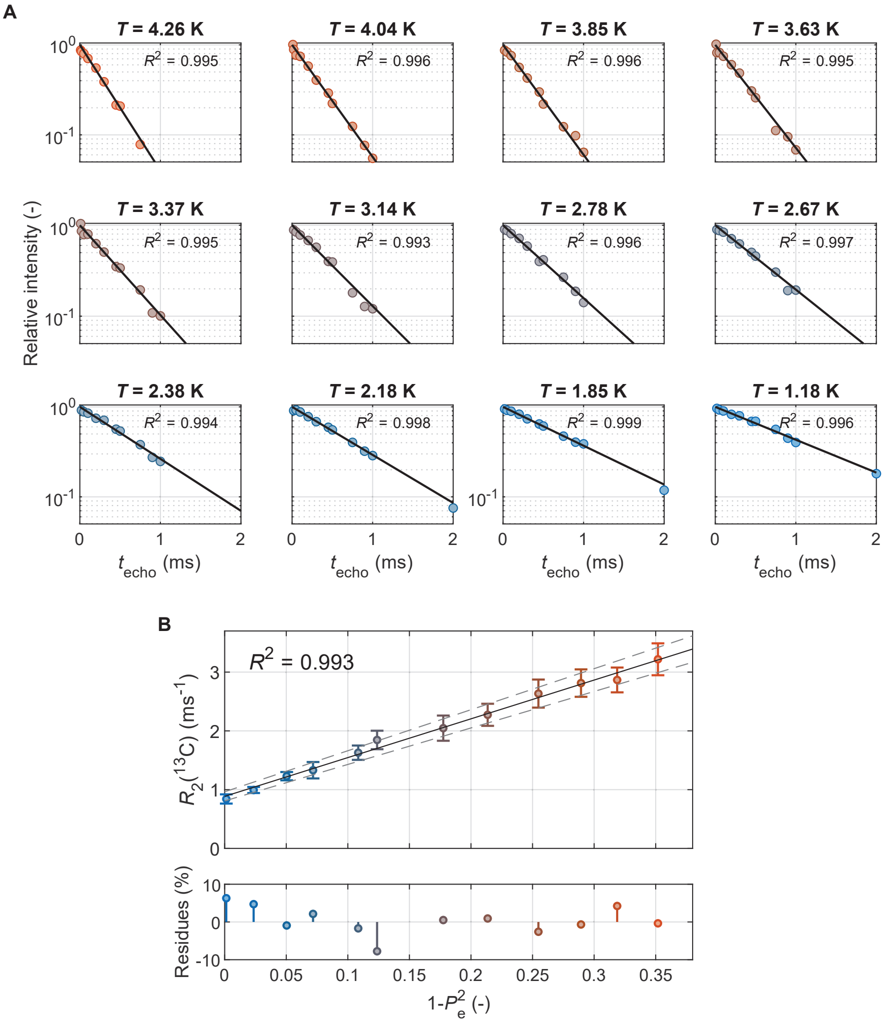

Figure 4.2: **A.** $R_2^*(^{13}\mathrm{C})$ measurement by solid echo after ^{1}H DNP and $^1\mathrm{H}\rightarrow{}^{13}\mathrm{C}$ CP, as described in Fig. 4.1A, at various temperatures, fitted with Eq. 4.10, shown as colored dots and black lines, respectively. The curves are normalized by the fitted value of I_0. **B.** Linear regression of the $R_2^*(^{13}\mathrm{C})$ values displayed in Panel A against $1-P_e^2$, where P_e is the polarization of the electron. The solid and dashed lines represent the linear regression and the 95% confidence interval, respectively.

The obtained rates are plotted on Fig. 4.2B as a function of $1-P_e^2$. Eq. 4.7 predicts a linear dependence of the relaxation rate on $1-P_e^2$, which is verified by the linear regression. The linear regression gave the values for the diamagnetic relaxation rate constant $R_{2,dia}^* = 0.89 \pm 0.08$ ms^{-1} and the paramagnetic relaxation rate constant at null electron polarization $R_{2,para}^{0*} = 6.6 \pm 0.4$ ms^{-1}.

4.2.2 Measurement of the electron polarization under μw irradiation

The relaxation rates $R_2^*(^{13}\mathrm{C})$ under μw irradiation were measured at 1.2 K using the pulse sequence of Fig. 4.1B as a function of the μw power for both positive and negative DNP. The echos were measured using pulse angles $\theta = 40°$. Each R_2^* measurement took 10-20 min to record. The number of scans was increased for the measurements at lower μw power, resulting in longer experimental time, to compensate for the lower sensitivity. The results are shown in Fig. 4.3A-B, respectively. As for Fig. 4.2A, the maximum delay for all measurements was $t_e = 10$ ms but is not visible on the plots. The decays were fitted with Eq. 4.10 and the relaxation rates were converted into electron polarization using Eq. 4.8. The error on the electron polarization P_e was calculated as

$$\sigma(P_e) = \left| \frac{1 - P_e^2}{P_e} \right| \sqrt{\left(\frac{\sigma(R_{2,para}^{0*})}{R_{2,para}^{0*}} \right)^2 + \frac{\sigma(R_2^*)^2 + \sigma(R_{2,dia}^*)^2}{R_2^* - R_{2,dia}^*}} \tag{4.11}$$

$\sigma(R_{2,para}^{0*})$, $\sigma(R_{2,dia}^*)$ and $\sigma(R_2^*)$ are the errors on the parameters of the linear regression shown in Fig. 4.2B and the error on the fitted rates of Fig. 4.3A-B, respectively. The electron polarization was also calculated according to Bornet *et al.*'s Eq. 4.9 for comparison. In this case, the error was calculated as

$$\sigma(P_{\mu w}) = \left| \frac{1 - P_{\mu w} P_{eq}}{P_{eq}} \right| \sqrt{\left(\frac{\sigma(R_{2,para}^{0*})}{R_{2,para}^{0*}} \right)^2 + \frac{\sigma(R_2^*)^2 + \sigma(R_{2,dia}^*)^2}{R_2^* - R_{2,dia}^*}}. \tag{4.12}$$

The electron polarization under μw irradiation inferred using Eq. 4.8 and Bornet *et al.*'s Eq. 4.9 are showed as colored and gray symbols, respectively, on 4.3C-D.

The measurements at low μw are much noisier than those at higher powers. The reason is that our hardware allows for the control of the μw gating from the pulse program with <ms resolution but not of the μw power and frequency. Instead, the μw power and frequency are controlled with a ≈ 2 s resolution *via* the AlphaController (see Fig. 3.3). Ideally, one would use the optimal μw power to polarize the ^{1}H spins during the first part of the pulse sequence of Fig. 4.1B and then lower the power to measure the ^{13}C relaxation rate at the desired value of μw power. This would allow one to measure the electron polarization at any μw power with maximum sensitivity. Because we could not switch the μw power fast enough, we had to keep it constant throughout the pulse sequence. As a consequence, the lower the μw power, the poorer the sensitivity, as can be seen in Fig. 4.3.

Using Eq. 4.8, we found electron polarizations $P_e \approx 69\% \pm 3\%$ and $P_e \approx 66\% \pm 4\%$ under positive and negative DNP, at the maximum available powers corresponding to 125 and 118 mW, respectively (see the colored symbols on Fig. 4.3C-D). Using Bornet *et al.*'s Eq. 4.9, we found $P_e \approx 47\% \pm 6\%$ and $P_e \approx 43\% \pm 7\%$ (see the gray symbols on Fig. 4.3C-D). Eq. 4.8 infers a higher electron polarization under μw irradiation than Eq. 4.9 but the experimental data that we present here cannot distinguish which of the two expressions is more appropriate. Interestingly, Bornet *et al.* found a polarization of 48% under μw irradiation (using Eq. 4.9) using an experimental setup very similar to ours and $R_{1\rho}(^1\mathrm{H})$ as an indirect measure of electron properties. Even though we used another relaxation parameter, namely ^{13}C transverse relaxation, our measured value of $P_e \approx 47\% \pm 6\%$ agrees with theirs (at least if we use the same equation to interpret the relaxation values).

Our measurements verify that the stronger the μw irradiation the lower the electron polarization. At low μw power, the electron polarization tends towards $\approx$ 100% in the case of negative DNP (see insert on Panel D). In the case of positive DNP, the value tends towards an unphysical value of the electron polarization above 100% (see insert on Panel C). This could be due to the poor sensitivity of the measurement at low power, as discussed above. However, there seems to be a bias that is not dominated by the noise in the measurement. This could be the result of a more fundamental limitation of our method, which remains to be explained.

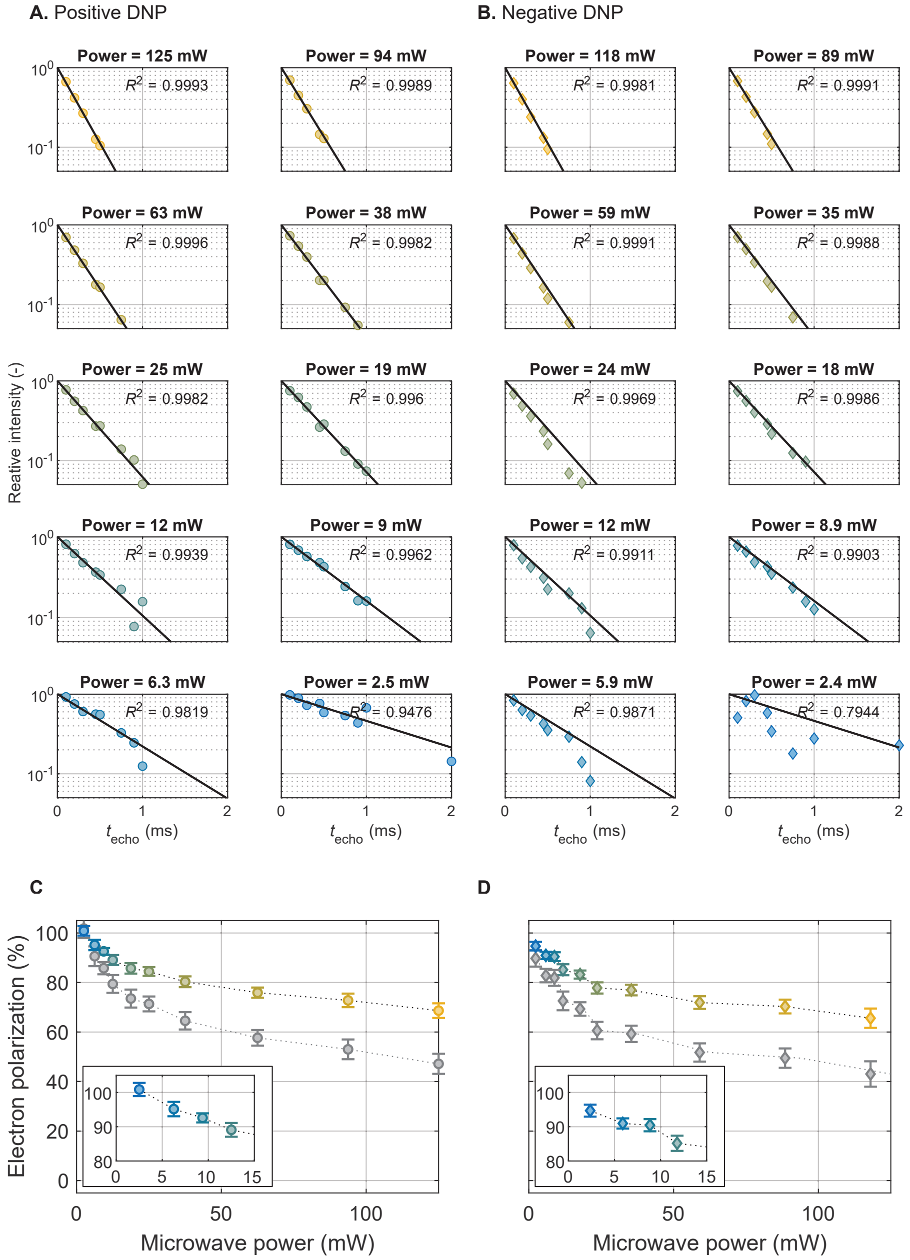

Figure 4.3: **A-B.** $R_2(^{13}\text{C})$ measurement by solid echo under μw irradiation at the optimal frequency for positive and negative DNP, respectively, after ^{1}H DNP and $^1\text{H}\rightarrow^{13}\text{C}$ CP, as described on Fig. 4.1B, at various μw powers, fitted with Eq. 4.10, shown as colored dots and black lines, respectively. The curves are normalized by the fitted value of I_0. **C-D.** Polarization of the electron under positive and negative DNP, respectively, as a function of μw power inferred from the relaxation rates obtained from the data of Panels A and B. The colored and gray symbol represents polarization values inferred using Eq. 4.8 and Bornet *et al.*'s Eq. 4.9, respectively. Each R_2^* measurement took 10-20 min to record.

4.2.3 Measurement of T_{1e}

The electron polarization can also be measured in a time-resolved manner using the above approach. We measured the electron spin-lattice relaxation time constant T_{1e} and the electron saturation time constant $T_{e,sat}$ at 1.2 K using the pulse sequences of Fig. 4.4A-B, respectively.

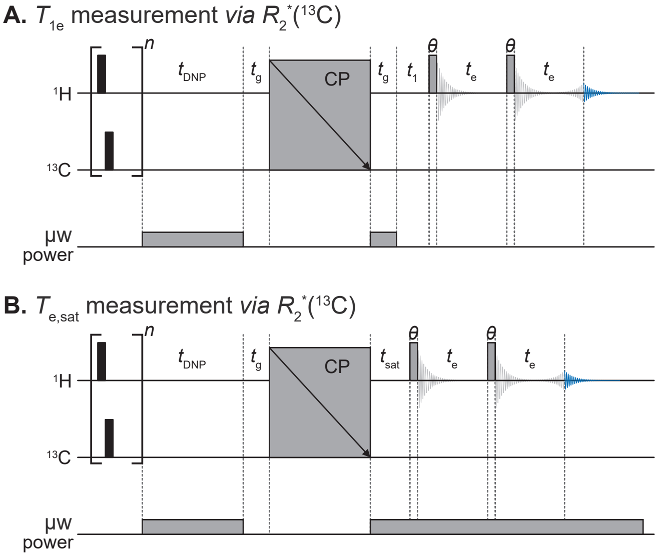

Figure 4.4: **A-B**. Pulse sequences for the measurement of the time constant of the electron spin-lattice relaxation T_{1e} and the electron saturation $T_{e,sat}$, respectively. Gating delay t_g is chosen to be five times T_{1e} and $T_{e,sat}$. The measurement is repeated $n_1 \times n_e$ times and $n_1 \times n_{sat}$ times for sequence A and B, respectively, where n_1, n_e and n_{sat} are the numbers of increments of t_1, t_e and t_{sat}, respectively. All other symbols have the same meaning as those in Fig. 4.1. A single R_2^* measurement typically takes $\approx$ 2 min to record.

In the pulse sequence of Fig. 4.4A, the second delay t_g allows the electron spins to reach their dynamic equilibrium polarization (which we measured to be $P_e \approx 69\% \pm 3\%$ and $P_e \approx 66\% \pm 4\%$ under positive and negative DNP, respectively). Then, μw irradiation is switched off and the electron spins return to Boltzmann equilibrium polarization $P_{eq} \approx 99.93\%$ at 1.2 K, with characteristic time constant T_{1e}, during delay t_1. The electron polarization of the electron is measured using the procedure described above for a range of values of t_1 between 0 and $> 5T_{1e}$. In the pulse sequence of Fig. 4.4B, the electron spin polarization is moved away from Boltzmann equilibrium towards the dynamic equilibrium value under DNP during delay t_{sat}. P_e is measured for a range of values of t_{sat} between 0 and $> 5T_{e,sat}$, as the electron spins are being saturated, which gives access to the time constant of the equilibration of the electron polarization. The transverse relaxation of ^{13}C spins is an order of magnitude faster than the measured EPR processes (see below) and so the electron polarization can be considered stationary on the time scale of the measurement.

The electron polarizations along t_1 and t_{sat} were measured on the same sample as that used for Fig. 4.3. Each of the measurements took $\approx$ 0.5 h to record. The results are plotted on Fig. 4.5A-B for positive and negative DNP, respectively. The obtained polarization traces were fitted with a monoexponential model

$$P(t_k) = P_\infty + (P_0 - P_\infty)\exp\left(-\frac{t_k}{T_k}\right), \tag{4.13}$$

where $t_k = t_1, t_{sat}$, $T_k = T_{1e}, T_{sat,e}$, P_0 and P_∞ are the variable relaxation delay, the fitted relaxation time constant and the fitted initial and final polarizations, respectively. The fitted curves are shown as black solid lines in Fig. 4.5C-D and the fitted relaxation time constants are given in Table 4.1. In the case of the $T_{e,sat}$ measurement under negative DNP, the measurement had to be stopped before completion because the cryostat ran out of helium. Therefore, the measurement was not performed with $t_{sat} \gg T_{e,sat}$ and so the fit performs poorly, yielding $T_{e,sat} \approx 71 \pm 52$ ms. The fit was repeated fixing P_∞ to the value of P_0 obtained from the T_{1e} measurement under negative DNP, yielding $T_{e,sat} \approx 27 \pm 18$ ms. The model curve is shown as a dotted line in Fig. 4.5B.

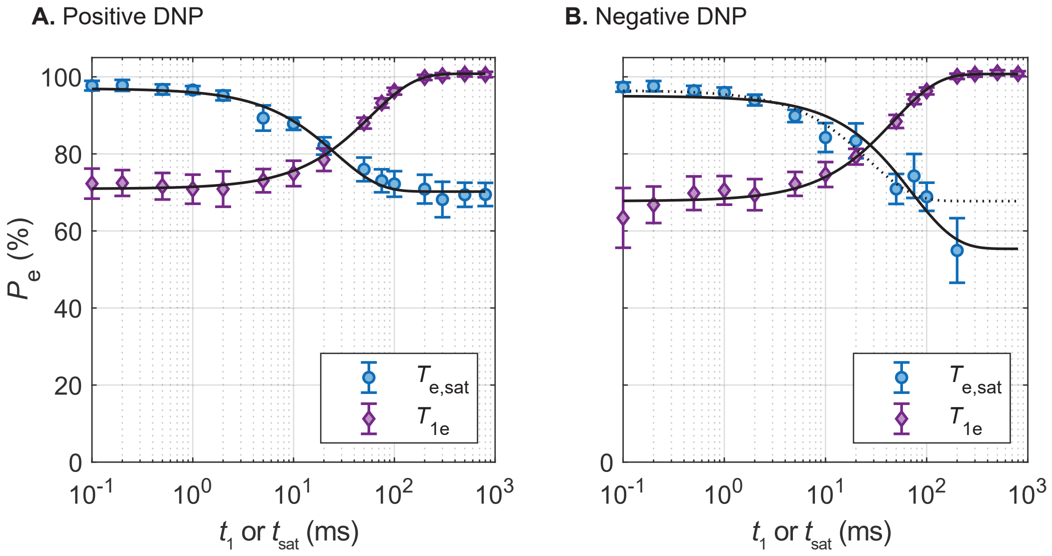

Figure 4.5: **A-B**. Measurement of the time constant of the electron spin-lattice relaxation time T_{1e} and the electron saturation time $T_{e,sat}$ using the pulse sequences in Fig. 4.4, under positive and negative DNP, respectively. Colored dots and black solid lines correspond to measured electron polarizations and model curves (see Eq. 4.13), respectively. The model shown as a dotted line on Panel B was performed fixing P_∞ to the value of P_0 obtained from the T_{1e} measurement under negative DNP. Each curve was recorded in 30 − 35 min.

	T_{1e} (ms)	$T_{e,sat}$ (ms)
Negative DNP	58 ± 7	26 ± 7
Positive DNP	47 ± 10	$27 \pm 18^*$

Table 4.1: Values of T_{1e} and $T_{e,sat}$ obtained by fitting Eq. 4.13 to the data of Fig. 4.5C-D. The value with a (*) sign corresponds to the model shown as a dotted line on Fig. 4.5D, for which P_∞ was fixed to the value of P_0 obtained from the T_{1e} measurement under negative DNP.

Table 4.1 shows that the measured T_{1e} values are the same whether positive or negative DNP is performed. The same is true for the saturation time constant $T_{e,sat}$. It is interesting to notice, again, that our results are in agreement with Bornet *et al.* who found $T_1 \approx 48 \pm 1$ ms, although we should note that their measurement was performed at 6.7 T whilst ours at 7.05 T.

4.3 EPR properties *via* $R_{1\rho}^{*}(^{1}\mathrm{H})$

In addition to EPR measurements *via* $R_2^*(^{13}\mathrm{C})$, we have also used $R_{1\rho}(^{1}\mathrm{H})$. We present the measurement of T_{1e} using $R_{1\rho}(^{1}\mathrm{H})$ as function of temperature between 1.6 and 3.8 K as a well as a rudimentary EPR spectrum. We used a sample of 0.5 M [1-^{13}C]-sodium acetate and 50 mM TEMPOL in DNP juice. Note that the presence of [1-^{13}C]-sodium acetate was meant for other purposes than the present measurements.

4.3.1 Measurement of T_{1e}

The procedure used here is very similar to that presented above for indirect EPR measurement *via* ^{13}C relaxation: $R_{1\rho}$ was first measured while the electron spins were at Boltzmann equilibrium, using the pulse sequence of Fig. 4.6A at eleven temperatures between 1.6 and 3.8 K.

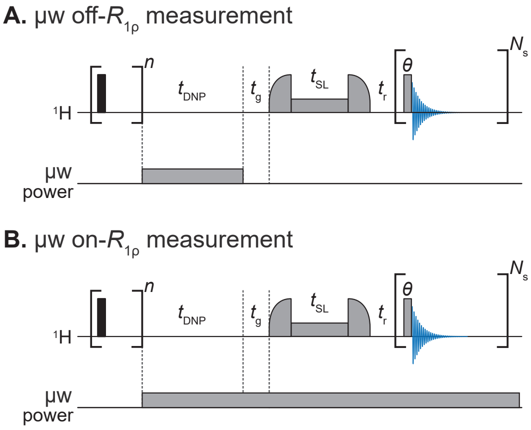

Figure 4.6: **A-B**. Pulse sequence diagrams for the measurement of $R_{1\rho}(^{1}\mathrm{H})$ in the absence of and under μw irradiation, respectively. In Panel A, if $R_{1\rho}$ is to be measured while the electron polarization is at Boltzmann equilibrium, t_g is set to 0.5 s, so that it is large compared to T_{1e} and so the electrons have time to relax between the instant where μw irradiation is gated and the spinlock. The pulse sequence in Panel A is used here for the determination of the relaxation parameters and T_{1e} measurements, whilst that in Panel B is used for the measurement of the EPR spectrum. A single $R_{1\rho}$ measurement typically takes ≈ 30 s to record.

After the ^{1}H spins were polarized during t_{DNP}, gating delay t_g was set to 0.5 s to let the electron spins relax towards Boltzmann equilibrium. An adiabatic half passage pulse of 175 μs put the ^{1}H magnetization into the transverse plane and a pulse of constant amplitude locked the spins during variable spin lock delay t_{SL}. A second adiabatic half passage pulse of 175 μs brought the remaining magnetization along the z-axis. After a resting delay $t_r = 110$ μs, the magnetization along the z-axis was read out by a train of $N_S = 64$ pulse and acquisition blocks using pulses with angle $\theta = 0.1^\circ$. The measurement with 64 scans takes ≈ 17 ms. Note that at this point the electron polarization has already been encoded in the ^{1}H polarization. Therefore, the time it takes to perform the 64 scans does not affect the measured electron polarization. The curves were fitted with a stretched exponential decay model

$$I(t) = I_0 \exp\left(-\left(\frac{t_{SL}}{T_{1\rho}}\right)^{\beta}\right), \tag{4.14}$$

where I_0, $T_{1\rho}$, and β are the signal intensity at $t_{SL} = 0$, the relaxation rate in the rotating frame, and the stretched coefficient, respectively. The resulting curves are shown in Fig. 4.7A.

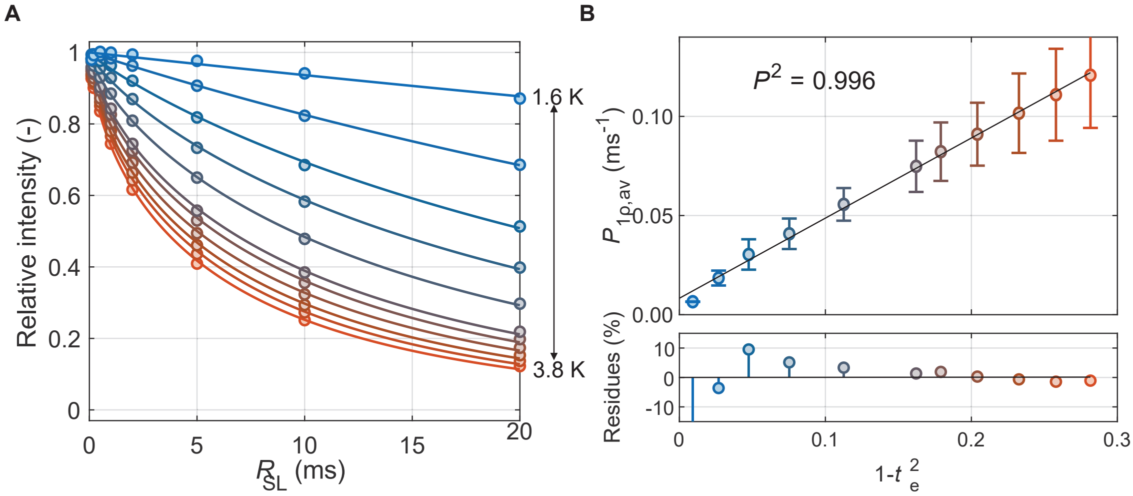

Figure 4.7: **A**. $R_{1\rho}(^1\text{H})$ measurements at various temperatures measured using the pulse sequence shown in Fig. 4.6A. The measured signal integrals are fitted with Eq. 4.14 shown as dots and lines, respectively. The curves are normalized by the fitted value of I_0. **B**. Linear regression of the average relaxation rate $R_{1\rho,\text{av}}$ (obtained from the fitted parameters of the curves in Panel A using Eq. 3.34) against $1 - P_e^2$.

The diamagnetic rate constant $R_{1\rho,dia} \approx 0.008\pm0.032$ ms^{-1} the and paramagnetic rate constant at null electron polarization $R^0_{1\rho,para} \approx 0.40 \pm 0.02$ ms^{-1} were obtained by linear regression of the measured rate against $1 - P_e^2$ (shown in Fig. 4.7B), assuming that the rate has the form

$$R_{1\rho} = R_{1\rho,dia} + R^0_{1\rho,para}(1 - P_e^2). \tag{4.15}$$

We note that the residues in the linear regression in Fig. 4.7B are not randomly dispersed around zero, indicating that the model of Eq. 4.15 might be too simplistic.

T_{1e} was measured at seven temperatures between 1.6 and 3.8 K using the pulse sequence of Fig. 4.6A. For each temperature, $R_{1\rho}(^1\text{H})$ was measured using eighteen values of the gating delay t_g from 0 to 510 ms. The longer t_g, the more the electron spins have relaxed and the less ^{1}H spins relax during the spinlock. Each curve was fitted with Eq. 4.14 as in Fig. 4.7A (not shown). The polarization of the electron spin was inferred from the fitted $R_{1\rho}$ values using

$$P_e = \sqrt{1 - \frac{R_{1\rho} - R_{1\rho,dia}}{R^0_{1\rho,para}}}, \tag{4.16}$$

which follows from Eq. 4.15. The error on P_e was calculated using Eq. 4.11 (where R_2^* is substituted by $R_{1\rho}$). The obtained polarizations as a function of the gating delay t_g for the various temperatures are shown in Fig. 4.8A as colored dots. They were fitted with the monoexponential model of Eq. 4.13 (shown as black lines in Fig. 4.8A).

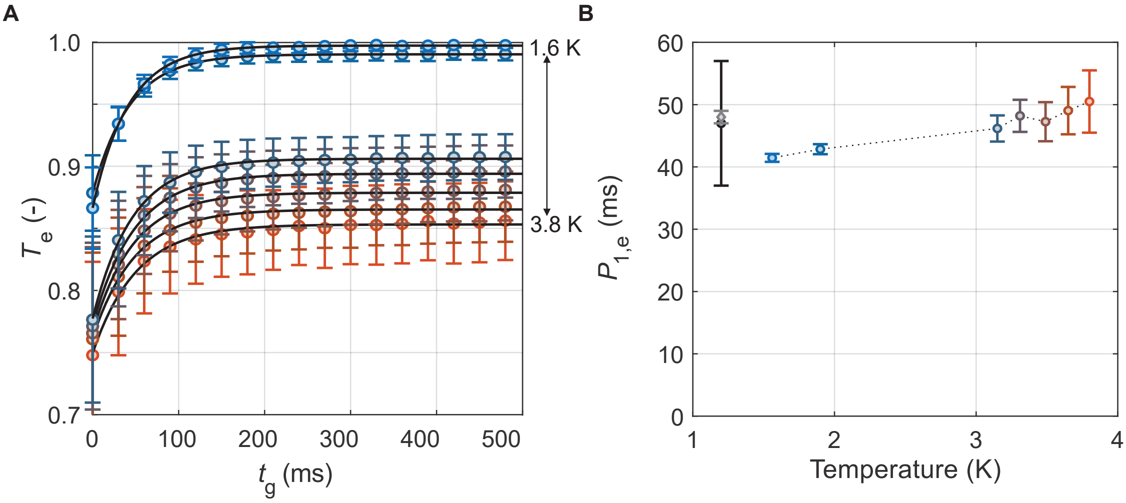

Figure 4.8: **A**. T_{1e} measurement *via* $R_{1\rho}(^1\mathrm{H})$. Colored dots represent individual $R_{1\rho}$ measurement using the pulse sequence of Fig. 4.6A converted into electron polarization using Eq. 4.16 and the rates obtained in Fig. 4.7B. The obtained electron polarizations as a function of the gating delay t_g are fitted with the monoexponential model of Eq. 4.13. **B**. Electron spin-lattice relaxation time constant T_{1e} obtained in Panel A plotted against temperature as colored dots. The black and gray dots are the values that we measured using $R_2^*(^{13}\mathrm{C})$ (see Sec. 4.2.3) and the value measured by Bornet *et al.* at 6.7 T using $R_{1\rho}(^1\mathrm{H})$, [48] respectively. One T_{1e} measurement typically takes ≈ 8 s.

The resulting T_{1e} values are plotted as a function of temperature in Fig. 4.8B (represented by colored dots). The T_{1e} value for the same sample that we measured using $R_2^*(^{13}\mathrm{C})$ in Sec. 4.2.3 and that measured by Bornet *et al.* at 6.7 T using $R_{1\rho}(^1\mathrm{H})$ are shown for comparison, as black and gray dots, respectively. To our surprise, the measured values of T_{1e} exhibits a slight increase with temperature. However, due to the large error bar at increasing temperatures, the trend is barely significant.

Using $R_{1\rho}(^1\mathrm{H})$, we found an electron polarization under μw irradiation at 1.6 K $P_e \approx 87\% \pm 3\%$ while we found $P_e \approx 69\% \pm 3\%$ using $R_2(^{13}\mathrm{C})$ at 1.2 K. This discrepancy between the methods tends to indicate that at least one of them is biased. A possible explanation will be given in Sec. 4.3.3.

4.3.2 Measurement of an EPR spectrum

We now show that $R_{1\rho}$ measurements of ^{1}H spins can also be used to record a complete EPR spectrum. To do so, we measured the electron polarization *via* $R_{1\rho}(^1\mathrm{H})$ under the effect of μw irradiation using the pulse sequence of Fig 4.6B and we repeated this measurement, scanning through the EPR line. The result of this measurement is shown in Fig. 4.9A. We then convert the measured rates into polarization using Eq. 4.16, as shown in Fig. 4.9B.

To convert the electron polarization into an EPR signal, we assume that μw irradiation is weak and hence the change in electron polarization is linear with the number of electron spins $f(\omega)$ resonating at the μw frequency ω [48, 51, 114]

$$\Delta P = P_{eq} - P_e \propto f(\omega), \tag{4.17}$$

where P_{eq} are P_e are the polarization of the electron at Boltzmann equilibrium and the measured

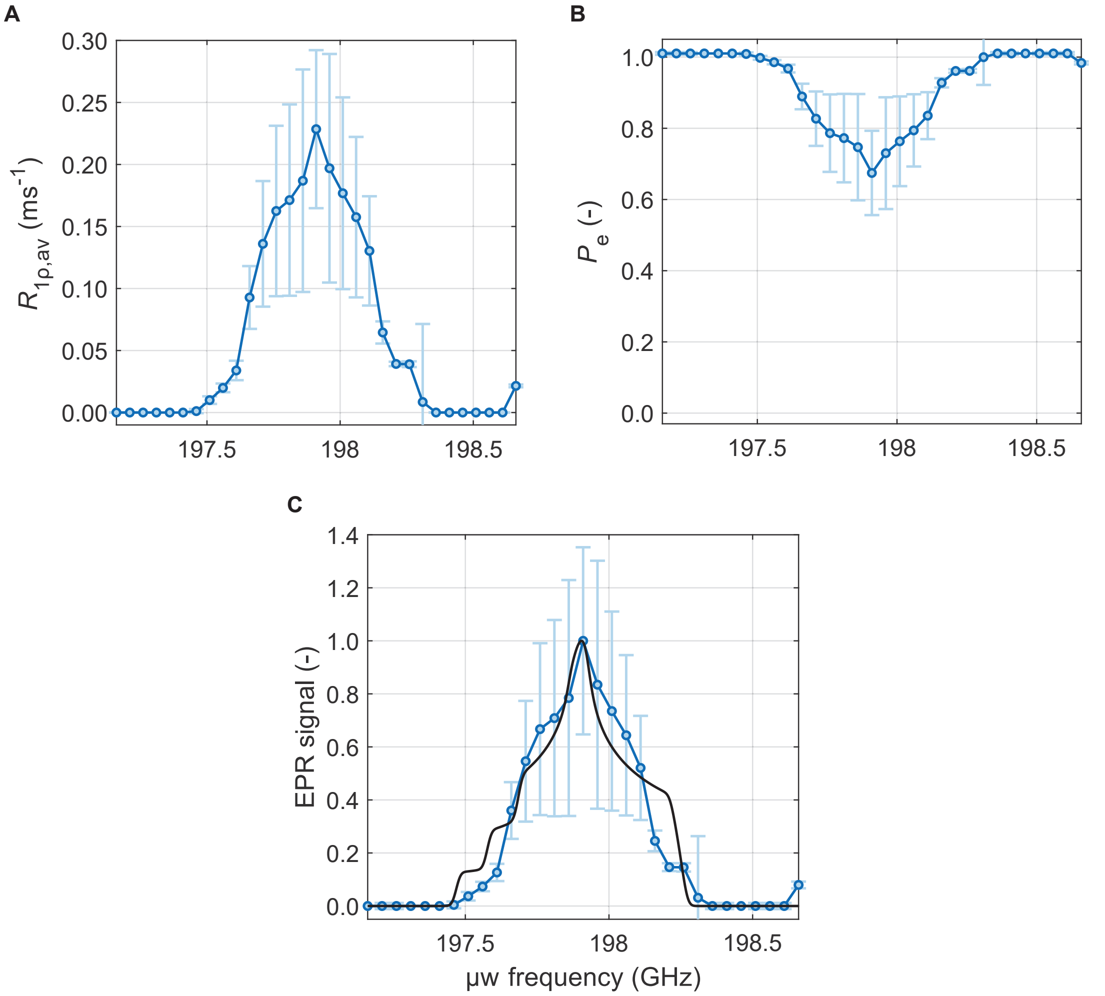

Figure 4.9: **A-B**. $R_{1\rho,\mathrm{av}}(^1\mathrm{H})$ as a function of the μw irradiation frequency measured using the pulse sequence in Fig. 4.6B and corresponding electron polarization calculated using Eq. 4.16, respectively. **C** EPR signal calculated using Eq. 4.18 from the measured electron polarization under μw irradiation of Panel B. A simulated spectrum of TEMPOL is shown for comparison as a black line. The simulation was performed using the same parameters as in Fig. 3.17. Both the simulated and measured spectra are normalized to 1.

electron polarization under irradiation at ω, respectively. It follows that the EPR signal is given by

$$f(\omega) \propto P_{eq} - P_e. \tag{4.18}$$

The result is shown in Fig. 4.9C, after normalization to 1, as blue dots. A simulation of the EPR spectrum is shown for comparison as a black line. The overall shape of the measured EPR spectrum matches coarsely the simulation. In particular, the position of the maximum matches the simulation. However, the measured lineshape is narrower than the simulated one. We note that using Bornet *et al.*'s Eq. 4.4 rather than Eq. 4.6 only modifies the appearance of the spectrum very slightly (not shown).

The fact that we cannot change the μw parameters between the part where we prepolarize the spins and that where we record relaxation inevitably hampers the sensitivity of the measurement, as it did for the measurements presented in Sec. 4.2.2. In the latter case, it was the low μw power that made the measurement insensitive while here it is the μw frequency that gets away from the DNP optima as we scan through the EPR line. Furthermore, to ensure sufficient sensitivity, we used the maximum available power and so the hypothesis of weak saturation is likely to be violated. This could explain why the intensity of the spectrum is distorted. This should cause the spectrum to be "saturated" and would therefore explain why the spectrum appears broader near the maximum. However, this would hardly explain why the intensity of the spectrum is lower than the simulation on the edges. A possible explanation is that spectral diffusion is not fast enough to communicate the saturation from the edges of the EPR line to the whole, resulting in a distribution of electron polarization values in the EPR and hence a distribution of $R_{1\rho}$ values. Since the nuclear polarization decays during the spinlock already have a marked stretched character in the absence of μw irradiation (β spreads from 0.65 to 1.0 between 3.8 and 1.8 K), it is not clear how the heterogeneity of the $R_{1\rho}$ would affect the decay curves.

This measurement of an EPR spectrum using nuclear relaxation would highly benefit from the implementation of programmable fast switching of the μw frequency and power. The nuclear spins could therefore be polarized at high μw power and the optimal μw frequency to ensure maximum sensitivity. The frequency would then be switched to the incremented frequency and the μw power would be lowered to measure the EPR intensity at the incremented frequency ensuring that μw irradiation can be considered as a linear perturbation.

4.3.3 Comparison of ^{1}H and ^{13}C relaxation as indirect probes

We have used both ^{1}H and ^{13}C relaxation properties as indirect probes of the electron polarization and used them to measure T_{1e}. The comparison of the measurement shown 4.8B shows that there is a reasonable agreement between the two measurements, at least to the order of magnitude. The reported value of Bornet *et al.* is higher than ours recorded with a very similar method (both using $R_{1\rho}(^1\mathrm{H})$) although recorded at a slightly lower magnetic field (6.7 compared to 7.05 T).

What motivated our choice to use ^{13}C relaxation was the following. First, the values of $R_{1\rho,\mathrm{av}}(^1\mathrm{H})$ ranges from $\approx$ 10 to $\approx$ 100 ms. This is not negligible compared to the measured electron T_{1e} which is on the order of $40 - 50$ ms in our temperature range. Thus, the polarization of the electron cannot be considered constant during the ^{1}H spin lock and so the measurement cannot be considered instantaneous, which is a clear disadvantage of this method. To circumvent this issue, one could use $R_2^*(^1\mathrm{H})$ as an indirect probe for EPR measurements, since the relaxation time constants are typically on the order of tens of μs, [67] i.e., three orders of magnitude lower than the electron relaxation time constant that we aim at measuring. In this case, the measurement of the electron polarization would certainly be considered instantaneous on the timescale of electron spin-lattice relaxation.

However, we believe that the T_{1e} measurements by ^{1}H relaxation properties are likely to be polluted by another effect, namely nuclear spin diffusion in the vicinity of the electron spin. Indeed, as will be shown in the next chapter, nuclear spin diffusion is hindered in the vicinity of the electron and this effect is highly sensitive to the polarization of the electron; at 1.2 K, the polarization of the electron at Boltzmann equilibrium is $\approx 99.93\%$ and nuclear spin diffusion is strongly hindered. At lower electron polarization (either under μw irradiation or at a higher temperature), the efficiency of nuclear spin diffusion increases. In the pulse sequence of Fig. 4.6A, after the μw are gated, not only the electron spins relax towards Boltzmann equilibrium but the gradient of polarization which was induced by DNP during t_{DNP} starts equilibrating. The nuclear spins closer to the electron which do not participate in the NMR signal because they are shifted by the hyperfine interaction start sharing their polarization with the visible bulk spins. Because this process depends on the polarization of the electron, the nuclear magnetization along the z-axis before the spin lock is not independent of t_g and so the decay by $R_{1\rho}$ during the spin lock is not the only process affecting the final magnetization along the z-axis after the spinlock.

In their data analysis, Bornet *et al.* accounted for spin diffusion using numerical simulation by finite element methods. However, they only modeled the nuclear spin diffusion and relaxation dynamics *during* the spin lock and not prior to it during t_g. Taking this effect into account would certainly be a very difficult task. To the best of our understanding, the data we have acquired do not allow us to verify whether this effect is significant or not. We may only affirm that this effect could potentially bias our analysis. It could explain the surprising increase of T_{1e} with temperature that we measured using $R_{1\rho}(^1\text{H})$ as an indirect probe (see Fig. 4.8B) and the higher electron polarization under μw irradiation obtained by $R_{1\rho}(^1\text{H})$ measurements. It could also possibly explain the deviation from linearity of the relation between $R_{1\rho}(^1\text{H})$ and $1 - P_e^2$ in Fig. 4.7B.

In the absence of certitude regarding the strength of this effect, using $R_2^*(^{13}\text{C})$ seems to be a reasonable choice. In the pulse sequences of Fig. 4.4, the ^{1}H polarization is transferred to the ^{13}C spins in a repeatable way which does *not* depend on the electron polarization during t_g. During the remaining of the pulse sequence (< 1 s), the electron polarization is manipulated by μw irradiation until it is measured by *via* ^{13}C spins. During this time, the ^{13}C polarization does not have time to evolve neither by spin-lattice relaxation nor by spin diffusion because of the low γ of ^{13}C spins. Furthermore, the longest value of $T_2^*(^{13}\text{C})$ that we measured was ≈ 1 ms, which is short compared to T_{1e} and so the measurement of the electron polarization can be considered instantaneous on the timescale of T_{1e} relaxation.

We believe that these arguments make ^{13}C spin-spin relaxation a better-suited reporter for T_{1e} (as well as $T_{e,sat}$) processes. However, we note that these limitations should only affect T_{1e} and $T_{e,sat}$ measurement but not measurements where relaxation (either ^{13}C or ^{1}H) is measured with the electron polarization at steady state, such as the electron polarization measurements of Sec. 4.2.2 and the EPR spectrum measurement of Sec. 4.3.2.

4.4 Perspectives

We have introduced the use of the ^{13}C spin-spin relaxation rate $R_2(^{13}\text{C})$ as an indirect probe to measure EPR properties and applied the method for measurements in DNP juice doped with 50 mM TEMPOL. The polarization of electron spins under μw irradiation was measured at 1.2 K as a function of μw power using $R_2(^{13}\text{C})$. The value under irradiation at the positive DNP optimum was found to be $P_e \approx 69\% \pm 3\%$ at the maximum available μw power. Using $R_{1\rho}(^1\text{H})$, we found a higher electron polarization under μw irradiation $P_e \approx 87\% \pm 3\%$ at 1.6 K. The electron spin-lattice relaxation time constant T_{1e} and the characteristic time constant of the electron saturation $T_{e,sat}$ were measured at 1.2 K using irradiation at the maximum available μw power both at the positive and negative DNP optima. The T_{1e} using irradiation at the positive optimum was found to be 47 ± 10 ms, in reasonable agreement with Bornet *et al.*'s findings at a slightly lower magnetic field (6.7 T compared with 7.05 T). We found that T_{1e} was ≈ 2 larger than $T_{e,sat}$ both under irradiation at positive and negative DNP optima. T_{1e} was also measured as a function of temperature using $R_{1\rho}(^1\text{H})$ using positive DNP. An unexpected trend of T_{1e} increases with temperature was observed using this method. Finally, a rudimentary EPR spectrum of TEMPOL was recorded indirectly by measuring $R_{1\rho}(^1\text{H})$ as a function of the μw irradiation frequency.

Since the efficiency of ^{1}H spin diffusion depends on the electron polarization, we speculated that some indirect EPR measurements (in particular T_{1e} measurements) based on ^{1}H relaxation properties could be biased by the equilibration of nuclear polarization gradients during gating delays. We further suggested that this effect possibly could explain the discrepancy between EPR measurements using ^{1}H and ^{13}C relaxation properties. To confirm this hypothesis, the measurements should be repeated on the same sample in a single session of experiments. The measurements should also be compared with the barycenter method, where the electron polarization is revealed by the shift it causes on the NMR line. We note that measuring T_{1e} using the barycenter method is considerably faster. The interest of the methods presented here is not only to obtain EPR data but also to gain insights into the interplay between the electron spin state and NMR properties. Furthermore, if the barycenter method has been used to measure T_{1e}, it is not obvious whether it could be used to measure an indirect EPR spectrum.

The method that we have presented could be improved in several ways. First, regarding the hardware, being able to switch the μw irradiation frequency and power would greatly improve the sensitivity of the measurements and possibly provide a more repeatable initial state of the nuclear polarization before probing the electron polarization at different μw irradiation frequencies and powers. As pointed out in the Perspectives section of Chapter 3 (see Sec. 3.5), this would require designing a dedicated LabView program receiving TTL pulses from the NMR console to control the μw source. Second, the method would benefit from clarifying the autocorrelation function of the electron spin state which should be used to calculate NMR relaxation rates, based on a more complete theoretical argument. In Sec. 4.1, we only presented an intuitive description of the mechanisms which could lead to the different prefactors ($1 - P_{\mu w}^2$ and $1 - P_{eq}P_{\mu w}$) found in the literature. Last, the effect of spectral diffusion on the EPR lineshape could be simulated for the different μw irradiation powers and frequencies. The predicted EPR lineshape could in turn be used to predict the distribution of R_2^* or $R_{1\rho}$ values, which would help understand the discrepancy between the simulated and measured EPR spectrum.

We note that the measurements of $T_{e,sat}$ could be used to estimate the B_1 field of the μw in our experimental setup, which would be of value when simulating the DNP mechanisms operating in our sample, as proposed in Sec. 3.5. Finally, NMR detected EPR could also be used to measure the dependence of T_{1e} across the EPR line, which was studied in similar conditions by Weber *et al.* [144], provided lower radical concentrations are used (to limit spectral diffusion).

Chapter 5

The Spin Diffusion Barrier

DNP mechanisms describe how the electron spin polarization is transferred to the nuclear spins by μw irradiation. These mechanisms have a strong $1/r^6$ dependence on the distance r between the electron and the nuclear spins. It follows that nuclear spins that are far from an electron spin are inefficiently polarized by direct DNP. Thanks to nuclear spin diffusion, these nuclear spins may still be polarized indirectly. In this case, nuclear spins close to an electron spin are polarized by DNP, and the accrued polarization transfers spontaneously to the rest of the nuclear spins across the sample *via* nuclear dipolar interactions or nuclear flip-flops. However, spin diffusion becomes inefficient close to the electron because the field gradient caused by the electron dipolar field strongly shifts the nuclear spin frequencies. Neighboring nuclear spins with different Larmor frequencies cannot share polarization by flip-flops because the latter are no longer energy-conservative. Fig. 5.1 gives a schematic representation of the interplay between the efficiency of DNP and spin diffusion as a function of the distance to the closest electron. The radius within which spin diffusion is quenched is referred to as the *spin diffusion barrier*. [161, 173, 174, 175, 176]

In this chapter, we first review the evolution of the concept since the introduction of spin diffusion by Bloembergen in 1949. [161] We focus mainly on how the spin diffusion barrier was defined by different authors and the methods used to study it, whether experimental or theoretical. Then, we present the hyperpolarization resurgence experiment (HypRes) and its variants, which we introduced in 2021 to study spin diffusion in the vicinity of the electron spin and represents the main contribution of my Ph.D. [68, 177] An overview of the results is given in Sec. 5.1.6.

5.1 The spin diffusion barrier from its origins to today

5.1.1 Bloembergen's diffusion model and its analytical solutions

The introduction of spin diffusion is older than DNP. It was first proposed in 1949 by Bloembergen to account for nuclear relaxation in solids containing paramagnetic species, even dilute. [161] Prior to Bloembergen's foundational work, the only known mechanism for nuclear relaxation in solids was through fluctuations of the local magnetic field experienced by nuclei due to lattice vibrations. Whether the local magnetic field is that of neighboring nuclei or that of a paramagnetic impurity, in this model, lattice vibrations modulate the distance r and angle θ of dipolar interactions and hence cause nuclear relaxation. [178] Bloembergen proposed a two-step mechanism to explain paramagnetic relaxation: first, the nuclei near paramagnetic impurities are relaxed by the fluctuation of the spin state of the impurity (rather than by the fluctuations of the coordinates r and angle θ); second, spin diffusion spreads the effect to remote nuclei. He introduced an approach where the nuclear spin system is described as a continuum using a formalism similar to the diffusion of

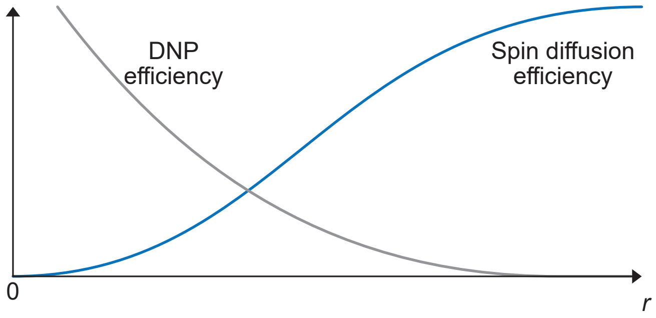

Figure 5.1: Schematic representation of the efficiency of DNP and spin diffusion as a function of the distance to the electron r.

heat. In this formalism, the variation of nuclear polarization P along the static magnetic field at position $\boldsymbol{r}$ and time t is

$$\frac{\partial}{\partial t}P(\boldsymbol{r},t) = D\nabla^2 P(\boldsymbol{r},t) - C\left(P(\boldsymbol{r},t) - P_{eq}\right)\sum_i |\boldsymbol{r}-\boldsymbol{r}_i|^{-6} - 2AP(\boldsymbol{r},t), \tag{5.1}$$

where D, P_{eq}, $\boldsymbol{r}_i$ and A are the nuclear spin diffusion coefficient, the nuclear Boltzmann polarization, the position of the paramagnetic impurity, and a constant related to saturation of nuclear spins by an rf field, respectively. C is a constant related to the dipole-dipole coupling between the nuclei I and the paramagnetic impurities S. Neglecting the angular dependence of the hyperfine interaction, C is given in the case of spin 1/2 nuclei by [109]

$$C = \frac{3}{10}\frac{\mu_0}{4\pi}\hbar^2\gamma_I^2\gamma_S^2\frac{\tau_c}{1+(\tau_c\omega_I)^2}, \tag{5.2}$$

where τ_c is the correlation time of the electron spin state along the static magnetic field (see Eq. 2.159 for more details). The spin diffusion coefficient D was estimated based on the linewidth of the NMR signal assuming that the width of the signal was dominated by nuclear dipolar interactions, yielding[1]

$$D \approx \frac{r_a^2}{50T_2} \tag{5.3}$$

where T_2 and r_a are the nuclear spin-spin relaxation time constant estimated from the width of the NMR line and the internuclear distance, respectively. Importantly, Bloembergen recognized that nuclear spins in the nearest vicinity of the electron (i.e., for small values of r) represented a special case; he stated that when the field generated by the electron spin was larger than that of the neighboring nuclear spins, spin diffusion was hindered. He called the radius within which this criterion is met, the “critical radius” r_b. The diffusion coefficient may therefore be written more precisely as

---

[1] Note that authors following Bloembergen use a factor of 30 instead of 50 (e.g., Ref [174]). Surprisingly, the authors quote Bloembergen’s calculation and use a different numeric value without explaining why.

$$D(r) \approx \begin{cases} \frac{r_a^2}{50T_2} & \text{if } r > r_b \\ 0 & \text{if } r < r_b, \end{cases} \tag{5.4}$$

In the simpler case where only a single paramagnetic impurity is considered and in the absence of an rf field, the diffusion equation reduces to

$$\frac{\partial}{\partial t}P(r,t) = D\nabla^2 P(r,t) - \frac{C}{r^6}\left(P(r,t) - P_0\right), \tag{5.5}$$

where r is the distance to the electron. The first member of the equation represents the energy conservative diffusion of nuclear polarization throughout the sample while the second term represents the relaxation of nuclear polarization towards Boltzmann equilibrium, mediated by the fluctuation of the electron spin state, i.e., paramagnetic relaxation. Bloembergen used this equation to model saturation recovery at liquid helium temperature. At higher temperatures, it was not possible to record the saturation recovery with sufficient time resolution and so he used an opposite strategy based on the interplay between simultaneous saturation and relaxation. This is why Eq. 5.1 contains a term related to saturation by rf irradiation.

To model experimental results, the polarization $P(r,t)$ was numerically predicted by Eq. 5.1 or 5.5. Then, $P(r,t)$ was integrated at each point of time t over a reasonable range of values r, yielding a signal as a function of time

$$S(t) \propto \int_{r_{\min}}^{r_{\max}} P(r,t) 4\pi r^2 dr \tag{5.6}$$

Assuming a homogeneous distribution of electron spins in the sample, $r_{\max}$ may be chosen as the radius of mean volume per electron spin

$$R_{MV} = \left(\frac{3}{4\pi N_A C}\right)^{1/3}, \tag{5.7}$$

where N_A and C are Avogadro's number and the concentration of electron spins in mol.m^{-3}, respectively. As for $r_{\min}$, one might be tempted to simply set it to 0 (i.e., at the location of the electron spin). However, nuclear spins near the electron are strongly shifted and so they do not contribute to the NMR signal. Bloembergen chose $r_{\min} = r_b$, assuming in first approximation that the radius of nucleus for which diffusion was hindered coincided with those which did not contribute to the NMR signal.

Bloembergen applied this model to a range of different crystals with different orientations with respect to the magnetic field, at different radical concentrations and from 1.2 K to room temperature. He obtained an order of magnitude agreement between the model and the experiment over these very broad experimental conditions. His paper [161] laid the foundations for decades of work on spin diffusion and paramagnetic relaxation.

In 1958, De Gennes gave an explicit analytical solution to Bloembergen's diffusion equation (see Eq. 5.5) and studied in particular the behavior of the nuclear spins close to an electron spin. [179] Based on his solution, he found that when the distribution of nuclear polarization is perturbed by rf irradiation, nuclear polarization returns to equilibrium in two phases. First, it equilibrates along the distance to the electron spin r. During this phase, the observed signal is non-exponential and has a $t^{1/2}$ dependence. This transient phase is followed by a slower return of the whole system to equilibrium which follows an exponential law

$$P(t) = P(\infty)\left(1 - \exp\left(-\frac{t}{T_1}\right)\right), \tag{5.8}$$

where $P(\infty)$ and T_1 are the polarization for $t \to \infty$ and the bulk longitudinal relaxation time constant, respectively. The weaker spin diffusion, the longer the first phase. In extreme cases of no diffusion and free diffusion, the second and first phases are absent, respectively.

De Gennes found the relaxation time constant for the second phase [179]

$$\frac{1}{T_1} = 4\pi N\rho D \approx 8.5NC^{1/4}D^{3/4}, \tag{5.9}$$

where N and ρ are the concentration of electronic spins in m^{-3} and a characteristic length parameter

$$\rho \approx 0.68\left(\frac{C}{D}\right)^{1/4}, \tag{5.10}$$

respectively.

To derive his solutions to the diffusion equation, De Gennes used the hypothesis $r_b \ll \rho \ll R_{MV}$. Furthermore, he derived his analytical solution considering that the diffusion coefficient was constant even for $r < r_b$, contrary to Bloembergen's approach (see Eq. 5.4, [161]). Note that Blumberg [173] mentions that Khutsishvili [180] obtained a similar result as De Gennes' [179] independently. However, to the best of my knowledge, this paper [180] is not accessible online.

5.1.2 The definitions of the spin diffusion barrier

Based on Khustishvili's solution [180], Blumberg then presented an extension of the solution to the case $r_b > \rho$, which corresponds to the situation where "nuclear Zeeman energy can diffuse to the paramagnetic ion faster than the paramagnetic ion can transmit it to the lattice" [173] i.e. rapid spin diffusion. On the contrary, De Gennes' solution was only valid in the diffusion-limited case. Fig. 5.2 shows a schematic representation of the two cases. He tested his model on a sample with dense nuclear spins and found a good agreement between the model and the experimental data. [173] In this paper, Blumberg introduced the term *spin diffusion barrier* for the length r_b and gave it a more precise definition than Bloembergen

$$r_b = \begin{cases} r_a\left(\frac{\mu_S}{\mu_I}\right)^{1/3} & \text{if } \tau_c \gg T_2 \\ r_a\left(\frac{\mu_S B_0}{k_B T}\frac{\mu_S}{\mu_I}\right)^{1/3} & \text{if } \tau_c \ll T_2, \end{cases} \tag{5.11}$$

where μ_S, μ_I, τ_c and T_2 are the magnetic moments of the electron and nuclear spins, the correlation time of the electron and the nuclear spin-spin relaxation time, respectively. In this definition, r_b corresponds to the radius at which the hyperfine interaction is equal to the dipolar interaction between the nuclei. In the case where the correlation of the electron spin state τ_c is short compared to the nuclear T_2 ($\tau_c \ll T_2$), the nuclei experience an averaged hyperfine interaction, which reduces the length of the diffusion barrier. As Bloembergen, Blumberg considered that the nuclei for which spin diffusion was hindered matched those which did not contribute to the NMR signal.

In 1962, Khutsishvili improved his solution to the diffusion equation by taking into account the restricted diffusion for $r < r_b$ with a diffusion coefficient of the form of Eq. 5.4. [174] Furthermore, he proposed a new definition of the diffusion barrier; in his definition, the limit is set where the nuclear dipolar interaction matches the difference in hyperfine interaction (and not the hyperfine interaction itself), leading to

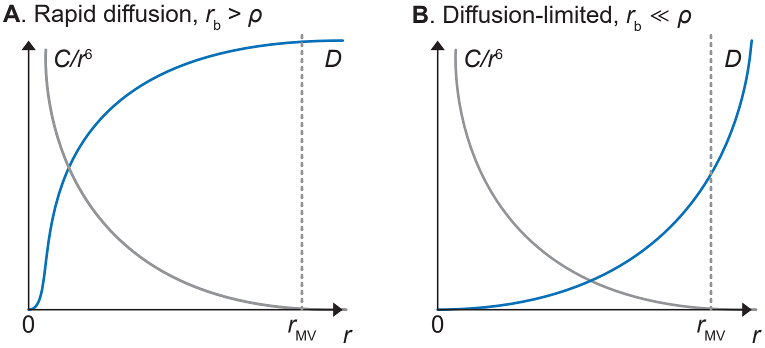

Figure 5.2: Schematic representation of rapid spin diffusion (A) vs diffusion-limited (B)

$$r_b = \begin{cases} r_a \left(\frac{\mu_S}{\mu_I}\right)^{1/4} & \text{if } \tau_c \gg T_2 \\ r_a \left(\frac{\mu_S B_0}{k_B T} \frac{\mu_S}{\mu_I}\right)^{1/4} & \text{if } \tau_c \ll T_2, \end{cases} \tag{5.12}$$

which corresponds to a shorter length compared to Blumberg's definition (see Eq. 5.11). Khutsishvili's model proved to be in reasonable agreement with most of the reported data at the time. In his paper, Khutsishvili mentions that the Heaviside-type function of $D(r)$ is a coarse approximation (see Eq. 5.4) and suggests that a function of the type [174]

$$D(r) = D(\infty) \exp\left(-cr^{-8}\right), \tag{5.13}$$

where c is a constant, is to be expected. However, obtaining an analytical solution to the diffusion equation with such a function is impossible, according to Khutsishvili.

Goldman used Khutsishvili's model to study ^{1}H relaxation in a single crystal of paradibromobenzene between 2.7 and 4.2 K at low-field (between 0 and 14 mT) as well as at higher temperatures (100 and 300 K). [181] The paramagnetic species present in the sample were unknown impurities. Despite the absence of knowledge on the types of impurities and their concentration, Goldman's measurements confirmed the validity of Khutsishvili's model, in particular the magnetic field dependence at low temperature. Contrary to Khutsishvili's conjecture of a smooth barrier (see Eq. 5.13), Goldman concluded that the barrier must be steep, according to his measurements.

Leifson and Jeffries were the first to consider the role of spin diffusion in the context of DNP. [147, 13, 148] Contrary to Khutsishvili's complex model, they introduced in 1961 a much more simplistic model of "spheres-of-influence". [147] The latter consists of estimating the bulk nuclear T_1 as the weighted average of the direct T_1^{dir} rather than solving the diffusion equation. The authors state that this approximation is valid in the case of rapid diffusion. In parallel, Khutsishvili extended his model of Ref. [174] to include DNP under SE conditions. [182] Essentially, this extension consists of including an additional term with a r^{-6} dependence into the diffusion equation. This term represents the DNP pumping and brings the polarization away from Boltzmann's equilibrium. However, this modification does not affect the description of spin diffusion. A notable difference between the nuclear diffusion dynamics under DNP as compared with at thermal equilibrium is the change in electron spin dynamics under μw irradiation. As pointed out by Leifson and Jeffries, [147] this is likely to affect the radius of the spin diffusion barrier.

The calculation of the radius of diffusion barrier r_b and hence of the bulk T_1 was refined by describing in more detail the dynamics of the electron spin. Rorschach proposed the following definition of the spins diffusion barrier [175]

$$r_b = r_a \left(3 \frac{\langle \mu_S \rangle}{\mu_I} \right)^{1/4}. \tag{5.14}$$

Like in Khutsishvili's definition (see Eq. 5.12), the limit is set where the difference in Larmor frequency of the nuclei equalizes their mutual dipolar interaction. The factor 3 appears because Rorschach explicitly calculated the derivative of the hyperfine interaction (which has a r^{-3} dependence), while Khutsishvili expressed the radius more coarsely, dropping numeric factors. The important difference with Khutsishvili's definition is how the averaging of the electron magnetic moment is calculated. Instead of simply assuming that the nuclei see an averaged field proportional to the polarization of the electron, Rorschach calculated the field experienced by the nuclei by integrating the spectral density of the electron spin state around 0

$$\langle \mu_S \rangle^2 = \frac{1}{2\pi} \int_{-2\pi/T_2}^{+2\pi/T_2} J(\omega) d\omega, \tag{5.15}$$

where T_2 and $J(\omega)$ are the nuclear spin-spin relaxation time and the spectral density function of the z-component of the electron magnetic moment, respectively, with

$$J(\omega) = (\bar{\mu}_S)^2 2\pi\delta(\omega) + \left(\overline{\mu_S^2} - (\bar{\mu}_S)^2 \right) \frac{2\tau_c}{1 + \omega^2 \tau_c^2}, \tag{5.16}$$

where $\delta(\omega)$ is the Dirac delta-function. Rorschach then expressed $(\bar{\mu}_S)^2$ and $\overline{\mu_S^2} - (\bar{\mu}_S)^2$ in terms of Brillouin's function. This spectral density function contains a static and a dynamic component (first and second terms, respectively). Rorschach's work mainly consisted of calculating the field of the electron experienced by nuclei using the static component of Eq. 5.16. His definition of the diffusion barrier has the advantage of covering the intermediate regime where τ_c is on the order of T_2. Furthermore, it treats the electron dynamics with more precision in the case where the electron polarization goes to unity, i.e., for low temperatures and high magnetic fields.

Rorschach's definition was later used by Lowe and Tse. [183] Contrary to preceding authors, they made the distinction between nuclear spins for which diffusion is quenched and those that do not contribute to the NMR signal. For the former, they used Rorschach's definition of the spin diffusion barrier (see Eq. 5.14) while for the latter, they used Blumberg's definition (see Eq. 5.11). They also treated the case where electron-electron couplings could not be neglected. [183, 184, 185] This case became more important in the seventies, after TM-DNP became popular. [15] Several authors then used the concept of electron NZ reservoir to describe electron dynamics with spin temperatures and statistical tools. [186, 187, 188]

In recent years, Hovav *et al.*'s proposed a definition of the spin diffusion barrier which includes the pseudo-secular contribution. [189, 190, 69] Furthermore, it includes an arbitrary parameter ζ that determines to which extent diffusion has to be quenched, for nuclear spins to be considered within the barrier. According to their definition, nuclear spins with Larmor frequency ω_n are within the barrier if they satisfy the following criterion

$$\zeta |D_{i,j}/2| < \frac{1}{2} \left(|A_{zz,i} - A_{zz,j}| + \frac{1}{8\omega_n} \Big| |A_{\pm,i}|^2 - |A_{\pm,j}|^2 \Big| \right), \tag{5.17}$$

where $A_{zz,i}$, $A_{zz,j}$, $A_{\pm,i}$, $A_{\pm j}$ and $D_{i,j}$ are the secular and pseudo-secular hyperfine interaction constants of nuclear spin i and j and their mutual dipolar coupling constant, respectively. Hovav *et al.* proposed this definition mainly for visualization purposes rather than using it in simulation.

5.1.3 "Leaks" in the barrier

Already during the sixties, it was found in several experimental studies that the diffusion barrier radii predicted by Khutsishvili and Rorschach's definitions were too large to account for experimental observations. Based on their ^{1}H DNP experiments on the hydration water in neodymium-doped lanthanum magnesium nitrate, Ramakrishna and Robinson estimated the diffusion barrier radius to be $r_b \approx 7-8$ Å while Khutsishvili's definition predicted 9 Å. [191, 192] They based their analysis on an innovative approach consisting of creating a gradient of nuclear polarization along the distance to the paramagnetic ion by performing negative and subsequently positive DNP. Tse and Lowe also found a spin diffusion barrier radius twice as small as that predicted by Rorschach's definition (see Eq. 5.14) in their experiments on crystalline $\mathrm{CaF_2}$. [193]

In 1971, Horvitz proposed a mechanism that could explain spin diffusion in the vicinity of the electron spin by considering the influence of the dynamic component of the electron spin in Eq. 5.16. [108] If the static component hinders spin diffusion, Horvitz showed that the dynamic component acts as a drive for spin diffusion even *within* the spin diffusion barrier. We have already mentioned this dynamic component in Sec. 2.3.4 (see Eq. 2.150) and in Chapter 4. We showed that it gave rise to a $1 - P_e^2$ dependence of paramagnetic relaxation rates (with P_e being the electron polarization). In the example of T_1 relaxation, the fluctuations of the electron spin state drive the transition between the $|\alpha\rangle$ and $|\beta\rangle$ states; in the context of spin diffusion, the fluctuations of the electron spin state drive the transition between the non-degenerate $|\alpha\beta\rangle$ and $|\beta\alpha\rangle$ states. Because the amplitude of these fluctuations is proportional to $1-P_e^2$, this spin diffusion mechanism is quenched when the electron polarization goes to unity, which leads to slower spin diffusion at lower temperatures and higher magnetic fields.

As Khutsishvili could not solve the diffusion equation for a non-constant diffusion coefficient, [174] Horvitz mentioned that his findings should be taken into account in diffusion models but he did not calculate the resulting T_1. [108] However, he computed the diffusion coefficient obtained with his model for several experimental cases reported by other authors and compared it with the reported diffusion coefficient. He found that, in many cases, the diffusion coefficient was stronger within the diffusion barrier than outside. This mechanism was later investigated in several studies and compared with experimental results. [194, 195, 196] Surprisingly, Horvitz's work received little attention and the following theoretical studies received even less.

Experimental or theoretical, these studies tended to show more and more that the concept of a rigid diffusion barrier was probably not a satisfactory picture.

So far, all the studies we have mentioned approached the spin diffusion barrier as a theoretical concept used to construct a diffusion model, except for Ramakrishna and Robinson's experiment which used an extra experimental manipulation, namely the creation of a nuclear polarization gradient [191, 192]. The main way this theoretical concept could be confronted with experiments was by predicting bulk T_1 values using the diffusion model and comparing it with measured values. At best, the theoretical and experimental T_1 were compared over a range of experimental conditions (paramagnetic species concentration, nuclear spin density, temperature, magnetic field) so that the trends predicted by theory could be confronted to experiment trends, rather than comparing a single T_1 value. However, diffusion models require a large number of input variables (τ_c, T_2, r_b, r_a, N), and their solutions are obtained at the cost of simplifications, which make the verification of the models difficult.

A one-of-a-kind experiment was proposed by Wolfe in 1973, giving the first direct experimental evidence of the spin diffusion barrier. [197] Wolfe's experiments were performed on a single crystal of ytterbium-doped yttrium ethyl sulfate at 1.62 T and between 1.4 and 4.0 K. He had previously shown that the ^{1}H resonances of the lattice positions nearest to the electron could be resolved individually, owing to their strong hyperfine interaction of up to ≈ 2 MHz. [198] In his 1973 Letter, he showed with a very simple experiment that ^{1}H spins located as close as 3 Å to the electron were still able to exchange polarization with bulk spins on a time scale much shorter than the bulk T_1. On the contrary, ^{1}H spins at 5.2 and 6.2 Å from the electron had larger hyperfine interactions than those at 3 Å (due to the anisotropy of the interaction) and were isolated from bulk spins. This result was in stark contradiction with common definitions of the spin diffusion barrier (see Eq. 5.11, 5.12 and 5.14), which predicted a radius of the diffusion barrier on the order of $r_b \approx 12$ Å. Wolfe was also able to show that the rate at which ^{1}H spins near the electron spin exchanged polarization with the bulk spins exhibited a $1 - P_e^2$ dependence on the electron polarization P_e. In that, Wolfe's work gave strong evidence in favor of the mechanism proposed by Horvitz.

Wolfe proposed an "*operational definition [of the diffusion barrier] that a spin is inside the barrier if it is in stronger thermal contact with the lattice phonons than with the bulk spins*" and he found that the only spins meeting this criterion were located at $r = 5.2$ and 6.2 Å from the electron. [197] This definition of the diffusion barrier differs from all those mentioned previously in that it is defined based on the output of an experiment rather than on theoretical arguments.

5.1.4 Experimental and theoretical approaches in modern DNP

In the past few years, several experimental pieces of evidence of efficient nuclear spin diffusion in the vicinity of electron spins have been reported. In 2019, Tan *et al.* showed that ^{1}H spins at $<$ 6 Å of a trityl radical in DNP juice were able to exchange polarization with bulk spins using selective deuteration of the polarizing agent and the three-spin SE in DNP experiments at 100 K and 0.3 T. [199] Pagliero *et al.* reported similar findings in the field of color centers in diamonds used for ^{13}C hyperpolarization. They showed that nuclear spin diffusion was possible for ^{13}C spins with coupling constants to paramagnetic centers of no less than 100 MHz. Furthermore, they proposed a mechanism to account for this peculiar diffusion process. [200] Jain *et al.* used synthetic chemistry to precisely control the distance between the closest ^{1}H spin to a V^{4+} center acting as polarizing agent at 6.9 T and 4 K. They could show that spins at 4.0 Å could not share polarization with bulk spins while those at 6.6 Å could. Using Wolfe's terminology, this implies that the spin diffusion barrier must be between 4.0 and 6.6 Å in their conditions. [201] In 2021 and 2022, we proposed the HypRes experiment, [68, 177] which will be presented in more detail in Sec. 5.1.6. Similarly to Ramakrishna and Robinson's, [191, 192] our approach consists of creating a gradient of polarization between the nuclear spins near the electron and those further away and monitoring the polarization flow from the former to the latter in a time-resolved fashion. We applied our method to DNP on glassy matrices at 7.05 T between 1.2 and 4.2 K in static mode and at 14.0 and 100 K under MAS. Our measurement showed that ^{1}H spins as close as 3 Å to the radicals were able to exchange polarization with bulk spins and gave experimental evidence of a gradient of the diffusion rate along the distance to the electron. [68] In a second study, we showed experimentally and in theory the strong influence of electron polarization on nuclear spin diffusion, [177] in agreement with Wolfe [197] and Horvitz. [108] Finally, Wili *et al.* used short steps of pulsed DNP to polarize ^{1}H spins in DNP juice in the near vicinity of a trityl radical at 1.2 T and at 50 or 80 K, followed by reverse DNP to read out the remaining nuclear polarization by EPR. [202] By varying the delay between the DNP and reverse DNP steps, they could monitor the leakage of polarization from the spins near the electron to those further away. Their study showed a minor increase in spin diffusion going from 50 to 80 K but a drastic increase upon changing the solvent from deuterated to protonated. Their results also confirmed the influence of electron dynamics on spin diffusion. [108, 197, 177]

In parallel to these experimental approaches, modern computational tools have been used by several groups to simulate DNP dynamics including the effect of spin diffusion and the spin diffusion barrier both in static mode and under DNP. Hovav *et al.* [189, 190, 69] and Karabanov *et al.* [71, 203, 72] simulated DNP dynamics in static mode in many-spin systems using full-quantum simulation. In these studies, the slowdown of nuclear polarization transfer in the vicinity of the electron is a direct consequence of how the interactions of the system are modeled; the spin diffusion barrier does not enter the model as a hypothesis, as in Blumberg or Khustishvili's early works. [173, 174]

Full quantum mechanical descriptions were also used in a number of studies of MAS-DNP by Perras *et al.* [141, 142, 143] and by Mentink-Vigier *et al.* [135, 140, 136] By including the hyperfine interaction or not in the simulations, Perras *et al* studied to which extent hindered spin diffusion in the vicinity of the electron limited to the DNP enhancement. [142] They also found that polarizing agents with a high local ^{1}H concentration around the electron spins (such as TEKpol with its phenyl-cyclohexyl substituents around the nitroxide radical) provided a path for nuclear spin diffusion from nuclear spins very near the electron to bulk spins. These studies also highlighted a spin diffusion mechanism that is specific to MAS, where the modulation of the hyperfine interactions by the MAS enables polarization transfers among nuclear spins near the electron spin. [135] This mechanism can be explained in terms of so-called avoided crossings and the transfer probability can be calculated conveniently using Landau-Zener formula [204] (avoided crossings and Landau-Zener transitions will be treated in detail in Sec. 6.2)

In an alternative approach, two studies used rate equations to describe transfers and relaxation within a large number of individual spins, in both static and MAS-DNP. [205, 206] Smith *et al.* used this approach to understand the polarization pathways in static SE-DNP of ^{1}H spins at 80 K and 5 T and concluded that polarization transport from the electron directly to bulk nuclei is more efficient than through the intermediate core nuclei. [205] In the second study, Wittmann *et al.* used the same approach to simulate the build-up curves of ^{13}C MAS-DNP on endohedral fullerene N@C60. They gave a mechanistic account of how polarization could efficiently be transferred from the core to bulk spins in this context, [206] based on the modulation of the hyperfine interaction by MAS. [135] Last, a recent study used a model based on diffusion laws reminiscent of earlier works but in the context of MAS-DNP. [207] This approach gave a phenomenological picture of the dependence of polarization transfer in the vicinity of the electron on the concentration of nuclear spins.

In summary, in the early days of the theory of spin diffusion, the main approach to study this process was by building models based on diffusion equations to predict bulk T_1 values and compare them with experimental values. The spin diffusion barrier was defined as the maximum distance where the hyperfine interaction truncates the dipolar Hamiltonian and prevents efficient spin diffusion. Several mathematical formulations were proposed (see Sec. 5.1.2). A first shift came with Horvitz who showed that spin diffusion could be driven by the fluctuations of the electron spin state, even *within* the spin diffusion barrier (as defined by the previous authors). A second shift came with Wolfe's experimental approach which showed that spin diffusion was efficient much closer to the electron than predicted by preceding definitions of the spin diffusion barrier. He proposed a new definition of the barrier as an experimental observable rather than as a theoretical concept.

In modern DNP, new experimental approaches were devised to assess the size of the barrier or more generally to study spin diffusion in the vicinity of the electron spin. In addition, modern computational tools have enabled spin dynamical simulations of systems including thousands of spins, whether in static mode or under MAS. These theoretical models have led to new insights into the mechanisms enabling spin diffusion near the electron spin.

5.1.5 The spin diffusion barrier in modern samples

While most DNP experiments in the sixties were performed on oriented crystals, [147, 13, 148, 191], modern DNP usually uses amorphous samples such as frozen solutions. [21, 25] This poses a problem for the estimation of the radius of the diffusion barrier using the definitions presented in Sec. 5.1.2. Indeed, they are based on the internuclear distance r_a. If this parameter is well-defined in a crystal, it takes a distribution of values in a glassy matrix. Here, we try to estimate the internuclear distance to deduce the size of the barrier according to the different definitions for a sample of DNP juice doped with 50 mM TEMPOL. We propose to use the radius of mean volume per spin r_{MV} (see Eq. 5.7) to estimate the distance between neighboring spins as [68]

$$r_a = 2\, r_{\mathrm{MV}}. \tag{5.18}$$

In Ref. [147, 13, 148], this distance is used to estimate the distance between neighbors among randomly distributed electrons; here, we use it to estimate the distance between neighbors among randomly distributed ^{1}H in DNP juice (only in the solvent and not among the ^{1}H of the radical molecule itself).

It was suggested to us to use the average closest neighbor instead, which is given by [150]

$$r_{\min} = \Gamma\left(\frac{4}{3}\right)\left(\frac{3}{4\pi N_A C}\right)^{1/3} \approx 0.89\; r_{\mathrm{MV}} \approx 0.45\; r_a, \tag{5.19}$$

where Γ is the gamma-function. This distance is shorter than half r_a. We believe that the average closest neighbor is not the best-suited choice because the closest neighbor can be found in any direction around a spin. Yet, only neighbors in specific directions are relevant to spin diffusion, namely those which are further away from the electron. If the closest neighbor is found at $r_{\min}$ from a spin on average, the closest neighbor *in the relevant direction* is certainly found at a longer distance, on average. In an attempt to account for this, we use the double of the radius of mean volume, as in the model of the spheres of influence. [147, 13, 148] Using this estimate, we find that the distance between neighbors in DNP juice ($C(^1\mathrm{H}) \approx 11$ mol.L^{-3}) is $r_a \approx 6.6$ Å.

Based on this estimate of r_a, Fig. 5.3 shows a visual representation of the diffusion barriers according to Blumberg, Khutsishvili and Hovav *et al.*'s definitions (see Eq. 5.11, 5.12 and 5.17, respectively) for DNP juice doped with 50 mM TEMPOL in red. They correspond to the case of high electron polarization (for example when the electron spins are at thermal equilibrium at 1.2 K and 7.05 T). For Hovav *et al.*'s definition, the hyperfine and dipolar coupling constants are orientation-dependent and so they had to be averaged over all orientations using

$$Q_{\mathrm{av}} = \sqrt{\frac{\int_0^\pi d\theta |Q(\theta)|^2 \sin\theta}{\int_0^\pi d\theta \sin\theta}}, \tag{5.20}$$

where $|Q(\theta)|$ is the norm of the quantity Q which depends on angle θ, to yield a diffusion barrier expressed as a single radius.

The radii of the diffusion barrier in Fig. 5.3 are compared with the mean volume per electron $r_{\mathrm{MV}}(e^-)$, represented in blue, which can be seen as the limits of the system. For all three definitions, the spin diffusion barrier is larger than the mean volume per electron. In other words, there should be no spin diffusion among the solvent ^{1}H spins. We ought to point out that these predictions are only rough estimates, which assume that spins are statistically distributed in space. The resulting radii of the diffusion barriers are representative of diffusion among solvent ^{1}H and not among the protons of the radical itself, where the local density of ^{1}H spins is higher.

5.1.6 HypRes, a new tool to study the diffusion barrier

In the first year of my Ph.D., we once noticed that it was not easy to saturate the signal of ^{1}H spins in DNP juice so as to obtain a spectrum of pure flat noise; a tiny signal would always remain. My supervisor argued that this persistent signal could arise from polarization within the diffusion barrier which was not affected by the saturation pulses, due to their limited bandwidth;

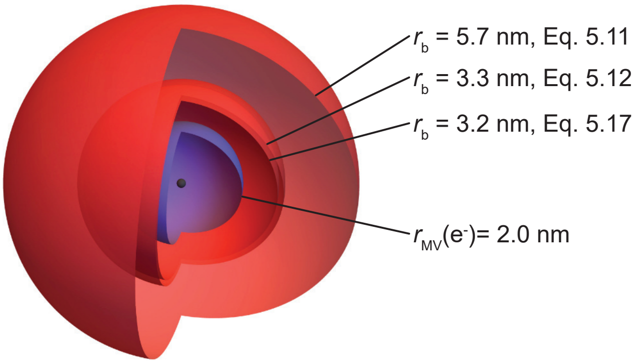

Figure 5.3: Representation of the spin diffusion barrier r_b for the solvent ^{1}H spins in DNP juice doped with 50 mM TEMPOL according to Blumberg, [173] Khutsishvili, [174] and Hovav *et al.* [190, 69] (see Eq. 5.11, 5.12 and 5.17, respectively) represented as red spheres compared with the mean volume per electron spin $r_{\mathrm{MV}}(e^-)$ represented as a blue sphere. The black sphere represents the electron. Adapted from Ref. [68] according to the terms of the Creative Commons Attribution-NonCommercial 4.0 International Public License.

this hidden polarization was able to resurge out from inside the diffusion barrier to the bulk spins. This observation gave me the idea to perform a simple experiment where we would polarize the spins until they reached the DNP plateau and then, after a short train of saturation pulses, observe the return of polarization to Boltzmann equilibrium without μw irradiation. What I expected to see was an overshoot of polarization with the same sign as the polarization acquired under DNP followed by the return from this transient state towards Boltzmann equilibrium. That is what happened indeed and we dubbed this method the HypRes experiment.

Fig. 5.4 shows a typical measurement of HypRes curve on DNP juice doped with 50 mM TEMPOL at 7.05 T and 3.8 K. The ^{1}H spins are first polarized during a delay which is long compared to the DNP build-up time constant T_{DNP}. Then, μw irradiation is gated and, after delay τ_{g}, the polarization of the visible spins is saturated with a train of m $\pi/2$ pulses. A standard saturation recovery experiment (i.e., with no DNP prior to recording the curve) is shown for comparison. In the standard saturation recovery, the polarization starts at 0 and rises monotonically to $P_{eq} = 0.19\%$. In the HypRes experiments, the polarization acquired during DNP resurges from the hidden spins, i.e., those inaccessible to direct NMR detection, to the visible spins causing a strong polarization overshoot. Importantly, when the maximum of the polarization overshoot is reached, the standard saturation experiment has just started rising, indicating that the diffusion process monitored by the HypRes experiment is faster than bulk relaxation towards Boltzmann equilibrium.

In the remainder of this chapter, we first present the results that were published in Ref. [68]. We show HypRes measurements on DNP juice doped with 50 mM TEMPOL as a function of temperature fitted with a simple two-reservoir model, giving access to an estimate of the temperature dependence of the polarization transfer between hidden and visible spins. We present unpublished data of HypRes experiments on ^{13}C DNP in [1-^{13}C]-pyruvic acid doped with 25 mM trityl, displaying a strong temperature dependence, as in the ^{1}H case. We give an example of HypRes experiment under MAS-DNP. Coming back to static DNP, we extend the possibilities of the HypRes experiment by the introduction of broadband adiabatic inversion pulses; we use these pulses to manipulate the spins within the hidden reservoir to get access to further information on spin diffusion within the hidden reservoir (these results are also published in Ref. [68]). Finally, we present the μw on-HypRes experiment where μw irradiation is turned back on during detec-

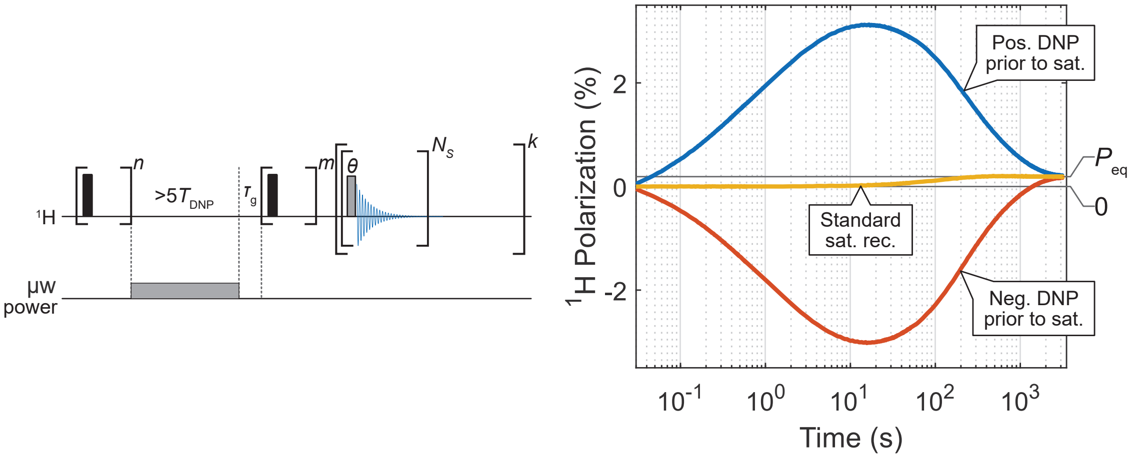

Figure 5.4: HypRes pulse sequence and typical results at 3.8 K and 7.05 T in DNP juice with 50 mM TEMPOL. The two curves with positive and negative DNP prior to HypRes measurements are compared with a standard saturation recovery experiment where no DNP was performed prior to recording the curve. Adapted from Ref. [68] according to the terms of the Creative Commons Attribution-NonCommercial 4.0 International Public License.

tion in order to monitor spin diffusion at a controlled electron polarization. The role of electron polarization on spin diffusion is rationalized using a 2 nucleus-1 electron model similar to that of Horvitz. We find that nuclear spin diffusion strongly depends on the level of electron polarization, which explains the strong temperature dependence observed both for ^{1}H and ^{13}C μw off-HypRes experiments. These results are presented in a preprint deposited on Arxiv [177].

Fig. 5.5 shows pulse sequence diagrams and typical results for the three experiments: HypRes, HypRes with inversion, and μw on-HypRes.

5.2 μw off-HypRes without inversion

In the section, we present results of the μw off-HypRes experiment in DNP juice doped with 50 mM TEMPOL under static DNP between 1.2 and 4.2 K. [68] Rather than referring to bulk and core spins, we refer to visible and hidden spins, corresponding to spins which are and are not accessible to NMR detection, respectively, depending on the strength of their paramagnetic shift. We choose this terminology to avoid ambiguity but we note that the core spins – if any – are a subset of the hidden spins. The visible and hidden spin reservoirs have average polarization P_v and P_h, respectively.

The detailed steps of the HypRes experiment are the following:

1. **Full saturation**. The polarization of the nuclear spins is wiped out so that the experiment starts in known conditions by a series of hard rf pulses

2. **Prepolarization**. μw are turned on during a delay set to be at least five times the ^{1}H DNP build-up time constant so that, when the μw are gated, the sample is assumed to have reached DNP equilibrium with a spatially homogeneous polarization $P_{\mathrm{DNP}}^{\mathrm{max}}$.

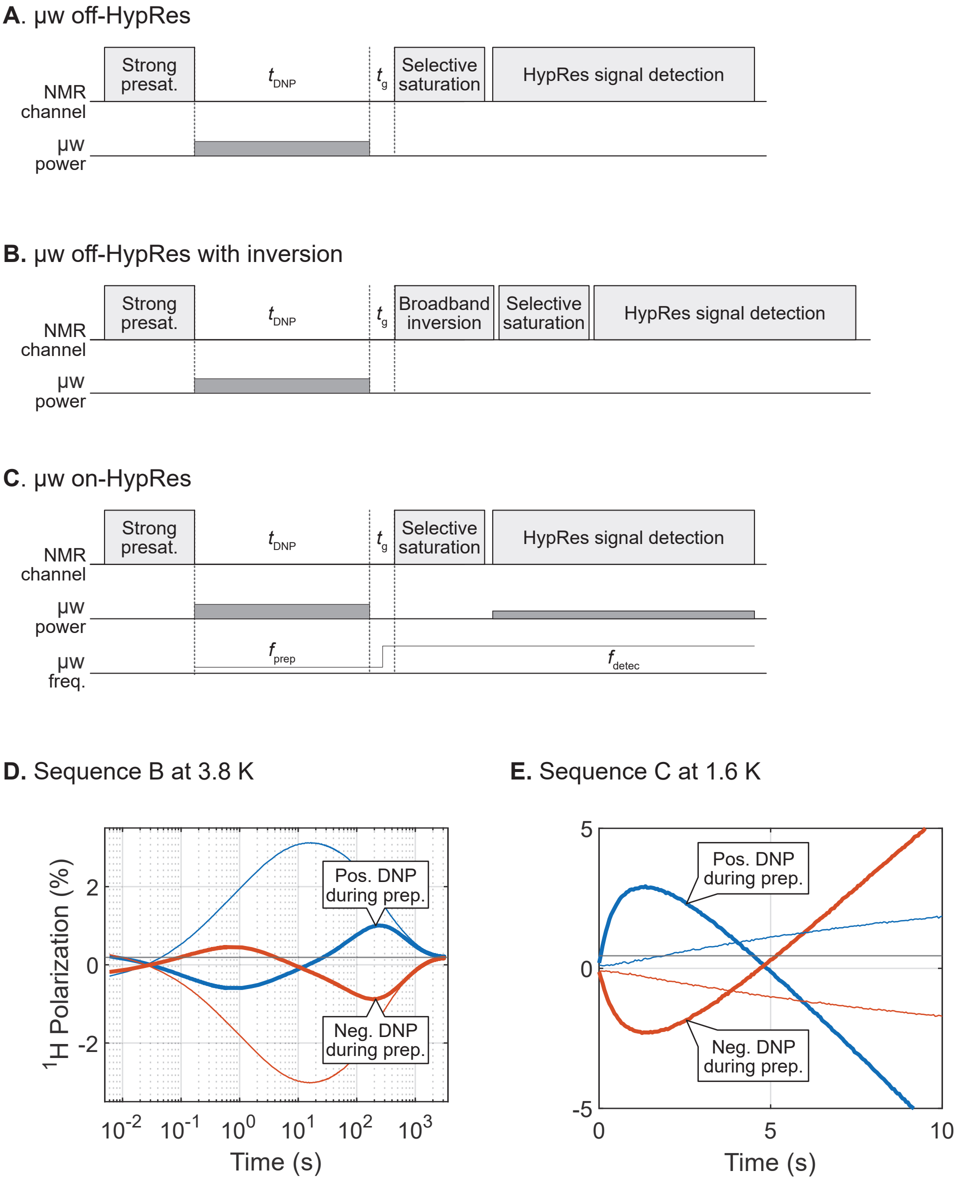

Figure 5.5: **A-C**. Pulse sequence diagrams of HypRes experiments. **D-E**. Typical results of experiments of Panels B and C, respectively, on DNP juice doped with 50 mM TEMPOL. The faint lines are the results of experiments of Panel A on the same sample and in the same conditions, shown for comparison.

3. **Visible spins saturation**. The NMR signal is saturated using a train of hard rf pulses. Since the saturation pulses have limited bandwidth, the spins that experience a strong hyperfine shift due to a nearby paramagnetic center are not affected. The saturation scheme is optimized to be efficient for the visible nuclear spin with the polarization of the visible spins $P_v \approx 0$, while remaining as short as possible in order to leave the hidden nuclear spins unaffected with $P_h = (1{-}\eta_{\mathrm{sat}})P_{\mathrm{DNP}}^{\mathrm{max}}$ where η_{sat} is an attenuation factor ideally close to 0.

The saturation block is terminated by a delay to accommodate acoustic ringing and allow remaining transverse magnetization to dephase before detection. At this point, the proton spin system has polarization values $P_v \approx 0$ and $P_h = (1-\eta_{\mathrm{sat}})P_{\mathrm{DNP}}^{\mathrm{max}}$.

4. **Resurgence monitoring**. The hyperpolarization resurgence is monitored for the visible spin reservoir by NMR acquisition blocks separated by time delays.
5. **Decay monitoring**. The return to thermal equilibrium is monitored.

5.2.1 Two-reservoir model

A model is used to interpret the data assuming that the visible and hidden spins behave as reservoirs exchanging polarization at flow rate R_f and that each reservoir returns to thermal equilibrium with respective intrinsic relaxation rates, $R_{1,v}$ and $R_{1,h}$, which is reminiscent of typical spin temperature models. [3] Fig. 5.6 shows a schematic representation of the model. The underlying assumption is that diffusion within the reservoirs is fast with respect to the flow between them which allows the polarization to be considered as "instantly" uniform inside each reservoir. This assumption is reasonable within the bulk. But, of course, diffusion is expected to be hindered within the hidden reservoir by the presence of the electron. This simplification is a tradeoff to describe the system with a simple model in first approximation. It is also assumed that no other reservoirs significantly influence the proton spin system. In particular, it is assumed and later verified, that the deuterium nuclei present within the sample are not responsible for the observed effect.

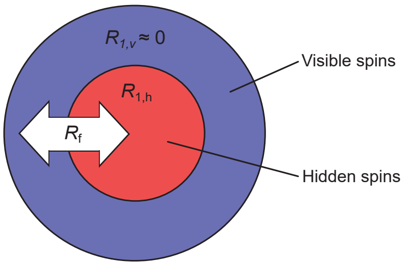

Figure 5.6: Schematic representation of the model used to analyze HypRes results. The relaxation rate constant of the visible spins $R_{1,v}$ is assumed to be negligible. Polarization flows between the visible and hidden reservoirs at flow rate R_f, while the hidden spins relax to thermal equilibrium at rate $R_{1,h}$. Adapted from Ref. [68] according to the terms of the Creative Commons Attribution-NonCommercial 4.0 International Public License.

Under the assumptions above, the evolution of the polarizations in the visible and hidden reservoir, $P_v(t)$ and $P_h(t)$, is given by the following differential equation

$$\frac{d}{dt}\begin{pmatrix} P_v \\ P_h \end{pmatrix} = \begin{pmatrix} -\chi_h R_f - R_{1,v} & \chi_h R_f \\ (1-\chi_h)R_f & -(1-\chi_h)R_f - R_{1,h} \end{pmatrix}\begin{pmatrix} P_v \\ P_h \end{pmatrix} + P_{eq}\begin{pmatrix} R_{1,v} \\ R_{1,h} \end{pmatrix}, \tag{5.21}$$

where χ_h is the fraction of the nuclear spins in the hidden reservoir and P_{eq} is the nuclear polarization at Boltzmann equilibrium. The derivation of the model is given in Supplementary Material of Ref [68]. The solution to this differential equation is

$$\begin{pmatrix} P_v \\ \\ P_h \end{pmatrix} = P_{eq} - \alpha V_- e^{-\lambda_- t} - \beta V_+ e^{-\lambda_+ t}, \tag{5.22}$$

with the eigenvalues λ_+ and λ_- and eigenvectors V_+ and V_- given by

$$\lambda_\pm = \frac{-R_f - R_{1,h} - R_{1,v} \pm \sqrt{(R_f + R_{1,h} - R_{1,v})^2 + 4\chi_h R_f (R_{1,v} - R_{1,h})}}{2} \tag{5.23}$$

and

$$V_\pm = \begin{pmatrix} 1 + \frac{R_{1,h}+\lambda_\pm}{R_f(1-\chi_h)} \\ \\ 1 \end{pmatrix}, \tag{5.24}$$

respectively. The coefficients α and β depend on the initial conditions and are given by

$$\begin{aligned} \alpha &= \tfrac{(\lambda_+ + R_{1,h})(P_{eq} - P_h^0) + (1-\chi_h) R_f (P_v^0 - P_h^0)}{\lambda_+ - \lambda_-} \\ \beta &= \tfrac{(\lambda_- + R_{1,h})(P_{eq} - P_h^0) + (1-\chi_h) R_f (P_v^0 - P_h^0)}{\lambda_- - \lambda_+} \end{aligned},$$

where P_v^0 and P_h^0 are the polarizations of the visible and hidden reservoirs at $t = 0$, respectively, which corresponds to the beginning of NMR signal detection. Since the visible reservoir is saturated, we have $P_v^0 = 0$. Since the polarization is assumed to be homogeneous throughout each reservoir at $t = 0$, the polarization of the hidden reservoir is equal to the polarization at the DNP equilibrium, that is, $P_h^0 = P_{\text{DNP}}^{\text{max}}$. The eigenvalues λ_+ and λ_- determine the two relevant time scales predicted by the model. $-\lambda_-$ corresponds to the rate at which the two reservoirs equilibrate with each other while $-\lambda_+$ corresponds to the rate at which their polarizations return toward Boltzmann equilibrium, after equilibration. This rate thus corresponds to the longitudinal relaxation rate constant R_1, and so we write

$$R_1 = -\lambda_+. \tag{5.25}$$

In our conditions, we approximate that the intrinsic relaxation rate constant of the bulk spins $R_{1,v}$ is 0, that is, the visible spins only reach Boltzmann equilibrium through spin diffusion towards the hidden spins which are efficiently relaxed by the nearby electrons. In the data set presented below, the curves obtained in the HypRes experiment are expressed in terms of polarization excess with respect to thermal equilibrium, the thermal build-up must therefore be subtracted yielding

$$\begin{pmatrix} E_v \\ \\ E_h \end{pmatrix} = \begin{pmatrix} P_v \\ \\ P_h \end{pmatrix} - P_{eq}(1 - e^{\lambda_+ t}) = -\alpha V_- e^{\lambda_- t} - (\beta V_+ - P_{eq}) e^{\lambda_+ t}, \tag{5.26}$$

where E_v and E_h are the polarization excess in the visible and hidden reservoirs, respectively.

5.2.2 Temperature-dependent spin diffusion

The HypRes experiment was performed on DNP juice doped with 50 mM TEMPOL at 7.05 T between 1.2 and 4.2 K. For each temperature, a standard saturation recovery experiment was recorded in addition and was subtracted from the HypRes curve to yield a polarization excess. The obtained polarization excess along time is shown in Fig. 5.7a (grey crosses). During the preparation step, the sample was polarized in positive mode, causing a positive polarization overshoot in the HypRes experiment. Because of the prohibitively slow relaxation at the lowest temperatures, the curves were not recorded until they had reached thermal equilibrium. In particular, at 1.2 K, the polarization had reached its maximum but was only starting to decay when the monitoring was stopped.

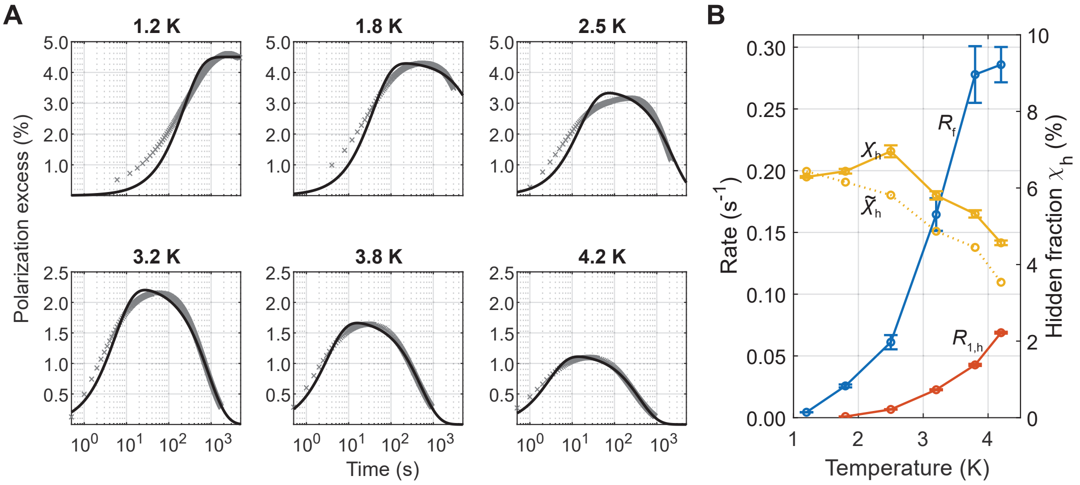

Figure 5.7: **A**. Results of the HypRes experiment at 7.05 T between 1.2 and 4.2 K for DNP juice doped with 50 mM TEMPOL, monitored with small-angle pulses expressed in terms of polarization excess with respect to thermal equilibrium. The gray crosses and the black lines represent the experimental data and the fit of the two-reservoir model (see Eq. 5.26), respectively. **B**. Fitted parameters of the two-reservoir model plotted against temperature. The size of the hidden reservoir is given according to the two-reservoir model (χ_h) and according to Eq. 5.27 ($\tilde{\chi}_h$). The error bars correspond to the error of the fit with 95% confidence. Adapted from Ref. [68] according to the terms of the Creative Commons Attribution-NonCommercial 4.0 International Public License.

The two-reservoir model described above was applied to these HypRes curves (black curves in Fig. 5.7a). As explained in the previous section, it was assumed that the polarization of the visible and hidden reservoirs at the beginning of detection were 0 and $P_{\mathrm{DNP}}^{\mathrm{max}}$, respectively, and that the intrinsic relaxation rate of the visible reservoir was negligible $R_{1,v} \approx 0$. The three remaining free parameters are $R_{1,h}$, R_f and χ_h. Their fitted values are shown in Fig. 5.7b. The flow rate R_f spreads over two orders of magnitude from $4.4 \cdot 10^{-3}$ s^{-1} to 0.29 s^{-1}. The relaxation rate of the hidden reservoir R_h is not shown for 1.2 K because its fitted value is unrealistically small and out of the trend (the fitted value is between 10^{-14} and 10^{-11} s^{-1} depending on the starting point of the fit algorithm). However, neither the quality of the fit nor the fitted values of R_f and χ_h are significantly affected by the value of $R_{1,h}$ (the fit was repeated fixing $R_{1,h}$ between 0 and 10^{-5} s^{-1} which did not affect R_f and χ_h significantly). For the available range, $R_{1,h}$ spreads from $9.4 \cdot 10^{-4}$ to $6.9 \cdot 10^{-2}$ s^{-1}. The fitted size of the hidden reservoir χ_h is between 5 and 7%. We show in Fig. 5.8 that the HypRes effect occurs also in a fully protonated sample, that is, in the absence of a deuterium spin reservoir.

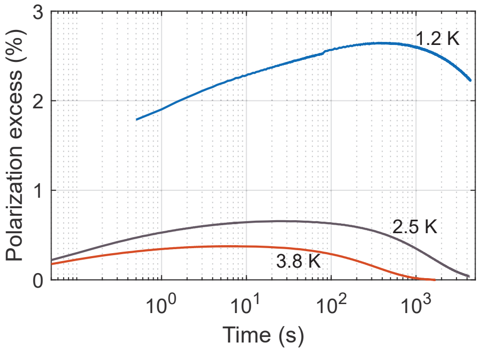

Figure 5.8: HypRes experiment in 2:3 H_2O:glycerol (v/v), i.e., the fully protonated equivalent of DNP juice, doped with 50 mM TEMPOL. Adapted from Ref. [68] according to the terms of the Creative Commons Attribution-NonCommercial 4.0 International Public License.

The model fits the data appropriately during the decay of the curves, that is, once the strong polarization gradient between hidden and visible spins has already disappeared. As expected, the quality of fit is poorer at the beginning of the curve, during the equilibration. The simplicity of the model that assumes two homogeneous reservoirs does not account for the complex dynamics of the spin system when gradients are equilibrating among the hidden spins. Nonetheless, it allows for at least an order of magnitude estimate of the flow between the reservoirs and shows its tremendous temperature dependence.

The relaxation rate of the hidden reservoir $R_{1,h}$ is found to be slow compared with the flow between the reservoirs R_f (the ratio $R_{1,h}/R_f$ goes from $\approx 1/4$ to $\approx 1/27$ at 4.2 and 1.8 K, respectively). This implies that the two domains of the HypRes curve (the equilibration and the decay) can be interpreted separately; the rise of the polarization excess informs on the flow between the reservoirs R_f, while the decay informs on the relaxation rate $R_{1,h}$. It also implies that polarization is able to equilibrate throughout the spin system before relaxation becomes substantial. In this limit, the size of the hidden reservoir is directly proportional to the intensity of the overshoot P_{HypRes}

$$\tilde{\chi}_h \geq \frac{P_{\mathrm{HypRes}}}{P_h^0} = \frac{P_{\mathrm{HypRes}}}{(1-\eta_{\mathrm{sat}})P_{\mathrm{DNP}}^{\mathrm{max}}} \geq \frac{P_{\mathrm{HypRes}}}{P_{\mathrm{DNP}}^{\mathrm{max}}}, \tag{5.27}$$

where η_{sat} and $P_{\mathrm{DNP}}^{\mathrm{max}}$ are the attenuation of the polarization in the hidden reservoir caused by the saturation block at the end of preparation and the polarization measured at DNP equilibrium, respectively. The size of the hidden reservoir can be obtained with this method ($\tilde{\chi}_h$) or with the two-reservoir model (χ_h). While the latter is biased by the poor match of the two-reservoir model, the former gives a more direct estimate of the size of the hidden reservoir by the HypRes experiment. Fig. 5.7b shows that the size of the hidden reservoir, evaluated with Eq. 5.26, seems to decrease when temperature increases. Two effects can explain this apparent dependence. First, due to the increase of flow rate R_f with temperature, more polarization is able to leak out of the hidden reservoir during saturation at higher temperatures. As the saturation scheme was identical for all six HypRes curves, an increased saturation of the hidden reservoir η_{sat} with temperature can be expected and thus a smaller "apparent" size. Second, the condition that the polarization flow is much faster than relaxation is better satisfied at the lowest experimental temperatures.

5.2.3 The size of the hidden reservoir

The size of the hidden reservoir was quantified in a separate experiment for comparison with the values obtained above. The ^{1}H thermal equilibrium signal build-up of DNP juice was recorded as a function of TEMPOL concentration at 3.8 K and fitted with a stretched exponential model. These results were already presented in Sec. 3.3.1 (see Fig. 3.20) and are reproduced in Fig. 5.9A. They show how the thermal equilibrium signal decreases with increasing TEMPOL concentration. The signal was not recorded without TEMPOL because of the very slow relaxation of ^{1}H spins in the absence of paramagnetic relaxation. Assuming that the signal loss is linear with the TEMPOL concentration in the low range, we extrapolate the intensity at a concentration of 0 (here, we simply used the slope between the first two points) to normalize the curve with a y-intercept of 100%. From this curve, we find that the presence of 50 mM of TEMPOL in DNP juice removes $\approx$ 30% of the ^{1}H signal.

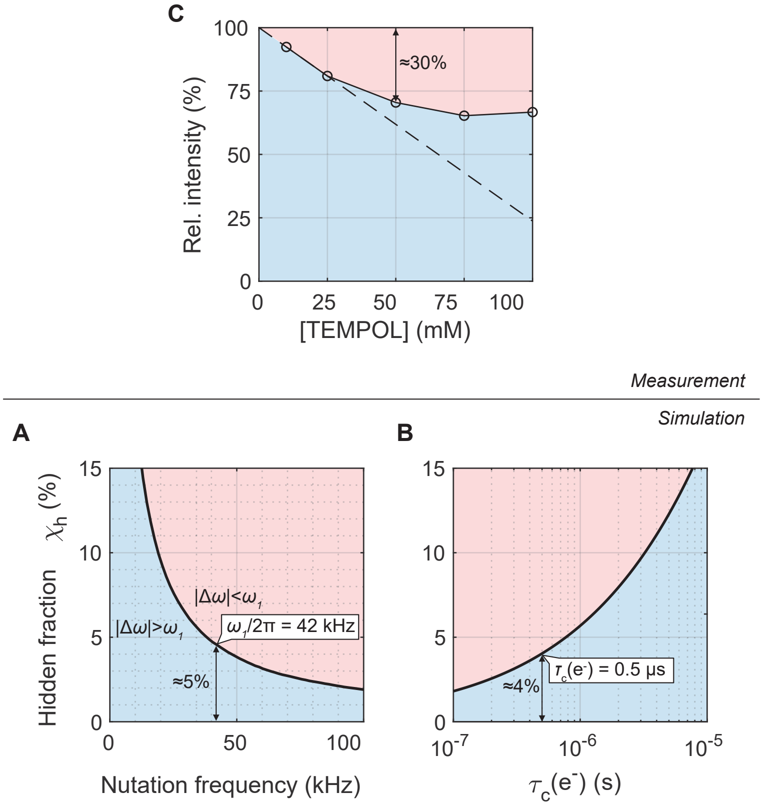

Figure 5.9: **A**. Relative ^{1}H signal as a function of TEMPOL radical concentration in DNP juice at 3.8 K (open circles) showing that the presence of the radical quenches $\approx$ 30% of the NMR signal for a concentration of 50 mM. The dashed line represents a linear interpolation of the first two points. **B**. Simulated fraction of the spins that are hidden because they are unaffected by rf pulses as a function of the pulse bandwidth. $\Delta\omega$ and ω_1 are the paramagnetic shift and nutation frequency of the pulses, respectively, used to discriminate between visible and hidden spins. **C**. Simulated fraction of the spins that are hidden because of the reduction in transverse relaxation time constant due to PRE. The light blue and pink areas represent the visible and hidden fraction of the ^{1}H spins, respectively.

Two effects may account for the signal loss in the presence of a paramagnetic species. First, the hyperfine interaction with electrons shifts the Larmor frequency of the close nuclei outside of the detection limits. Second, the interaction with electrons shortens the transverse relaxation time of the nuclei, an effect known as paramagnetic relaxation enhancement (PRE), which increases the signal loss during the dead time between the pulse and the acquisition. [149] Fig. 5.9B and 5.9C show simulations of the two contributions, which were performed assuming a random distribution of 1926 electrons in a cube of 40 nm (corresponding to the concentration of 50 mM). The paramagnetic shifts and the PRE were averaged over 1000 random nuclear coordinates within the cube (5 nm widths on the edges of the box were excluded) using the equation detailed below. The values were averaged over 200 repetitions of this procedure. Fig. 5.10 shows the convergence of the algorithm along the repetitions.

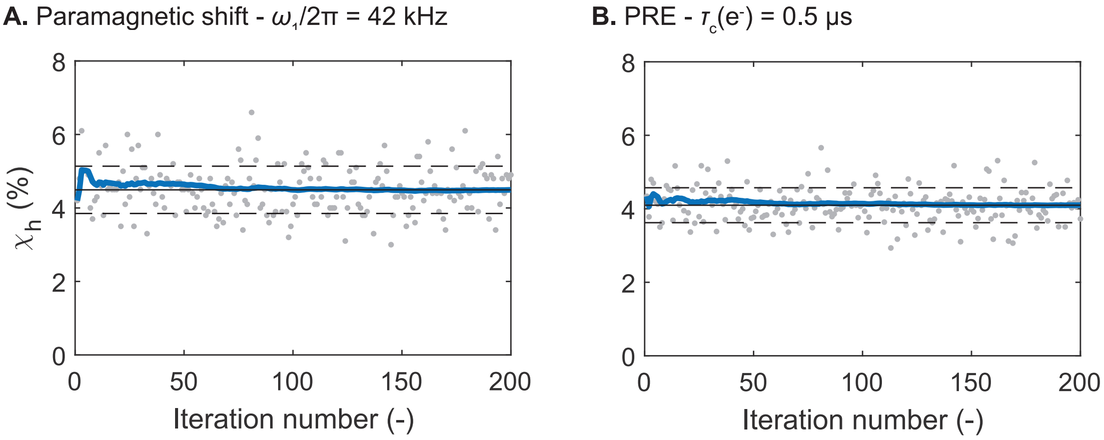

Figure 5.10: Convergence of the algorithm for the calculation of the hidden fraction of the ^{1}H spins χ_h due to paramagnetic shifts and PRE, obtained with Eq. 5.29 and Eq. 5.33, **A** and **B**, respectively. These plots correspond to single points on the curves shown in Fig. 5.9, obtained for $\omega_1/2\pi = 42$ kHz and $\tau_c(e^-) = 0.5$ μs, respectively. The grey dots and the blue line correspond to the values of individual iterations and of the mean value up to a given iteration, respectively. The solid and dashed black lines correspond to the total average and the standard deviation, respectively.

The ^{1}H paramagnetic shift of the j^{th} ^{1}H spin due the i^{th} electron is given by

$$\Delta\omega_i(\boldsymbol{r}_j) = \frac{1}{4}\frac{\mu_0}{4\pi}\frac{\hbar\gamma_e\gamma_n}{r_{ij}^3}\left(1 - 3\cos^2\theta_{ij}\right), \tag{5.28}$$

where $\boldsymbol{r}_j$, r_{ij} and θ_{ij} are the position of the nucleus, the distance between the nucleus and the electron, and the angle between the vector connecting them and the main magnetic field, respectively. The contributions of all electrons in the random distribution were summed as

$$\begin{aligned}\Delta\omega(\boldsymbol{r}_j) &= \sum_i \Delta\omega_i(\boldsymbol{r}_j)\\ &= \frac{\mu_0}{4\pi}\frac{\hbar\gamma_e\gamma_n}{4}\sum_i \frac{1}{|\boldsymbol{r}_j - \boldsymbol{r}_i|^3}\left(1 - 3\left(\frac{r_{j,z} - r_{i,z}}{|\boldsymbol{r}_j - \boldsymbol{r}_i|}\right)^2\right).\end{aligned} \tag{5.29}$$

^{1}H spins were considered undetectable when their paramagnetic shift was larger than the excitation bandwidth of the pulse, which we estimated to be equal to the nutation frequency (42 kHz).

$$|\Delta\omega| > \omega_1 \tag{5.30}$$

We found that $\approx 5\%$ of the spins are hidden according to this criterion (see Fig. 5.9).

The transverse relaxation rate of ^{1}H spins was assumed to be dominated by paramagnetic interactions and any other contribution was neglected

$$T_2 \approx T_{2,para}. \tag{5.31}$$

The paramagnetic transverse relaxation time of the j^{th} nuclear spin under the fluctuating field of the i^{th} electron was calculated using the formula of PRE, neglecting the angular dependence of the hyperfine interaction [149] but including the $1 - P_e^2$ correction accounting for high electron polarization (with $P_e \approx 0.85$ at 3.8 K and 7.05 T)[2]

$$\frac{1}{T_{2,para}^{ij}} = (1 - P_e^2)\left(\frac{\mu_0}{4\pi}\right)^2 \frac{\hbar^2\gamma_e^2\gamma_n^2}{r_{ij}^6}\left(\frac{3}{20}\frac{\tau_c}{1+\omega_n^2\tau_c^2} + \frac{1}{5}\tau_c\right) \tag{5.32}$$

where ω_n is the ^{1}H Larmor frequency. The contribution to PRE of all electrons was assumed to be additive and so the total relaxation of the j^{th} nuclear spin is

$$\frac{1}{T_{2,para}^{j}} = (1 - P_e^2)\left(\frac{\mu_0}{4\pi}\right)^2 \hbar^2\gamma_e^2\gamma_n^2\left(\frac{3}{20}\frac{\tau_c}{1+\omega_n^2\tau_c^2} + \frac{1}{5}\tau_c\right)\sum_i \frac{1}{|\boldsymbol{r}_i - \boldsymbol{r}_j|^6} \tag{5.33}$$

Assuming that the signal integral is proportional to the first point of the FID, the contribution of nuclear spin j to the signal integral was computed as

$$I_j = \exp\left(-\frac{\tau_{DE}}{T_2^j}\right), \tag{5.34}$$

where τ_{DE} is the dead time between the pulse and the start of the acquisition. The contribution to the signal integral obtained using Eq. 5.34 was averaged over all nuclear spins.

The correlation time of the electron spin state $\tau_c(e^-)$ was calculated using Eq. 2.161, that is, as the inverse of the dipolar interaction with the neighboring electron spins. Because each electron interacts with many others, the correlation time was calculated using the strongest dipolar interactions of each electron. The resulting correlation time was averaged over all electrons in the box and over 1000 repetitions of the algorithm. The correlation time was found to be $\tau_c(\mathrm{e}^-) \approx 0.5$ μs. Fig. 5.9B shows that 4% of the ^{1}H spins are hidden by PRE for this value of $\tau_c(e^-)$.

Both paramagnetic shifts and PRE simulations lead to the conclusion that the fraction of hidden spins χ_h is on the order of 4-5%. The contributions of the two effects simulated here may have different angular dependencies but they do not add up together in such a way that could explain the experimentally determined signal loss of $\approx 30\%$ shown in Fig. 5.9A.

It should be noted that even if the PRE may contribute to the signal losses shown in Fig. 5.9A, it is not the effect that enables HypRes. On the contrary, the frequency shift causes the ^{1}H spins near the electron spins to be immune to saturation pulses, which is the essential ingredient allowing the creation of a polarization gradient near the electron and thus for the HypRes effect. Interestingly, our simulation shows that $\approx 5\%$ of the ^{1}H spins in DNP juice with 50 mM TEMPOL

---

[2] Note that, in Ref [68], we improperly used an expression of the paramagnetic relaxation rate which is appropriate for molecules in the liquid-state. Here, we repeated the simulation with the appropriate Eq. 5.33. Yet, the results are not significantly affected.

are beyond the bandwidth of the pulses, in reasonable agreement with the result of the HypRes experiment shown in Fig. 5.7 (hidden reservoir size between 5 and ≈ 7%).

The HypRes experiment was repeated at 3.8 K with various saturation pulse nutation frequencies with a constant pulse angle $\pi/2$ (see Fig. 5.11A). We found that the dependence of the hidden fraction on the nutation frequency of the saturation pulses follows the same trend for experiment and simulation (see Fig. 5.11B). The curve obtained after saturation by pulses with 50 kHz nutation frequency does not follow the trend. This is probably because the amplifier is not able to output the sufficient power to realize a pulse with a nutation frequency of 50 kHz and so the actual nutation frequency is lower, resulting in an incomplete saturation of the visible spins. Note that the curve obtained with 42 kHz nutation frequency saturation yielded a hidden fraction $\chi_h = 8\%$ while the results of Fig. 5.7 with the same nutation frequency and the same temperature. The reason for this is that the experiments of Fig. 5.11 were performed later, with a better-optimized but probably incomplete saturation scheme (the optimized parameters are the number of pulses and the delay between the pulses).

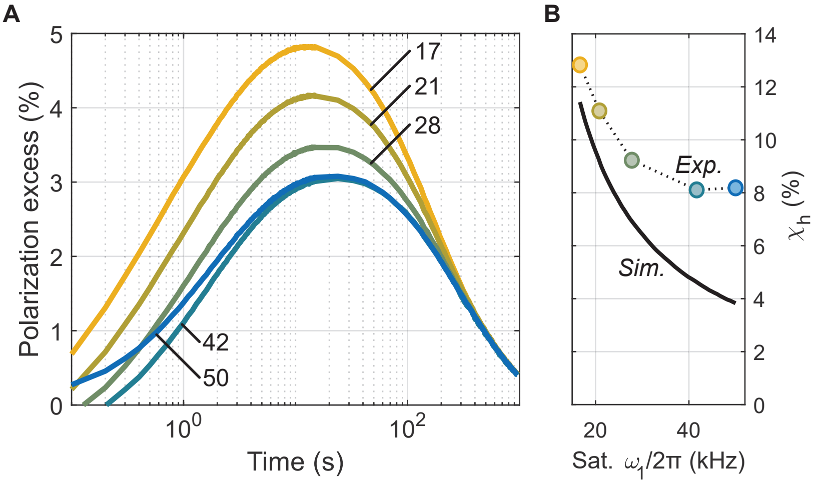

Figure 5.11: **A**. HypRes at 3.8 K after DNP in positive mode using a range of nutation frequencies for the $\pi/2$ saturation pulses (marked next to the curves in kHz). **B**. Size of the hidden reservoir measured experimentally (colored dots) using the maximum of the HypRes curves of panel A (see Eq. 5.27) and simulated using the procedure described above (black solid line). Adapted from Ref. [68] according to the terms of the Creative Commons Attribution-NonCommercial 4.0 International Public License.

The relatively good match between the results of the HypRes experiment and the simulated hidden fraction further confirms that the HypRes polarization overshoots are indeed due to polarization flowing from hidden to visible ^{1}H spins and not due to cross-relaxation from another reservoir such as ^{2}H spins.

5.3 Other examples of HypRes data

5.3.1 ^{13}C-HypRes with trityl radical

So far, the HypRes experiment was only demonstrated for ^{1}H spins. We now show that it is also applicable to ^{13}C-DNP in dDNP conditions. We chose the most typical sample in this context, i.e., 25 mM trityl OX063 in neat [1-^{13}C]-pyruvic acid. [45] HypRes experiments were performed on 100

μL of this sample between 1.8 and 3.8 K. Experiments were not performed at lower temperatures due to the prohibitively long time scale of ^{13}C relaxation.

Fig. 5.12A and B show a hyperpolarized ^{13}C spectrum and DNP build-ups under negative DNP, respectively, which were fitted with a monoexponential function

$$P(t) = P_{\mathrm{DNP}}^{\mathrm{max}} \left(1 - \exp\left(-\frac{t}{T_{\mathrm{DNP}}}\right)\right), \tag{5.35}$$

where $P_{\mathrm{DNP}}^{\mathrm{max}}$ and T_{DNP} are the maximum DNP polarization and the DNP build-up time constant, respectively. The fit parameters are shown on Fig. 5.12C and D.

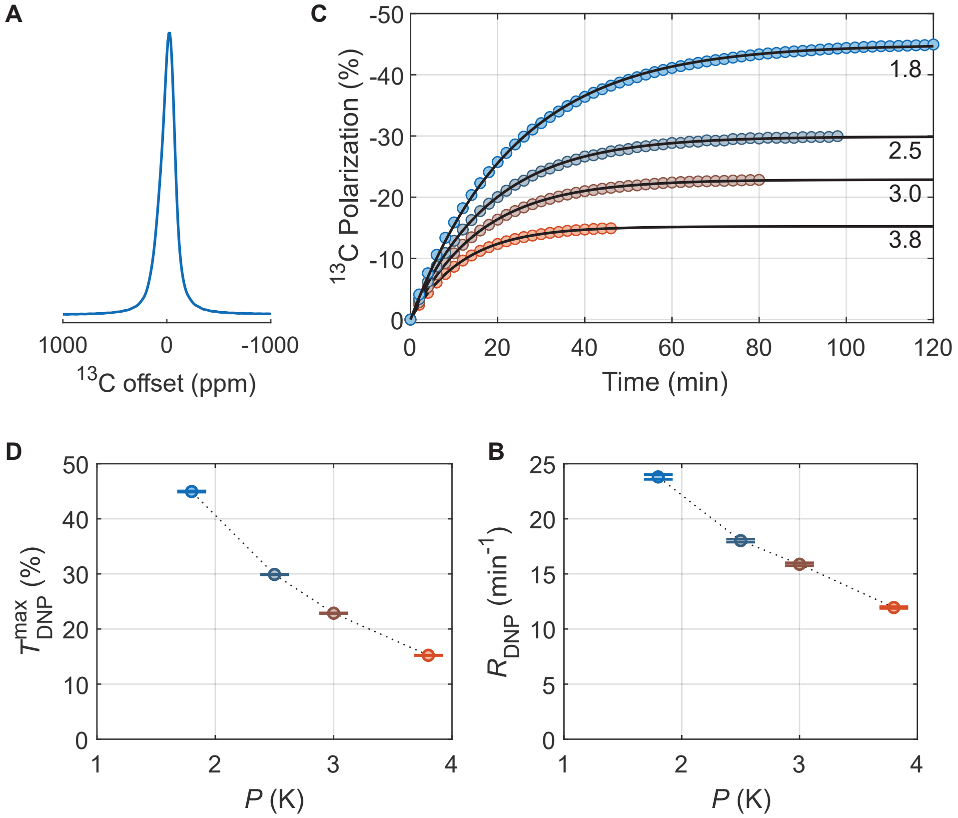

Figure 5.12: **A**. Hyperpolarized ^{13}C spectrum at 1.8 K after 120 min of DNP in neat [1-^{13}C]-pyruvic acid doped with 25 mM trityl OX063. **B**. DNP build-up curves in the same sample detected with 5° pulses at various temperatures (shown next to the curves in K). Colored circles and black lines represent experimental data and monoexponential fits (see Eq. 5.35), respectively. **C-D**. Fit results of the two free parameters of the monoexponential functions. The error bars correspond to the error of the fit with 95% confidence.

Following DNP build-ups, after the μw had been gated, the visible spins were saturated by a train of 20 $\pi/2$ pulses separated by 200 μs with a nutation frequency $\omega_1/2\pi = 20$ kHz (saturation pulses were also applied on the ^{1}H channel), shifting the phase of the pulse by $\pi/2$ after each pulse. Then, the ^{13}C-HypRes signal was detected using single 5° pulses. To maximize the time resolution without allowing detection to retrieve too much ^{13}C polarization, the delays between detection blocks at the beginning of the HypRes detection were defined in a list of variable delays (chosen individually for each experiment). Following the end of the list, the signal was detected with a constant delay between detection blocks (2, 4, 10, and 15 min for HypRes at 3.8, 3.0, 2.5, and 1.8 K, respectively).

The resulting HypRes curves are shown in Fig. 5.13. Contrary to ^{1}H HypRes experiments, note that the curves are not displayed as polarization excess but rather as polarization. Therefore the curves tend towards the ^{13}C Bolzmann equilibrium polarization P_{eq} rather than towards 0. However, because the polarization retrieved by the detection pulses is non-negligible towards the end of the experiment, the HypRes curves end up tending towards a lower value than P_{eq}. Note that during the experiment at 3.0 K, the cryostat had to be refilled. The procedure failed which caused the temperature to raise momentarily up to 3.8 K. The temperature was then lowered back down to 3.0 K. This certainly explains the discontinuity of the curve at $\approx 10^3$ s.

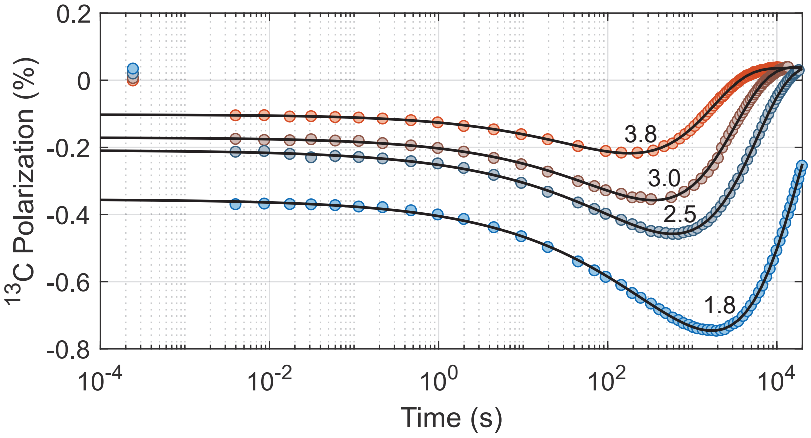

Figure 5.13: ^{13}C-HypRes experiment in neat [1-^{13}C]-pyruvic acid doped with 25 mM trityl OX063 detected with 5° pulses at various temperatures (shown next to the curves in K) after DNP in negative mode. Colored dots and black curves represent experimental data and stretched biexponential fits (see Eq. 5.36), respectively.

A peculiar feature of this set of experiments is that the first spectrum of each HypRes experiment features an antiphase pattern with an integral near 0 (see Fig. 5.13), suggesting the presence of multispin-order, despite prior intense saturation. Fig. 5.14A and B show the first spectrum and the following spectra, respectively, in the case of the experiment at 1.8 K. However, already at the second detection, i.e., less than a ms later, the spectrum is in-phase with a non-negligible polarization. All four experiments exhibit this same change from anti-phase to in-phase signal, from the first to the second detection block. After that, the signal remains stable for several hundreds of ms until the negative polarization of the hidden spins acquired during preparation starts reaching the visible spins by spin diffusion, on a time scale of hundreds of seconds to hours (depending on temperature). It is clear that the mechanism which causes the signal to go from anti-phase to in-phase is much faster than spin diffusion. A possible explanation is that the saturation pulses, which are separated by constant delays, lead to an echo in addition to the (incomplete) saturation. However, this does not explain how the anti-phase pattern would spontaneously convert into in-phase. In the following discussion, we assume that the saturation scheme is imperfect leaving $P_v^0 > 0$. Furthermore, we discard the first point of each HypRes curve in the fits that will be detailed next.

The four HypRes experiments presented in Fig. 5.13 were fitted with a biexponential function with a stretched coefficient β on the faster time component T_f

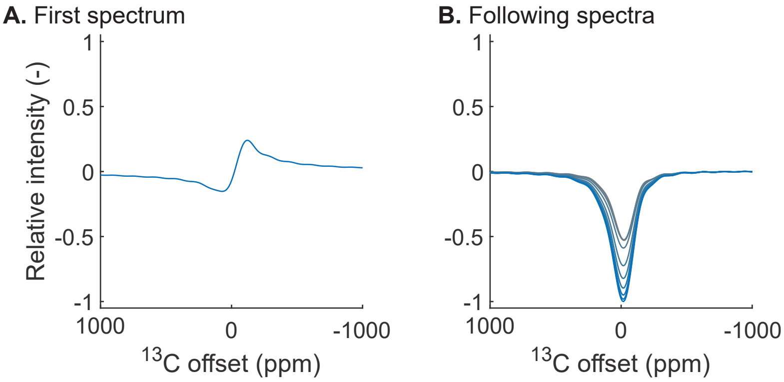

Figure 5.14: **A**. First spectrum of the HypRes experiment at 1.8 K recorded short after saturation. **B**. Selection of spectra following that shown in panel A.

$$P(t) = P_\infty + (P_0 - P_{\max}) \exp\left(-\left(\frac{t}{T_f}\right)^\beta\right) + (P_{\max} - P_\infty) \exp\left(-\frac{t}{T_s}\right), \tag{5.36}$$

where P_0, $P_{\max}$, P_∞, T_f, T_s and β are free fit parameters (see the black lines on Fig. 5.13). P_0 and $P_{\max}$ are constants that depend on the initial polarization and the HypRes signal intensity. Ideally, P_∞ should be set to the Boltzmann polarization of ^{13}C spins but the effect of the detection pulses is non-negligible and prevents the signal to reach thermal equilibrium. Therefore, P_∞ is let free in the fit. T_f and T_s are fast and slow time constants, respectively. β is the stretch coefficient of the fast time constant, between 0 and 1. The average value of the fast time constant is obtained by

$$T_{f,\mathrm{av}} = \frac{T_f}{\beta}\Gamma\left(\frac{1}{\beta}\right), \tag{5.37}$$

and the error on $T_{f,\mathrm{av}}$ is calculated using Eq. 3.35. The fitted rates (including both the fast component $R_f = 1/T_f$ and the average fast component $R_{f,\mathrm{av}} = 1/T_{f,\mathrm{av}}$) and the fitted β-coefficient are shown on Fig. 5.15.

As we did for the ^{1}H-HypRes measurement, we can use the HypRes curves to estimate the size of the hidden reservoir. In this case, because the HypRes curves do not start at 0, Eq. 5.27 cannot be used to estimate the size of the hidden reservoir. Instead, it must be corrected by subtracting the initial polarization P_0 to the HypRes polarization P_{HypRes}, yielding

$$\tilde{\chi}_h \geq \left|\frac{P_{\mathrm{HypRes}} - P_0}{P_h^0}\right| = \left|\frac{P_{\mathrm{HypRes}} - P_0}{(1-\eta_{\mathrm{sat}})P_{\mathrm{DNP}}^{\max}}\right| \geq \left|\frac{P_{\mathrm{HypRes}} - P_0}{P_{\mathrm{DNP}}^{\max}}\right|. \tag{5.38}$$

The results are shown on Fig. 5.15D. The obtained size of the hidden reservoir is on the order of $\tilde{\chi}_h \approx 0.8\%$ with a slight decrease with increasing temperature.

We now discuss the results of the ^{13}C-HypRes experiments. We first note that the curves do feature the expected polarization overshoot, which is negative in this case due to negative prepolarization during preparation, although not starting with $P(t=0) = 0$ due to the imperfect saturation of the visible spins.

Model equation Eq. 5.36 fits the data particularly well (see Fig. 5.13), although we have to concede it has an important number of free parameters (six in total). The reason for using this

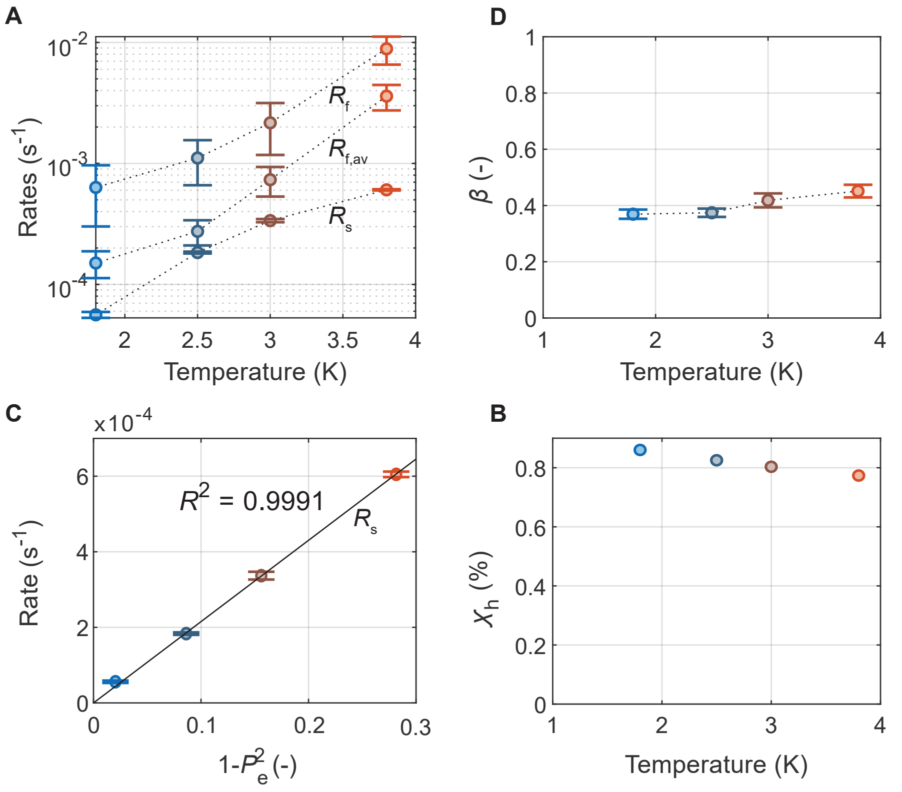

Figure 5.15: **A-B**. Rate constants and β-coefficient fitted with Eq. 5.36 to the data of Fig. 5.13 and plotted against temperature. **C**. Correlation of the slow rate constant R_s with $1 - P_e^2$, where P_e is the polarization of the electron spin. The colored dots and the black line represent the fitted rates and a linear regression, respectively. The error bars correspond to the error of the fit with 95% confidence. **D**. Size of the hidden reservoir estimated using Eq. 5.38.

equation rather than the two-reservoir model described earlier is that the fast time component exhibits a strongly stretched behavior ($\beta < 0.5$, see Fig. 5.15B), which makes the fit of the two-reservoir model very poor. We attempted to modify the two-reservoir model by including a stretch coefficient to the fast time constant but this gave equally poor results (not shown). Nonetheless, this phenomenological model allows us to draw several conclusions. First, we do find a faster and a slower time component in the ^{13}C-HypRes experiments (see $R_f = 1/T_f$ and $R_{f,\mathrm{av}} = 1/T_{f,\mathrm{av}}$ vs $R_s = 1/T_s$ on Fig. 5.15B), as in the ^{1}H case. We, therefore, interpret R_f and R_s as the rate of polarization flow between the hidden and visible spins and of relaxation towards Boltzmann equilibrium, respectively.

The separation between R_f and R_s, suggests that relaxation is not limited by diffusion from the hidden to visible spins in our experimental conditions. This is in line with a recent study by Wenckebach and coworkers. [106] This is further supported by the fact that the slow rate constant R_s exhibits the expected correlation with the term $1 - P_e^2$ (see Eq. 2.159), where P_e is the electron Boltzmann's polarization, as can be seen on Fig. 5.15C.

On the contrary, neither the fast rate constant R_f nor its average $R_{f,\mathrm{av}}$ are correlated with $1 - P_e^2$ (not shown) but they exhibit a marked and more complex dependence on temperature or electron polarization. The strong stretched character of the polarization exchange rate suggests, as in the ^{1}H case, that diffusion becomes slower closer to the electron spin. Indeed, a stretched rate indicates a distribution of rates, which implies that the diffusion coefficient takes a distribution of values as a function of the distance to the electron spin (further experimental evidence of a gradient of the spin diffusion coefficient along the distance to the electron spin will be given in the next section on μw off-HypRes with inversion for ^{1}H spins, see Sec. 5.4).

Finally, the size of the hidden reservoir obtained here is in agreement with that found for ^{1}H spins. Indeed, we found a hidden reservoir size $\chi_h \approx 4 - 7\%$ in the case of the ^{1}H-HypRes experiments on DNP juice doped with 50 mM TEMPOL (see Fig. 5.7). In first approximation, the size of the hidden reservoir should be proportional to the intensity of the electron-nucleus hyperfine interaction and in turn to the nuclear gyromagnetic ratio, which brings a factor $\gamma(^{13}C)/\gamma(^1H) \approx 1/4$. It should also be approximatively proportional to the concentration of radicals, bringing a factor $C(\text{trityl})/C(\text{TEMPOL}) \approx 1/2$. Altogether, the size of the ^{13}C-hidden reservoir should therefore be on the order of $4/8\% \approx 0.25\%$ to $7/8\% \approx 0.88\%$, while we found $\approx 0.8\%$. However, it should be noted that trityl is a larger radical than TEMPOL and it does not bear any ^{13}C spins, which increases the minimum possible distance between ^{13}C spins and the electron spin. This should lead to a lower size of the ^{13}C-hidden reservoir.

5.3.2 HypRes under MAS

In Ref. [68], we also demonstrated the applicability of the HypRes method in the context of MAS-DNP at 100 K and 14.0 T. The method requires the use of time-resolved μw gating, which is not common for MAS-DNP setups. The experiment was hence performed by our collaborator Dr. Frédéric Mentink-Vigier, at the Maglab in Tallahassee, Florida.

The experiments were performed on a sample of 10 mM ASYMPolPOK in 2:3 H_2O:glycerol (v/v). We chose to use a fully protonated medium to avoid cross-relaxation from ^{2}H to ^{1}H spins [208] and thus ensure that any overshoot is strictly due to the contribution of the hidden ^{1}H spins. The high proton concentration results in a strong dipolar broadening of the NMR line of $\approx$ 70 kHz (see Fig. 5.16A). The sample was polarized during 4 s prior to saturation. Fig. 5.16B shows the μw on- and off-curves together with the excess. Contrary to all other HypRes experiments presented in this dissertation, each point of the curve on Fig. 5.16B was acquired separately using a $\pi/2$ rf pulse and repeating the acquisition with another delay. Although not as strong as at lower temperatures, a HypRes overshoot is observed.

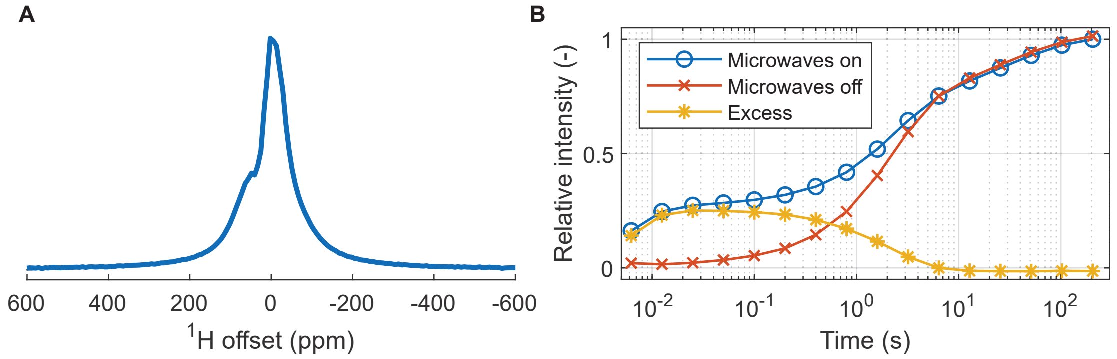

Figure 5.16: **A**. ^{1}H spectrum of 10 mM ASYMPolPOK in 4:6 H_2O:glycerol (v/v) at 14.0 T and 100 K under MAS at 8 kHz obtained by DNP. **B**. Corresponding HypRes curves. Contrary to experiments in static mode at low temperatures, these measurements were obtained with $\pi/2$ pulses, each point being an individual measurement. Adapted from Ref. [68] according to the terms of the Creative Commons Attribution-NonCommercial 4.0 International Public License.

Due to the low number of data points at short delays (between 0 and 50 ms), the two-reservoir model cannot be fitted to the data. However, visual inspection of the HypRes curve shows that the maximum of the excess is reached $\approx$ 30 ms after saturation. The flow rate can thus be estimated to be on the order of $R_f \approx 30$ s^{-1}. As a comparison, for 50 mM TEMPOL in DNP juice at 4.2 K in static mode, the maximum of the excess is reached $\approx$ 3 s after saturation, with a flow rate of $R_f = 0.29$ s^{-1}, indicating that the flow is two orders of magnitude slower. This may be due to the combined effects of increased spin concentration, MAS, and higher temperature. The low-temperature measurements were performed on DNP juice, with 11 M of ^{1}H, while the MAS measurements were performed on 2:3 H_2O:glycerol (v/v), with 110 M. Increasing the ^{1}H concentration decreases the average distance between neighbors and therefore increases the dipolar couplings and the diffusion coefficient. MAS is known to influence the spin diffusion coefficient and, in some cases, it may enhance spin diffusion. [209] We note that studying the dependence of the flow rate on the MAS rate would be of great interest but is beyond the scope of the current study.

The CE-DNP mechanism under MAS leads to a depolarized nuclear state with lower polarization compared to Boltzmann equilibrium. [141, 210] During the HypRes experiment, after μw are turned off, the electrons rapidly return to Boltzmann equilibrium (within $5T_{1,e} \approx 1.5$ ms) [141, 210] and start depolarizing the nuclei, probably even before they relax with T_1 . The observation of the overshoot indicates that hidden spins exchange polarization with the visible spins faster than they are depolarized.

The reason why the overshoot is so weak as compared to thermal equilibrium is likely to be explained by the saturation scheme. The visible spins were saturated with a train of 100 pulses separated by 5 ms, which yields a total of 500 ms. As the exchange between the reservoir is on the order of 30 ms, a significant portion of polarization can escape from the hidden reservoir in between pulses resulting in a non-ideal saturation factor of the hidden reservoir $\eta_{\text{sat}} > 0$. Furthermore, the radical concentration in the MAS-DNP sample is 5 times lower than in the sample used for low-temperature DNP, which hides a smaller fraction of the spins and hence causes a smaller overshoot.

5.4 μw off-HypRes with inversion

Further insights into the spin diffusion processes near the electron can be obtained by the use of broadband inversion pulses in the HypRes experiment. In this section, we show how diffusion among the hidden spin can be indirectly assessed using the HypRes experiment with inversion. [68]

5.4.1 HypRes results with inversion

Fig. 5.5 shows the general scheme of ^{1}H-HypRes experiment with inversion. A broadband inversion pulse centered at the middle of the NMR line is applied before saturating the visible spins. The HypRes experiment was repeated at 3.8 K on DNP juice doped with 50 mM TEMPOL using inversion chirp pulses with maximum nutation frequency $\omega_1/2\pi = 34$ kHz and widths of 0.5, 1, 2, 3 and 4 MHz, intended to invert ^{1}H spins over ±0.25, ±0.5, ±1, ±0.5 and ±2 MHz, respectively. These pulses thus invert ^{1}H spins far off-resonance (from the detectable NMR range). Because the Q-factor of the ^{1}H channel of our probe is typically on the order of 150-250, an inversion pulse with 4 MHz width is broader than the probe resonance and is therefore inefficient at the edges. To compensate for this, the Q-factor of the probe was diminished by adding a 50 Ω resistance (Barry industries 50W BeO flanged resistor) in the NMR circuit. The resistance was located on the coaxial line between the tunning & matching box and the coil (outside the probe).

After inversion, the ^{1}H spins were saturated by a train of pulses, that acted only on a narrow bandwidth, as in the pulse sequence presented in Fig. 5.4.

At the end of the preparation, the ^{1}H spins can be separated into three parts:

1. those far from the electron have a polarization of 0 due to the narrow saturation pulses;
2. those closer to the electron which have been inverted by the broadband pulse have polarization with opposite sign compared to what they acquired under DNP (but reduced by the inversion pulse imperfection);
3. finally, those that are close enough to the electron with Larmor frequencies outside of the range of inversion of the pulse have kept the sign of polarization that they acquired under DNP.

Following preparation, the signal resurgence was recorded by small angle pulses, varying the delay between the detection blocks to capture processes occurring on all time scales. The results are shown on Fig. 5.19. On a fast timescale of hundreds of milliseconds to seconds (depending on the inversion width), the inverted hidden spins equilibrated their polarization with the visible spins, causing a negative overshoot. Then, on a longer timescale of hundreds of seconds, the polarization of the spins which had not been inverted and had therefore kept their positive polarization reached the visible spins causing a positive polarization overshoot.

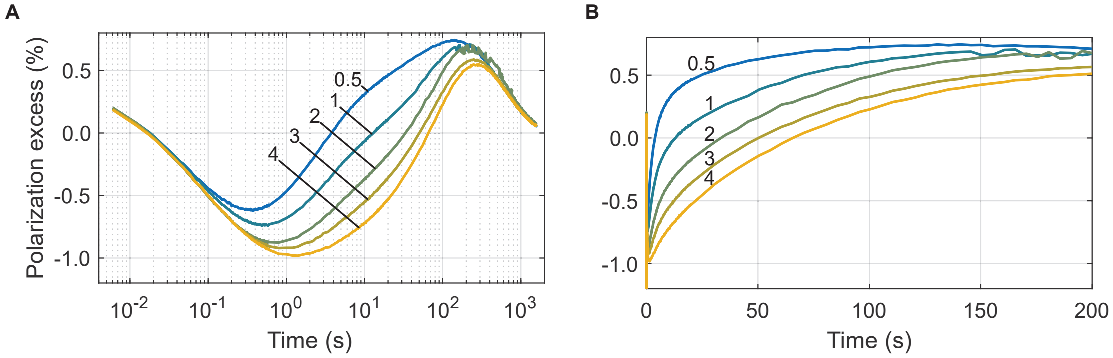

Figure 5.17: **A-B**. Results of the HypRes experiment with inversion pulses at 3.8 K recorded with small angle pulses for DNP juice doped with 50 mM TEMPOL with inversion widths from 0.5 to 4 MHz, in logarithmic and linear scale, respectively. The numbers by the curves indicate the theoretical widths of inversion chirp pulses in MHz. Adapted from Ref. [68] according to the terms of the Creative Commons Attribution-NonCommercial 4.0 International Public License.

The width of the inversion pulses influences the curves in several regards. First, the wider the inversion, the stronger the negative overshoot, and the weaker the positive overshoot, which is consistent with the assumption that more spins are inverted with a larger pulse bandwidth and that they do exchange polarization with the visible spins. Second, the wider the range of inversion, the later the negative extremum is reached (after 0.4 and 1.4 s for the 0.5 and 4 MHz inversion pulses, respectively) and the same is true for the positive extremum (after 150 and 300 s for the 0.5 and 4 MHz inversion pulses, respectively). A larger pulse inversion bandwidth implies that the non-inverted spins are more coupled to the electron. Therefore, the fact that the overshoot occurs later demonstrates that the stronger the protons are coupled with the electron, the more spin diffusion is hindered. Finally, the slopes of the curves going from the negative to the positive extrema are also affected by the inversion width which supports this argument. These measurements thus provide experimental evidence that the Larmor frequency gradient caused by the electron spin is responsible for a gradient of the nuclear spin diffusion coefficient.

5.4.2 Characterization of broadband pulses

The quality of the inversion pulses was assessed in a separate experiment and further confirmed by simulation. The measurement was performed for inversion widths of 0.5, 1, and 2 MHz and not higher because the intensity of the reflected power could damage the amplifier. Fig. 5.18 shows the result. The inversion is maximal up to $\approx 3/5$ of the theoretical inversion width. The intensity was manually fitted with a hyperbolic tangent function

$$I(\nu) = \frac{\alpha+1}{2} + \frac{\alpha-1}{2}\tanh\left(\gamma\left(\frac{\beta}{2} - \frac{\nu}{\nu_{\max}}\right)\right), \tag{5.39}$$

where $\nu_{\max}$ is the theoretical inversion width and $\alpha = 0.72$, $\beta = 0.83$ and $\gamma = 20$ are adimensional fit parameters reflecting the maximum inversion efficiency, the effective width and the slope, respectively.

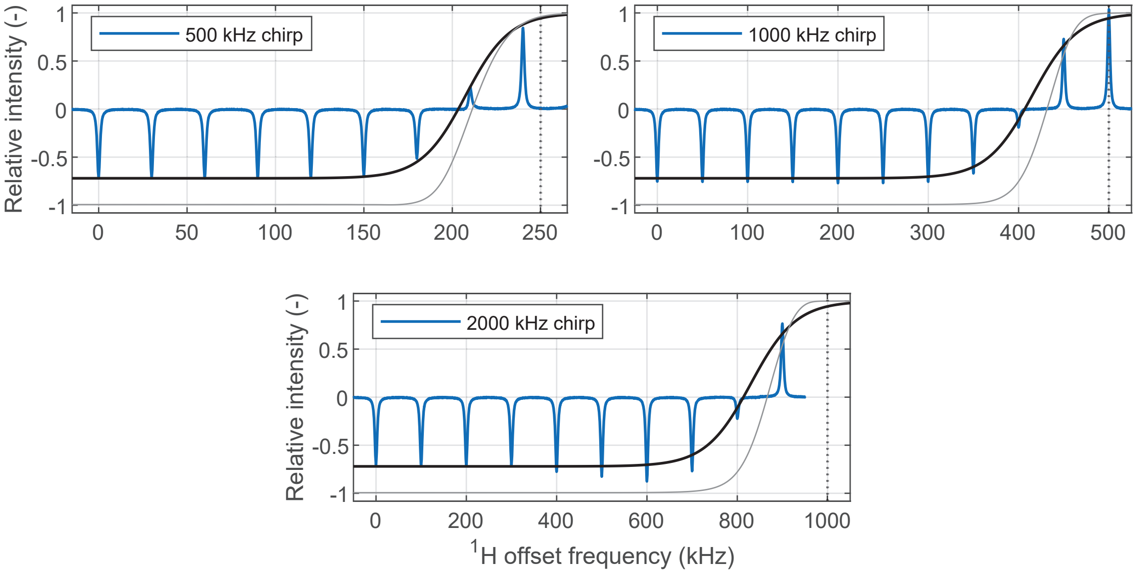

Figure 5.18: Relative inversion efficiency for chirp pulses of 0.5, 1, and 2 MHz inversion width, recorded by moving the center of the pulse. The blue lines are the data points. The vertical black dashed lines represent the theoretical inversion width. The black solid line is a manually fitted hyperbolic tangent function. The gray faint line is the simulated profile. Adapted from Ref. [68] according to the terms of the Creative Commons Attribution-NonCommercial 4.0 International Public License.

The inversion profile of the pulse was simulated using a single-spin Hilbert space with the time-dependent Hamiltonian [3]

$$\hat{H}(t) = \Delta\Omega \hat{I}_z + \omega_1 A(t)\left(\hat{I}_x \cos\phi(t) + \hat{I}_y \sin\phi(t)\right), \tag{5.40}$$

where $\Delta\Omega$, ω_1, $A(t)$ and $\phi(t)$ are the offset between the Larmor frequency of the spin and the carrier frequency of the pulse, the nutation frequency of the pulse and the time-dependent pulse amplitude (between 0 and 1) and the phase of the pulse generated by Topspin. The initial state of the density matrix was assumed to be $\hat{\rho}_0 = \hat{I}_z$. It was propagated under the time-dependent

---

[3] Note that using Bloch equations to simulate the pulses would be easier than using a spin dynamical simulation. It was in fact the opposite for me simply "by habit".

Hamiltonian during time steps of 0.1 μs (corresponding to the discretization of the pulse) using the sandwich formula $\hat{\rho}(t+dt) = \exp(-i\hat{H}(t)dt)\hat{\rho}(t)\exp(+i\hat{H}(t)dt)$. The polarization along the z-axis after the inversion pulse was computed with the trace $P_z = \mathrm{Tr}(\hat{I}_z\hat{\rho})/|I|$. The simulation was repeated for 300 offset frequencies $\Delta\Omega$ over the displayed range of each spectrum. Plotting the final polarization $P_z(\Delta\Omega)$ against the offset frequency $\Delta\Omega$ gives the profile of the inverted polarization along the z-axis after the inversion pulses. The simulated inversion profiles are shown as gray faint lines in Fig. 5.18.

The simulation predicts more efficient inversion than what is found experimentally (see Fig. 5.18). This is likely due to paramagnetic relaxation which was not taken into account in the simulation.

Those measurements were used to estimate the polarization of the ^{1}H spins at the beginning of detection as a function of their dipolar coupling constant to the electron (see Fig. 5.19A). The polarization dip at the center corresponds to the saturated visible spins. Assuming that the offset frequency of the nuclei is governed by the paramagnetic shift, we can translate the offset into a distance. For a given shift $\Delta\omega$, the distance between the electron and the nucleus can take any value between 0 and $r_{e-n}^{\max}$, depending on the angle θ between the main magnetic field and the vector connecting the electron and the nucleus. The maximal possible distance $r_{e-n}^{\max}$ corresponds to $\theta = 0, \pi$ and is given by

$$r_{e-n}^{\max} = \left| \frac{1}{2} \frac{\mu_0}{4\pi} \frac{\hbar\gamma_e\gamma_n}{\Delta\omega} \right|^{1/3}. \tag{5.41}$$

The profiles in Fig. 5.19A are expressed as a function of the electron-nucleus coupling and were converted into profiles as a function of the maximum electron-nucleus distance $r_{e-n}^{\max}$ using Eq. 5.41, in Fig. 5.19B.

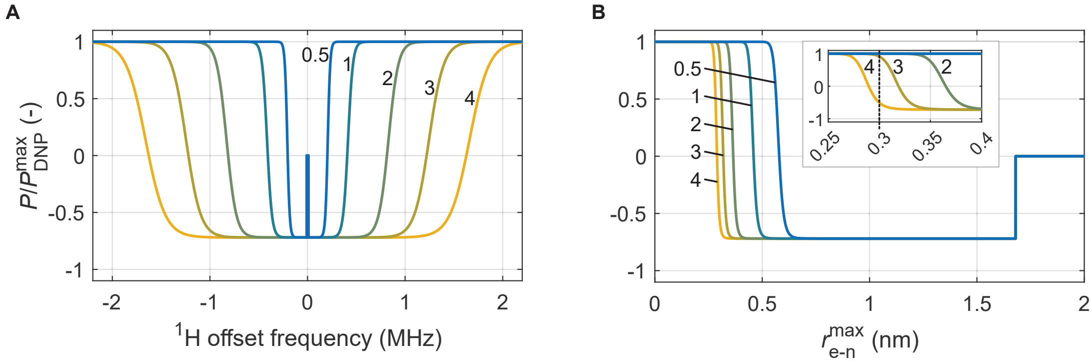

Figure 5.19: **A**. Estimated relative polarization profiles of the ^{1}H spins at the end of the preparation as a function of Larmor frequency shift taking into account the imperfection of the pulses. The dip near zero is due to the narrow band saturation at the end of the preparation phase. **B**. Estimated relative polarization profiles of the ^{1}H spins at the end of the preparation as a function of the distance to the electron spin, converted from panel A using Eq. 5.41. The numbers next to the curves indicate the theoretical widths of the inversion pulses in MHz. Adapted from Ref. [68] according to the terms of the Creative Commons Attribution-NonCommercial 4.0 International Public License.

5.4.3 Implications regarding the spin diffusion barrier

The HypRes experiment with inversion shows that spins as close as 0.3 nm to the electron can exchange polarization with the visible spins, faster than they relax toward thermal equilibrium. In other words, they are outside the diffusion barrier according to Wolfe's terminology (see Sec. 5.1.3). [197] Indeed, the HypRes experiment with a 4 MHz inversion width resulted in a stronger negative overshoot than with a 3 MHz inversion width. Therefore, there are spins that were not inverted by the 3 MHz inversion pulse but were inverted by the 4 MHz inversion pulse and yet could still share their polarization with the visible spins. According to Fig. 5.19B, such spins are at a maximum distance of 0.3 nm to the electron. Tan et al. and coauthors have shown in 2019 that ^{1}H spins within a radius of < 0.6 nm to a trityl radical were in contact with the bulk at 100 K and 0.3 T. [199] Our results confirm this observation at 3.8 K and 7.05 T.

This interpretation relies on the assumption that the inversion pulses are efficient even far away from the center of the NMR line. However, the efficiency of the inversion pulses is diminished at its edges due to the finite width of the resonance of the NMR probe. Furthermore, paramagnetic relaxation in the transverse plane is expected to be intense for far-off-resonance nuclei as they are nearer to the electron spin, causing them to relax during the inversion pulse. Yet, since we observe a stronger effect of the inversion as we increase the chirp width, we conclude that the broadest pulse must still be reasonably efficient at its edges. Indeed, if the 3 MHz inversion pulse was inefficient at its edges, the 4 MHz inversion pulse would not be more efficient over the same range and the same results would be observed for the two experiments.

It is interesting to remark that a sphere with a radius of 0.3 nm in a solution with 11 M of ^{1}H contains less than a single ^{1}H spin on average. Yet, the TEMPOL molecule itself contains 12 ^{1}H on the four methyl groups which surround the radical and a further four ^{1}H on the next positions of the ring. As a consequence, the ^{1}H spin concentration is stronger in the vicinity of the electron than in the bulk of the sample. This local heterogeneity could be part of the reason why nuclear polarization appears to escape so easily, a feature that could be used for the rational design of new polarizing agents.

5.5 μw on-HypRes

The HypRes experiments in static mode presented above showed that nuclear spin diffusion in the vicinity of the electron spin had a strong dependence on temperature both in ^{1}H and ^{13}C cases. One might be tempted to attribute this temperature dependence to a change in phonon density with temperature. One theoretical study does indeed investigate the role of phonons in spin diffusion. [211] Yet, a more likely explanation is to be found in an "electron-driven" process. Bloembergen showed in 1949 that the modulation of dipolar interactions by lattice vibrations was not an efficient mechanism for nuclear relaxation in the solid-state; instead, the fluctuations of the electron spin state of (even dilute) paramagnetic impurities drive nuclear $|\alpha\rangle \leftrightarrow |\beta\rangle$ transitions, therefore allowing for relaxation. [161] The same is possible for spin diffusion: if the presence of an electron spin hinders nuclear $|\alpha\beta\rangle \leftrightarrow |\beta\alpha\rangle$ transitions and hence spin diffusion, the fluctuation of the electron spin state can drive these very transitions. [108, 176] However, this mechanism vanishes when the electron polarization tends towards unity, just as nuclear paramagnetic relaxation vanishes because the term $1 - P_e^2$ (where P_e is the polarization of the electron) tends towards 0 (see Eq. 2.150 in Sec. 2.3.4 and Chapter 4).

In our conditions, electron polarization goes from 85% at 3.8 K to 99.93% at 1.2 K and so nuclear spin diffusion in the vicinity of electron spins can be expected to be much slower at 1.2 K. In this section, we verify this hypothesis both experimentally and in theory. To do so, we introduce the μw on-HypRes experiment, which allows us to monitor spin diffusion under controlled electron polarization. We then rationalize our findings by constructing a 1 electron-2 nuclei model of spin diffusion accounting for the dependence of the electron dynamics on electron polarization.

5.5.1 Saturation with shaped pulses

In all HypRes experiments presented until now, the saturation of the visible spins was performed using square pulses. However, because we aim at saturating the spins on a well-defined window, it is more sensible to use shaped pulses. Furthermore, because we suspected that constant delays between saturation pulses may lead to echoes (see Sec. 5.3.1), we used random delays between the pulses.

In the following, we used a saturation scheme consisting of 19 sinc excitation pulses of 100 μs with a nutation frequency $\omega_1/2\pi = 51$ kHz, discretized in 1000 points and separated by random delays on the order of ≈ 10 ms (10.100, 100.105, 100.023, 100.157, 100.101, 100.011, 100.073, 100.054, 100.097, 100.047, 100.026, 100.084, 100.065, 100.105, 100.023, 100.157, 100.101 and 100.011 ms). The sequence of the pulse phases was randomly chosen to be $x, -x,\ y, -y, -x,\ x,\ y, -y, -y,\ y$. The sinc pulse shape was generated using Topspin's built-in functions and chosen to excite over a bandwidth of 200 kHz, with $n = 10$. The profile of the saturation scheme was measured experimentally and confirmed by simulation (see Fig. 5.20).

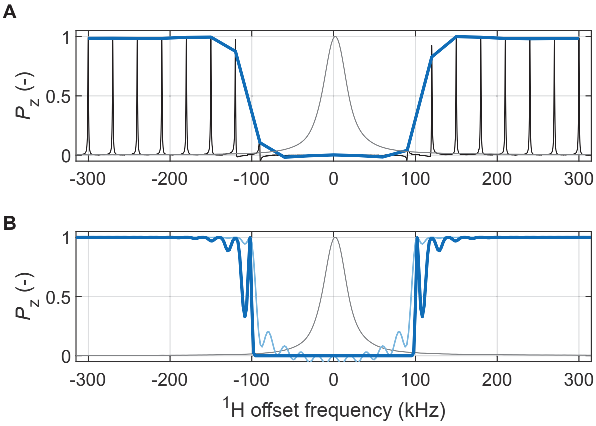

Figure 5.20: **A**. Measured saturation profile of the train of sinc pulses. The black signals are the measured signals as a function of the offset of the saturation pulses. The bold blue line is the integral of the measured signals in black. **B** Simulated saturation profile of the train of sinc pulses. The faint and bold blue lines are the simulated remaining polarization along the z-axis after a single saturation pulse and after the train of 19 saturation pulses, respectively. The faint grey line on both plots represents the experimental NMR signal before saturation.

Experimentally, we first recorded a reference spectrum without saturation (faint gray lines on Fig. 5.20A) after 10 s of DNP at 1.2 K. Then, we repeated the measurement using the saturation scheme described above varying the carrier frequency of the saturation pulses from -300 to $+300$ MHz and obtained the traces represented in black in Fig. 5.20A. The blue line is the integral which shows that the saturation width has indeed a bandwidth of 200 kHz.

The excitation profile of the pulse was simulated using the exact same procedure as above for the inversion pulses (see Fig. 5.18). The simulation was repeated for 300 offset frequencies $\Delta\Omega$ between -300 and $+300$ MHz. Plotting the remaining polarization along the z-axis $P_z(\Delta\Omega)$ against the offset frequency $\Delta\Omega$ gives the saturation profile for a single pulse (see the faint blue line in Fig. 5.20B). To take into account the fact that the saturation scheme consists of 19 pulses, we assumed that the magnetization in the transverse plane decays during the delay between the saturation pulses and so the remaining polarization along the z-axis after the k^{th} pulse is

$P_z^{final}(\Delta\Omega) = P_z(\Delta\Omega)^k$. The resulting simulated saturation profile is shown as a bold blue line in Fig. 5.20B. It confirms that the excitation scheme saturates the spins from -100 kHz to $+100$ kHz.

For comparison, the simulated saturation profile for a train of 19 square pulses with a nutation frequency $\omega/2\pi = 42$ kHz is shown in Fig. 5.21. Saturation is effective at frequencies beyond those where a significant density of visible spins is found, causing an unnecessary saturation of the hidden spins ($\eta_{\text{sat}} > 0$). The saturation scheme using sinc pulses yields a profile much closer to a square and therefore provides a better starting point for the HypRes experiments.

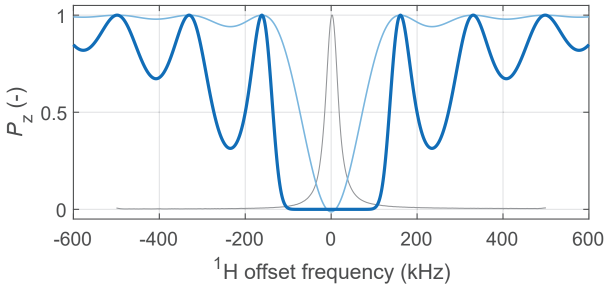

Figure 5.21: Simulated saturation profile of a train of $\pi/2$ square pulses of strength $\omega/2\pi = 42$ kHz. The faint and bold blue lines are the simulated remaining polarization along the z-axis after a single saturation pulse and after the train of 19 saturation pulses, respectively. The faint grey line represents the experimental NMR signal before saturation.

5.5.2 μw on-HypRes results

We first performed the μw-off HypRes experiment as described above on the same sample of 50 mM TEMPOL in DNP juice at 1.2 K but this time using the saturation scheme consisting of sinc pulses (the pulse sequence is shown on Fig. 5.22A). The experiment was performed setting the μw frequency during preparation so as to reach either positive or negative nuclear polarization. The positive (or negative) polarization acquired during preparation was wiped out by the saturation pulses only for the visible spins, far from the electron ($<$ 0.2% remaining polarization). The spins closer to the electron retained their invisible polarization, which surged onto the visible spins during the course of detection, causing an observable positive overshoot (or negative, respectively), as expected. The two resulting curves are shown in Fig. 5.22B. The Boltzmann equilibrium polarization of ^{1}H spins is indicated by a dashed line for comparison (0.60% in these conditions). The experimental traces feature two processes: the equilibration of the hidden and visible spins polarization *via* spin diffusion far beyond Boltzmann equilibrium within ≈ 0.5 h, followed by their slow relaxation towards it. The spin diffusion process monitored during the first part occurs while the electron polarization is that of Boltzmann equilibrium, which is 99.93% in these conditions. We obtained a higher polarization overshoot than what we did in the experiment presented in Fig. 5.7 (5.9% compared to 4.6%). This is likely due to the cleaner saturation scheme using sinc pulses which is expected to affect the hidden spins less than the saturation scheme with square pulses (η_{sat} closer to 0).

To monitor spin diffusion in the same conditions but with a lower electron polarization, we repeated the experiment using the pulse sequence presented in Fig. 5.22C. In this case, after μw irradiation was switched off, the μw frequency was changed from the value yielding positive nuclear spin polarization to that yielding negative polarization, a strategy which is reminiscent of the work by Ramakrishna and Robinson. [191] μw irradiation was then switched back on during detection. This experiment was repeated with different values of μw power during detection from 0 to 118

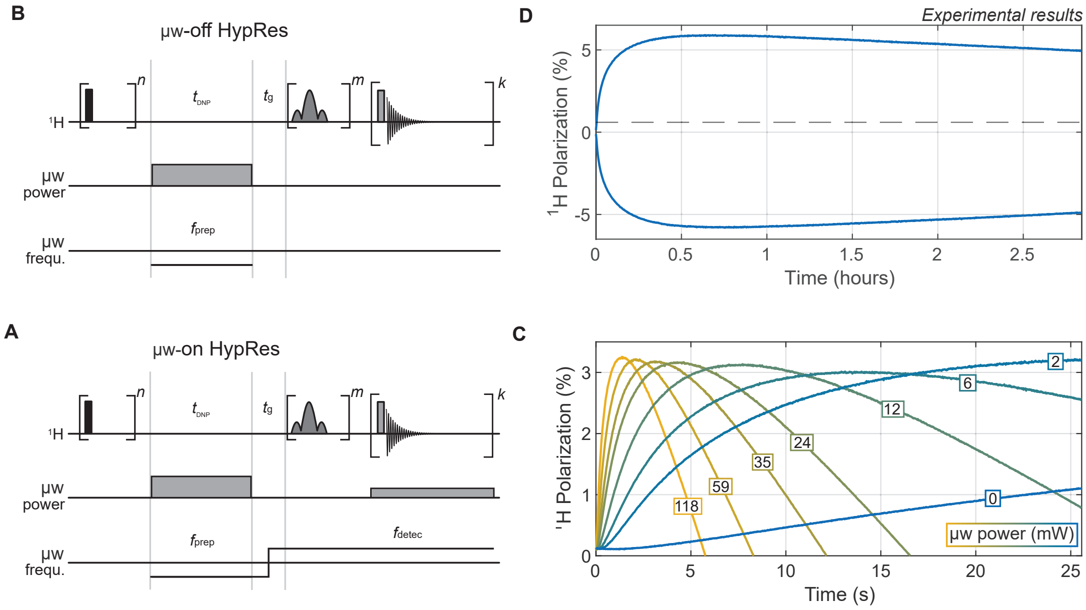

Figure 5.22: **A, C**. Pulse sequence diagrams of the μw off- and -on HypRes experiments, respectively. On the ^{1}H channel, the black and gray rectangles represent square pulses, with nutation angles of $\pi/2$ and 0.1°, respectively. **B, D**. Results of the μw off- and -on HypRes experiments, respectively, at 1.2 K. The μw power applied during detection from 0 to 118 mW is indicated on the curves of Panel D.

mW, yielding the curves shown in Fig. 5.22D. The μw power used during detection is indicated on the curves. Like for the μw-off HypRes experiment, the nuclear polarization acquired by the hidden spins during preparation first surged onto the visible spins causing a positive polarization overshoot. Then, instead of decaying towards thermal equilibrium (only 0.60% polarization), negative DNP started pulling the polarization towards the opposite direction at the negative DNP equilibrium value. Most importantly, the stronger the μw power during the equilibration of polarization between the visible and hidden spins, and hence the weaker the electron polarization, the faster the flow of nuclear polarization from the hidden to the visible spins. μw irradiation does not influence the nuclei other than through the electron spins (the helium bath heating by μw irradiation is less than 10 mK). Therefore, only the electron dynamics can be responsible for the observed rapid spin diffusion from hidden to visible spins.

5.5.3 Comparison of μw on- and μw off-HypRes

To further confirm that nuclear spin diffusion is controlled by the electron polarization, it is interesting to compare the results obtained here with those obtained with the μw off-HypRes experiments presented in Sec. 5.2.2 (see Fig. 5.7). Indeed, μw off-HypRes experiments as a function of temperature give a measure of diffusion in the electron polarization is well known and is simply given by Boltzmann's equation (see Eq. 1.3).

To compare the data sets, Eq. 5.36 was fitted to both of them. In the case of the μw on-HypRes experiments, the variables P_0, $P_{\max}$ and P_∞ were all free parameters. Ideally, the initial polarization should be set to $P_0 = 0$ but it yields a poor fit. Furthermore, the first points of the curve were not taken into account in the fit. One could argue that this procedure leaves a lot of parameters free and results in overfitting. However, our aim is only to use a phenomenological model to appropriately fit the rise of the curve and extract a flow rate constant $1/T_f$. In the case of the μw off-HypRes experiment, the initial and final polarizations were set to $P_0 = P_\infty = 0$. Only the maximum polarization $P_{\max}$ was left free. Overall, this phenomenological model fits the data well. The fit is notably poor for the μw off-HypRes curve at 2.5 K ($R^2 = 0.93$, compared with $R^2 > 0.98$ for all other curves).

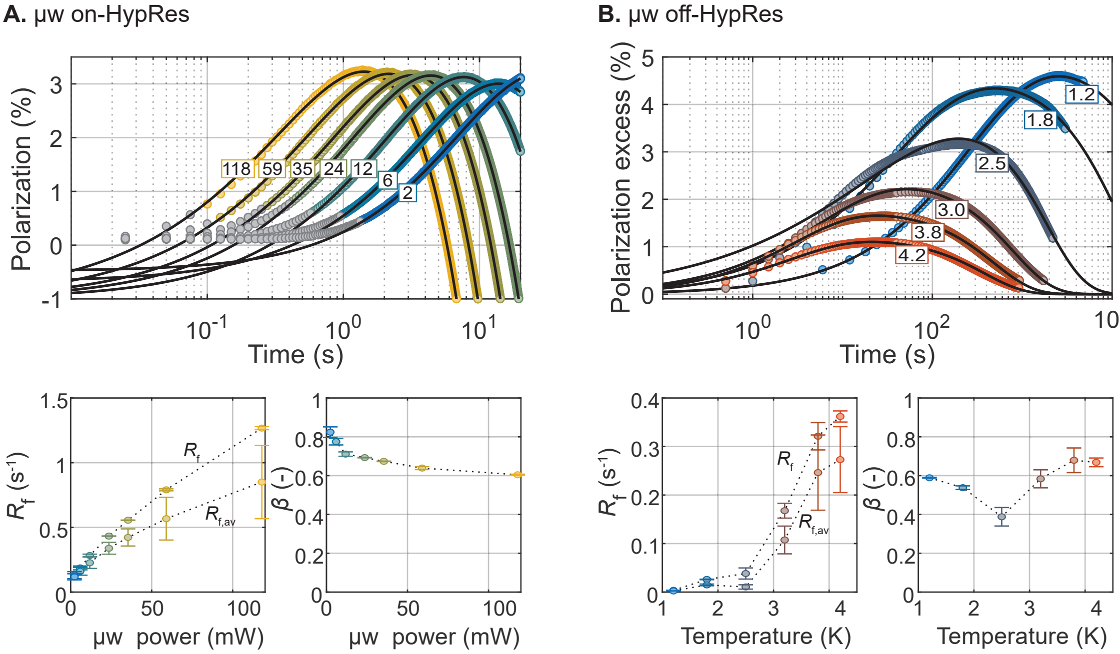

Figure 5.23: **A-B**. Fit of Eq. 5.36 to the μw on- and μw off-HypRes curves shown on Fig. 5.22 and 5.7, respectively. The μw powers in mW and the temperatures in K are shown next to the μw on- and μw off-experiments, respectively. For the μw off-experiment, it was assumed that the initial and final polarization excess were 0 while only the maximum polarization was left free in the fit. The curves in Panel B are expressed in terms of polarization with respect to a standard saturation recovery experiment (see Sec. 5.2.1).

We have now obtained average polarization flow rates $R_{f,\text{av}}$ for both data sets using the phenomenological model of Eq. 5.36. In Fig. 5.23, the rates are shown as a function of μw power for the μw on-HypRes experiment and as a function of temperature for μw off-HypRes experiment. Fig. 5.24 shows $R_{f,\text{av}}$ as a function of the electron polarization P_e for both data sets. For the μw off-HypRes experiments, the temperature was converted into electron polarization simply using Boltzmann's equation (see Eq. 1.3). For the μw on-HypRes experiments, μw power was converted into electron polarization using the data presented in Sec. 4.2, where the electron polarization was measured indirectly by monitoring the change of in transverse relaxation rate of ^{13}C spins $R_2(^{13}\text{C})$ upon switching on μw irradiation (see Fig. 4.3). It should be noted that both the μw on-HypRes experiment and the electron polarization (indirectly *via* $R_2(^{13}\text{C})$) were measured on the same sample, just one after the other.

Despite very large error bars, Fig. 5.24 shows that the polarization exchange rates as a function of electron polarization measured using the μw on- and off-HypRes experiments agree, at least within an order of magnitude. A notable outlier is the data point corresponding to μw off-HypRes at 2.5 K (marked with a * symbol), which is not surprising since the corresponding HypRes curve was particularly badly fitted by the model (see Fig. 5.23). The data points at $P_e \approx 100\%$ are in good agreement but this is not meaningful; indeed, the μw on-data point with $P_e \approx 100\%$ is that of a "μw on-HypRes" measurement with a μw power of 0 mW and therefore corresponds to a μw-off measurement. The agreement between these data points merely shows that the repetition of the same measurement on different sample replicates (using a different probe and a different saturation scheme) yields the same measured rate $R_{f,av}$. On the contrary, the agreement between the points for $75\% < P_e < 85\%$ is much more meaningful; indeed, the two μw off-data points were acquired at temperatures of 3.8 and 4.2 K, and yet they are perfectly in the trend of the μw off-data points, which were measured at 1.2 K. These results give further experimental confirmation of the dominant role of electron polarization on nuclear spin diffusion, independently from temperature.

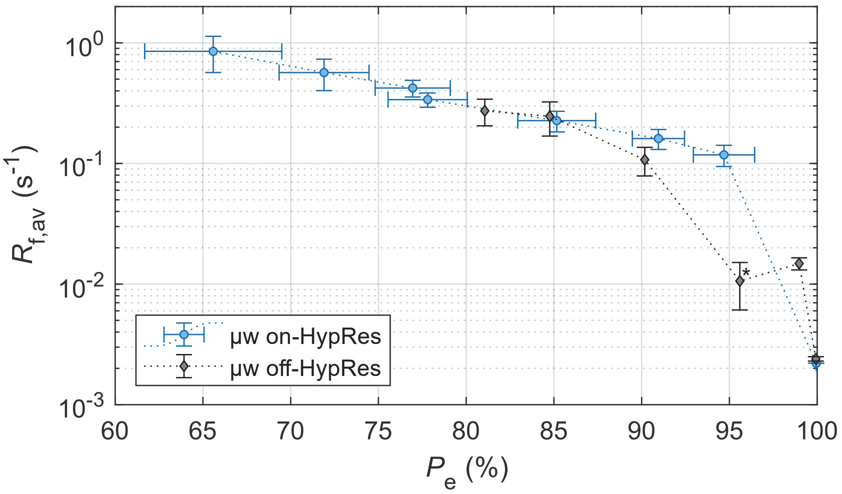

Figure 5.24: Average polarization flow rate $R_{f,\mathrm{av}}$ between the hidden and visible ^{1}H spins as a function of the electron polarization P_e obtained by fitting the phenomenological model of Eq. 5.36 to μw on- and off-HypRes curves. The data point indicted with a * symbol corresponds to the μw off-HypRes at 2.5 K, for which the phenomenological model gave a poor fit ($R^2 = 0.93$, compared with $R^2 > 0.98$ for all other curves, see Fig. 5.23). The values of P_e in the case of μw off-HypRes experiments were obtained by conversion from temperature using Boltzmann law (see Eq. 1.3). The values of P_e in the case of μw on-HypRes experiments were obtained by monitoring the change in transverse relaxation rate of ^{13}C spins $R_2^*(^{13}\mathrm{C})$ upon switching on μw irradiation (see Sec. 4.2 and Fig. 4.3) on the same sample.

5.5.4 Spin diffusion model

To understand how electron spin polarization influences nuclear spin diffusion, we attempted to calculate the transition rate probability W between the states $|\alpha\beta\rangle$ and $|\beta\alpha\rangle$ of a pair of coupled nuclear spins, at an internuclear distance a, with dipolar coupling constant D_{12}, both subject to the dipolar field of an electron spin, at distances r_i and with hyperfine coupling constants $A_{zz,i}$, as shown in Fig. 5.25. For this, I tasked a Master's student, Alessandro Chessari, to perform this calculation based on Horvitz' model [108] but in a slightly more general way. Indeed, in Horvitz' results, nuclear coordinates are expressed in terms of lattice positions in a crystal, while we are concerned with frozen solutions and so we needed to calculate the rate in the case of a statistical distribution of spins.

Alessandro Chessari realized this task with an unexpected level of sophistication. He performed

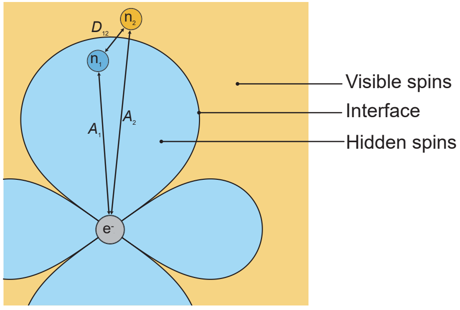

Figure 5.25: Schematic representation of the hidden and visible nuclear spins interacting with the electron spin through the hyperfine interaction with intensities A_{zz1} and A_{zz2}. The two nuclei interact together with the dipole-dipole coupling constant D_{12}.

the calculation in a more general way than Horvitz' resulting in an expression that is valid for a broader range of distances to the electron (see below). Furthermore, he used Lindblad's Master equation to describe the influence of the surrounding nuclear spins on the two nuclear spins for which the transition is computed. The derivation of the rate is presented in the Supplementary Material of Ref. [177]. Because several steps are out of my reach, we only detail here the hypothesis and the general steps of the calculation.

Following Horvitz [108] the electron is treated semi-classically, taking into account the stochastic time dependence of its state. The nuclear dipole coupling D_{12} is also assumed to be weak compared to the broadening of the nuclear levels $|\alpha\beta\rangle$ and $|\beta\alpha\rangle$ due to the interactions with the surrounding nuclei. Since the system is immersed in a strong magnetic field that shifts the spin paired levels $|\alpha\alpha\rangle$ and $|\beta\beta\rangle$ far from that of the unpaired subsystem, we can restrict the Hilbert space to the $|\alpha\beta\rangle$ and $|\beta\alpha\rangle$ subspace. The total Hamiltonian in the rotating frame of the nuclei may be expressed as

$$\hat{H}(t) = \hat{H}_D + \hat{H}_{HF}(t), \tag{5.42}$$

where the nuclear dipolar Hamiltonian $\hat{H}_D$ and the time-depend hyperfine Hamiltonian $\hat{H}_{HF}(t)$ are expressed in terms of the Pauli matrices $\hat{\sigma}_\pm = \hat{I}_{1\pm}\hat{I}_{2\mp}$ and $\hat{\sigma}_z = \hat{I}_{1z} - \hat{I}_{2z}$ as

$$\hat{H}_D = -\frac{1}{2}D_{12}(\hat{\sigma}_+ + \hat{\sigma}_-) \tag{5.43}$$

$$\hat{H}_{HF}(t) = \frac{1}{2}\Delta(\bar{P} + P'(t))\hat{\sigma}_z, \tag{5.44}$$

where $\Delta = A_{zz,1} - A_{zz,2}$ is the difference of the hyperfine interaction strength. For simplicity, we ignore any diagonal terms giving rise to an overall shift of the two energy levels.

The dynamics of the electron polarization $P(t)$ is decomposed into a static contribution given by the average value $\bar{P}$ and an unbiased signal $P'(t)$, with an autocorrelation function

$$\langle P'(0)P'(\tau)\rangle = (1 - \bar{P}^2)e^{-\Gamma_c|\tau|}, \tag{5.45}$$

where $1/\Gamma_c = \tau_c$ is the correlation time of the electron spin state. [108] In other words, the nuclear spins experience two contributions of the hyperfine interaction. The static part causes a time-independent nuclear frequency shift proportional to the average nuclear polarization $\bar{P}$ (as depicted in Fig. 2.13), while the dynamic part averages to 0 over time but enables transition between the $|\alpha\beta\rangle$ and $|\beta\alpha\rangle$ states. This dynamic part of the electron dynamics, which is proportional to $1-\bar{P}^2$, was exploited in Chapter 4 to measure EPR properties *via* nuclear R_2 and $R_{1\rho}$ relaxation rates.

Here, we investigate its contribution to spin diffusion. Note that this decomposition of the electron state is only valid for nuclear spins with a hyperfine interaction constant weaker than the inverse of the electron correlation time $|A_z| < 1/\tau_c$. [107]

The steps of the calculation are the following. First, the transition probability induced by the nuclear dipolar interaction is calculated in the interaction frame of the hyperfine interaction given by $U_0 = e^{-i\int_0^t \hat{H}'_{HF}(\tau)d\tau}$. In this frame, the Hamiltonian reads

$$\hat{H} = \frac{1}{2}\Delta\bar{P}\hat{\sigma}_z - \frac{1}{2}D_{12}\left(\hat{\sigma}_+ f(t) + \hat{\sigma}_- f^*(t)\right), \tag{5.46}$$

where $f(t) = e^{i\Delta\int_0^t P'(s)ds}$. The transitions probability is calculated using first-order perturbation theory and yields, after simplifications,

$$W_{|\alpha\beta\rangle\to|\beta\alpha\rangle} = \frac{D_{12}^2}{4}\int_{-\infty}^{\infty} d\tau\langle\hat{\sigma}_-(\tau)\hat{\sigma}_+(0)\rangle_{P'}. \tag{5.47}$$

Then, the influence of the surrounding bath of nuclei is taken into account in the correlator of Eq. 5.47 for a particular realization of the stochastic trajectory of $P'(t)$ using Lindblad's Master equation, [212, 213, 214, 107] yielding

$$\langle\hat{\sigma}_-(\tau)\hat{\sigma}_+(0)\rangle_{P'} = e^{-\Gamma_2|\tau|}e^{-i\Delta\bar{P}\tau - i\Delta\int_0^\tau P'(s)ds}, \tag{5.48}$$

where Γ_2 is the spin-spin relaxation rate of the nuclei, i.e., the broadening of the nuclear levels, which is assumed to be governed by the interaction with the bath of surrounding nuclei. Finally, the integral of Eq. 5.47 is calculated using Eq. 5.48 assuming the autocorrelation function of Eq. 5.45, yielding [215, 216, 217]

$$\begin{aligned} W_{|\alpha\beta\rangle\to|\beta\alpha\rangle} &= \frac{D_{12}^2}{4}\int_{-\infty}^{\infty} e^{-i\Delta\bar{P}\tau - \Gamma_2|\tau|}\langle f(\tau)\rangle_{P'}d\tau \\ &= \frac{D_{12}^2}{4}\frac{1}{2\pi}\int_{-\infty}^{\infty} S_{\Gamma_2}(\omega - \Delta\bar{P})F(\omega)d\omega \\ &= \frac{D_{12}^2}{2}\frac{\Gamma_c(1-\bar{P}^2)\Delta^2 + \Gamma_2(\bar{\Gamma}^2 + \Delta^2)}{\left((1-2\bar{P}^2)\Delta^2 + \Gamma_2\bar{\Gamma}\right)^2 + \Delta^2\bar{P}^2(\Gamma_2 + \bar{\Gamma})^2}, \end{aligned} \tag{5.49}$$

where $\Gamma = \Gamma_2 + \Gamma_c$, $F(\omega)$ is the spectrum of the modulation of $\langle f(t)\rangle_{P'}$ given by

$$F(\omega) = \frac{2\Gamma_c(1-\bar{P}^2)\Delta^2}{(\omega^2 - (1-\bar{P}^2)\Delta^2)^2 + \omega^2\Gamma_c^2}, \tag{5.50}$$

and S_{Γ_2} is the spectrum of the difference between the nuclear levels given by

$$S_{\Gamma_2}(\omega - \Delta\bar{P}) = \frac{2\Gamma_2}{(\omega + \Delta\bar{P})^2 + \Gamma_2^2}. \tag{5.51}$$

The transition rate is only non-zero if the convolution product $S_{\Gamma_2}(\omega - \Delta\bar{P})F(\omega)$ is non-zero for some frequency ω, which is realized when the difference between the Larmor frequency of the nuclei (given by $S_{\Gamma_2}(\omega - \Delta\bar{P})$) matches the frequency of the fluctuation of the electron spin state (given by $F(\omega)$). In other words, the electron flip-flops induce spin diffusion by compensating for the frequency mismatch between the $|\alpha\beta\rangle$ and $|\beta\alpha\rangle$ nuclear levels.

When the electron polarization tends towards unity, the electron flip-flops get frozen out (i.e., $\Gamma_c \to \infty$ and $\bar{P} \to 1$) [3] and so they stop contributing to the transition rate given by Eq. 5.49, leading to

$$W_{|\alpha\beta\rangle\to|\beta\alpha\rangle} = \frac{D_{12}^2}{2}\frac{\Gamma_2}{\Gamma_2^2+\Delta^2}. \tag{5.52}$$

This corresponds to the transition rate between two non-degenerate nuclear levels commonly found in the literature. [218, 219, 71, 72] In the limit of high electron polarization with $\bar{P} \neq 1$ and close to the electron, Eq. 5.49 simplifies to

$$W_{|\alpha\beta\rangle\to|\beta\alpha\rangle} = \frac{D_{12}^2}{2}\frac{1-\bar{P}^2}{\bar{P}^2}\frac{\bar{\Gamma}}{\Delta^2\bar{P}^2+\bar{\Gamma}^2}, \tag{5.53}$$

which is equivalent to the transition rate obtained by Horvitz' perturbative approach in 1971. [108]

Based on the transition rate, we calculate the diffusion coefficient as $D = Wr_a^2$, with r_a the average internuclear distance, following Bloembergen. [161] Fig. 5.26A shows the diffusion coefficient as a function of the distance of the closest nucleus to the electron for various electron polarizations. The dipolar interaction D_{12} and the hyperfine interaction constants $A_{zz,1}$ and $A_{zz,2}$ were averaged over all orientations so that the diffusion coefficient depends only on r (and not on the angles between the vectors connecting the spins and the magnetic field). The black and gray vertical lines indicate the radius of mean volume per electron $r_{\mathrm{MV}} \approx 2.0$ nm and the radius of the hidden spin reservoir $r_h \approx 0.9$ nm, respectively (which we define as the interface between the hidden and visible spins, where the ^{1}H spins have a coupling of 100 kHz with the electron). The grayed area represents the distance to the electron where the assumption that the nuclear spins experience an average value of the hyperfine interaction is no longer valid, i.e., $\Gamma_c < |A_{zzi}|$. Fig. 5.26B shows the spin diffusion coefficient at the interface between the hidden and visible spins, for an electron polarization from 0 to 100%. As depicted by the hollow circles in Fig. 5.26, our model predicts that spin diffusion at the interface is ≈ 7 times faster when the electron polarization is $\bar{P} \approx 50\%$ (that is, under μw irradiation [49, 67]) compared to that at Boltzmann equilibrium $\bar{P} = 99.93\%$. As Fig. 5.26A shows, the contrast of spin diffuson between μw-on and -off is even stronger closer to the electron.

The rate at which polarization rises in the HypRes curves (see Fig. 5.22) is sensitive to the spin diffusion coefficient at the interface between the hidden and visible spins. As we have seen, when the polarization of the electron approaches unity, diffusion is dramatically reduced. In that sense, our theoretical model matches qualitatively with our experimental observations. Because DNP occurs under μw irradiation, that is, at low electron polarization, both our experimental results and our theoretical model lead to the conclusion that spin diffusion in the vicinity of the electron is efficient in our conditions, precisely when DNP is active.

Our model is based on simplifying assumptions which could be improved in several ways. First, we have assumed that the decorrelation rate of the electron spin Γ_c is large compared to the hyperfine interaction but this assumption breaks down at $r = 0.34$ nm (see Fig. 5.26). A more precise calculation would require the use of slow-motion theories. [220] Moreover, we have only considered the anisotropic part of the hyperfine interaction. Improving these points would be necessary if one intends to treat the important case of nuclei on the radical molecule; We have only considered 2-spin order but considering coupled spin terms between more than two spins would lead to predicting faster spin diffusion; [72] We have represented the electron spin state using a spectral density function assuming a homogeneous positive electron polarization. Yet, the predicted number of flip-flops could be higher if the non-Zeeman spin temperature of the electron is considered as it leads to significant variation of electron spin polarization along the spectrum of the electron spin, even though with an apparent constant average Zeemann polarization (see Fig. 3.18).

We found that, in this sample, spin diffusion in the vicinity of the electron is effectively quenched when the electron polarization approaches unity. In other samples, other mechanisms that couple

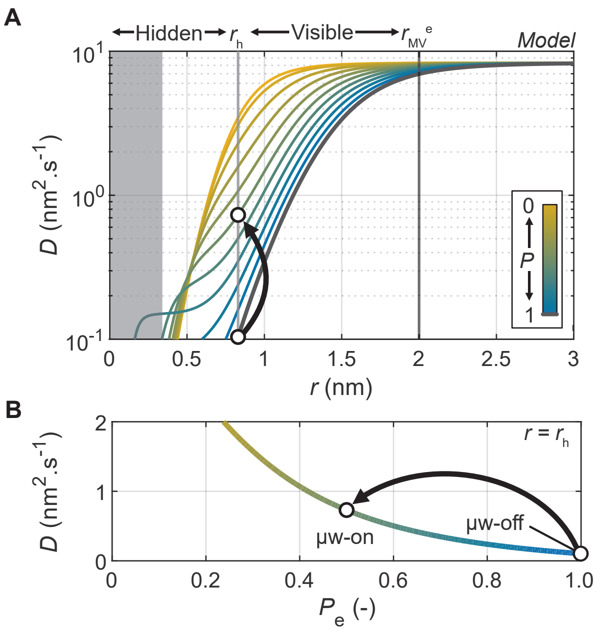

Figure 5.26: **A**. Calculated spin diffusion coefficient as a function of the distance to the electron for the same spin system for different electron polarization $\bar{P}$ between 0 and 1 in steps of 0.1 (see Eq. 5.49). The vertical black and gray lines represent the radius of the mean volume per electron and the limit between the visible and hidden spins, respectively. The gray area indicates the region where the model hypothesis breaks down ($1/\tau_c < |A_{zzi}|$). **B**. Spin diffusion coefficient as a function of the electron polarization at the interface between hidden and visible spins. The arrow between the two hollow circles on both panels indicates the increase in diffusion coefficient upon switching on μw irradiation. The nuclear interdistance r_a, the nuclear broadening due to nucleus-nucleus interactions, and the electron correlation time τ_c are assumed to be 0.66 nm, 18 kHz, and 0.5 μs, respectively.

the nuclear spins to the lattice phonons could be at play. [211] In particular, methyl rotation which is still active at temperatures as low as 1 K could contribute to enhancing spin diffusion. [221]

5.6 Perspectives

We presented a new method, HypRes, and its variants to study nuclear spin polarization transfers between hidden and visible nuclear spins, i.e., those close to the electron and those further away, respectively. While such transfers are most often studied in theory, the HypRes method gives experimental access to them by creating a gradient of polarization between the hidden and visible reservoirs and observing how their polarizations equilibrate with time. We applied the method to several cases: ^{1}H and ^{13}C DNP using TEMPOL and trityl radicals, respectively, in dDNP conditions between 1.2 and 4.2 K at 7.05 T and ^{1}H DNP under MAS-DNP at 100 K and 14.0 T. In all cases, we found that diffusion in the vicinity of the electron is faster than the return of the bulk polarization towards Boltzmann equilibrium.

Spin diffusion of ^{1}H spins was investigated in DNP juice doped with 50 TEMPOL using HypRes as a function of temperature and revealed that the polarization flow rate between hidden and visible spins spreads over two orders of magnitude between 1.2 and 4.2 K. The same data set was also used to estimate the size of the hidden reservoir, i.e., the fraction of nuclear spins which do not contribute to the NMR signal, and we found that the hidden fraction was of the order of $4-7\%$. The hidden fraction was simulated numerically taking into account paramagnetic relaxation enhancement and paramagnetic shifts and the simulated value was found to be in reasonable agreement with the experimental one. On the contrary, a much larger fraction of $\approx 30\%$ was obtained by recording the ^{1}H thermal equilibrium signal of DNP juice as a function of TEMPOL concentration. For now, this discrepancy remains unexplained. The fraction of hidden ^{1}H spins in DNP juice with 50 mM of $4-7\%$ was found to be consistent with that of ^{13}C spins in neat [1-^{13}C]-pyruvic acid doped with 25 mM trityl ($\approx 0.8\%$), considering the ratio of the radical concentrations and the ratio of gyromagnetic ratios of ^{1}H and ^{13}C spins.

The use of broadband inversion pulses in HypRes experiments was shown to enable the manipulation of ^{1}H spins among the invisible spins. The HypRes experiment with inversion was performed on DNP juice doped with 50 mM TEMPOL and showed that ^{1}H spins as close as 3 Å to the electron were still able to exchange polarization with bulk ^{1}H spins on a shorter time scale than T_1 relaxation at 3.8 K and 7.05 T. In Wolfe's definition of the spin diffusion barrier, this result implies that the barrier must be smaller or equal to 3 Å. The HypRes results with inversion pulses also showed experimentally that the nuclear spin diffusion coefficient decreases gradually for spins closer to the electron. If this is to be expected in theory, it had not been verified experimentally, to the best of our knowledge.

The HypRes pulse sequence makes use of a train of saturation pulses to saturate selectively the visible spins and not the hidden spins. In the most recent experiments, we replaced square saturation pulses by sinc pulses and showed that the saturation profile is better defined with sinc pulses, which facilitates the interpretation of the results.

We introduced a third variant of the method, namely, the μw on-HypRes experiment, where spin diffusion between hidden and visible spins is recorded while the electron spin polarization is not at Boltzmann equilibrium but a lower value controlled by the intensity of μw irradiation. We applied this method to ^{1}H spin diffusion in DNP juice doped with 50 mM TEMPOL at 1.2 K to investigate the effect of electron polarization on nuclear spin diffusion. We found that the polarization flow rate between the hidden and visible reservoirs spreads over two orders of magnitude depending on the intensity of μw irradiation, as was the case for the measurements of μw off-HypRes as a function of temperature. We showed that the polarization flow rates measured by μw on- and off-HypRes experiments have the same dependence on the electron polarization. In the case of the μw-off experiment, the electron polarization was simply calculated using Boltzmann's equation, while, in the case of the μw on-experiment, we used the measured values presented in Chapter 4 (see Sec. 4.2). μw off-HypRes experiments were recorded at temperatures between 1.2 and 4.2 K, while μw on-HypRes experiments were all measured at 1.2 K; the fact that the dependence of the nuclear spin diffusion flow rate on electron polarization is the same in both cases is a strong indication that nuclear spin diffusion in the vicinity of electron spins is mediated by electron spin dynamics and not by lattice phonons.

Finally, we rationalized the dependence of nuclear spin diffusion on electron polarization by constructing a model of spin diffusion based on a 2 nucleus-1 electron model inspired by the work of Horvitz. [108] This model treats the dynamics of the electron spin semi-classically and assumes that the field experienced by the nuclei due to the nearby electron averages to a value proportional to the electron polarization due to rapid electron flip-flops. On one hand, the presence of the electron lifts the degeneracy between the $|\alpha\beta\rangle$ and $|\beta\alpha\rangle$ nuclear levels which hinders spin diffusion; on the other hand, the fluctuation of the electron spin state may compensate for the energy mismatch and act as a drive for the $|\alpha\beta\rangle \leftrightarrow |\beta\alpha\rangle$ transition, enabling nuclear spin diffusion. The higher the electron polarization, the stronger the energy mismatch and at the same time the weaker the drive provided by the electron spin state fluctuations. Both effects act together to decrease the efficiency of spin diffusion at increasing electron polarizations. In our DNP conditions, the electron polarization at 1.2 K is lowered from 99.93% to $\approx 60\%$ by μw irradiation. Both our experimental and theoretical results show the fact that μw irradiation lowers the electron polarization is determining for the efficiency of spin diffusion and hence of DNP.

The HypRes experiments presented in this work were performed mostly on DNP juice doped with 50 mM TEMPOL, but several other samples could be of interest. In dDNP conditions, HypRes as a function of radical concentration could be used to confirm that stronger electron-electron interactions increase electron flip-flops and hence spin diffusion. We have found evidence that DNP is faster in samples containing methyl groups, which are known to rotate even at 1.2 K. [221] HypRes could be performed in a sample with various concentrations of methyl-containing molecules (e.g., acetate or methanol) to verify if methyl rotation mediates spin diffusion in the vicinity of the electron spin. All the HypRes measurements we have performed were on fixed electrons. HypRes on PANI could be used to study the mobility of the electron spins in our conditions. Indeed, if electrons in PANI move along the polymer chain, their tendency to hinder nuclear spin diffusion should be much weaker. Finally, in the context of MAS-DNP, HypRes could be used to study the efficiency of nuclear spin diffusion with different radicals. In particular, Perras *et al.* have shown by simulation that the strong ^{1}H density around the electron spin in TEKpol acted like channels for nuclear spin diffusion. [141, 142, 143] HypRes could be used to assess this effect experimentally.

The model for spin diffusion that was presented in this work was only compared qualitatively with experimental results. To test its validity quantitatively, two approaches could be used. HypRes curves (as well as DNP and thermal equilibrium build-up curves) could be fitted with temperature-like models, [207] where the input parameters are the initial distribution of nuclear polarization, the nuclear T_1 and the spin diffusion coefficient, all three as a function of the distance to the electron. The first can be determined experimentally, the second is given by the paramagnetic relaxation rate and the last would be the result of our model. The other possible approach is full quantum mechanical simulations as that performed by Hovav *et al.* [189, 190, 69] or Karabanov *et al.* [71, 203, 72].

So far, we have mainly used HypRes as a tool to understand nuclear spin diffusion in the vicinity of the electron on a fundamental level. In the future, it could be used for the design of optimal sample architecture. As an example, clusters of electrons surrounded by a strong ^{1}H density could be constructed to reach optimal electron-electron interactions for TM while the high ^{1}H density would enable efficient spin diffusion from the electron spin clusters to the bulk nuclear spins. Since the HypRes method allows one to disentangle the efficiency of DNP and spin diffusion, such a sample architecture could be optimized by assessing the efficiency of spin diffusion independently of that of the DNP mechanism.

Chapter 6

Hyperpolarized liquid-state NMR at zero-field

In this final chapter, we move to the liquid-state side of dDNP experiments. As we did in the chapter where we introduced the solid-state side of dDNP (see Chapter 3), we first introduce the instrumentation and the methods for dissolution experiments. We start by detailing the hardware for fast dissolution, transfer and, injection experiments that our team has developed. [222] Next, we show how to quantify polarization in the liquid-state. [121] Finally, we discuss possible sources of polarization losses during dissolution experiments and strategies to mitigate them. [121]

We then present two projects where we used ZULF methods in combination with dDNP. The first project uses spin dynamics at ZULF to mediate a ^{1}H $\rightarrow^{13}$ C polarization transfer in the liquid-state. The method consists of polarizing ^{1}H spins in the solid-state and, after dissolution, propelling the hyperpolarized solution through a well-controlled magnetic field inversion. If the magnetic field inversion is adiabatic, polarization transfers from ^{1}H to ^{13}C spins (provided they are J-coupled) and the molecules reach the liquid-state spectrometer bearing hyperpolarization on ^{13}C spins. We present experimental results as well as numerical simulations of the polarization transfers.

The second project consists of coupling dDNP hyperpolarization with detection at ZULF. An example of such experiment was already reported by Barskiy *et al.* using direct ^{13}C-DNP from trityl radicals. [91] Here, we use ^{1}H-DNP with ^{1}H $\rightarrow^{13}$ C to polarize ^{1}H and ^{13}C spins at the same time, as they both contribute to the signal at zero-field. [223] We first detail the hardware for ZULF detection. We show experimental results of ZULF detection of mixtures of compound hyperpolarized by dDNP. Finally, we discuss the contribution of paramagnetic relaxation to polarization losses during the transfer and strategies to overcome them.

6.1 dDNP instrumentation and methods

The dissolution step of common dDNP experiments consists of injecting a hot solvent, often D_2O, onto the hyperpolarized sample to dissolve it and push the mixture to the liquid-state spectrometer (or MRI scanner) using a pressurized propeller fluid. [224, 121] The transfer and injection can be realized in several ways. The first approach which was introduced in 2003 by Jan-Henrik Ardenkjær-Larsen is to push the sample using pressurized helium gas. [25] This strategy has been improved and optimized in several ways since then, as detailed in Ref. [121]. Depending on the application, the dissolution process has different requirements. For rapidly relaxing species, it should be fast. Transfer times down to 1.2 – 2.0 s are reported. [225, 226, 55] For *in vivo* applications, the injected solution should be sterile. [227] For applications such as drug screening [30, 31] and protein dynamics monitoring, [36, 228] the injected volume needs to be well controlled. For the analysis of complex mixtures such as in the case of metabolomics, the signal linewidth should be narrow to enable signal assignment. [229, 34, 230]

Inspired by Bowen *et al.*'s work, [231] our team has developed an approach for sample dissolution transfer, and injection in less ≈ 1.8 s for a transfer over 2 m and in ≈ 3.5 s for a transfer over 10 m, with control of the injected volume. This method was tested on a mixture of [1-^{13}C]-alanine, [1-^{13}C]-acetate, ^{13}C-formate and ^{13}C-urea. The hyperpolarized signals had ^{13}C signal linewidth below 0.8 Hz 5 s after injection (note that the signal was not measured between 0 and 5 s). However, the ^{13}C polarization was only of the order of 4%. [222] Since then, we were able to improve the magnetic field profile along the transfer which allowed us to minimize polarization losses and reach a ^{13}C polarization of $51\% \pm 13\%$ over seven dissolution runs. The hyperpolarized signal of [1-^{13}C]-acetate had linewidth below 1 Hz and 0.4 Hz, 2 s, and 12 s after injection, respectively. The injected volume had a standard deviation of 37 μl. These recent results are not published yet.

This work has been the struggle and combined effort of the whole HMRlab team but particularly of my former colleague Morgan Ceillier who developed the instrumentation as part of his Ph.D. My contributions to this effort were to understand the sources of polarization losses during dissolution experiments whether by non-adiabatic variations of the magnetic field (intensity or orientation) or through relaxation; to design strategies to control the magnetic field profile along the transfer (in close collaboration with Morgan Ceillier); and to develop data analysis tools on MATLAB so that non-experts of programming could quantify polarizations after dissolution, fit T_1 constants to polarization decays and extract linewidths as a function of time after injection. In this section, we briefly present the instrumentation for fast dissolution, transfer, and injection. Then, we show how polarization can be quantified in the liquid-state after dDNP. Finally, we list the possible sources of polarization losses during dissolution experiments and present strategies to mitigate them.

6.1.1 Fast dissolution, transfer, and injection

The *AlphaPolarizer*, our Bruker functional model dDNP polarizer was initially equipped with a simple dissolution system working according to the following procedure (see diagram in Fig. 6.1). A pressure cooker heats the dissolution solvent prior to dissolution. At this point, the hyperpolarized sample is held in liquid helium at the bottom end of the sample stick. To perform the dissolution process, the operator lifts the sample stick to bring the sample above the level of liquid helium but still inside the cryostat and at high magnetic field. Then, the operator introduces the dissolution stick inside the sample stick and connects it to the sample cup. The dissolution stick consists of a tube that contains two capillaries, the input capillary, which is connected to the pressure cooker, and the output capillary, which is connected to the NMR tube in the liquid-state spectrometer *via* the injector. Immediately after connecting the dissolution stick to the sample cup, the operator triggers the dissolution process, which sends the dissolution solvent onto the hyperpolarized sample and the mixture is propelled to the injector by pressurized He gas (which flows through the pressure cooker) during a defined delay. The solution fills in the injector and flows down in the NMR tube under the effect of gravity and capillarity. At the end of the sequence, a TTL trigger is sent to the liquid-state spectrometer to launch acquisition.

This system has the advantage to be relatively simple to operate. Its main disadvantage is that, after switching off the He gas flow, the pressure takes a few seconds to equilibrate with atmospheric pressure, time during which turbulences and gas bubbles prevent high-resolution NMR acquisition. During this time, the sample starts relaxing, which is an important limitation for hyperpolarized species with T_1 of a few seconds or below. Furthermore, even after the pressures have equilibrated, the He gas, which has dissolved into the solution during the dissolution process, starts forming microbubbles, causing linebroadening of the NMR signal. Nonetheless, this approach has been

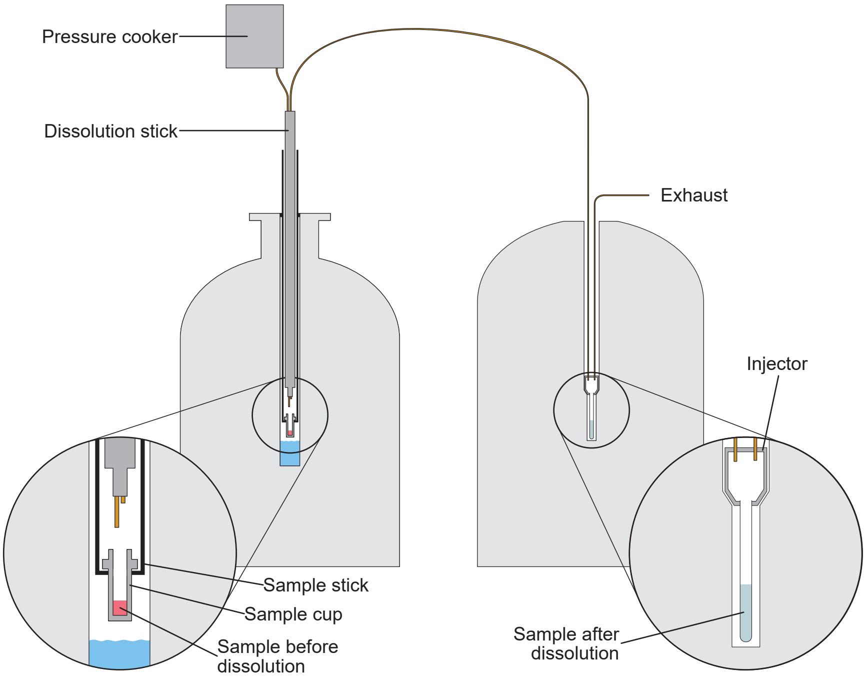

Figure 6.1: Diagram of the main components of the gas-driven dissolution setup from the polarizer to the liquid-state spectrometer (from left to right), represented just before the sample stick is connected to the sample cup when the sample has already been lifted up above the liquid helium bath.

shown to yield high repeatability, in particular using methanol as dissolution solvent. [230]

In the approach that our team has developed (inspired by Bowen *et al.*'s work [231]), the beginning of the sequence is the same and the solution still leaves the polarizer pushed by He gas, which flows through the pressure cooker (referred to as "Dissolution box" in Fig. 6.2). However, in this case, the solution does not go straight to the liquid-state spectrometer; it first goes through a ten way-valve and fills a capillary loop. Once the capillary loop is filled, the front end of the sample bolus reaches an optical sensor, which triggers a second sequence of events. The ten way-valve turns and the volume of sample that was trapped in the capillary loop is now connected to a liquid pump on one side and to the capillary going to the liquid-state spectrometer on the other side. The liquid pump immediately starts pushing liquid isopropanol towards the capillary loop which propels the hyperpolarized solution to the NMR tube. The pump is configured to make a precise number of turns before stopping, which enables control of the volume injected into the NMR tube. Once the pump has stopped turning, a second ten way-valve (the right one in Fig. 6.2) turns so that a back pressure is applied onto the hyperpolarized solution. This back pressure prevents the He gas which dissolved in the hyperpolarized solution during the first part of the dissolution process to degas and cause line broadening of the NMR signal. Finally, a TTL trigger is sent to the liquid-state spectrometer, which launches the NMR acquisition.

The time between the instant where the operator triggers the dissolution process and the instant where the optical sensor detects liquid (i.e., the time for the dissolution solvent to go through the sample cup to the end of the capillary loop) is 1.35 ± 0.01 s. From this point, the time of the remainder of the sequence depends on the distance between the polarizer and the liquid-state spectrometer. [222] With a capillary of 10 m, the transfer takes ≈ 2.1 s, resulting in a total

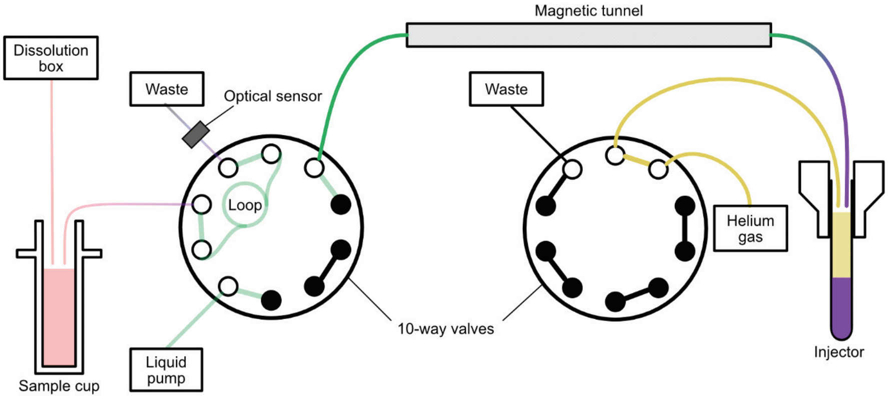

Figure 6.2: Diagram of the setup for fast dissolution, transfer, and injection.

dissolution time of ≈ 3.5 s (including extra delays to turn the valves). With a capillary of < 2 m, the transfer time is below 0.5 s, resulting in a total dissolution time of ≈ 1.8 s and so the longest part of the process is, in this case, to fill the capillary loop.

This method combines the advantage of a rapid time of dissolution, even over long distances (10 m) with control of the injected volume (standard deviation of 37 μl) and excellent signal linewidth below 1 Hz for ^{13}C, 2 s after injection on a benchtop spectrometer. The contamination due to the propeller liquid was found to be negligible, provided the tubing was thoroughly cleaned between dissolution runs. However, all this is hardly useful if most of the polarization is lost during the dissolution and transfer. Indeed, in Ref. [222], we reported polarization of only $\approx 4\%$, while our typical solid-state ^{13}C polarization after multiple contact ^{1}H$\rightarrow$^{13}C-CP is $> 50\%$. Understanding where the polarization was lost during the transfer has been a tremendous effort for our whole team. In Sec. 6.1.3, we will detail the mechanisms which we think used to make us lose so much polarization during the transfer and how we have eventually tamed these losses.

6.1.2 Liquid-state detection and polarization quantification

In Ref. [121] (Sec. 8), I presented in detail how the liquid-state signal is acquired after a dDNP experiment and how to quantify the polarization. Here, we will focus on the key aspects.

Virtually all conventional NMR experiments can be applied to samples hyperpolarized by dDNP. However, since the polarization and signal decay with time, one has to adapt the rf pulse sequences and experimental schemes. As an example, 2D experiments may be performed on a dDNP hyperpolarized sample, provided one uses ultrafast versions of the rf pulse sequences. [232] Here, we will be concerned with the simplest type of liquid-state detection, which consists of a series of 1D acquisitions with small angle rf pulses separated by a constant delay. This type of detection, referred to as pseudo-2D, is the only one I used during my Ph.D. Fig. 6.3A illustrates the pulse sequence. After the sample was injected, a delay t_{wait} allows the solution to settle before the detection starts. The repetition time between acquisitions t_r is usually set to be long compared to the nuclear transverse relaxation time constant T_2^* (typically $t_r > 5T_2^*$) to avoid that one FID pollutes the following. Alternatively, one may use gradients to dephase remaining coherence from the previous FID before the next.

As an example, Fig. 6.3B shows the decay of the ^{13}C signal of hyperpolarized [1-^{13}C]-acetate after injection into a benchtop spectrometer operating at 1.88 T (Bruker Fourier 80), monitored by 5° pulses. To convert the signal integral into polarization, one needs to record a thermal equilibrium

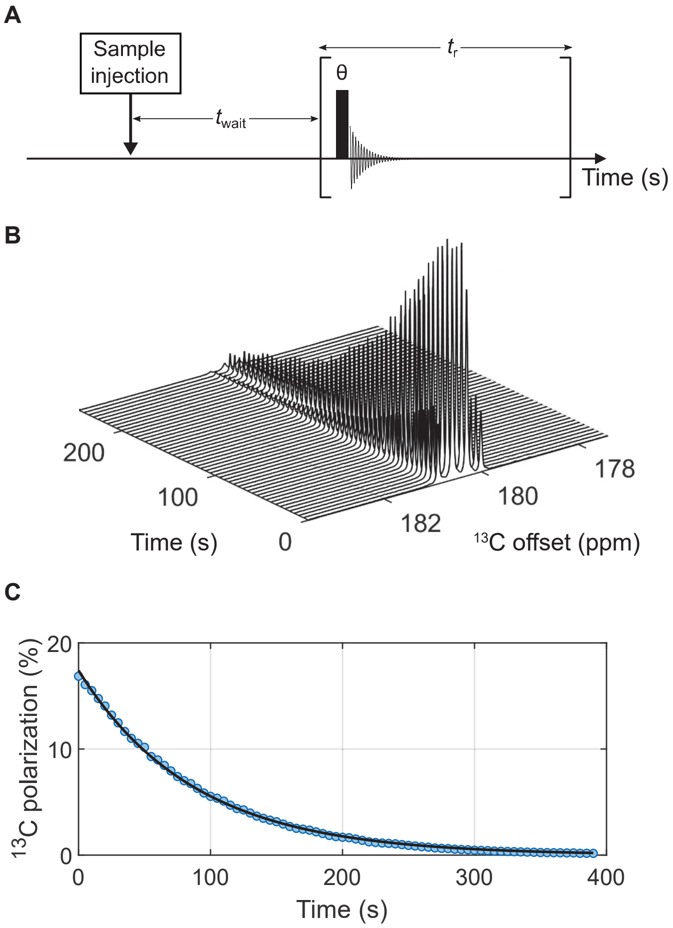

Figure 6.3: **A**. Pulse sequence for the detection of hyperpolarized species in liquids. The symbols t_{wait} and t_r stand for the waiting delay and repetition time, respectively. **B**. Typical decay of the hyperpolarized quadruplet of [1-^{13}C]-sodium acetate recorded at 1.88 T using rf pulses with a 5° nutation angle without ^{1}H decoupling with a repetition time of 5 s and a waiting delay of 8 s. **C**. Decay of the signal integral (blue circles) fitted with a monoexponential decay including the correction for the effect of rf pulses. Reproduced with permission from Ref. [121]

reference signal, as we detailed for the case of solid-state polarization (see Sec. 3.1.3 and 3.1.3). In the liquid-state detection, the signal enhancement is often so high that the hyperpolarized signal cannot be recorded with the same parameters as the thermal equilibrium (unless with poor sensitivity of the thermal equilibrium signal or with saturation of the receiver for the hyperpolarized signal). The polarization is therefore computed as

$$P_{DNP} = \frac{I^n_{DNP}}{I^n_{Th}} P_{Th}, \tag{6.1}$$

where I^n_{DNP}, I^n_{Th} and P_{Th} are the normalized signal integrals of the hyperpolarized and thermal equilibrium signals and the thermal equilibrium Boltzmann polarization of the nuclear spins at the magnetic field of the liquid-state spectrometer and the temperature at which the thermal equilibrium signal was recorded (see Eq. 1.3), respectively. The integrals are normalized as

$$I_k^n = \frac{I_k}{N_S R_G \sin\theta}, \tag{6.2}$$

where I_k, R_G, N_S and θ are the raw signal integral of either the hyperpolarized or the thermal equilibrium signal, the receiver gain, the number of scans, and the pulse angle used to acquire the signal, respectively. For the thermal equilibrium, the pulse angle is usually $\pi/2$ and the number of scans is set high enough to enable sufficient SNR. For the hyperpolarized signal, the pulse angle is usually set to a lower value, e.g., 5°, and the number of scans to 1.

In the example shown in Fig. 6.3B, acquiring the thermal equilibrium signal of ^{13}C spins after dissolution is hopeless. Indeed, with a concentration of a few tens of mM, the sensitivity of ^{13}C spins at 1.88 T does not yield a signal with sufficient SNR, even after a full week of signal averaging. To circumvent this limitation, if the concentration of the solute for which the polarization is to be computed can be quantified in the solution after dissolution, one can compare the integral of the hyperpolarized signal with that of a more concentrated reference sample, for which a decent SNR can be obtained. In this case, the normalization of the signal must account for the concentration of the solute C in addition to the other parameters

$$I_k^n = \frac{I_k}{N_S R_G \sin\theta}\frac{1}{nC}, \tag{6.3}$$

where n is the number of equivalent spins for which the integral is computed. A convenient way to quantify the molecule is to use ^{1}H NMR but this is of course limited to molecules bearing quantifiable ^{1}H spins. This approach assumes that the sensitivity of the probe is not affected by increasing the solute concentration. While at high-field the Q-factor of the probe may be sensitive to the sample composition, in particular to the ionic strength of the solution, it is not the case at 1.88 T, where we have verified that the signal integral was linear with the concentration of [1-^{13}C]-sodium acetate up to 2.5 M, both for the ^{1}H and ^{13}C channels.

The ^{13}C signal along time of Fig. 6.3B was converted into polarization using Eq. 6.3 and is shown in Fig. 6.3C. In this case, the reference ^{13}C sample contained 2.5 M of [1-^{13}C]-acetate. The concentration of [1-^{13}C]-acetate was measured to be 8.4 mM by comparison of the thermal equilibrium of the ^{1}H signal of the sample resulting from the dDNP experiment with that of the reference sample.

6.1.3 Polarization losses

As mentioned in the introduction of Sec. 6.1, our team has struggled for several years to maintain the hyperpolarization accrued in the solid-state during the dissolution process, until detection in the liquid-state. It is well-known that regions of low-field (or zero-field) can cause polarization losses in dDNP experiments [53, 233] In Ref. [121] (Sec. 7), I presented a detailed account of the possible mechanisms that can cause polarization losses during dissolution experiments, which are separated into two types: the return towards Boltzmann equilibrium by relaxation (incoherent losses) and the excitation of coherence by non-adiabatic variation of the magnetic field intensity or direction (coherent losses). Here, we summarize these mechanisms, restricting to those occurring in the liquid-state and paying particular attention to the magnetic field dependence of the mechanisms (in the case of relaxation). We then present the strategies we came up with to mitigate them.

Hyperpolarized nuclear spins return to Boltzmann equilibrium because they are subject to random fluctuations of their Hamiltonian. These fluctuations are stochastic and depend on the physical parameters related to the experimental setup (temperature, magnetic field profile, etc.), the sample formulation, dissolution solvent (presence of radicals, dissolved oxygen, protonation level, etc.), and the properties of the hyperpolarized molecule (dipolar couplings, chemical shift anisotropy (CSA), J-couplings, chemical exchange, etc). By definition, these fluctuations average to zero if we consider a single spin on a sufficiently long timescale or a sufficiently large number of spins. Intuitively, one can say that a nuclear spin ensemble may relax to thermal equilibrium whenever it experiences magnetic fields which oscillate near or at the Larmor frequency. In general, relaxation rates are proportional to the probability to find the perturbating field oscillating at the Larmor frequency (as well as at the difference and sum of the Larmor frequencies between coupled spins in some cases); this probability as a function of frequency is called the spectral density. In addition, relaxation rates are proportional to the square of the strength of the perturbating field (see Eq. 2.155).

The dipolar interaction between nuclear spins within molecules gives rise to intermolecular nuclear dipolar relaxation. In the case of rigid molecules, rotational diffusion modulates the interactions, therefore causing relaxation. The molecules that we studied here (e.g., ^{13}C-formate, [1-^{13}C]-acetate, [1-^{13}C]-pyruvate, [2-^{13}C]-pyruvate, and [3-^{13}C]-pyruvate) are small and tumble rapidly in solution, which makes the spectral density function of their rotational state flat on the range of interest and so it does not depend significantly on the magnetic field (in the range of interest, i.e., < 1 T). This makes the rate of intramolecular dipolar relaxation field-independent for these small molecules. This rate is inversely proportional to the 6^{th} power of the distance between the spins, which makes this mechanism vanishingly weak as soon as the nuclear spins are more than a few Å apart. This explains why the T_1 of the ^{13}C nucleus at 1.88 T and room temperature in D_2O goes from < 20 s in [3-^{13}C]-pyruvate, where the ^{1}H-^{13}C distance corresponds to a single bond length, to > 100 s in [1-^{13}C]-pyruvate, where the ^{1}H and ^{13}C spins are three bonds apart. In the case of CSA relaxation, the intensity of the CSA increases linearly with magnetic field and so the CSA relaxation rate increases with the square of the magnetic field. This mechanism is therefore inefficient at the low magnetic fields of dissolution experiments.

In addition to relaxation mediated by interactions within the molecules, intermolecular interactions can also cause relaxation and are often the strongest source of relaxation in our experiments. In the case of intermolecular dipolar relaxation, a spin on one molecule relaxes through the dipolar interaction with a spin on another molecule, and the interaction is modulated by translational diffusion. The spin acting as relaxing agent can either be borne by an electron (paramagnetic relaxation[1]) or a nucleus (intermolecular nuclear dipolar relaxation). In contrast with rotational diffusion, the spectral density of the interactions modulated by translational diffusion is usually not flat. Therefore, intermolecular dipolar relaxation increases when magnetic field strength decreases. [234, 235] Common sources of intermolecular dipolar relaxation are solvent ^{1}H spins. Common sources of paramagnetic relaxation in dDNP experiments are of course the polarizing agent but also dissolved oxygen. As an example, the paramagnetic ^{13}C-relaxation rate of [1-^{13}C]-acetate in D_2O in the presence of 2.5 mM TEMPOL was measured by Mieville *et al.* as a function of magnetic field from 2 mT to high-field. [234] Their measurements showed that the relaxation rate was below 0.2 s^{-1} (T_1 of at least 5 s) on the whole field range and fell below 0.1 s^{-1} (T_1 of at least 10 s) above 0.1 T. 2.5 mM is a higher concentration than that in our experiments, where the solid-state sample has an initial concentration of 50 mM TEMPOL and the dissolution process dilutes it by ≈ 50. However, it gives conservative lower bounds for $T_1(^{13}\mathrm{C})$ values in our conditions.

Other mechanisms exist (e.g., chemical exchange, scalar relaxation of the second kind, and spin rotation) but they are not effective for the molecules of interest in our conditions.

Among the mechanisms mentioned above, all can be mitigated by increasing temperature, as this reduces the correlation time of the interaction and flattens the spectral density. Intramolecular dipolar relaxation can only be further acted upon by modifying the molecules of interest. For example, the position of the ^{13}C label in pyruvate plays an important role for the $T_1(^{13}\mathrm{C})$. As we have mentioned, $T_1(^{13}\mathrm{C})$ in D_2O is much shorter for [3-^{13}C]-pyruvate than for [1-^{13}C]-pyruvate.

---

[1] We implicitly refer to "intermolecular paramagnetic relaxation" as "paramagnetic relaxation" for simplicity because we are not concerned by relaxation of electron spin bearing molecules in the liquid-state.

Deuteration of the molecule can also be an efficient strategy in some cases. However, because the spectral density of the interaction causing relaxation is flat, it is useless to increase the magnetic field to mitigate this mechanism. To mitigate intermolecular nuclear dipolar relaxation, it is common to use deuterated solvents as D_2O instead of H_2O.

To mitigate paramagnetic relaxation, many strategies have been proposed. Performing DNP with a lower radical concentration may of course help but it might affect the DNP performance. Alternatively, some radicals can be precipitated after dissolution so that they can be filtered out; [227, 236] radicals can be grafted on porous materials and be filtered as well; [57, 54] in the case of TEMPOL, radicals can be degraded chemically using ascorbic acid after dissolution, which has the advantage to quench paramagnetic dissolved oxygen at the same time; [237] finally, non-persistent radicals, such as UV-generated radicals, recombine as temperature increases leaving no radical molecules in solution. [55, 56]

If the solution does contain radicals, paramagnetic relaxation can in some cases be efficiently mitigated by increasing the magnetic field strength. Milani *et al.* have introduced the use of magnetic tunnels made of permanent magnets producing a field of ≈ 0.9 T along the transfer of the solution from the polarizer to the liquid-state spectrometer. [53] They found an increase in the liquid-state polarization by up to a factor of 25 by using a magnetic tunnel. The field-dependence of paramagnetic relaxation depends strongly on the molecule, the solvent, and the temperature; and the field profile between the magnets depends strongly on the laboratory configuration. Therefore, adding a magnetic tunnel might have a tremendous role or no role at all depending on the situation, as shown by Milani *et al.*'s results. In particular, in laboratories equipped with shielded magnets, spins will experience a much lower magnetic field along the transfer (down to Earth's magnetic field) than in laboratories with non-shielded magnets. In our laboratory, the magnetic field goes down to about tens of μT between the polarizer and the liquid-state spectrometers.

The losses caused by relaxation become significant when spins spend a time that is comparable with their T_1 under the effect of the relaxation mechanism. There exists another source of polarization losses that is capable of wiping out the polarization accrued under DNP almost instantaneously. Imagine that fully polarized spins are moving through space in a homogeneous magnetic field B_0 along the z-axis and that, at some point in space the magnetic field rotates from the z- to the x-axis, nearly instantaneously. As they reach the region where the magnetic field points along the x-axis, the spins are no longer in an eigenstate of the Hamiltonian; instead they are in a superposition of states or, in other words, a coherence is excited between the eigenstates corresponding to this region in space. Unless this coherent state is converted back into population by a second synchronized field rotation before the coherence has decayed with T_2 (which has little chance to occur unless on purpose), the polarization that has been converted to coherence is no longer available for measurement. On the contrary, if the magnetic field rotates infinitely slowly from z to x, the spins simply follow the magnetic field, constantly aligning with it. Such a transformation is said to be *adiabatic* and we will come back to it in detail in Sec. 6.2. The field rotation can be considered adiabatic with respect to the spins if its rate ω_r is small compared to the Larmor frequency of the spins ω_0. [238, 53] The limit in which it is adiabatic can therefore be expressed simply as

$$\frac{\omega_0}{\omega_r} \gg 1. \tag{6.4}$$

This criterion may be used to assess if the field profile experienced by the spins during a particular experiment, provided the field profile is known. For example, we used it to estimate if a solution of hyperpolarized ^{13}C spins entering our benchtop spectrometer at a speed of 5 m.s^{-1}, which is typical of our experiments, would experience an adiabatic field trajectory. Fig. 6.4A-B show the complex profile of the stray field as a function of the distance to the center of the magnet.

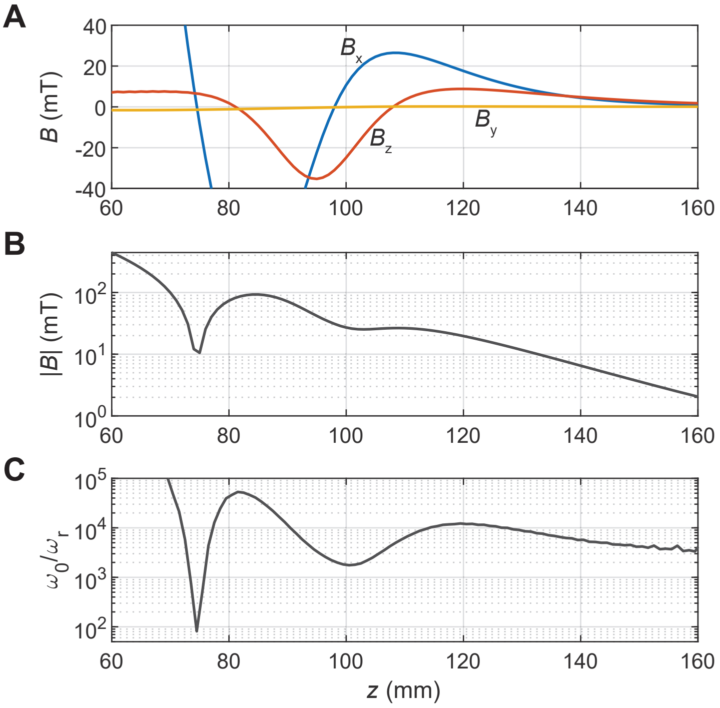

Figure 6.4: **A-B**. Projections along Cartesian axes and norm of the stray field of the Bruker Fourier 80 benchtop spectrometer as a function of the distance to the center, respectively. **C**. Ratio of the Larmor frequency of ^{13}C spins moving at 5 m.s^{-1} along the z-axis and the rotation rate of the magnetic field.

From the field profile, the rate of change of the angle of the magnetic field was computed for a velocity v of the spins as

$$\omega_r = \frac{d\alpha}{dt} = v\frac{d\alpha}{dz}, \tag{6.5}$$

where $d\alpha$ is the angle between $\boldsymbol{B}(z)$ and $\boldsymbol{B}(z+dz)$. The ratio ω_0/ω_r is shown for a ^{13}C spin in Fig. 6.4C. It reaches a minimum of $\approx 80 \gg 1$, which indicates that, despite the complexity of the field profile, ^{13}C spins should be able to follow the field trajectory if traveling with a velocity $v = 5$ m.s^{-1}.

A rapid variation of the intensity of the magnetic field (rather than its angle) may also induce coherence in some spin systems but not for single spin-systems. Indeed, for single spin-systems, a change in the intensity of the magnetic field influences the eigenvalues but not the eigenstates and therefore does not induce mixing of the states. For J-coupled spins, coherence may be induced by going rapidly to low-field, if the coupled spins have a non-zero polarization difference. [235] The critical field where this phenomenon may occur is the field where the J-coupling matches the Larmor frequency difference between the coupled spins (see Sec. 6.2). For heteronuclear spin systems, it will occur at magnetic fields below tens of μT. If such low field values are reached during a dissolution (at least not on purpose), chances are high that polarization will be lost anyway by uncontrolled non-adiabatic magnetic field rotations, as described above. In the case of homonuclear coupled spins, this mechanism can only be expected to be significant in rare cases because it requires a polarization difference between the spins, which is not frequent for molecules polarized by dDNP. The mechanism of polarization losses by a rapid change in the magnetic field intensity should therefore not be critical in our spin systems.

6.1.4 Magnetic field control

Because our dDNP polarizer is shielded and our liquid-state spectrometer is a benchtop spectrometer, their stray fields are not significant during the transfer of the hyperpolarized solution. The most critical point is right at the output of the dDNP polarizer where the stray field is partly canceled by that of two other non-shielded magnets even though they are located ≈ 20 and 10 m away. At this point, the field reaches values below 10 μT and the orientation of the field is not constant along the output capillary of the dissolution stick. Between the polarizer and the bencthop spectrometer, the magnetic field is stable with a strength of ≈ 200 μT.

This configuration is rather dangerous in terms of polarization losses, especially at the output of the polarizer, where the field is low and poorly defined. To minimize polarization losses, we equipped the capillaries through which the hyperpolarized solution travels with a 0.5 mm copper wire wound as shown in Fig. 6.5. A current of $I = 2$ A can be flowed through the wire without noticeable heating, providing a current of $B \leq \mu_0 n I \approx 5$ mT, where $n \leq 2000$ m^{-1} is the number of turns per meter. This value represents a maximum because the distance between the turn is in practice slightly larger than the width of the wire. We use low-price laboratory supplies to feed the solenoid. Stronger fields could be reached using more powerful current supplies such as that used by Kouřil *et al.*, which yield fields of ≈ 70 mT. [239] We chose to use weaker fields and current for ease of use and safety.

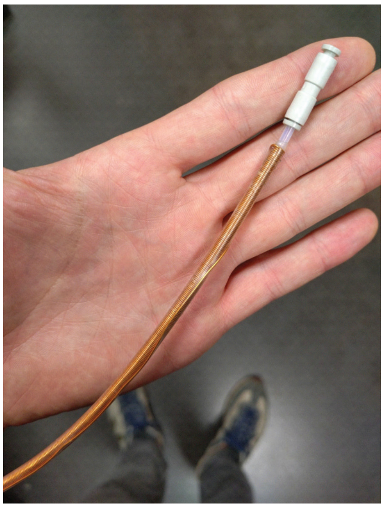

Figure 6.5: Typical transfer line used in our dDNP experiments, consisting of a KelF capillary (O.D. 3.2 mm) surrounded by a 0.5 mm copper wire wound around it.

The capillary output of the dissolution stick is surrounded by a solenoid as shown in Fig. 6.5 from a few cm after its beginning and until its end. Once it reaches the 10 way-valve, it is impractical to sustain the magnetic field using a solenoid coil and so we surrounded the 10 way-valve and the capillary loop (see Fig. 6.2 for details on these components) with a pair of magnetic plates consisting of a 3D-printed structure holding an array of N52 magnets arranged to create a vertical magnetic field. In the center between the plates, the magnetic field is relatively homogeneous and has a value of ≈ 6 mT (see Fig. 6.6A). The solenoid which leaves the 10 way-valve and goes to the liquid-state spectrometer is also surrounded by a solenoid coil with a field of ≈ 4 mT. The connection between this solenoid and the stray field of the benchtop spectrometer is ensured by an insert that is also surrounded by a solenoid (see Fig. 6.6B).

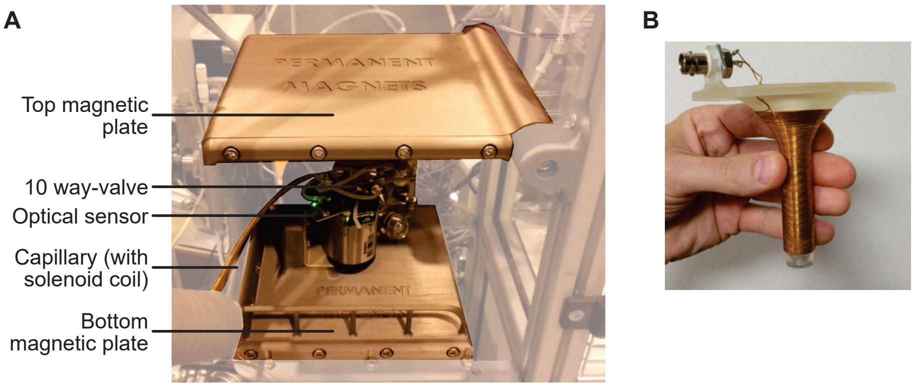

Figure 6.6: **A**. 10 way-valve of the fast dissolution, transfer, and injection system surrounded by a pair of magnetic plates. The capillary surrounded by a solenoid coil is the output capillary of the dissolution stick. **B**. Insert of the benchtop spectrometer surrounded by a solenoid coil.

One may wonder whether the transition from the solenoid to the space in between the magnetic plates is adiabatic. The criterion of Eq. 6.4 may be used to estimate it. The magnetic fields produced by the solenoid and the magnetic plates are depicted in Fig. 6.7A. At the center of the solenoid, the magnetic field is only along the x-axis. If we assume for simplicity that the solenoid is equidistant from the plates, the magnetic generated by the plate is only along the z-axis. There are two critical points as the spins travel in the capillary along the x-axis: as they approach the plates, the field along the x-axis increases and as they leave the solenoid, the field along the z-axis diminishes. Because the magnetic plates have larger dimensions than the solenoid, the first transition is smoother than the second and so we focus on the second, which is limiting the adiabaticity. The field produced by a solenoid decays on a distance on the order of four times its radius R. The $\pi/2$ rotation from x to z therefore occurs over a distance $\approx 4R$ (see Fig. 6.7B). For a solution velocity $v = 5$ m.s^{-1} and a solenoid radius $R = 1.6$ mm, we get using Eq. 6.5 that the field rotation has frequency $\omega_r/2\pi \approx 200$ Hz. The ^{13}C Larmor frequency at 6 mT is ≈ 64 kHz and the ratio between the Larmor frequency and the frequency of rotation of the magnetic field is of the order $\omega_0/\omega_r \approx 320 \gg 1$.

This rough estimation shows that the field rotation experienced by ^{13}C spins as they move out from inside the solenoid into the space between the magnetic plates should be adiabatic. Yet, we obtained ^{13}C polarizations of only $\approx 4\%$ using this setup. [222] Because the field trajectory is rather complex, we chose to perform experiments where the more "rudimentary" gas-driven dissolution setup (see Fig. 6.1) and a single solenoid going from inside the polarizer to inside the benchtop spectrometer. We obtained better preservation of the polarization along the transfer, as reported in Ref. [119]; starting from $\approx 44\%$ ^{13}C polarization in the solid-state, we obtained $\approx 28\%$ in the liquid-state. We then performed experiments where the output capillary of the dissolution stick was connected directly to the capillary loop but bypassing the 10 way-valve (again using the gas-driven dissolution system). From the capillary loop, the solution was going to the benchtop spectrometer surrounded by a solenoid, as previously. We obtained polarization up to 20% (the solid-state was not quantified). Let us recall that there is no solenoid around the capillary loop, which is surrounded by magnetic plates. This experiment, therefore, showed that the transition from the solenoid to the magnetic plates was not the culprit of our polarization losses. We concluded that the stainless steel 10 way-valve through which the hyperpolarized solution was

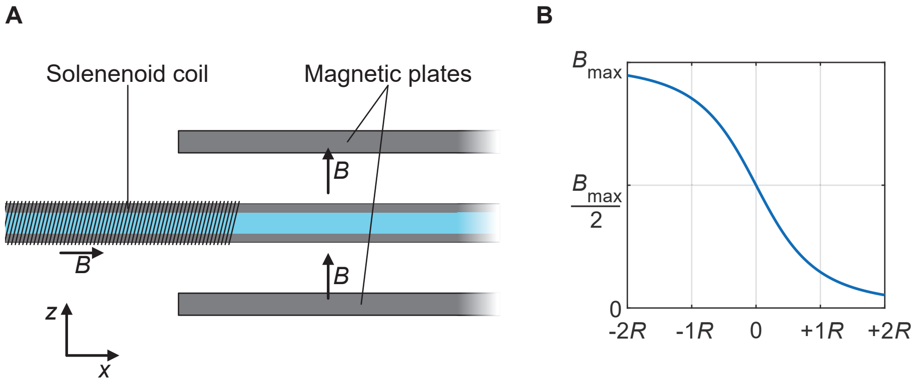

Figure 6.7: **A**. Schematic representation of a capillary surrounded by a solenoid coil on one side and by two magnetic plates on the other. **B**. Magnetic field at the center of a solenoid (with $L \gg R$, where L and R are the radius and the length of the solenoid, respectively), with respect to its maximum field strength B_{max}, as a function of position, calculated using Eq. 6.19 (more details in Sec. 6.2.3). The origin is located at the edge of the solenoid.

flowing was screening the magnetic field of the permanent magnets around it and hence causing a non-adiabatic field profile and subsequent polarization losses. We replaced the stainless steel valve with a titanium equivalent and finally obtained liquid-state ^{13}C polarizations of $\approx 50\%$.

6.2 ^{1}H→^{13}C polarization transfer by adiabatic field inversion

As we saw in the introduction of this work (see Sec. 1.2.2), the production of ^{13}C-hyperpolarized metabolites is the main driving force for the development of dDNP. The most common strategy is by far to polarize ^{13}C spins directly using the narrow EPR line radical trityl, which typically reaches $P(^{13}\text{C}) > 50\%$ in 1-2 hours. [45] Our usual approach at the HMRlab is to polarize ^{1}H spins using the broad EPR line radical TEMPOL and to transfer the polarization to ^{13}C spins in the solid-state by multiple contact CP. [47, 49, 116, 117, 118, 119, 120, 121] This method can reach similar polarization levels but in only $10 - 20$ min. However, CP requires high power pulses which tend to cause coil arcing in superfluidic helium. The CP-based approach, therefore, requires complex and sensitive instrumentation, which can break down and need fixing by highly skilled technicians. An approach based on simpler instrumentation yet faster than direct ^{13}C-DNP would be an advantage for clinical applications.

In this section, building on the instrumentation presented in Sec. 6.1, we investigate the use of an *an in-line adiabatic magnetic field inversion* to transfer the polarization of dDNP hyperpolarized ^{1}H spins to ^{13}C spins in the liquid-state *via* ^{1}H-^{13}C J-couplings. The magnetic field inversion is produced by an *inversion chamber* consisting of a pair of co-linear solenoid coils placed in the middle of μ-metal magnetic shields, and producing opposing magnetic fields which cancel in the middle of the distance between the coils (see Fig. 6.8). As the solution flows through the inversion chamber, the spins experience the magnetic field inversion through space. The variation of field in space is therefore used to produce a variation of field in time, thanks to the velocity of the solution during the dissolution experiment. This method makes use of so-called "avoided crossings" between singlet and triplet nuclear spin states at zero-field which enable the polarization transfer between the heteronuclei.

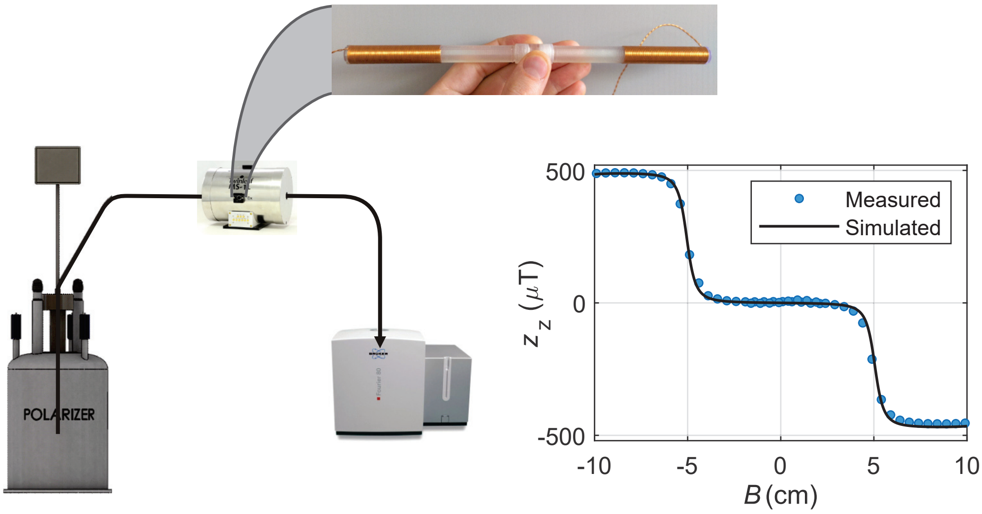

Figure 6.8: Experimetnal setup, where a ^{1}H-dDNP hyperpolarized solution is transferred to a liquid-state spectrometer *via* a magnetic field inversion chamber, consisting of μ-metal magnetic shields and a pair of solenoids producing opposing magnetic fields which cancel in the middle.

We first briefly present the theory of avoided crossings and calculate the minimum field inversion time for an adiabatic polarization transfer in a heteronuclear two spin-system using the Landau-Zener formula. We find that the minimum inversion time is proportional to the inverse of the J-coupling. Then, we use numerical simulations to predict precisely the polarizations after field inversion for two spin- and four spin-systems with different J-couplings.

We present experimental results on model spin systems of ^{13}C-formate, [3-^{13}C]-pyruvate, [2-^{13}C]-pyruvate and [1-^{13}C]-pyruvate, which have J-couplings in D_2O of 195, 125, 6.2, and 1.3 Hz, respectively. ^{1}H spins in a sample containing these four molecules were hyperpolarized by dDNP and the solution was pushed through the inversion chamber during the transfer before detection in the liquid-state. We found hyperpolarized signals in the liquid-state for the two molecules with the strongest J-coupling, while not for the two other molecules, in agreement with numerical simulations.

We demonstrate that the method is capable of producing $P(^{13}\mathrm{C}) \approx 9 - 12\%$ in the liquid-state after $\approx$ 10 min of DNP in the solid-state. Considering the ^{1}H polarization in the solid-state, a perfect transfer should yield $P(^{13}\mathrm{C}) > 50\%$ in the liquid-state for two molecules with strong J-couplings. The lower $P(^{13}\mathrm{C})$ polarization obtained experimentally is rationalized by rapid ^{1}H relaxation prior to the transfer.

Finally, we propose strategies to polarize ^{13}C spins in molecules with lower J-couplings, like [2-^{13}C]-pyruvate and [1-^{13}C]-pyruvate, which have higher clinical relevance. In particular, we present an algorithm to compute field profiles with constant adiabaticity, which enables the fastest possible transfers. We also discuss the risks associated with uncontrolled residual fields, which would prevent an efficient transfer.

This project was started as a collaboration with Prof. Konstantin L'vovich Ivanov, who passed away on 5 March 2021 as a victim of COVID-19. [240] I would like to acknowledge his contribution not only to this project but to my understanding of spin dynamics and NMR simulation. Kostya helped me start the simulation presented in this section, which then put me on track for the remainder of my Ph.D. This section is dedicated to his memory, his kindness, and his availability to help students.

6.2.1 Avoided crossings in a two spin-system

Coherent spin dynamics at ZULF have already been exploited extensively in the context of PHIP to convert ^{1}H singlet order from parahydrogen into ^{13}C magnetization for the preparation of ^{13}C-hyperpolarized metabolites. Some techniques use a magnetic field jump to zero-field followed by an adiabatic increase of the magnetic field [241, 89, 242, 243]. Others use pulses at ultra low-field [90] or adiabatic field inversions. [95]

In the context of dDNP, hyperpolarized solutions may happen to go through regions of low-field and even through field inversions, during the transfer from the polarizer to the liquid-state spectrometer. If the consequences of such spin dynamics at ZULF have been reported, they have not been actively made use of. [235, 233] Here, we use spin dynamics at ZULF to transfer the polarization of ^{1}H spins hyperpolarized by dDNP to ^{13}C spins in a controlled way, building on the well-understood theory developed by these many authors before us. We now introduce the necessary basic theoretical concepts behind our method.

Consider a pair of heteronuclei ensemble S and I, with gyromagnetic ratio γ_S and γ_I, respectively, where S initially has polarization $P_\mathrm{S} = 1$ along a strong magnetic field B_0, while I has no net polarization along any axis. Now, let us consider what happens if the magnetic field inverts linearly along time from positive to negative values as

$$B(t) = B_0 \left(1 - 2\frac{t}{\tau}\right), \tag{6.6}$$

where τ is the time that the field takes to invert from $+B_0$ to $-B_0$. We first assume that τ is infinitely long and so the evolution of the system is *adiabatic*. The fact that the variation is adiabatic can be defined as follows: if a parameter of a quantum mechanical system varies with time, the variation is said to be adiabatic if it is *slow enough* for populations to remain in eigenstates all along the process. [244] We will soon come back to what “slow” means but for now we just assume it is slow enough. Fig. 6.9A shows the energy levels during the field inversion, for S and I being a ^{1}H and ^{13}C spin, respectively, in the absence of coupling. Because the spins are not coupled, they are only subject to the Zeeman Hamiltonian and the eigenfrequencies vary linearly with magnetic field. At time $t = 0$, the populations are $p_{\alpha\alpha} = p_{\alpha\beta} = 1/2$ (represented by white dots) while $p_{\beta\alpha} = p_{\beta\beta} = 0$. As the magnetic field inverts, populations follow their eigenstates and end up in the positions represented by black dots. Nothing interesting happened: the populations remained exactly what they were before inversion and so the polarizations still are $P_\mathrm{S} = 1$ and $P_\mathrm{I} = 0$.

On the contrary, if the two spins are J-coupled, the J-coupling Hamiltonian mixes the $|\alpha\beta\rangle$ and $|\beta\alpha\rangle$ at zero-field, as represented in Fig. 6.9B, which results in an avoided crossing (see Sec. 2.3.2). After the field inversion, the population which was initially in the $|\alpha\beta\rangle$ state is converted into $|\beta\alpha\rangle$, while the population of the $|\alpha\alpha\rangle$ state remains on the same state. The final polarizations are hence $P_\mathrm{S} = 0$ and $P_\mathrm{I} = 1$, which means that the polarization has been transferred from S to I.

This simple argument shows that if we can make a J-coupled ^{1}H-^{13}C spin pair experience an adiabatic field inversion, the polarization of the ^{1}H spins acquired during dDNP will be transferred to the ^{13}C spins. The question is now to determine how slow the inversion needs to be. We use the Landau-Zener formula to get a first estimate, which we will refine in Sec. 6.2.2 using numerical simulations. Landau-Zener formula gives the probability for a diabatic transition (i.e., what we do not want) [245, 246, 204]

$$P_d = \exp\left(-2\pi\omega_{12}\tau\right), \tag{6.7}$$

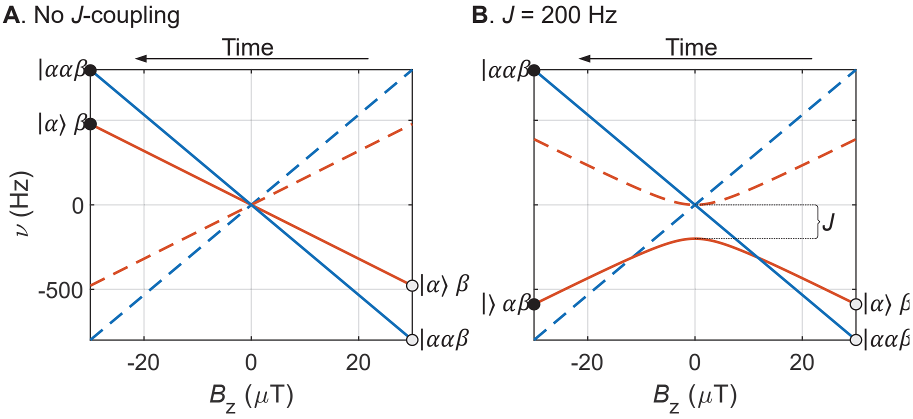

Figure 6.9: **A-B**. Comparison of the eigenfrequencies of the four levels of a ^{1}H-^{13}C pair as a function of magnetic field without J-coupling and with $J = 200$ Hz, respectively. The white and black dots represent the populations of the states before and after the adiabatic field inversion, respectively, assuming initial polarization $P(^1\text{H}) = 1$ and $P(^{13}\text{C}) = 0$.

where ω_{12} is the frequency separation between the perturbed states at the crossing point of the unperturbed states. τ is the time of interaction, i.e., the time during which the perturbation mixes the states. This formula is valid in the specific case where the energies of the unperturbed state vary linearly with time (as is the case with field trajectory of Eq. 6.6). It follows that the linear transformation has to take place over time

$$\begin{aligned} \tau &= \frac{1}{2\pi\omega_{12}} \log\left(\frac{1}{P_d}\right) \\ &= \frac{1}{2\pi\omega_{12}} \log\left(\frac{1}{1-P_a}\right), \end{aligned} \tag{6.8}$$

to have probability P_a to be adiabatic. In our case, the separation between the unperturbed states is $\omega_{12} = 2\pi J$ (see Fig. 6.9) and so

$$\tau = \frac{1}{4\pi^2 J} \log\left(\frac{1}{1-P_a}\right), \tag{6.9}$$

which shows that the time during which the magnetic field must invert from $+B_0$ to $-B_0$ for an arbitrary value of P_a is inversely proportional to the J-coupling between the spins. To determine the value of B_0, we recall that τ is the time during which the states interact (or are mixed by the perturbation). In our case, this corresponds to the time during which the intensity of the J-coupling Hamiltonian $|\hat{H}_J|$ is significant compared to that of the Zeeman Hamiltonian $|\hat{H}_Z|$. The limit where $|\hat{H}_J|$ becomes insignificant may be expressed as a function of an arbitrary parameter ζ

$$|\hat{H}_Z| = \zeta|\hat{H}_J| \iff B_0 = \zeta\left|\frac{2\pi J}{\gamma_S - \gamma_I}\right|, \tag{6.10}$$

where the norms of the operators were calculated as the difference between the eigenvalues. The pair of values of τ and B_0 define the linear magnetic field profile as in Eq. 6.6 which results in a polarization transfer with yield P_a. Fig. 6.10A-B shows predicted values of τ and B_0, respectively, as a function of the J-coupling between a ^{1}H and a ^{13}C spin. It shows that, for $J = 200$ Hz, the magnetic field must invert from $+60$ μT to -60 μT within ≈ 0.6 ms in order to yield $P_a = 0.99$.

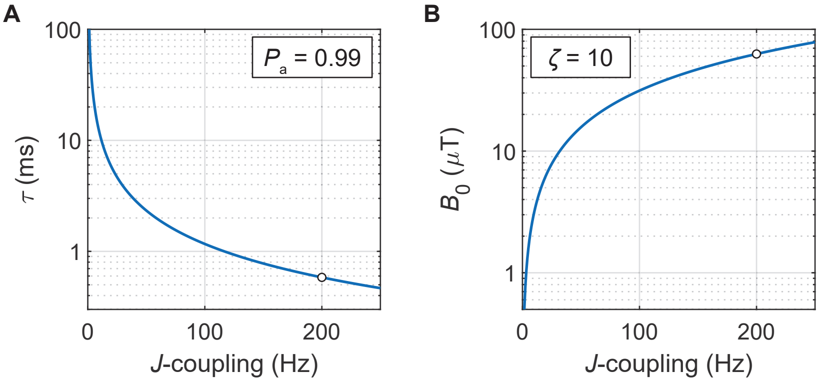

Figure 6.10: **A**. Magnetic field inversion time to transfer the polarization from ^{1}H to ^{13}C spins as a function of the J-coupling between them, with yield $P_a = 0.99$, computed using Eq. 6.9. **B**. Absolute value of the initial and final magnetic field intensity of the field profile for a polarization transfer from ^{1}H to ^{13}C spins as a function of J-coupling between them, with $\zeta = 10$, computed using Eq. 6.10.

As can be seen from Fig. 6.9B, $\zeta = 10$ is a rather conservative (and maybe excessive) value, as the $B_0 = \pm 60$ μT is far outside the plot, where the energies are linear with the magnetic field, i.e., where $\hat{H}_J$ is not causing a significant mixing.

6.2.2 Numerical simulation of the transfer

Using the Landau-Zener formula, we calculated the minimum field inversion time for a two spin-system experiencing a field inversion going linearly from a positive to a negative value B_0. However, a much shorter inversion time with the same transfer yield P_a can be afforded if a more optimized field profile is used. [244] Furthermore, realizing a linear field inversion profile is not particularly simple in practice. We now show how to compute the ^{1}H and ^{13}C polarizations of an XA$_n$ spin system (where X and A are ^{13}C and ^{1}H spins, respectively) along the inversion coordinate for arbitrary field profiles. In practice, we used these simulations to optimize the geometry of the solenoid coils shown in Fig. 6.8 and the applied current. Here, we only show the simulations for the field profile which was used in experiments, after manual optimization. This field profile is shown as a black curve in Fig. 6.11. The way this field profile was generated and controlled is detailed in the next section (see Sec. 6.2.3).

We assume that, before inversion, ^{1}H spins have polarization $P_{\mathrm{S}} = 1$ and ^{13}C spins have polarization $P_{\mathrm{I}} = 0$. The initial density matrix is given by the Kronecker product of single spin density matrices (see Eq. 2.86)

$$\hat{\rho}_0 = \otimes_{k=1}^{n} \left(\frac{\hat{\mathbb{1}}^{2\times 2}}{2} + P_{\mathrm{S}} \hat{S}_z^{2\times 2} \right) \otimes \left(\frac{\hat{\mathbb{1}}^{2\times 2}}{2} + P_{\mathrm{I}} \hat{I}_z^{2\times 2} \right), \tag{6.11}$$

where $\hat{\mathbb{1}}^{2\times 2}$, $\hat{S}_z^{2\times 2}$ and $\hat{I}_z^{2\times 2}$ are the identity operator and the z-angular momentum operators of the n spins S and spin I in single spin-space, respectively. If $B_z(t)$ is the magnetic field along the z-axis at time t, the total Hamiltonian is

$$\hat{H}_{tot}(t) = \hat{H}_Z(t) + \hat{H}_J, \tag{6.12}$$

where the time-dependent Zeeman Hamiltonian is

$$\hat{H}_Z(t) = -B_z(t)\left(\gamma_{\mathrm{I}}\hat{I}_z + \sum_{k=1}^{n}\gamma_{\mathrm{S}}\hat{S}_{kz}\right), \tag{6.13}$$

where $\hat{S}_{kz}$ and $\hat{I}_z$ are the z-angular momentum operators in the $n+1$ spin-space of the k^{th} spin S and spin I, respectively, and the time-independent J-Hamiltonian is

$$\hat{H}_J = J_{AA}\sum_{k>j}\hat{\boldsymbol{S}}_k \cdot \hat{\boldsymbol{S}}_j + J_{XA}\sum_{k=1}^{n}\hat{\boldsymbol{S}}_k \cdot \hat{\boldsymbol{I}}, \tag{6.14}$$

where J_{AA} and J_{XA} are the homonuclear J-coupling constants between S spins (if $n > 1$) and the heteronuclear J-coupling between S and I spins. The state of the system was propagated during short time intervals dt from t to $t + dt$ using the sandwich formula (see Eq. 2.76)

$$\hat{\rho}(t + dt) = \hat{U}(t)\hat{\rho}(t)\hat{U}^*(t), \tag{6.15}$$

where the time propagator from t to $t + dt$ is

$$\hat{U}(t) = \exp\left(-i\hat{H}_{tot}(t)dt\right). \tag{6.16}$$

Finally, for each time point t, the expectation value of the polarization of I was computed as

$$P_{\mathrm{I}}(t) = \frac{1}{|I|}\mathrm{Tr}\left\{\hat{\rho}(t)\hat{I}_z\right\}, \tag{6.17}$$

and that of S spins was computed as the average of the individual polarizations $P_{\mathrm{S,k}}(t)$

$$P_{\mathrm{S}}(t) = \frac{1}{n}\sum_{k=1}^{n}P_{\mathrm{S,k}}(t) = \frac{1}{n|S|}\sum_{k=1}^{n}\mathrm{Tr}\left\{\hat{\rho}(t)\hat{S}_{kz}\right\}. \tag{6.18}$$

This procedure was used to simulate the polarizations of ^{1}H and ^{13}C spins in ^{13}C-formate (with $J = 195$ Hz and $n = 1$) along the transfer through the inversion chamber assuming a velocity of $v = 4$ m.s^{-1} of the solution through space (see Fig. 6.11). The field profile, which starts at $+4400$ μT at -20 cm and terminates at -4400 μT at $+20$ cm, was discretized into 20'000 constant increments of 20 μm, corresponding to $dt = 5$ μs. The total transfer time through the inversion chamber is $\tau_{trans} = v/l = 100$ ms, where $l = 40$ cm is the length of the inversion chamber. Note that Fig. 6.11 only shows a central portion of the inversion chamber because the polarizations are stationary outside this range. The simulation was performed using a home-written MATLAB code and took < 1 s to run on a laptop computer.

Fig. 6.11 shows that pushing a solution of ^{13}C-formate through this particular field profile with a velocity of 4 m.s^{-1} fully transfers the ^{1}H polarization to the ^{13}C if relaxation can be neglected. It also shows that polarization starts transferring when the field gets below $\approx +60$ μT and stabilizes once the field has passed ≈ -60 μT. The fact that polarizations evolve almost linearly along the inversion coordinate (and hence along time) indicates that the field profile is nearly optimal (i.e., near constantly adiabaticity [244]).

The simulation was repeated for four molecules: ^{13}C-formate, [3-^{13}C]-pyruvate, [2-^{13}C]-pyruvate and [1-^{13}C]-pyruvate, which have J-couplings in D_2O of 195, 125, 6.2, and 1.3 Hz, respectively (the chemical structure of the molecules are shown in Fig. 6.12). The same field profile was discretized again into 20'000 increments. This time, the expectation values of the polarizations were not computed for all time increments but only for the final density matrix, and the simulation was repeated for 200 values of the transfer time through the inversion chamber τ_{trans} between 0 and 50 ms. The results are shown in Fig. 6.12. We ought to make it clear that these plots

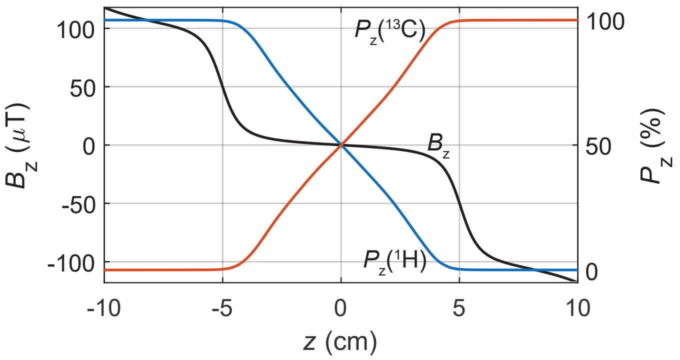

Figure 6.11: Simulated field profile inside the inversion chamber and ^{1}H and ^{13}C polarizations along the transfer in black, assuming a J-coupling of 195 Hz and initial polarization $P(^1\text{H}) = 1$ and $P(^{13}\text{C}) = 0$, corresponding to ^{13}C-formate in D_2O. Details of the spin dynamical simulation are given in the text. Details on the simulation of the field profile are given in Sec. 6.2.3

do not represent the polarizations of the spin along time but rather their polarization at the end of individual experiments, as a function of the time over which the experiment is realized. The simulation of each plot was realized in < 2 min on a laptop computer.

The first observation one can make on Fig. 6.12 is that for $\tau_{trans} = 0$, i.e., for an infinitely fast field inversion, the polarization does not transfer; it stays fully on the ^{1}H spins. As τ_{trans} increases, a significant amount of polarization transfers to ^{13}C spins, but only for the molecules with strong J-couplings. For ^{13}C-formate, $\tau_{trans} \approx 40$ ms is sufficient to transfer fully the ^{1}H polarization to the ^{13}C, i.e., the transfer is adiabatic, while for [3-^{13}C]-pyruvate, polarizations are not completely stable with $\tau_{trans} = 50$ ms (see Fig. 6.12A-B, respectively). For longer values of τ_{trans} (not shown), the polarizations in [3-^{13}C]-pyruvate tend towards $P(^1\text{H}) \approx 66.7\%$ and $P(^{13}\text{C}) \approx 100\%$. This can be seen as a result of the conservation of angular momentum in the case where three ^{1}H spins interact with a single ^{13}C spin. In the case [2-^{13}C]-pyruvate and [1-^{13}C]-pyruvate, owing to the low J-coupling values, the transformation is almost completely diabatic using this field profile and these transfer times, and results in almost null polarization transfer (see Fig. 6.12C-D, respectively).

It is surprising to find such long transfer times of ≈ 40 ms for an adiabatic inversion with ^{13}C-formate, considering that the Landau-Zener formula predicted values of below 1 ms. The numerically simulated transfers correspond to a field trajectory from $+4400$ μT to -4400 μT over 40 cm. The transfer time corresponding to the portion $+60$ μT to -60 μT is of $40\ \mu\text{T} \times 10/40 \approx 10$ ms, which is a fairer comparison with the transfer time of Landau-Zener formula for ^{13}C-formate. This is still more than an order of magnitude larger than the transfer time predicted by the Landau-Zener formula. Moreover, we found numerically that the non-linear field profile that we used allows the transfer to be much shorter than the linear trajectory with the same adiabaticity. If Landau-Zener theory allowed us to find a useful trend to guide our experimental choices, i.e., an inverse dependence of the transfer time on the J-coupling, it is unclear whether the numerical values we found are of interest.

6.2.3 Experimental setup and results

In the previous section, we predicted the efficiency of the polarization transfer for four molecules using the field profile of Fig. 6.11 using numerical simulation. We now show how this field profile was realized in practice. We then show the results of the hyperpolarized liquid-state results for

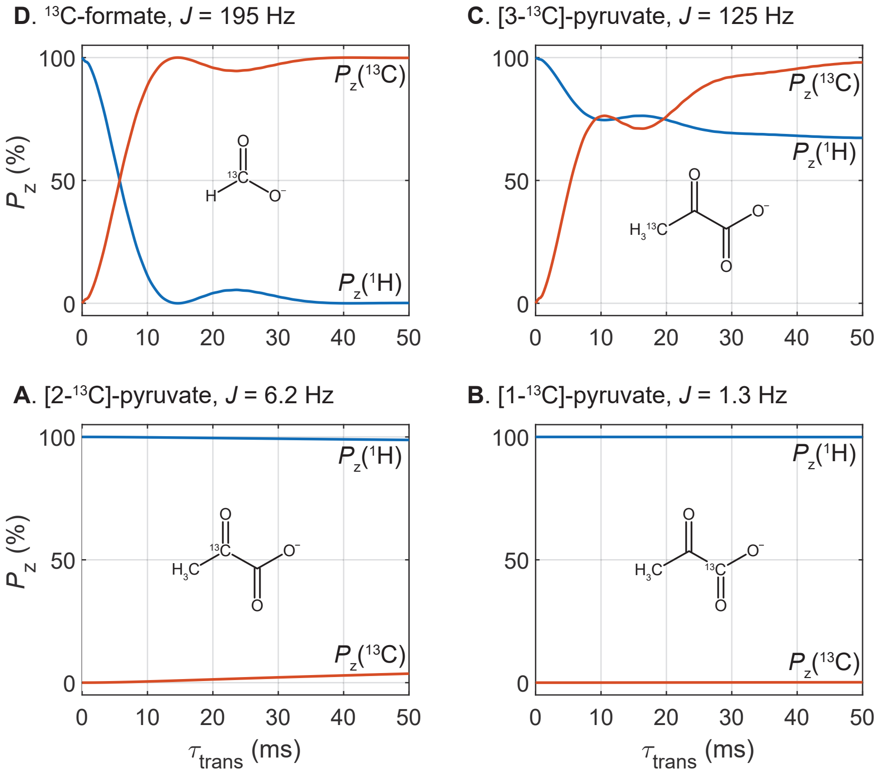

Figure 6.12: Numerical simulations of the final polarizations of ^{1}H and ^{13}C spins as a function of the time of transfer τ_{trans} through the inversion chamber with the field profile of Fig. 6.11.

the four molecules with and without field inversion, the latter experiment serving as a control experiment.

The components of the inversion chamber are detailed in Fig. 6.13. The main part is commercial μ-metal magnetic shields (MS-1, Twinleaf LCC). The capillary which gets out of the dissolution stick (see Sec. 6.1.1) is connected to the piercing capillary by a QuickConnect connector. This capillary has O.D. 3.2 mm and 0.5 mm copper wire is wound around it. This wire is fed with a current of $I = 2$ A, which generates a field of $B_z = \mu_0 n I$, where $\mu_0 = 4\pi \cdot 10^{-7}$ H.m^{-1} and n is the number of turn per meter, which is approximately 2000 at maximum. Because the distance between turns is never as short as the diameter of the wire, $n = 2000$ m^{-1} is a maximum and so the solenoid generates a magnetic field of maximum $B_z \leq 5$ mT. As the capillary gets out of the shields a similar solenoid coil is wound around it until the capillary reaches the fast injections setup (see Sec 6.1.4). The internal solenoids are the ones responsible for the field inversion. They consist of a 3D printed support with a groove that allows one to place a copper wire of 0.5 mm with high precision. The distance between the turns of the groove is 0.65 mm which is made greater than the wire diameter on purpose to make sure that the wire lies in the groove. These solenoid coils have an O.D. of 12 mm and a length of 70 mm and they are separated by $D = 101$ mm. They are fed with a current $I = 50$ mA in opposite direction. In order for the spins to experience a controlled magnetic field as they leave the capillary solenoid coil at the input of the shields (or enter the capillary solenoid coil at the output of the shields), the end of the capillary solenoid coils and that of the internal solenoids are surrounded by larger solenoid coils (referred to as "external solenoids" in Fig. 6.13). These coils also consist of a 3D-printed structure with 0.5 mm copper wire wound in a 0.65 mm groove. They are fed with a current $I = 2$ A.

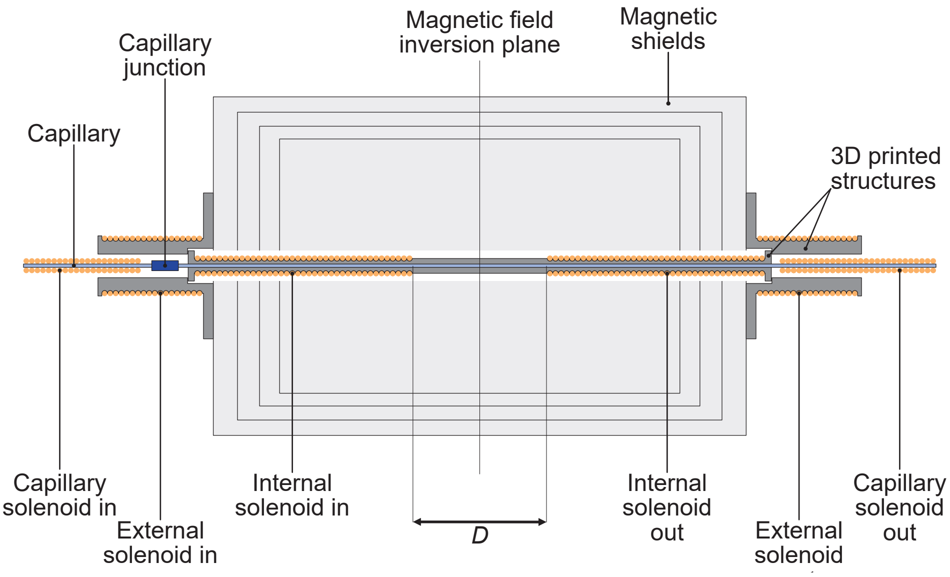

Figure 6.13: Schematic representation of the inversion chamber. Dark gray elements represent 3D-printed structures. Filled yellow circles represent wires of solenoid coils. A photograph of the internal coil is shown in Fig. 6.8.

The magnetic field in the direction of the velocity of the fluid, which we call z, with the origin at the center of the shield (i.e., the point of inversion), can be calculated using the standard equation of a perfect solenoid

$$B_z(z) = \frac{\mu_0 n I}{2}\left(\frac{L/2 - \Delta z}{\sqrt{R^2 + (L/2 - \Delta z)^2}} + \frac{L/2 + \Delta z}{\sqrt{R^2 + (L/2 + \Delta z)^2}}\right), \tag{6.19}$$

where L, R, and $\Delta z = z - z_0$ are the length of the solenoid coil, its radius, and the distance between the center of the shields ($z = 0$) and the center of the solenoid coil z_0, respectively. The field profile shown in Fig. 6.11 and used in the simulation was computed by summing the contribution of the two internal solenoid coils and the two external solenoid coils. To verify that the simulated magnetic field is correct, the field profile was measured using a teslameter (Lakeshore multi-axis teslameter F71-240 with a three-axis hall probe FP-2X-250-ZS15-6). However, a higher current was applied in the internal solenoid coils ($I = 250$ mA) so that the field could be measured with higher resolution. The measured and simulated field profiles are compared in Fig. 6.8, in the introduction of this section. The measurement and the simulation are in reasonable agreement, although the decay of the stray field (at -5 and $+5$ cm) has a softer slope for the measured profile. This discrepancy is likely due to the presence of the magnetic shields which distorts the field lines.

We now present four dDNP experiments which were performed to test the method. In all cases, 100 μl of a sample from the same batch containing the four molecules was hyperpolarized at 1.6 K. Fig. 6.14 shows the ^{1}H DNP build-up, which reaches an apparent polarization $P(^1\mathrm{H}) \approx 50\%$ within a few minutes. However, it should be noted that the polarization is underestimated because of intense RD. The actual value is expected to be of the order of $\approx 70\%$. [121, 68]

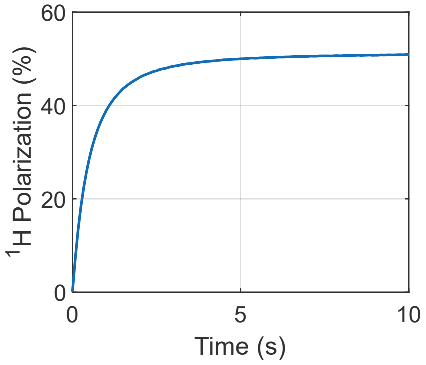

Figure 6.14: ^{1}H DNP build-up at 1.6 K and 7.05 T for 100 μl of 0.4 M ^{13}C-formate, [3-^{13}C]-pyruvate, [2-^{13}C]-pyruvate and [1-^{13}C]-pyruvate in DNP juice doped with 50 mM TEMPOL.

Before performing the dissolution step, the potential weak ^{13}C polarization resulting from direct DNP was wiped out by a train of saturation pulses. This ensured that the observed liquid-state ^{13}C polarization only originated from dynamics in the liquid-state. The dissolution step was performed using the fast dissolution, transfer, and injection system described in Sec. 6.1.1; the hyperpolarized solution was injected into a benchtop spectrometer operating at 1.88 T and the ^{13}C signal was detected using a 5° pulse. The total time between the start of the dissolution and the injection was 1.8 s. In the first two experiments, the solution was directed through the inversion chamber which was placed as close as possible to the output of the polarizer to minimize polarization losses by ^{1}H relaxation. Fig. 6.15 shows the hyperpolarized spectrum acquired for one of these two runs. The signals of ^{13}C-formate and [3-^{13}C]-pyruvate are visible but not that of [2-^{13}C]-pyruvate and [1-^{13}C]-pyruvate.

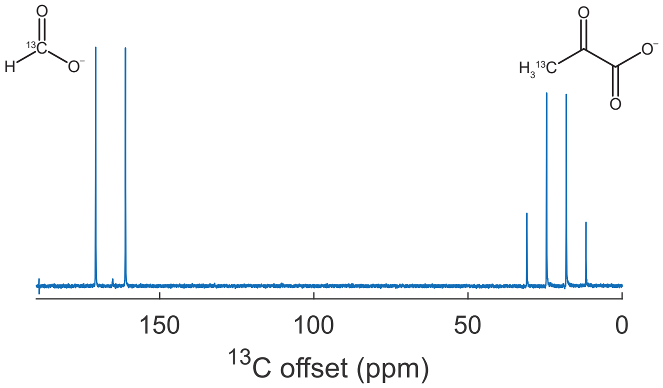

Figure 6.15: Hyperpoalarized ^{13}C signal spectrum detected at 1.88 T using a single 5° pulse obtained after ^{1}H-dDNP experiment by an adiabatic field inversion. The sample initially contained ≈ 0.4 M of ^{13}C-formate, [3-^{13}C]-pyruvate, [2-^{13}C]-pyruvate and [1-^{13}C]-pyruvate but only ^{13}C-formate and [3-^{13}C]-pyruvate are visible on the spectrum.

The next two runs are control experiments. In one of them, the hyperpolarized solution was directed through the inversion chamber but the current in the solenoids was set so that their stray field added up instead of canceling. Therefore, as the solution went through the chamber, the spins experienced a low magnetic field but no actual inversion. In the last experiment, the inversion chamber was bypassed and so the minimum field experienced by the spins was ≈ 4 mT in the guiding solenoid from the polarizer to the liquid-state spectrometer. In this case, the flow path from the dissolution stick to the rapid injection system was slightly shorter, which resulted in a total time between the start of the dissolution and the injection of 1.6 s (compared with 1.8 s for the other experiments). In these two control experiments, the signals of ^{13}C-formate and [3-^{13}C]-pyruvate are visible, albeit with lower intensity than in the experiments with inversion. Again, the signals of [2-^{13}C]-pyruvate and [1-^{13}C]-pyruvate are not visible. The polarization of ^{13}C-formate and [3-^{13}C]-pyruvate was quantified as detailed in Sec. 6.1.2 for the four experiments. The obtained values are presented in Table 6.1.

	Inversion run 1	Inversion run 2	No inversion run 1	No inversion run 2
^{13}C-formate	9.0%	12.3%	1.3%	1.1%
[3-^{13}C]-pyruvate	11.2%	10.4%	3.6%	3.9%
[2-^{13}C]-pyruvate	0	0	0	0
[1-^{13}C]-pyruvate	0	0	0	0

Table 6.1: ^{13}C-polarization of the four molecules in the liquid-state in four experiments. “Inversion run 1” and “Inversion run 2” are two replicates of the same experiment where the solution was pushed through the inversion chamber. “No inversion run 1” is a control experiment where the solution was pushed through the inversion chamber but the polarity of one solenoid coil was inverted so that the spins did not experience a field inversion. “No inversion run 2” is a second control experiment where the inversion chamber was bypassed.

The results summarized in Table 6.1 show that our method is indeed capable of transferring ^{1}H polarization obtained by dDNP to ^{13}C spins. The liquid-state ^{13}C polarization of ^{13}C-formate and [3-^{13}C]-pyruvate compared to that of [2-^{13}C]-pyruvate and [1-^{13}C]-pyruvate follow the prediction of the numerical simulations, i.e., the J-coupling of ^{13}C-formate and [3-^{13}C]-pyruvate is sufficiently strong to enable an efficient transfer with the chosen field inversion profile, while that of [2-^{13}C]-pyruvate and [1-^{13}C]-pyruvate is too weak to allow for any transfer. Considering the starting ^{1}H polarization of ≈ 70% in the solid-state, a perfect transfer should result in ≈ 70% ^{13}C polarization is the liquid-state for ^{13}C-formate and even more for [3-^{13}C]-pyruvate due to the 3:1 ^{1}H:^{13}C ratio. However, this does not take into account the rapid ^{1}H relaxation, in particular paramagnetic ^{1}H relaxation. A dDNP experiment was performed on the same sample without inversion and detecting the ^{1}H polarization in the liquid-state. We found ^{1}H polarization of ≈ 8.2% both for ^{13}C-formate and [3-^{13}C]-pyruvate. Because the ^{1}H→^{13}C transfer occurs earlier in the process than the stage where the ^{1}H polarization can be measured, the polarization of the ^{1}H spins at the moment of the transfer must be $8.2\% < P(^{1}\mathrm{H}) < 70\%$. Therefore, obtaining ^{13}C polarization of $9 - 12\%$ is reasonable. Finally, the ^{13}C polarization obtained in the control experiments can easily be rationalized by nuclear Overhauser effect (NOE) in the liquid-state. It is not surprising that the effect is significant for ^{13}C-formate and [3-^{13}C]-pyruvate and not for [2-^{13}C]-pyruvate and [1-^{13}C]-pyruvate, considering the distance between ^{1}H and ^{13}C spins in these molecules and $1/r^6$ dependence of the NOE rate, where r is the ^{1}H-^{13}C distance.

6.2.4 Strategies for molecules with low J-couplings

We have demonstrated that an adiabatic field inversion is capable of transferring ^{1}H polarization to ^{13}C spins provided they interact through a strong J-coupling. However, such molecules are not of great clinical relevance because they have short relaxation time due to the short intramolecular ^{1}H-^{13}C distance. Being able to apply the method to [2-^{13}C]-pyruvate and even more so to [1-^{13}C]-pyruvate would be of greater interest for clinical applications. In this section, we discuss possible strategies and associated risks to realize the transfer in such molecules.

To make the transfer as fast as possible and hence limit ^{1}H relaxation, we propose to use the strategy introduced by Rodin *et al.* of *constant adiabaticity.* [244] In principle, the field profile which makes the spin system experience an evolution with constant adiabaticity should allow for the shortest transfer time with complete polarization transfer. The adiabaticity parameter between two eigenstates $|i\rangle$ and $|j\rangle$ of the Hamiltonian $\hat{H}$ at time t, with energies ω_i and ω_j, respectively, is defined as

$$\xi_{ij}(t) = \frac{\langle i| \frac{d\hat{H}}{dt} |j\rangle}{(\omega_i - \omega_j)^2}, \tag{6.20}$$

which is summed over all pairs of states as

$$\langle\xi\rangle(t) = \sqrt{\sum_{i,j} \xi^2_{i,j}(t)}, \tag{6.21}$$

to obtain the generalized adiabaticity parameter. [244] The closer is $\langle\xi\rangle(t)$ to 0, the more adiabatic is the transformation. A transformation has constant adiabaticity if $\langle\xi\rangle(t) = \xi_0$ at all time. We aim at finding the field profile from $+B_0$ to $-B_0$ with $\langle\xi\rangle(t) = \xi_0$.

Because the J-Hamiltonian does not depend on time, the time-derivative of the Hamiltonian yields

$$\frac{d\hat{H}}{dt} = \frac{dB_z}{dt}\hat{O}, \tag{6.22}$$

where we defined the operator

$$\hat{O} = \gamma_{\mathrm{I}}\hat{I}_z + \sum_{k=1}^{n} \gamma_{\mathrm{S}}\hat{S}_{kz}. \tag{6.23}$$

Inserting Eq. 6.22 into Eq. 6.21 with $\langle\xi\rangle(t) = \xi_0$, we get

$$\xi_0 = \left|\frac{dB_z}{dt}\right| \sqrt{\sum_{i,j} \frac{\left(\langle i| \hat{O} |j\rangle\right)^2}{(\omega_i - \omega_j)^4}}, \tag{6.24}$$

and so the variation of the magnetic field during a positive time step dt with arbitrary adiabaticity ξ_0 must be

$$|dB_z| = \xi_0 dt \left(\sum_{i,j} \frac{\left(\langle i| \hat{O} |j\rangle\right)^2}{(\omega_i - \omega_j)^4}\right)^{-1/2}. \tag{6.25}$$

We used Eq. 6.25 to compute the constant adiabatic field profile for several spin systems according to the following algorithm: a value B_0 is chosen as the first point of the profile and a value for the product $\xi_0 dt$ is defined. Then, for each point along the profile $B(t)$, the next point is calculated using Eq. 6.25. To do so, the eigenstates $|i\rangle$ and the corresponding eigenfrequencies ω_i are computed by diagonalizing the Hamiltonian $\hat{H}(t)$. Before Eq. 6.25 can be used, some precautions must be taken. Because there exist allowed crossings (e.g., between $|\alpha\alpha\rangle$ and $|\beta\beta\rangle$ in the case of a two spin-system), the fraction in Eq. 6.25 explodes if we compute it around allowed crossings. This issue is solved by restricting the pairs of i and j states for which we compute ξ_{ij} to those with equal total angular momentum $m_F^i = m_F^j$. Indeed, as pointed out by Rodin *et al.*, $\hat{H}_J$ only mixes states with equal total angular momentum. The total angular momentum of the states $|i\rangle$ obtained from the numerical diagonalization of the Hamiltonian is computed as

$$m_F^i = \langle i| \left(\hat{I}_z + \sum_{k=1}^{n} \hat{S}_{kz} \right) |i\rangle \,. \tag{6.26}$$

In practice, due to the limited machine precision, m_F^i and m_F^j are rounded before they are compared. Furthermore, spin systems XA$_n$ with $n > 1$ have degenerate levels which also make the fraction in Eq. 6.25 explode. This is circumvented by computing ξ_{ij} only for states with $\omega_i \neq \omega_j$. In practice, due to the limited machine precision, the non-degeneracy is verified by the condition

$$\left| \frac{\omega_i - \omega_i}{\omega_i + \omega_i} \right| < \delta, \tag{6.27}$$

where δ is a tolerance parameter set to 10^{-2}.

The algorithm is stopped when $B(t) \leq -B_0$. Depending on the chosen value of the product $dt\xi_0$, the field profile may contain too few points to be smooth or too many points to be computed in a reasonable time. In practice, one may run the algorithm with a lower value of $dt\xi_0$ if the curve contains too few points or stop the algorithm and run it again with a larger value of $dt\xi_0$ if it takes too long to complete. The number of points is then changed to a convenient value using a spline interpolation of the points computed by the algorithm.

The constant adiabaticity field profiles were computed for XA$_n$ spin systems with A and X being a ^{13}C spin and ^{1}H spins, respectively, with $J = 200$ Hz and n between 1 and 6. The starting field value was chosen to be $B_0 = 100$ μT and the steps were computed using $\xi_0 dt = 5 \cdot 10^{-7}$ s. Fig. 6.16 shows the simulated profiles as a function of time along the transfer normalized by the transfer time. The curves are arbitrarily normalized to their value at 40 μT. In addition to those of Fig. 6.16, we computed the constant adiabaticity field profiles for values of J of 1, 10, 20, 50, 100, and 200 Hz in the case of XA and XA$_3$ spins systems (not shown). We found that the only effect of the intensity of the J-coupling on the curves was to rescale the y-axis. Therefore, apart from the y-scale, the curves in Fig. 6.16 represent the general form of the constant adiabaticity field profile for XA$_n$ spin systems.

We simulated the ^{1}H and ^{13}C polarizations along the transfer for XA with $J = 195$ Hz (corresponding to ^{13}C-formate) using a constant adiabaticity field profile with $B_0 = +385$ μT discretized into 20'000 points, for an exceedingly long transfer time of 100 ms (see Fig. 6.16A). We also simulated the final polarizations as a function of transfer time for the same spin system and field profile (see Fig. 6.16B). Fig. 6.16A shows that, with a constant adiabaticity filed profile, polarization starts exchanging immediately and changes almost linearly with time. The oscillations on the curves are probably due to some non-zero level of coherence in the initial state. We tried to increase the digitization of the propagation (up to 200'000), lower $\xi_0 dt$ (down to 10^{-10} s), and secularize the initial density matrix (by expressing it in the eigenbasis of $\hat{H}_{tot}(t = 0)$, setting off-diagonal elements to zero and reexpressing the resulting density matrix in the Zeeman basis) but the appearance of the curves did not change. The very steep slope of the field profile near $+B_0$ may make it difficult to satisfy the conditions that the Hamiltonian can be considered time-independent during dt.

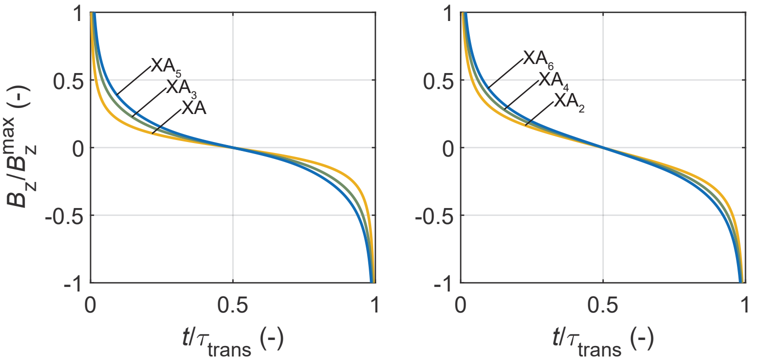

Figure 6.16: Normalized constant adiabaticity field profiles for ^{13}C-^{1}H XA$_n$ spin systems for n between 1 and 6.

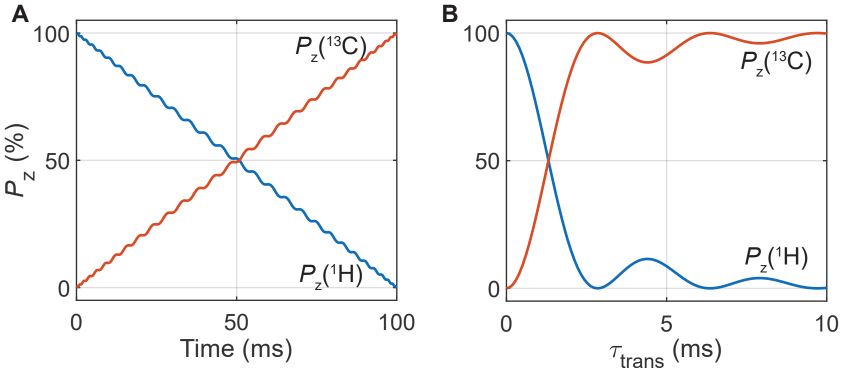

Figure 6.17: **A-B**. ^{1}H and ^{13}C polarizations along time for a transfer time of 100 ms and as a function of the transfer time, respectively, for ^{13}C-formate for a field inversion with constant adiabaticity ($\xi_0 dt = 10^{-10}$ s, $B_0 = +385$ μT with 200'000 propagation steps).

An interesting feature of Fig. 6.16B is that it gives the "most relevant" value of the minimum transfer time for an adiabatic field inversion in a given spin system. Indeed, except with constant adiabaticity field profiles, the transfer time must always be defined with respect to $+B_0$. With the constant adiabaticity, as long as B_0 is defined so that $|\hat{H}_{tot}(t=0)| \gg |\hat{H}_J|$, the curves in Fig. 6.16B are not affected by the choice of B_0 because the field profile goes to infinity on the edges of the curve. Furthermore, because the inverse transfer time is proportional to $1/J$, the results of Fig. 6.16B are also valid for different values of J, provided the x-axis is rescaled.

The field inversion under constant adiabaticity was also simulated for [1-^{13}C]-pyruvate ($J \approx 1.3$ Hz), as a function of time for a transfer time of 2 s and as a function of the transfer time. The results are shown in Fig. 6.18 A and B, respectively. The trajectories of the polarizations as a function of time are more complex than in the XA case. Importantly, Fig. 6.18B shows that the transfer time for an adiabatic field inversion must be on the order of 1-2 s for [1-^{13}C]-pyruvate. This shows an inherent limit for our method: if the transfer time must be on the order of seconds even with constant adiabaticity, it means that it can by no means be short compared to ^{1}H relaxation.

Molecules with low J-couplings pose another difficulty. In all the simulations that we presented

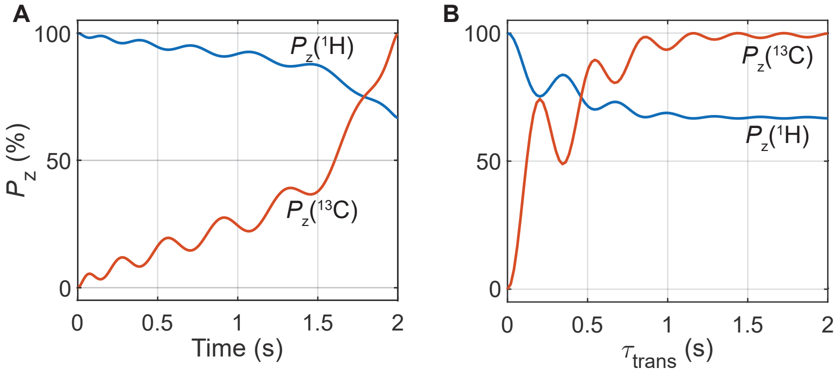

Figure 6.18: **A-B**. ^{1}H and ^{13}C polarizations along time for a transfer time of 2 s and as a function of the transfer time, respectively, for [1-^{13}C]-pyruvate for a field inversion with constant adiabaticity ($\xi_0 dt = 10^{-6}$ s, $B_0 = +4.1\ \mu$T with 20'000 propagation steps).

above, we always assumed that $B_z(t)$ was strictly defined by the coil array. However, even in magnetic shields, some residual fields are to be expected. For example, if in addition to the field along z generated by the coils, the spins experience a constant field orthogonal to the z-axis, this field will act as an extra perturbation (in addition to J). This additional Zeeman perturbation $\hat{H}_Z^{\perp}$ will limit the efficiency of the polarization transfer if it is too strong. In the worst case, if it is larger than J, instead of a field inversion through 0, the spins will experience a field rotation and no polarization transfer can take place. If $B_{\perp}$ is the residual field orthogonal to B_z, the limit in which $\hat{H}_Z^{\perp}$ is weak in front $\hat{H}_J$ made be expressed as

$$|\hat{H}_J| = \zeta|\hat{H}_Z^{\perp}| = \Longleftrightarrow\ B_{\perp} \approx \frac{1}{\zeta}\left|\frac{2\pi J}{\max\{\gamma_S, \gamma_I\}}\right|, \tag{6.28}$$

where we took the highest of the gyromagnetic ratio to yield a conservative criterion. For ^{13}C-formate, this criterion yields $B_{\perp} \approx 460$ nT with $\zeta = 10$, which is easily achieved with well degaussed magnetic shields. For [1-^{13}C]-pyruvate, the criterion yields $B_{\perp} \approx 3$ nT, which can be achieved but is more challenging. In the experiment presented above, the cancellation of external magnetic fields was realized by the use of magnetic shields. To reach the best performance, such shields need to be "degaussed" after being placed at their point of use (i.e., applying an oscillating current of decreasing intensity within 5-10 min [78]). In experiments with signal detection at ZULF, the residual fields can be further decreased by the use of coils (the equivalent of "shimming" in high-field NMR), reaching residual fields typically below 0.1 nT. [247, 78] This is typically done by monitoring the change in Zeeman splittings of the J-lines of a sample like neat ^{13}C-formic acid or ^{13}C-methanol at ultra low-field, using field-cycling; the current in the coils is optimized to suppress the splittings. In addition, the sensitivity vs. frequency response of the magnetometer to a test signal can also be used as its spectral features are indicative of residual fields. [247, 78, 81] Both these procedures require the setup to be equipped with a sensitive magnetometer. Such procedures might be necessary to ensure sufficient field-zeroing for polarization transfer by field inversion in [1-^{13}C]-pyruvate.

These requirements of the ^{1}H→^{13}C polarization transfer by adiabatic field inversion for molecules with weak J-couplings make the use of an in-line field inversion very challenging (by in-line, we mean that the spins experience the field inversion by moving through space). It might turn out to be more feasible to inject the sample into a vessel within the shields and apply the field inversion on the static sample using a pair of Helmholtz coils controlled by an arbitrary waveform generator (AWG) as represented in Fig. 6.19. First, if implementing a constant adiabaticity field profile is possible through space, it is much easier to feed the field profile to an AWG, which will then generate the field profile with high fidelity. Furthermore, the in-line inversion requires the field to be properly zeroed on a much more extended region in space, which would be difficult to realize if magnetometry is to be used for field zeroing.

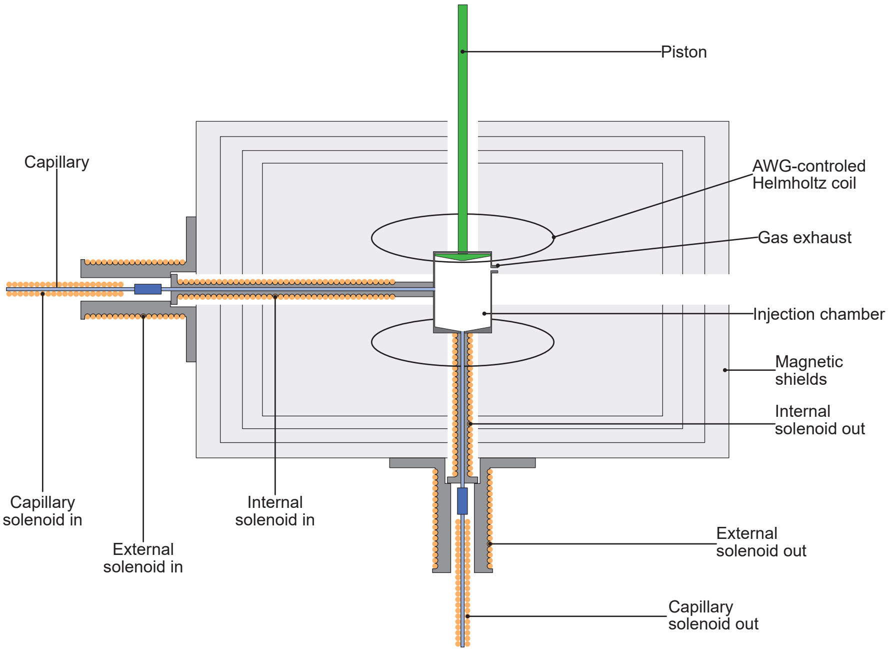

Figure 6.19: Schematic representation of an experimental setup for ^{1}H→^{13}C polarization transfer by adiabatic field inversion on a static sample, where the field profile over time is generated by an AWG controlled-Helmholtz coil.

The strategy of field inversion on a static sample may also be of benefit for clinical applications because the sample needs to be degassed before it can be injected into a patient (in addition to pH and salinity adjustments). The injection chamber represented in Fig. 6.19 may therefore be used for this purpose. Because the field homogeneity and the residual fields are not affected by turbulences and bubbles, the field inversion may be applied as the solution is settling down, without requiring extra delays in the dissolution process.

6.3 dDNP-hyperpolarized ZULF-NMR

In the previous section, ZULF dynamics were used as a means to transfer polarization from ^{1}H to ^{13}C spins but the hyperpolarized liquid-state solutions were detected at high-field. In this final section, we present the results of dDNP-hyperpolarized samples detected at ZULF. This project was realized in collaboration with Dmitry Budker's group from the Helmholtz Institute Mainz (HIM), in particular with Román Picazo-Frutos and with the contribution of James Eills and John Blanchard. Dmitry Budker's team developed the ZULF spectrometer in Mainz and brought it to Lyon in July 2019, where we coupled it to our dDNP polarizer. This collaboration resulted in the publication of Ref. [223].

As pointed out in the introduction of this dissertation (see Sec. 1.2.3), the main limitation of ZULF-NMR is low sensitivity but this can be circumvented by hyperpolarization. In particular, PHIP [88, 248] and spin-exchange optical pumping [249, 250, 251, 252] have been used to hyperpolarize samples for zero- and moderate-field NMR experiments, but PHIP relies on specific chemical reactions with hydrogen gas, and spin-exchange optical pumping is limited to polarizing noble gas atoms. In this context, dDNP could be of benefit, thanks to its wider applicability. The first demonstration of dDNP coupled with ZULF-NMR detection was recently presented, where [1-^{13}C]-pyruvic acid was hyperpolarized and detected with a portable zero-field spectrometer. [91]

In this section, we first present the instrumentation that we developed for combined dDNP-ZULF experiments. We then show hyperpolarized ZULF spectra of two mixtures of small organic molecules, with an order of magnitude improvement in sensitivity compared to reported results. [91] We obtained spin polarization of the order of tens of percent and therefore sensitivity enhancements of 11’000 with respect to a conventional ZULF-NMR experiment with sample prepolarization at 2 T. We evaluate paramagnetic relaxation induced by the DNP polarizing agent as a possible reason for the obtained signal enhancement of 11’000 while up to >50k could be expected theoretically.

6.3.1 Experimental setup and detection at ZULF

The experimental sequence consists of three steps: hyperpolarization by low-temperature DNP with multiple contact-CP, sample dissolution and transfer from the polarizer to the ZULF spectrometer, and liquid-state detection at zero-field. The experimental sequence and setup are summarized in Fig. 6.20. The hyperpolarization step is performed using the gas-driven approach described in Sec 6.1.1 (and not the fast dissolution, transfer, and injection system). As we showed in Sec. 2.3.2, the signal at zero-field is proportional to the difference in polarization between the ^{1}H and ^{13}C spins $P(^{1}\mathrm{H}) - P(^{13}\mathrm{C})$ and so the signal is maximal if the respective polarizations have opposite signs. Therefore, once the polarization plateaued in the solid-state, the μw source was turned off and the ^{13}C polarization was inverted using an adiabatic frequency swept inversion pulse (chirp pulse) of 1 ms duration and 80 kHz bandwidth. At this point, the ^{1}H and ^{13}C spins had positive and negative polarization, respectively, which maximizes the signal at zero-field.

While polarization was building up in the solid-state, 5 ml of D_2O with 30 mM ascorbic acid was loaded into a heating module, pressurized to 6 bar with He gas, and subsequently heated to 180 °C corresponding to a pressure of 9 bar. The dissolution step consisted of a series of programmed events triggered by the operator. The pressurized hot solvent was injected onto the sample and pushed with He gas at 9 bar through a KelF capillary to the ZULF spectrometer. The capillary was inside a solenoid maintaining a field of 4 mT along the transfer (similarly to that of Fig. 6.5), from the polarizer to the magnet used for thermal-prepolarization experiments. The flow of He gas was stopped after a transfer time $t_{trans} = 2$ s.

We used a home-built ZULF spectrometer for signal detection which is a modified version of the setup described in reference [253]. Using a four-layer μ-metal shield (MS-1, Twinleaf LCC) and additional shimming coils, the residual field at the sample location was brought down to sub-nT levels. At the center of the detection region, a 3D-printed holder accommodated a standard NMR tube and a Helmholtz-coil pair along the sensitive axis (z-axis). A solenoid coil is used to guide the sample from the prepolarization magnet to the Helmholtz coils during experiments without hyperpolarization. In the context of hyperpolarized experiments, the output of the dDNP polarizer was connected to the NMR tube inside the ZULF spectrometer *via* the prepolarization magnet and the guiding solenoid.

At the beginning of the dissolution sequence, the ZULF spectrometer received a trigger from the dDNP system, which immediately switched on the guiding solenoid and the Helmholtz-coil pair, both providing a 100 μT field. After the transfer, the hyperpolarized sample reached the NMR tube awaiting in the detection region which had a PEEK assembly containing input and output capillaries for injection and exhaust (see the inset in the black rectangle in Fig. 6.20A).

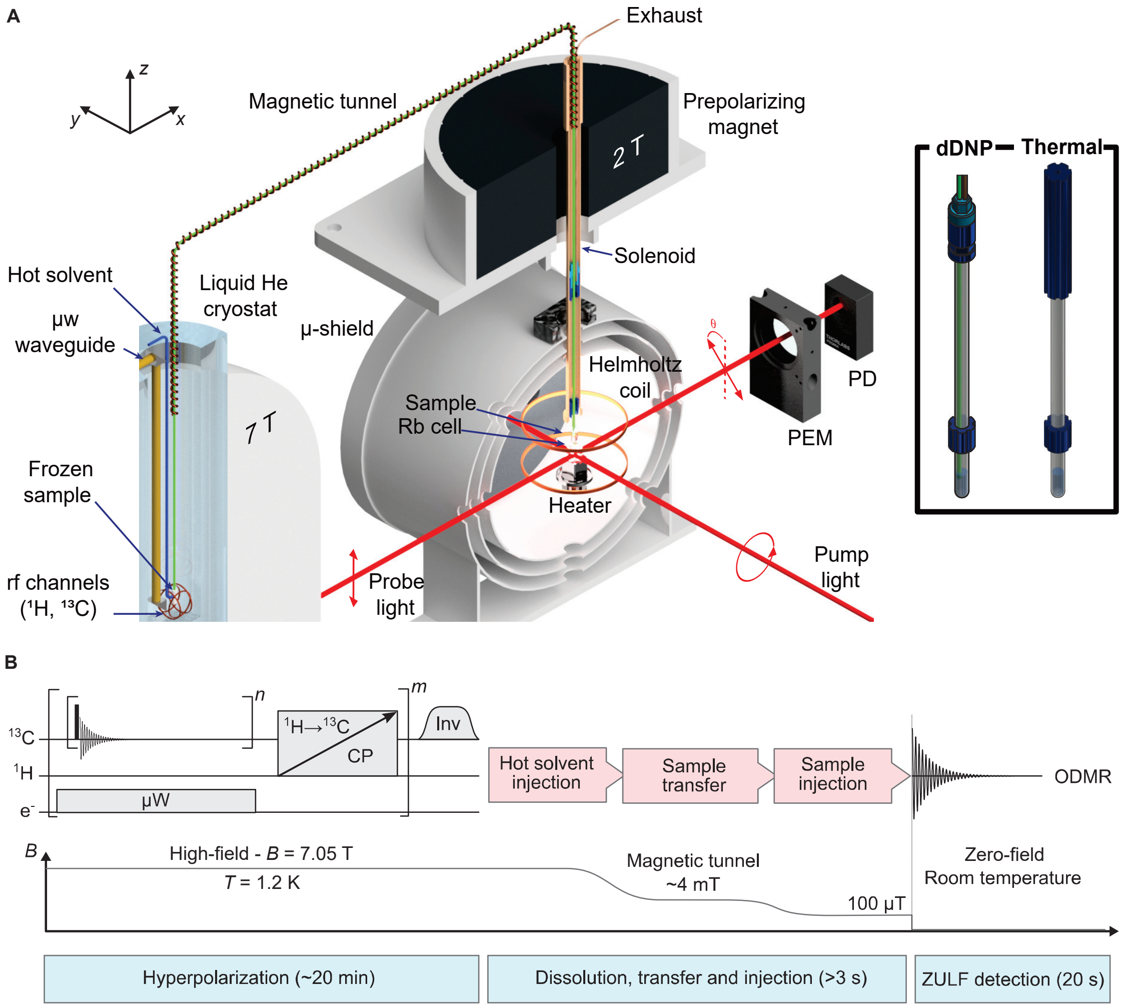

Figure 6.20: A-B Schematic representation of the experimental setup and sequence for dDNP-ZULF experiments, respectively. The inset in Panel A shows the NMR tube in the dDNP injector and that used for pneumatic shuttling in field cycling experiments. Adapted with permission from Ref. [223] (Copyright 2023 American Chemical Society).

4 s after receiving the trigger, the guiding solenoid was switched off. After an additional delay of 100 ms allowing the solenoid field to decay, the Helmholtz coil was switched off within 10 μs, bringing the spins non-adiabatically to zero-field to generate an observable signal (see Sec 2.3.2 for more details). As mentioned above, a flow of He gas pushed the solution from the polarizer during $t_{trans} = 2$ s. The detection was performed 4.1 s after the ZULF spectrometer received the trigger from the dDNP system, meaning that the solution was left at 100 μT during a settling time $t_{settle} = 2.1$ s. This delay allowed the pressure of the He propeller gas to equilibrate with atmospheric pressure for the sample to settle.

Signals at ZULF are usually not detected using inductive methods; this would be highly insensitive due to the low frequencies of coherences at ZULF. The most widespread approach for J-spectroscopy at ZULF is currently to use atomic magnetometers. [254, 77, 80, 81, 78, 253, 80, 79, 93] The ZULF spectrometer developed by our collaborators uses a home-built magnetometer. The main components are two diode lasers (Cateye External Cavity DFB), an Rb vapor cell (with 500 Torr N_2 buffer gas) with outer dimensions of $8 \times 8 \times 10\,\mathrm{mm}^3$ and 1 mm-thickness walls (Twinleaf LCC), a photoelastic modulator (PEM) and a photodiode (PD) detector. The Rb vapor cell is placed below the sample tube and is heated to 180 °C (so that the Rb atoms are in the gas phase). The pump laser produces circularly polarized light along the y-axis tuned to the D1 transition of ^{87}Rb. [255, 254] This laser polarizes the single unpaired electron of ^{87}Rb along the y-axis. The nuclear magnetization of the sample along the z-axis causes the electron spin magnetization of ^{87}Rb to precess in the xy-plane. The probe laser, which produces linearly polarized light along the x-axis, tuned to the D2 transition of ^{87}Rb, is sensitive to rotating magnetization of the electron spins due to Faraday rotation: if the sample produces no magnetic field, the magnetization of the electron is along the y-axis and the angle of the linearly polarized light is not affected as it travels through the vapor cell. When the sample produces a magnetic field along the z-axis, the stronger the magnetic field, the more the angle of the plane of linearly polarized light is tilted.

A simple approach to measuring the angle of the plane of linearly polarized light after traveling through the vapor cell is to use of photobeam splitter and two detectors to measure the relative intensity of the orthogonal components of linearly polarized light. Here, a more sophisticated approach was used where the angle of the plane is modulated at 50 kHz by the PEM before it is detected by the PD and the signal is demodulated using a lock-in amplifier. This method lowers the low-frequency noise. In all experiments, the atomic magnetometer had a sensitivity of 40-80 $\mathrm{fT_{rms}}/\sqrt{\mathrm{Hz}}$ in the frequency range 1-300 Hz (which was characterized by Román Picazo-Frutos). It is worth noting that the PEEK assembly of the sample allows the user to keep the guiding solenoid and prepolarizing magnet used in the thermal experiment, which improves the duty cycle and polarization maintenance, respectively.

6.3.2 Experimental results

Two samples were hyperpolarized by dDNP and detected at ZULF: a sample containing 1.5 M ^{13}C-sodium formate and 1.5 M [2-^{13}C]-sodium acetate and a sample containing 0.76 M [1-^{13}C]-pyruvate, 0.85 M [1-^{13}C]-glycine and 0.80 M ^{13}C-sodium formate (see the chemical structures in Fig. 6.21A). They are referred to as HP1 and HP2, respectively. Both samples contained 50 mM TEMPOL as the polarizing agent and DNP juice as the solvent. They were placed in the sample holder as 10 beads of 10 μL. In addition, 10 beads of 10 μL of 3 M ascorbic acid in D_2O were added to the sample holder. Their purpose is to quench paramagnetic relaxation when they mix with the hyperpolarized solution during dissolution. [237] The ZULF spectra of hyperpolarized samples HP1 and HP2 are shown in Fig. 6.21B-C. A thermal-reference spectrum with prepolarization at 2 T of a sample of 5.2 M ^{13}C-sodium formate in D_2O is shown for comparison in Fig. 6.21D (the signal is the sum of 16 transients and is further magnified by a factor ×4 for better visualization). The noise peaks arising from the power line at 50 Hz and overtones (commonly found in ZULF NMR [253]) and that of the probe-laser noise are marked with hash and asterisks, respectively, in Fig. 6.21D. They are also present (but not marked) in the spectra of Fig. 6.21B-C, albeit at a lower intensity relative to the peaks of interest.

To understand the peaks in the ZULF spectrum it is useful to consider the Pople notation. [256] The molecules of interest can be modeled as an XA_n system, where magnetically equivalent spins A_n are equally coupled to a heteronuclear spin X. The J-coupling interaction causes observable transitions at integer and half-integer multiples of the J-coupling constant. ^{13}C-sodium formate, [1-^{13}C]-glycine, and [2-^{13}C]- acetate correspond to XA, XA_2, and XA_3, spin systems, respectively. These systems have observable transitions at J_{XA}, $3/2 \cdot J_{\mathrm{XA}}$, and $\{J_{\mathrm{XA}};\, 2 \cdot J_{\mathrm{XA}}\}$, respectively [257, 247].

The ZULF spectrum of the hyperpolarized sample HP1 features peaks at $J_{\mathrm{CH}} = 194.7$ Hz for formate and two peaks at $J_{\mathrm{CH}} = 127.3$ Hz and $2 \cdot J_{\mathrm{CH}}$ for acetate (see Fig. 6.21), as expected. In the

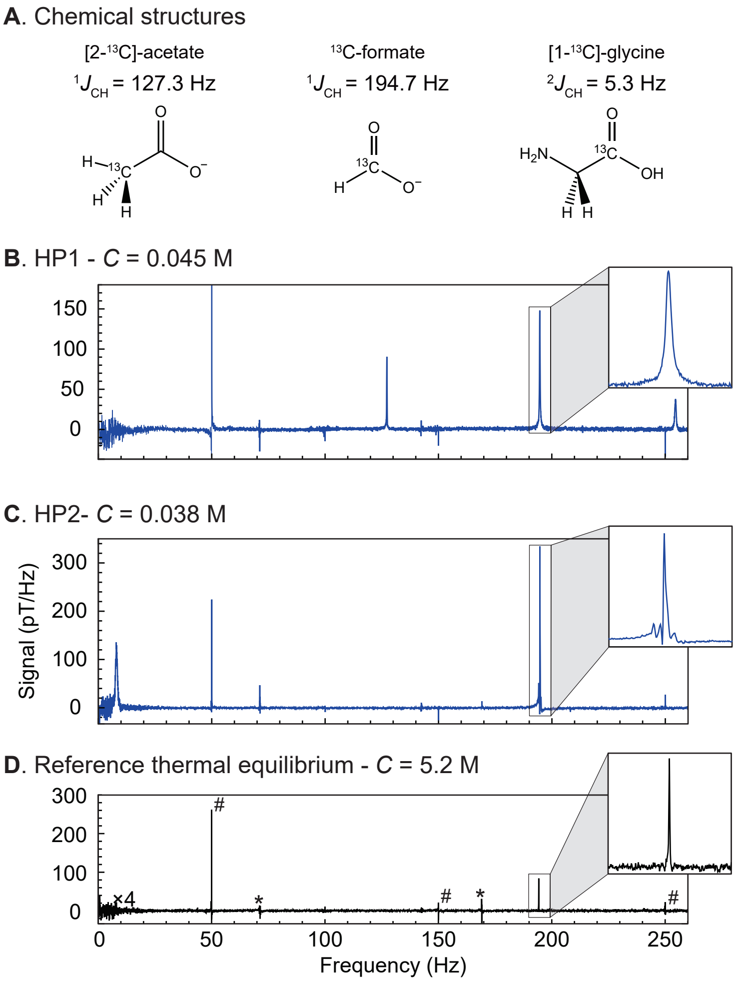

Figure 6.21: **A**. Chemical structures of the molecules whose signals appear in Panel B-C. **B-C**. Hyperpolarized ZULF spectra of sample HP1 and HP2, respectively. The concentration of ^{13}C-formate shown in the title was quantified by ^{1}H-NMR at 1.88 T. **D**. Reference signal of 5.2 M ^{13}C-sodium formate in D_2O with thermal prepolarization at 2 T. The signal is the sum of 16 scans and is magnified by a factor ×4. The hash and asterisk symbols indicate noise peaks arising from the power line at 50 Hz and overtones and that of the probe-laser noise, respectively. The insets in Panel B-D show zooms of the ^{13}C-formate signal. Adapted with permission from Ref. [223] (Copyright 2023 American Chemical Society).

ZULF spectrum of the hyperpolarized sample HP2, peaks can be clearly identified at $J_{\mathrm{CH}} = 194.7$ Hz for ^{13}C-formate and there is one peak at $3/2 \times J_{\mathrm{CH}} = 8.0$ Hz for [1-^{13}C]-glycine (see Fig. 6.21C). The peak of [1-^{13}C]-glycine is significantly broader than the other peaks. It is well known that quadrupolar relaxation [258, 259] is significant in spin systems where nuclei with spins $> 1/2$ are involved. The broadening is possibly due to quadrupole relaxation caused by the spin-1 ^{14}N nucleus. Surprisingly, the expected signals of [1-^{13}C]-pyruvate at $J_{\mathrm{CH}} = 1.3$ Hz and $2 \times J_{\mathrm{CH}} = 2.6$ Hz are not visible in the spectrum.

The formate peak of Fig. 6.21C has SNR > 500, over an order of magnitude higher as compared with previously published work. [91]. Yet, as we shall see, the signal enhancement is lower than what it could be considering the performance of our dDNP apparatus. We define the signal enhancement as the ratio between the signal integral of the hyperpolarized experiment and that of thermal reference with prepolarization at 2 T S_{DNP} and S_{Th}, respectively,

$$\epsilon = \frac{S_{DNP}}{S_{Th}}, \tag{6.29}$$

where it is assumed that the signals are recorded on the same sample (normalized by the number of scans). Because the thermal reference signal is recorded on a more concentrated sample, the enhancement ϵ is obtained by compensating for the concentration ratio between the two samples

$$\epsilon = \tilde{\epsilon}\frac{C_{Th}}{C_{DNP}}, \tag{6.30}$$

where $\tilde{\epsilon}$ is the signal enhancement obtained by comparing the signal integrals of the hyperpolarized sample with that of the highly concentrated sample prepolarized at 2 T. Compared to prepolarization at 2 T, the ^{13}C-formate signal enhancement translates into a spin polarization enhancement of $\epsilon = 5000$. Indeed, the peak shows a signal enhancement $\tilde{\epsilon} = 44$ with a concentration of formate in the dissolved sample of HP1 determined to be 45 mM by high-field NMR, while the reference sample was at a higher concentration of 5.2 M. As for sample HP2, the ^{13}C-formate concentration in the dissolved sample was determined to be 38 mM. Compared to prepolarization at 2 T, the sodium formate peak shows a spin-polarization enhancement of ε =11'000 (concentration ratio of 137 and signal enhancement of $\tilde{\varepsilon} = 83$).

As we showed in Sec. 2.3.2, the signal at zero-field is proportional to the polarization difference between the ^{1}H and ^{13}C spins. Therefore, the expected enhancement is

$$\epsilon = \frac{P_{DNP}(^1\mathrm{H}) - P_{DNP}(^{13}\mathrm{C})}{P_{Th}(^1\mathrm{H}) - P_{Th}(^{13}\mathrm{C})}, \tag{6.31}$$

where $P_{DNP}(^1\mathrm{H})$, $P_{DNP}(^{13}\mathrm{C})$, $P_{Th}(^1\mathrm{H})$ and $P_{Th}(^{13}\mathrm{C})$ are the ^{1}H and ^{13}C polarizations in the hyperpolarization experiment and those of the thermal-reference experiment, respectively. To estimate the ^{1}H and ^{13}C polarizations of the analyte that could be expected from our dDNP experiments, we performed a similar dDNP experiment on [1-^{13}C]-acetate but injected into our benchtop spectrometer at 1.88 T. We found ^{1}H and ^{13}C polarizations of 6% and 20%, respectively (see Fig. 6.22A). In ZULF experiments, these polarization levels would translate into an enhancement of $\varepsilon = 51'000$ with respect to prepolarization at 2 T according to Eq. 6.31 (provided the ^{13}C spins are efficiently inverted prior to dissolution to yield $P(^{13}\mathrm{C}) = -20\%$). However, our best-performing experiment yielded an enhancement of $\varepsilon = 11'000$, less than a quarter of the expected 51'000.

Fig. 6.22B shows the signal enhancement of dDNP-ZULF experiments with respect to prepolarization at 2 T, calculated with Eq. 6.31. The result of our best-performing experiment is represented by the white bar. As both ^{1}H and ^{13}C polarization contribute to the enhancement, the value of $\varepsilon = 11'000$ cannot be represented as a point on the plane but rather as a linear combination of ^{1}H and ^{13}C polarization. For example, if the ^{1}H polarization was $P(^1\mathrm{H}) = 0\%$, the ^{13}C polarization of the 11'000-enhanced signal would be $P(^{13}\mathrm{C}) = -6.7\%$. Since we performed these experiments, we have improved our dDNP setup (see Sec. 6.1.4) and we obtained ^{1}H and ^{13}C polarizations up to 30% and 50%, respectively. If such polarizations were obtained at zero-field, they would translate into a signal enhancement of 156'000, which is represented as our "long-term goal" in Fig. 6.22B.

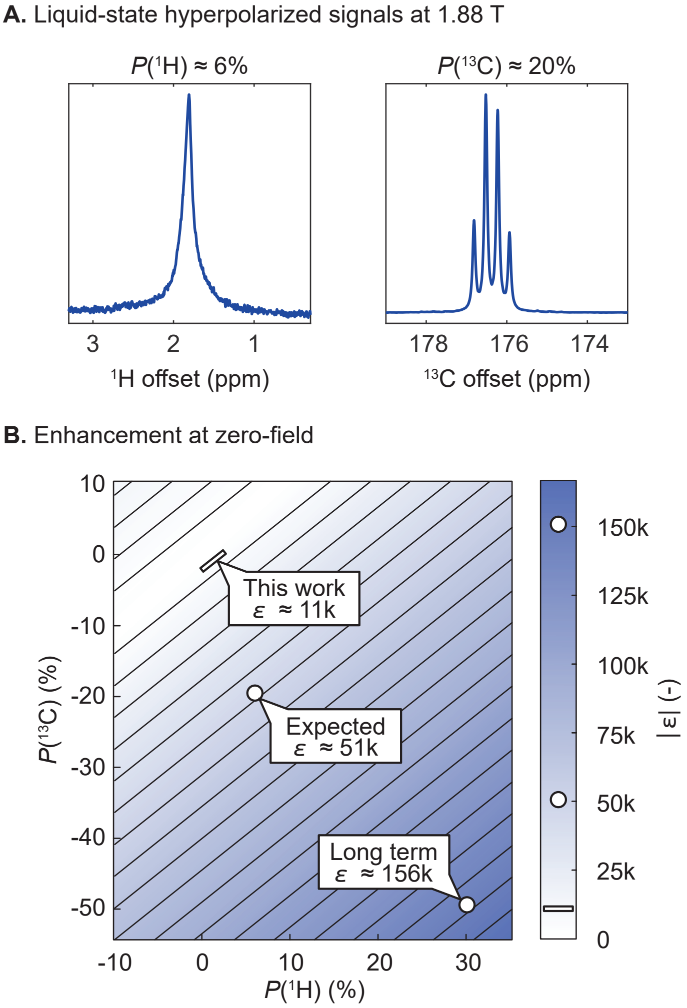

Figure 6.22: **A**. Typical results of dDNP experiments where a hyperpolarized sample of [1-^{13}C]-sodium acetate is detected at 1.88 T for both ^{1}H and ^{13}C channels. **B**. Map of the dDNP-ZULF enhancement with respect to thermal polarization at 2 T as a function of the ^{1}H and ^{13}C polarizations calculated using Eq. 6.31. Adapted with permission from Ref. [223] (Copyright 2023 American Chemical Society).

6.3.3 Paramagnetic relaxation

In an attempt to understand why we obtained such weak signal enhancements compared to expectations, our collaborators at HIM performed relaxation measurements on 5.2 M ^{13}C-sodium formate as a function of TEMPOL concentration between 0 and 7 mM in D_2O at 100 μT i.e., at low-field, and at zero-field, using thermal prepolarization of the sample at 2 T. Assuming that paramagnetic relaxation rates are linear with the concentration C of TEMPOL, measured rates $1/T_k$ can be expressed as

$$\frac{1}{T_k} = a_k C + b_k, \tag{6.32}$$

where a_k and b_k are the relaxivity of TEMPOL in $\mathrm{s}^{-1}\mathrm{mM}^{-1}$ and the sum of all relaxation rates which are assumed to be independent of TEMPOL concentration, respectively. Under this assumption, they found that the relaxivity at 100 μT of TEMPOL on ^{13}C-formate was $a_{LF} = 0.27(3)$ $\mathrm{s}^{-1}\mathrm{mM}^{-1}$. At zero-field, they found a relaxivity of $a_{ZF} = 0.19(4)$ $\mathrm{s}^{-1}\mathrm{mM}^{-1}$. The lineshape of the signal at zero-field was also studied as a function of C. The broadening of the signal by the presence of TEMPOL was found to be ≈ 100 mHz.mM^{-1}. These results are in agreement with recently reported data by Bodenstedt *et al.* [87]

The dissolution step of our dDNP experiments currently dilutes the sample by a factor of 30, bringing the TEMPOL concentration down to $1-2$ mM. The concentration is further reduced by the presence of sodium ascorbate in the beads placed in the DNP sample holder and in the dissolution solvent, which acts as a scavenger for TEMPOL radicals. [237] However, the reaction between ascorbate and TEMPOL is not instantaneous. Due to the complex temperature and concentration dynamics of the dissolution step, it is not possible to know the concentration of TEMPOL precisely at the moment of injection. Considering that the TEMPOL concentration after injection is at most on the order of 1 mM, the relaxation data show that the broadening due to paramagnetic relaxation is expected to be within a few hundreds of mHz, acceptable for our hyperpolarized experiment. The spectra of hyperpolarized samples in Fig.6.21B-C have linewidths of approximately ≈ 200 mHz: was this due only to TEMPOL, it would mean that $1-2$ mM of radical was present at the sample at the moment of detection, consistent with expectations based on our relaxation data. This broadening does not decrease the SNR sufficiently to prevent us from observing hyperpolarized peaks but leads to a non-negligible signal loss during the settling time $t_{settle} = 2.1$ s. The remaining signal after 2.1 s at 100 μT for a TEMPOL concentration of 2 mM should be $\exp\left(-(a_{LF}C + b_{LF})t_{settle}\right) \approx 0.3$ of the initial value (assuming that TEMPOL has not significantly been quenched by ascorbic acid at this point). Paramagnetic relaxation during the transfer and settling of the solution could therefore explain why the recorded enhancement is lower than expected. This shows that increasing the speed of the transfer, shortening settling time, and suppressing paramagnetic relaxation is of paramount importance to improving the sensitivity of dDNP-ZULF experiments.

Future efforts should focus on reducing polarization losses during the transfer and the settling of the solution to reach polarization enhancements of or $> 150'000$ (see Fig. 6.22). First, using the system for fast dissolution, transfer, and injection that we have recently introduced, [222] dDNP-ZULF experiments could be performed without any settling time. The only necessary delay following injection would be for the discharge of the guiding solenoid (≈ 0.1 instead of 2.1 s). In this case, the polarization losses after injection would only be of a few percents (the remaining polarization would be $\exp\left(-(a_{LF}C + b_{LF})t_{settle}\right) \approx 0.97$). It is worth noting that, contrary to detection at high-field, the resolution of ZULF-NMR is insensitive to microbubbles or turbulences caused by the dDNP process and so there is no necessity to let the solution settle down as long as it remains in the sensitive volume (i.e., the bottom of the tube).

Second, using polarization matrices such as HYPSOs [54] or HYPOPs [57], high DNP performance could be reached while the polarizing agent could be filtered out during the dissolution process leaving the solution free from paramagnetic relaxation. This would enable the detection of dDNP hyperpolarized solutions at ZULF with optimal linewidths, down to typically 50 mHz, and would increase the sensitivity by another factor ≈ 4.

6.4 Perspectives

We have presented hardware for fast dissolution, transfer, and injection experiments, where the total time for the sequence takes less than 2 s and enables injecting of a controlled volume, with ^{13}C linewidth 2 s after injection below 1 Hz. We showed how to control the magnetic field along the transfer to mitigate polarization losses and obtained ^{13}C polarizations up to $\approx 50\%$.

Fast dissolution with a controlled injected volume will be useful for applications of dDNP to spectroscopy. For now, dDNP is mainly used for nuclear spins with long T_1 such as ^{13}C spins in small molecules. A fast transfer is advantageous because it offers the possibility to study rapidly relaxing nuclear spins like ^{1}H spins or spins in larger molecules. In addition, the controlled injected volume is crucial for metabolomic reaction monitoring or drug screening applications.

Until recently, dDNP was mainly performed using non-shielded magnets (both for hyperpolarization in the solid-state and for detection in the liquid-state). With the development of dDNP in shielded magnets and the increasing use of benchtop spectrometers for the detection of hyperpolarized solutions, situations, where the hyperpolarized solution has to travel through regions where the stray field of the magnets is negligible, should become more and more frequent. Therefore, polarization losses by relaxation at low-field and by zero-field crossings should become more and more common. The strategies we have presented using arrays of permanent magnets and low-power solenoids will help minimize such losses with reasonably simple hardware.

We used this hardware for a proof-of-principle experiment where we polarized ^{1}H spins in small molecules by dDNP and transferred the polarization to ^{13}C spins using an *in line adiabatic magnetic field inversion.* This method makes use of spin dynamics at ZULF to perform a $^{1}\text{H} \rightarrow ^{13}\text{C}$ polarization transfer *via* the ^{1}H-^{13}C J-coupling. We obtained experimental ^{13}C polarizations of $9-12\%$ in the liquid-state for molecules with strong J-couplings. We then proposed strategies to reach higher polarizations and to extend the method to molecules with weaker J-couplings, which are of higher relevance for applications to *in vivo* imaging.

If the method can be successfully adapted to molecules with lower J-coupling, in particular to [1-^{13}C]-pyruvate, it could be used to increase the throughput of dDNP experiments in laboratories which usually use trityl radicals to polarize ^{13}C spins directly.

We finally presented experiments where a sample is hyperpolarized by dDNP and detected in the liquid-state at zero-field. An example of such experiment was already reported by Barskiy *et al.* using direct ^{13}C DNP from trityl radicals. [91] Here, we used ^{1}H DNP with $^{1}\text{H} \rightarrow ^{13}\text{C}$ multiple contact CP to polarize both ^{1}H and ^{13}C spins, which both contribute to the signal at zero-field. We obtained signal enhancement up to 11'000 with respect to standard prepolarization in a 2 T permanent magnet (the common ZULF equivalent of high-field NMR without hyperpolarization), while 51'000 could be expected from the ^{1}H and ^{13}C polarization levels. We rationalized this discrepancy by paramagnetic relaxation during the stabilization delay between injection and detection.

These experiments of ZULF detection of dDNP hyperpolarized molecules were not performed using our fast dissolution, transfer, and injection system. The signal enhancement would be much higher with the faster and better-controlled transfer that our hardware now permits. In addition, the method could be greatly improved by the use of polarizing materials like HYPSO or HYPOP, [260, 54, 57] which can be filtered out after dissolution. With a stronger signal enhancement and longer relaxation times due to the absence of paramagnetic relaxation, signals at ZULF could be observed over a longer time window.

A promising application of ZULF-NMR is the monitoring of catalytic chemical reactions in conditions that are relevant to the industry. Burueva et al. [86] have already shown an example where ZULF-NMR was combined with PHIP hyperpolarization in order to monitor a chemical reaction with high-resolution within a metal container and in presence of a heterogeneous catalyst. However, because this approach relies on PHIP hyperpolarization, it is limited to reactions where hydrogen gas is used as a reagent. Due to its low chemical specificity, dDNP-ZULF-NMR could be used for the monitoring of a wider range of chemical reactions. ZULF is a regime where chemical reactions may be monitored with high resolution for both homogeneous and heterogeneous catalysts, due to the insensitivity of ZULF to inhomogeneities induced by the magnetic susceptibility of the sample [261, 85]. The high sensitivity and chemical versatility offered by dDNP-ZULF-NMR may enable the study of the catalytic hydrogenation of unsaturated compounds or oligomerization and polymerization processes by high-resolution NMR. [262]

Conclusion

This work has explored spin dynamics at various stages of the dDNP process and in dDNP experiments coupled with ZULF methods in the liquid-state.

PANI polymers were proposed as a new polarizing substrate for DNP. Here, modest ^{1}H polarizations under DNP at 1.2 K of $\approx 3\%$ were obtained. However, the interest of these polymers is that electron spins can be polarized near unity at room temperature by flowing an electric current through chiral PANI polymers. This proof-of-principle of DNP in PANI opens the perspective of performing DNP from hyperpolarized electrons, which would not rely on liquid helium and high magnetic fields. This approach is similar to that of ^{13}C hyperpolarization using color centers in diamonds but with the advantage of relying on ^{1}H hyperpolarization. ^{1}H polarization could therefore spontaneously spin diffuse out from the polarizing material to a host solution and be transferred to ^{13}C spin by CP.

The understanding and the modeling of DNP dynamics require the knowledge of EPR parameters but common dDNP polarizers are not equipped with EPR detection capabilities. The ^{1}H relaxation rate in the rotating frame $R_{1\rho}$ can be used as an indirect probe to measure EPR properties. Here, we introduced the use of the ^{13}C spin-spin relaxation rate R_2^* as an alternative probe, which is free of possible biases due to spin diffusion during measurement. Indirect measurements of equilibrium electron polarizations under DNP, electron spin-lattice relaxation time constants, equilibration time constants of the electron polarization upon switching on μw irradiation, and a rudimentary EPR spectrum were presented.

The HypRes experiment was proposed as a method to study nuclear polarization transfers in the vicinity of the unpaired electron spin of a polarizing agent, i.e., near or through the spin diffusion barrier. While studying such transfers is usually only done in theory, the HypRes method enables monitoring these transfers in real-time. The applicability of the method was demonstrated for ^{1}H and ^{13}C DNP in dDNP conditions and for ^{1}H DNP under MAS at 100 K.

Our results showed that in all studied cases, polarization was able to escape from nuclear spins near the electron to those in the bulk faster than the bulk spin relaxation. It was also shown that ^{1}H spins as close as 3 Å from an electron spin could exchange polarization with bulk spins on a faster time scale than their spin-lattice relaxation, which means that the spin diffusion barrier must be $\leq$ 3 Å. Finally, it was shown experimentally and in theory that the level of electron polarization is a crucial parameter for nuclear spin diffusion in the vicinity of the electron; at high electron polarization, spin diffusion is quenched while, once the electron polarization is lowered by μw irradiation, spin diffusion becomes significant (on the time scale of a typical ^{1}H DNP build-up, i.e., $10 - 20$ min).

HypRes is a versatile method amenable to a variety of situations and can be used as a tool to understand nuclear spin dynamics in the vicinity of the electron spin. Such understanding could then be used for the rational design of new sample formulations or spin clusters with optimal DNP performance.

A new method was proposed for ^{1}H→^{13}C polarization transfers in the liquid-state between J-coupled ^{1}H-^{13}C ensembles by adiabatic magnetic field inversion. ^{1}H spins are hyperpolarized by dDNP and transferred to a liquid-state spectrometer. During the transfer, the solution travels through an inversion chamber, a device creating an in-line well-controlled magnetic field inversion. Numerical simulations of the polarization transfers were used to optimize the magnetic field inversion profile. Starting from a ^{1}H polarization above 50% in the solid-state, ^{13}C polarization of $9-12\%$ were obtained in the liquid-state after transfer, for molecules with large J-couplings.

The low final ^{13}C polarizations in the liquid-state are probably due to rapid ^{1}H relaxation between the dissolution and the polarization transfer. Envisioned solutions to mitigate ^{1}H relaxation before the polarization transfer and adapt the method to molecules with small J-couplings were described. If these two objectives were reached, the method could be used to prepare ^{13}C hyperpolarized metabolites with weak J-couplings like [1-^{13}C]-pyruvate. Since it relies on ^{1}H DNP, the method would be faster than the more commonly used direct ^{13}C hyperpolarization with narrow line-radicals ($10-20$ min compared with $1-2$ hours). Furthermore, this method relies on relatively simple and cheap hardware.

Finally, experiments, where dDNP was coupled with signal detection at zero-field by optical magnetometry, were presented. Both ^{1}H and ^{13}C spins were hyperpolarized at the same time by ^{1}H DNP and multiple contact CP. Signal enhancements up to 11'000 with respect to standard prepolarization at 2 T were obtained, while 51'000 was expected based on liquid-state polarizations determined using high-field NMR in the same conditions. Strategies to mitigate paramagnetic relaxation and improve the performance of the method were discussed.

A promising application of the combination of dDNP with ZULF-NMR detection is the monitoring of catalytic reactions in porous media within metal containers with high-resolution. Such reactions are relevant for the industry but are challenging to study with high-field NMR, which suffers from signal broadening due to the heterogeneity of porous media and signal quenching by the skin effect in metals. ZULF is the regime of choice for NMR in these media.

Bibliography

[1] P. Wikus, W. Frantz, R. Kümmerle, and P. Vonlanthen, “Commercial gigahertz-class nmr magnets,” *Superconductor Science and Technology*, vol. 35, 3 2022.

[2] K. Xue, R. Sarkar, D. Lalli, B. Koch, G. Pintacuda, Z. Tosner, and B. Reif, “Impact of magnetic field strength on resolution and sensitivity of proton resonances in biological solids,” *Journal of Physical Chemistry C*, vol. 124, pp. 22 631–22 637, 10 2020.

[3] A. Abragam and M. Goldman, “Principles of dynamic nuclear polarisation,” *Reports on Progress in Physics*, vol. 41, no. 3, p. 395, 1978.

[4] D. Hoult, “The nmr receiver: a description and analysis of design,” *Progress in Nuclear Magnetic Resonance Spectroscopy*, vol. 12, no. 1, pp. 41–77, 1978.

[5] D. I. Hoult and B. Bhakar, “Nmr signal reception: Virtual photons and coherent spontaneous emission,” vol. 9, pp. 277–297, 1997.

[6] F. Schick, “Whole-body mri at high field: Technical limits and clinical potential,” *European Radiology*, vol. 15, pp. 946–959, 5 2005.

[7] A. W. Overhauser, “Polarization of nuclei in metals,” *Physical Review*, vol. 92, no. 2, p. 411, 1953.

[8] T. R. Carver and C. P. Slichter, “Polarization of nuclear spins in metals,” *Physical Review*, vol. 92, no. 1, p. 212, 1953.

[9] M. Abraham, M. McCausland, and F. Robinson, “Dynamic nuclear polarization,” *Physical Review Letters*, vol. 2, no. 11, p. 449, 1959.

[10] C. F. Hwang, B. A. Hasher, D. A. Hill, and F. Markley, “The use of chemically doped polystyrene as a polarized proton target material,” *Nuclear Instruments and Methods*, vol. 51, no. 2, pp. 254–256, 1967.

[11] K. Kundu, F. Mentink-Vigier, A. Feintuch, and S. Vega, “Dnp mechanisms,” *Handbook of High Field Dynamic Nuclear Polarization*, p. 15, 2019.

[12] C. Jeffries, “Dynamic orientation of nuclei by forbidden transitions in paramagnetic resonance,” *Physical Review*, vol. 117, no. 4, p. 1056, 1960.

[13] T. Schmugge and C. Jeffries, “High dynamic polarization of protons,” *Physical Review*, vol. 138, no. 6A, p. A1785, 1965.

[14] C. F. Hwang and D. A. Hill, “Phenomenological model for the new effect in dynamic polarization,” *Physical Review Letters*, vol. 19, no. 18, p. 1011, 1967.

[15] M. Goldman, *Spin temperature and nuclear magnetic resonance in solids.* Clarendon Press, 1970.

[16] K. Scheffler, "Dynamic proton polarization in ammonia," *Nuclear Instruments and Methods*, vol. 82, pp. 205–207, 1970.

[17] W. Meyer, "Ammonia as a polarized solid target material - a review," vol. 526, 6 2004, pp. 12–21.

[18] R. A. Wind, F. Anthonio, M. Duijvestijn, J. Smidt, J. Trommel, and G. De Vette, "Experimental setup for enhanced 13c nmr spectroscopy in solids using dynamic nuclear polarization," *Journal of Magnetic Resonance (1969)*, vol. 52, no. 3, pp. 424–434, 1983.

[19] L. R. Becerra, G. J. Gerfen, R. J. Temkin, D. J. Singel, and R. G. Griffin, "Dynamic nuclear polarization with a cyclotron resonance maser at 5 t," *Physical Review Letters*, vol. 71, no. 21, p. 3561, 1993.

[20] L. R. Becerra, G. J. Gerfen, B. F. Bellew, J. A. Bryant, D. A. Hall, S. J. Inati, R. T. Weber, S. Un, T. F. Prisner, A. E. Mcdermott *et al.*, "A spectrometer for dynamic nuclear polarization and electron paramagnetic resonance at high frequencies," *Journal of Magnetic Resonance, Series A*, vol. 117, no. 1, pp. 28–40, 1995.

[21] D. A. Hall, D. C. Maus, G. J. Gerfen, S. J. Inati, L. R. Becerra, F. W. Dahlquist, and R. G. Griffin, "Polarization-enhanced nmr spectroscopy of biomolecules in frozen solution," *Science*, vol. 276, no. 5314, pp. 930–932, 1997.

[22] A. G. Rankin, J. Trébosc, F. Pourpoint, J.-P. Amoureux, and O. Lafon, "Recent developments in mas dnp-nmr of materials," *Solid State Nuclear Magnetic Resonance*, vol. 101, pp. 116–143, 2019.

[23] K. H. Hausser and D. Stehlik, *Dynamic nuclear polarization in liquids.* Elsevier, 1968, vol. 3.

[24] J. van Bentum, B. van Meerten, M. Sharma, and A. Kentgens, "Perspectives on dnp-enhanced nmr spectroscopy in solutions," *Journal of Magnetic Resonance*, vol. 264, pp. 59–67, 2016.

[25] J. H. Ardenkjær-Larsen, B. Fridlund, A. Gram, G. Hansson, L. Hansson, M. H. Lerche, R. Servin, M. Thaning, and K. Golman, "Increase in signal-to-noise ratio of¿ 10,000 times in liquid-state nmr," *Proceedings of the National Academy of Sciences*, vol. 100, no. 18, pp. 10 158–10 163, 2003.

[26] K. Golman, R. in 't Zandt, and M. Thaning, "Real-time metabolic imaging," *Proceedings of the National Academy of Sciences*, vol. 103, no. 30, pp. 11 270–11 275, 2006.

[27]

[28] S. J. Nelson, J. Kurhanewicz, D. B. Vigneron, P. E. Larson, A. L. Harzstark, M. Ferrone, M. Van Criekinge, J. W. Chang, R. Bok, I. Park *et al.*, "Metabolic imaging of patients with prostate cancer using hyperpolarized [1-13c] pyruvate," *Science translational medicine*, vol. 5, no. 198, pp. 198ra108–198ra108, 2013.

[29] H. Min, G. Sekar, and C. Hilty, "Polarization transfer from ligands hyperpolarized by dissolution dynamic nuclear polarization for screening in drug discovery," *ChemMedChem*, vol. 10, no. 9, pp. 1559–1563, 2015.

[30] Y. Kim and C. Hilty, “Affinity screening using competitive binding with fluorine-19 hyperpolarized ligands,” *Angewandte Chemie International Edition*, vol. 54, no. 16, pp. 4941–4944, 2015.

[31] Q. Chappuis, J. Milani, B. Vuichoud, A. Bornet, A. D. Gossert, G. Bodenhausen, and S. Jannin, “Hyperpolarized water to study protein–ligand interactions,” *The journal of physical chemistry letters*, vol. 6, no. 9, pp. 1674–1678, 2015.

[32] R. Buratto, A. Bornet, J. Milani, D. Mammoli, B. Vuichoud, N. Salvi, M. Singh, A. Laguerre, S. Passemard, S. Gerber-Lemaire *et al.*, “Drug screening boosted by hyperpolarized long-lived states in nmr,” *ChemMedChem*, vol. 9, no. 11, pp. 2509–2515, 2014.

[33] A. Bornet, M. Maucourt, C. Deborde, D. Jacob, J. Milani, B. Vuichoud, X. Ji, J.-N. Dumez, A. Moing, G. Bodenhausen *et al.*, “Highly repeatable dissolution dynamic nuclear polarization for heteronuclear nmr metabolomics,” *Analytical chemistry*, vol. 88, no. 12, pp. 6179–6183, 2016.

[34] A. Dey, B. Charrier, E. Martineau, C. Deborde, E. Gandriau, A. Moing, D. Jacob, D. Eshchenko, M. Schnell, R. Melzi *et al.*, “Hyperpolarized nmr metabolomics at natural 13c abundance,” *Analytical chemistry*, vol. 92, no. 22, pp. 14 867–14 871, 2020.

[35] T. Harris, O. Szekely, and L. Frydman, “On the potential of hyperpolarized water in biomolecular nmr studies,” *The Journal of Physical Chemistry B*, vol. 118, no. 12, pp. 3281–3290, 2014.

[36] C. Hilty, D. Kurzbach, and L. Frydman, “Hyperpolarized water as universal sensitivity booster in biomolecular nmr,” *Nature Protocols*, pp. 1–37, 2022.

[37] D. Kurzbach, E. Canet, A. G. Flamm, A. Jhajharia, E. M. Weber, R. Konrat, and G. Bodenhausen, “Investigation of intrinsically disordered proteins through exchange with hyperpolarized water,” *Angewandte Chemie International Edition*, vol. 56, no. 1, pp. 389–392, 2017.

[38] A. Bornet, X. Ji, D. Mammoli, B. Vuichoud, J. Milani, G. Bodenhausen, and S. Jannin, “Long-lived states of magnetically equivalent spins populated by dissolution-dnp and revealed by enzymatic reactions,” *Chemistry–A European Journal*, vol. 20, no. 51, pp. 17 113–17 118, 2014.

[39] G. Zhang, F. Schilling, S. J. Glaser, and C. Hilty, “Reaction monitoring using hyperpolarized nmr with scaling of heteronuclear couplings by optimal tracking,” *Journal of Magnetic Resonance*, vol. 272, pp. 123–128, 2016.

[40] G. Zhang and C. Hilty, “Applications of dissolution dynamic nuclear polarization in chemistry and biochemistry,” *Magnetic Resonance in Chemistry*, vol. 56, no. 7, pp. 566–582, 2018.

[41] S. Jannin, J.-N. Dumez, P. Giraudeau, and D. Kurzbach, “Application and methodology of dissolution dynamic nuclear polarization in physical, chemical and biological contexts,” *Journal of Magnetic Resonance*, vol. 305, pp. 41–50, 2019.

[42] S. Jannin, A. Bornet, R. Melzi, and G. Bodenhausen, “High field dynamic nuclear polarization at 6.7 t: Carbon-13 polarization above 70% within 20 min,” *Chemical Physics Letters*, vol. 549, pp. 99–102, 2012.

[43] F. Jähnig, G. Kwiatkowski, A. Däpp, A. Hunkeler, B. H. Meier, S. Kozerke, and M. Ernst, “Dissolution dnp using trityl radicals at 7 t field,” *Physical Chemistry Chemical Physics*, vol. 19, no. 29, pp. 19 196–19 204, 2017.

[44] M. Baudin, B. Vuichoud, A. Bornet, G. Bodenhausen, and S. Jannin, "A cryogen-consumption-free system for dynamic nuclear polarization at 9.4 t," *Journal of Magnetic Resonance*, vol. 294, pp. 115–121, 2018.

[45] J. H. Ardenkjær-Larsen, S. Bowen, J. R. Petersen, O. Rybalko, M. S. Vinding, M. Ullisch, and N. C. Nielsen, "Cryogen-free dissolution dynamic nuclear polarization polarizer operating at 3.35 t, 6.70 t, and 10.1 t," *Magnetic Resonance in Medicine*, vol. 81, no. 3, pp. 2184–2194, 2019.

[46] F. Kurdzesau, B. Van Den Brandt, A. Comment, P. Hautle, S. Jannin, J. Van Der Klink, and J. Konter, "Dynamic nuclear polarization of small labelled molecules in frozen water–alcohol solutions," *Journal of Physics D: Applied Physics*, vol. 41, no. 15, p. 155506, 2008.

[47] A. Bornet, R. Melzi, A. J. Perez Linde, P. Hautle, B. van den Brandt, S. Jannin, and G. Bodenhausen, "Boosting dissolution dynamic nuclear polarization by cross polarization," *The journal of physical chemistry letters*, vol. 4, no. 1, pp. 111–114, 2013.

[48] A. Bornet, J. Milani, B. Vuichoud, A. J. P. Linde, G. Bodenhausen, and S. Jannin, "Microwave frequency modulation to enhance dissolution dynamic nuclear polarization," *Chemical Physics Letters*, vol. 602, pp. 63–67, 2014.

[49] A. Bornet, A. Pinon, A. Jhajharia, M. Baudin, X. Ji, L. Emsley, G. Bodenhausen, J. H. Ardenkjaer-Larsen, and S. Jannin, "Microwave-gated dynamic nuclear polarization," *Physical Chemistry Chemical Physics*, vol. 18, no. 44, pp. 30 530–30 535, 2016.

[50] A. Kiswandhi, P. Niedbalski, C. Parish, P. Kaur, A. Martins, L. Fidelino, C. Khemtong, L. Song, A. D. Sherry, and L. Lumata, "Impact of ho 3+-doping on 13 c dynamic nuclear polarization using trityl ox063 free radical," *Physical Chemistry Chemical Physics*, vol. 18, no. 31, pp. 21 351–21 359, 2016.

[51] A. Capozzi, S. Patel, W. T. Wenckebach, M. Karlsson, M. H. Lerche, and J. H. Ardenkjær-Larsen, "Gadolinium effect at high-magnetic-field dnp: 70% 13c polarization of [u-13c] glucose using trityl," *The journal of physical chemistry letters*, vol. 10, no. 12, pp. 3420–3425, 2019.

[52] R. B. Khattri, A. A. Sirusi, E. H. Suh, Z. Kovacs, and M. E. Merritt, "The influence of ho 3+ doping on 13 c dnp in the presence of bdpa," *Physical Chemistry Chemical Physics*, vol. 21, no. 34, pp. 18 629–18 635, 2019.

[53] J. Milani, B. Vuichoud, A. Bornet, P. Miéville, R. Mottier, S. Jannin, and G. Bodenhausen, "A magnetic tunnel to shelter hyperpolarized fluids," *Review of Scientific Instruments*, vol. 86, no. 2, p. 024101, 2015.

[54] M. Cavaillès, A. Bornet, X. Jaurand, B. Vuichoud, D. Baudouin, M. Baudin, L. Veyre, G. Bodenhausen, J.-N. Dumez, S. Jannin *et al.*, "Tailored microstructured hyperpolarizing matrices for optimal magnetic resonance imaging," *Angewandte Chemie*, vol. 130, no. 25, pp. 7575–7579, 2018.

[55] A. C. Pinon, A. Capozzi, and J. H. Ardenkjær-Larsen, "Hyperpolarized water through dissolution dynamic nuclear polarization with uv-generated radicals," *Communications Chemistry*, vol. 3, no. 1, pp. 1–9, 2020.

[56] S. Patel, A. C. Pinon, M. H. Lerche, M. Karlsson, A. Capozzi, and J. H. Ardenkjær-Larsen, "Uv-irradiated 2-keto-(1-13c) isocaproic acid for high-performance 13c hyperpolarized mr," *The Journal of Physical Chemistry C*, vol. 124, no. 43, pp. 23 859–23 866, 2020.

[57] T. El Daraï, S. F. Cousin, Q. Stern, M. Ceillier, J. Kempf, D. Eshchenko, R. Melzi, M. Schnell, L. Gremillard, A. Bornet *et al.*, "Porous functionalized polymers enable generating and transporting hyperpolarized mixtures of metabolites," *Nature Communications*, vol. 12, no. 1, pp. 1–9, 2021.

[58] W. T. Wenckebach, "Dynamic nuclear polarization via the cross effect and thermal mixing: A. the role of triple spin flips," *Journal of Magnetic Resonance*, vol. 299, pp. 124–134, 2019.

[59] ——, "Dynamic nuclear polarization via the cross effect and thermal mixing: B. energy transport," *Journal of Magnetic Resonance*, vol. 299, pp. 151–167, 2019.

[60] W. T. Wenckebach and Y. Quan, "Monte carlo study of the spin-spin interactions between radicals used for dynamic nuclear polarization," *Journal of Magnetic Resonance*, vol. 326, p. 106948, 2021.

[61] W. T. Wenckebach, "Electron spin-spin interactions in dnp: Thermal mixing vs. the cross effect," *Applied Magnetic Resonance*, vol. 52, no. 7, pp. 731–748, 2021.

[62] H. Kouřilová, M. Jurkutat, D. Peat, K. Kouřil, A. S. Khan, A. J. Horsewill, J. F. MacDonald, J. Owers-Bradley, and B. Meier, "Radical-induced low-field relaxation and thermal mixing in pyruvic acid," *arXiv preprint arXiv:2202.05688*, 2022.

[63] A. Radaelli, H. A. Yoshihara, H. Nonaka, S. Sando, J. H. Ardenkjaer-Larsen, R. Gruetter, and A. Capozzi, "13c dynamic nuclear polarization using sa-bdpa at 6.7 t and 1.1 k: Coexistence of pure thermal mixing and well-resolved solid effect," *The Journal of Physical Chemistry Letters*, vol. 11, no. 16, pp. 6873–6879, 2020.

[64] B. Vuichoud, J. Milani, Q. Chappuis, A. Bornet, G. Bodenhausen, and S. Jannin, "Measuring absolute spin polarization in dissolution-dnp by spin polarimetry magnetic resonance (spymr)," *Journal of Magnetic Resonance*, vol. 260, pp. 127–135, 2015.

[65] S. J. Elliott, Q. Stern, and S. Jannin, "Solid-state 1 h spin polarimetry by 13 ch 3 nuclear magnetic resonance," *Magnetic Resonance*, vol. 2, no. 2, pp. 643–652, 2021.

[66] A. Leavesley, D. Shimon, T. A. Siaw, A. Feintuch, D. Goldfarb, S. Vega, I. Kaminker, and S. Han, "Effect of electron spectral diffusion on static dynamic nuclear polarization at 7 tesla," *Physical Chemistry Chemical Physics*, vol. 19, no. 5, pp. 3596–3605, 2017.

[67] D. Guarin, D. Carnevale, M. Baudin, P. Pelupessy, D. Abergel, and G. Bodenhausen, "Effects of microwave gating on nuclear spin echoes in dynamic nuclear polarization," *The Journal of Physical Chemistry Letters*, vol. 13, no. 1, pp. 175–182, 2021.

[68] Q. Stern, S. F. Cousin, F. Mentink-Vigier, A. C. Pinon, S. J. Elliott, O. Cala, and S. Jannin, "Direct observation of hyperpolarization breaking through the spin diffusion barrier," *Science Advances*, vol. 7, no. 18, p. eabf5735, 2021.

[69] Y. Hovav, A. Feintuch, and S. Vega, "Theoretical aspects of dynamic nuclear polarization in the solid state-the cross effect," *Journal of Magnetic Resonance*, vol. 214, pp. 29–41, 2012.

[70] D. Shimon, Y. Hovav, A. Feintuch, D. Goldfarb, and S. Vega, "Dynamic nuclear polarization in the solid state: a transition between the cross effect and the solid effect," *Physical Chemistry Chemical Physics*, vol. 14, no. 16, pp. 5729–5743, 2012.

[71] A. Karabanov, G. Kwiatkowski, and W. Köckenberger, "Spin dynamic simulations of solid effect dnp: The role of the relaxation superoperator," *Molecular Physics*, vol. 112, no. 14, pp. 1838–1854, 2014.

[72] A. Karabanov, D. Wiśniewski, F. Raimondi, I. Lesanovsky, and W. Köckenberger, "Many-body kinetics of dynamic nuclear polarization by the cross effect," *Physical Review A*, vol. 97, no. 3, p. 031404, 2018.

[73] D. Weitekamp, A. Bielecki, D. Zax, K. Zilm, and A. Pines, "Zero-field nuclear magnetic resonance," *Physical review letters*, vol. 50, no. 22, p. 1807, 1983.

[74] D. Zax, A. Bielecki, K. Zilm, A. Pines, and D. Weitekamp, "Zero field nmr and nqr," *The Journal of chemical physics*, vol. 83, no. 10, pp. 4877–4905, 1985.

[75] A. M. Thayer and A. Pines, "Zero-field nmr," *Accounts of Chemical Research*, vol. 20, no. 2, pp. 47–53, 1987.

[76] A. H. Trabesinger, R. McDermott, S. Lee, M. Mück, J. Clarke, and A. Pines, "Squid-detected liquid state nmr in microtesla fields," *The Journal of Physical Chemistry A*, vol. 108, no. 6, pp. 957–963, 2004.

[77] M. Ledbetter, I. Savukov, D. Budker, V. Shah, S. Knappe, J. Kitching, D. Michalak, S. Xu, and A. Pines, "Zero-field remote detection of nmr with a microfabricated atomic magnetometer," *Proceedings of the National Academy of Sciences*, vol. 105, no. 7, pp. 2286–2290, 2008.

[78] M. C. Tayler, T. Theis, T. F. Sjolander, J. W. Blanchard, A. Kentner, S. Pustelny, A. Pines, and D. Budker, "Invited review article: Instrumentation for nuclear magnetic resonance in zero and ultralow magnetic field," *Review of Scientific Instruments*, vol. 88, no. 9, p. 091101, 2017.

[79] P. Put, S. Pustelny, D. Budker, E. Druga, T. F. Sjolander, A. Pines, and D. A. Barskiy, "Zero-to ultralow-field nmr spectroscopy of small biomolecules," *Analytical Chemistry*, vol. 93, no. 6, pp. 3226–3232, 2021.

[80] J. W. Blanchard, T. Wu, J. Eills, Y. Hu, and D. Budker, "Zero-to ultralow-field nuclear magnetic resonance j-spectroscopy with commercial atomic magnetometers," *Journal of Magnetic Resonance*, vol. 314, p. 106723, 2020.

[81] J. W. Blanchard and D. Budker, "Zero-to ultralow-field nmr. emagres, 5: 1395–1410," 2016.

[82] J. W. Blanchard, D. Budker, and A. Trabesinger, "Lower than low: Perspectives on zero-to ultralow-field nuclear magnetic resonance," *Journal of Magnetic Resonance*, vol. 323, p. 106886, 2021.

[83] A. Wilzewski, S. Afach, J. W. Blanchard, and D. Budker, "A method for measurement of spin-spin couplings with sub-mhz precision using zero-to ultralow-field nuclear magnetic resonance," *Journal of Magnetic Resonance*, vol. 284, pp. 66–72, 2017.

[84] M. Carravetta, O. G. Johannessen, and M. H. Levitt, "Beyond the t 1 limit: singlet nuclear spin states in low magnetic fields," *Physical review letters*, vol. 92, no. 15, p. 153003, 2004.

[85] M. C. Tayler, J. Ward-Williams, and L. F. Gladden, "Nmr relaxation in porous materials at zero and ultralow magnetic fields," *Journal of Magnetic Resonance*, vol. 297, pp. 1–8, 2018.

[86] D. B. Burueva, J. Eills, J. W. Blanchard, A. Garcon, R. Picazo-Frutos, K. V. Kovtunov, I. V. Koptyug, and D. Budker, "Chemical reaction monitoring using zero-field nuclear magnetic resonance enables study of heterogeneous samples in metal containers," *Angewandte Chemie International Edition*, vol. 59, no. 39, pp. 17 026–17 032, 2020.

[87] S. Bodenstedt, M. W. Mitchell, and M. C. Tayler, “Fast-field-cycling ultralow-field nuclear magnetic relaxation dispersion,” *Nature Communications*, vol. 12, no. 1, pp. 1–8, 2021.

[88] T. Theis, P. Ganssle, G. Kervern, S. Knappe, K. J., M. P. Ledbetter, D. Budker, and A. Pines, “Parahydrogen-enhanced zero-field nuclear magnetic resonance,” *Nature Physics*, vol. 7, no. 7, pp. 571–575, 2011.

[89] F. Reineri, T. Boi, and S. Aime, “Parahydrogen induced polarization of 13c carboxylate resonance in acetate and pyruvate,” *Nature communications*, vol. 6, no. 1, pp. 1–6, 2015.

[90] L. Dagys, C. Bengs, and M. H. Levitt, “Low-frequency excitation of singlet–triplet transitions. application to nuclear hyperpolarization,” *The Journal of Chemical Physics*, vol. 155, no. 15, p. 154201, 2021.

[91] D. A. Barskiy, M. C. Tayler, I. Marco-Rius, J. Kurhanewicz, D. B. Vigneron, S. Cikrikci, A. Aydogdu, M. Reh, A. N. Pravdivtsev, J.-B. Hövener *et al.*, “Zero-field nuclear magnetic resonance of chemically exchanging systems,” *Nature communications*, vol. 10, no. 1, pp. 1–9, 2019.

[92] T. Wu, J. W. Blanchard, G. P. Centers, N. L. Figueroa, A. Garcon, P. W. Graham, D. F. J. Kimball, S. Rajendran, Y. V. Stadnik, A. O. Sushkov *et al.*, “Search for axionlike dark matter with a liquid-state nuclear spin comagnetometer,” *Physical review letters*, vol. 122, no. 19, p. 191302, 2019.

[93] S. Alcicek, P. Put, D. Barskiy, V. Kontul, and S. Pustelny, “Zero-field nmr of urea: Spin-topology engineering by chemical exchange,” *The journal of physical chemistry letters*, vol. 12, no. 43, pp. 10 671–10 676, 2021.

[94] E. Van Dyke, J. Eills, R. Picazo-Frutos, K. Sheberstov, Y. Hu, D. Budker, and D. Barskiy, “Relayed hyperpolarization for zero-field nuclear magnetic resonance,” 2022.

[95] J. Eills, J. W. Blanchard, T. Wu, C. Bengs, J. Hollenbach, D. Budker, and M. H. Levitt, “Polarization transfer via field sweeping in parahydrogen-enhanced nuclear magnetic resonance,” *The Journal of chemical physics*, vol. 150, no. 17, p. 174202, 2019.

[96] N. M. Zacharias, C. R. McCullough, S. Wagner, N. Sailasuta, H. R. Chan, Y. Lee, J. Hu, W. H. Perman, C. Henneberg, B. D. Ross *et al.*, “Towards real-time metabolic profiling of cancer with hyperpolarized succinate,” *Journal of molecular imaging & dynamics*, vol. 6, no. 1, 2016.

[97] J.-B. Hövener, A. N. Pravdivtsev, B. Kidd, C. R. Bowers, S. Glöggler, K. V. Kovtunov, M. Plaumann, R. Katz-Brull, K. Buckenmaier, A. Jerschow *et al.*, “Parahydrogen-based hyperpolarization for biomedicine,” *Angewandte Chemie International Edition*, vol. 57, no. 35, pp. 11 140–11 162, 2018.

[98] M. H. Levitt, *Spin dynamics: basics of nuclear magnetic resonance.* John Wiley & Sons, 2013.

[99] P. J. Hore, J. A. Jones, and S. Wimperis, *NMR: The toolkit: How pulse sequences work.* Oxford University Press, USA, 2015, vol. 92.

[100] C. Cohen-Tannoudji, B. Diu, and F. Laloe, “Quantum mechanics, volume 1,” *Quantum Mechanics*, vol. 1, p. 898, 1986.

[101] W. T. Wenckebach, *Essentials of dynamic nuclear polarization.* Spindrift Publications, 2016.

[102] G. Zhu, D. A. Torchia, and A. Bax, “Discrete fourier transformation of nmr signals. the relationship between sampling delay time and spectral baseline,” *Journal of Magnetic Resonance, Series A*, vol. 105, no. 2, pp. 219–222, 1993.

[103] G. Otting, H. Widmer, G. Wagner, and K. Wüthrich, “Origin of t 1 and t 2 ridges in 2d nmr spectra and procedures for suppression,” *NMR Struct. Biol*, pp. 389–395, 1995.

[104] J. P. King, T. F. Sjolander, and J. W. Blanchard, “Antisymmetric couplings enable direct observation of chirality in nuclear magnetic resonance spectroscopy,” *The Journal of Physical Chemistry Letters*, vol. 8, no. 4, pp. 710–714, 2017.

[105] M. C. Butler, G. Kervern, T. Theis, M. P. Ledbetter, P. J. Ganssle, J. W. Blanchard, D. Budker, and A. Pines, “Parahydrogen-induced polarization at zero magnetic field,” *The Journal of Chemical Physics*, vol. 138, no. 23, p. 234201, 2013.

[106] W. T. Wenckebach, A. Capozzi, S. Patel, and J. Ardenkjær-Larsen, “Direct measurement of the triple spin flip rate in dynamic nuclear polarization,” *Journal of Magnetic Resonance*, vol. 327, p. 106982, 2021.

[107] A. J. Pell, “A method to calculate the nmr spectra of paramagnetic species using thermalized electronic relaxation,” *Journal of Magnetic Resonance*, vol. 326, p. 106939, 2021.

[108] E. P. Horvitz, “Nuclear spin diffusion induced by paramagnetic impurities in nonconducting solids,” *Physical Review B*, vol. 3, no. 9, p. 2868, 1971.

[109] G. Khutsishvili, “Spin diffusion,” *Soviet Physics Uspekhi*, vol. 8, no. 5, p. 743, 1966.

[110] S. Cox, S. Read, and W. T. Wenchebach, “The behaviour of nuclear spins near highly polarised paramagnetic centres,” *Journal of Physics C: Solid State Physics*, vol. 10, no. 15, p. 2917, 1977.

[111] W. T. Wenchebach and S. F. J. Cox, “Nuclear dipolar relaxation induced by interacting ground state electron spins,” *Journal of Magnetic Resonance*, vol. 348, p. 107375, 2023. [Online]. Available: https://doi.org/10.1016/j.jmr.2023.107375

[112] S. Takahashi, R. Hanson, J. Van Tol, M. S. Sherwin, and D. D. Awschalom, “Quenching spin decoherence in diamond through spin bath polarization,” *Physical review letters*, vol. 101, no. 4, p. 047601, 2008.

[113] D. T. Edwards, S. Takahashi, M. S. Sherwin, and S. Han, “Distance measurements across randomly distributed nitroxide probes from the temperature dependence of the electron spin phase memory time at 240 ghz,” *Journal of Magnetic Resonance*, vol. 223, pp. 198–206, 2012.

[114] T. P. Lê, J.-N. Hyacinthe, and A. Capozzi, “How to improve the efficiency of a traditional dissolution dynamic nuclear polarization (ddnp) apparatus: Design and performance of a fluid path compatible ddnp/lod-esr probe,” *Journal of Magnetic Resonance*, vol. 338, p. 107197, 2022.

[115] A. Comment, B. v. van den Brandt, K. Uffmann, F. Kurdzesau, S. Jannin, J. Konter, P. Hautle, W. T. Wenckebach, R. Gruetter, and J. Van Der Klink, “Design and performance of a dnp prepolarizer coupled to a rodent mri scanner,” *Concepts in Magnetic Resonance Part B: Magnetic Resonance Engineering: An Educational Journal*, vol. 31, no. 4, pp. 255–269, 2007.

[116] S. J. Elliott, S. F. Cousin, Q. Chappuis, O. Cala, M. Ceillier, A. Bornet, and S. Jannin, "Dipolar order mediated 1 h→ 13 c cross-polarization for dissolution-dynamic nuclear polarization," *Magnetic Resonance*, vol. 1, no. 1, pp. 89–96, 2020.

[117] S. J. Elliott, O. Cala, Q. Stern, S. F. Cousin, D. Eshchenko, R. Melzi, J. G. Kempf, and S. Jannin, "Pulse sequence and sample formulation optimization for dipolar order mediated 1 h→ 13 c cross-polarization," *Physical Chemistry Chemical Physics*, vol. 23, no. 15, pp. 9457–9465, 2021.

[118] S. J. Elliott, Q. Stern, O. Cala, and S. Jannin, "Protonation tuned dipolar order mediated 1h→ 13c cross-polarization for dissolution-dynamic nuclear polarization experiments," *Solid State Nuclear Magnetic Resonance*, vol. 116, p. 101762, 2021.

[119] S. J. Elliott, O. Cala, Q. Stern, S. F. Cousin, M. Ceillier, V. Decker, and S. Jannin, "Boosting dissolution-dynamic nuclear polarization by multiple-step dipolar order mediated 1h→ 13c cross-polarization," *Journal of Magnetic Resonance Open*, vol. 8, p. 100018, 2021.

[120] S. J. Elliott, M. Ceillier, O. Cala, Q. Stern, S. F. Cousin, and S. Jannin, "Simple and cost-effective cross-polarization experiments under dissolution-dynamic nuclear polarization conditions with a 3d-printed 1h-13c background-free radiofrequency coil," *Journal of Magnetic Resonance Open*, vol. 10, p. 100033, 2022.

[121] S. J. Elliott, Q. Stern, M. Ceillier, T. El Daraï, S. F. Cousin, O. Cala, and S. Jannin, "Practical dissolution dynamic nuclear polarization," *Progress in Nuclear Magnetic Resonance Spectroscopy*, vol. 126, pp. 59–100, 2021.

[122] N. Bloembergen and R. Pound, "Radiation damping in magnetic resonance experiments," *Physical Review*, vol. 95, no. 1, p. 8, 1954.

[123] V. V. Krishnan and N. Murali, "Radiation damping in modern nmr experiments: Progress and challenges," *Progress in Nuclear Magnetic Resonance Spectroscopy*, vol. 68, pp. 41–57, 2013. [Online]. Available: http://dx.doi.org/10.1016/j.pnmrs.2012.06.001

[124] C. Jeffries, "Polarization of nuclei by resonance saturation in paramagnetic crystals," *Physical Review*, vol. 106, no. 1, p. 164, 1957.

[125] T. Can, Q. Ni, and R. Griffin, "Mechanisms of dynamic nuclear polarization in insulating solids," *Journal of Magnetic Resonance*, vol. 253, pp. 23–35, 2015.

[126] C. Griesinger, M. Bennati, H.-M. Vieth, C. Luchinat, G. Parigi, P. Höfer, F. Engelke, S. J. Glaser, V. Denysenkov, and T. F. Prisner, "Dynamic nuclear polarization at high magnetic fields in liquids." *Progress in nuclear magnetic resonance spectroscopy*, vol. 64, pp. 4–28, 2012.

[127] T. V. Can, M. A. Caporini, F. Mentink-Vigier, B. Corzilius, J. J. Walish, M. Rosay, W. E. Maas, M. Baldus, S. Vega, T. M. Swager *et al.*, "Overhauser effects in insulating solids," *The Journal of chemical physics*, vol. 141, no. 6, p. 064202, 2014.

[128] F. A. Perras, D. F. Flesariu, S. A. Southern, C. Nicolaides, J. D. Bazak, N. M. Washton, T. Trypiniotis, C. P. Constantinides, and P. A. Koutentis, "Methyl-driven overhauser dynamic nuclear polarization," *The Journal of Physical Chemistry Letters*, vol. 13, pp. 4000–4006, 2022.

[129] X. Ji, T. Can, F. Mentink-Vigier, A. Bornet, J. Milani, B. Vuichoud, M. Caporini, R. G. Griffin, S. Jannin, M. Goldman *et al.*, "Overhauser effects in non-conducting solids at 1.2 k," *Journal of Magnetic Resonance*, vol. 286, pp. 138–142, 2018.

[130] S. Pylaeva, K. L. Ivanov, M. Baldus, D. Sebastiani, and H. Elgabarty, “Molecular mechanism of overhauser dynamic nuclear polarization in insulating solids,” *The Journal of Physical Chemistry Letters*, vol. 8, no. 10, pp. 2137–2142, 2017.

[131] S. Pylaeva, P. Marx, G. Singh, T. D. Kühne, M. Roemelt, and H. Elgabarty, “Organic mixed-valence compounds and the overhauser effect in insulating solids,” *The Journal of Physical Chemistry A*, vol. 125, no. 3, pp. 867–874, 2021.

[132] Y. Hovav, D. Shimon, I. Kaminker, A. Feintuch, D. Goldfarb, and S. Vega, “Effects of the electron polarization on dynamic nuclear polarization in solids,” *Physical Chemistry Chemical Physics*, vol. 17, no. 8, pp. 6053–6065, 2015.

[133] K. Kundu, A. Feintuch, and S. Vega, “Electron-electron cross-relaxation and spectral diffusion during dynamic nuclear polarization experiments on solids,” *The Journal of Physical Chemistry Letters*, vol. 9, no. 7, pp. 1793–1802, 2018.

[134] ——, “Theoretical aspects of the cross effect enhancement of nuclear polarization under static dynamic nuclear polarization conditions,” *The Journal of Physical Chemistry Letters*, vol. 10, no. 8, pp. 1769–1778, 2019.

[135] F. Mentink-Vigier, Ü. Akbey, H. Oschkinat, S. Vega, and A. Feintuch, “Theoretical aspects of magic angle spinning-dynamic nuclear polarization,” *Journal of Magnetic Resonance*, vol. 258, pp. 102–120, 2015.

[136] F. Mentink-Vigier, I. Marin-Montesinos, A. P. Jagtap, T. Halbritter, J. van Tol, S. Hediger, D. Lee, S. T. Sigurdsson, and G. De Paëpe, “Computationally assisted design of polarizing agents for dynamic nuclear polarization enhanced nmr: the asympol family,” *Journal of the American Chemical Society*, vol. 140, no. 35, pp. 11 013–11 019, 2018.

[137] A. Lund, G. Casano, G. Menzildjian, M. Kaushik, G. Stevanato, M. Yulikov, R. Jabbour, D. Wisser, M. Renom-Carrasco, C. Thieuleux *et al.*, “Tinypols: a family of water-soluble binitroxides tailored for dynamic nuclear polarization enhanced nmr spectroscopy at 18.8 and 21.1 t,” *Chemical science*, vol. 11, no. 10, pp. 2810–2818, 2020.

[138] G. Mathies, M. A. Caporini, V. K. Michaelis, Y. Liu, K.-N. Hu, D. Mance, J. L. Zweier, M. Rosay, M. Baldus, and R. G. Griffin, “Efficient dynamic nuclear polarization at 800 mhz/527 ghz with trityl-nitroxide biradicals,” *Angewandte Chemie International Edition*, vol. 54, no. 40, pp. 11 770–11 774, 2015.

[139] X. Cai, A. Lucini Paioni, A. Adler, R. Yao, W. Zhang, D. Beriashvili, A. Safeer, A. Gurinov, A. Rockenbauer, Y. Song *et al.*, “Highly efficient trityl-nitroxide biradicals for biomolecular high-field dynamic nuclear polarization,” *Chemistry–A European Journal*, vol. 27, no. 50, pp. 12 758–12 762, 2021.

[140] F. Mentink-Vigier, S. Vega, and G. De Paëpe, “Fast and accurate mas–dnp simulations of large spin ensembles,” *Physical Chemistry Chemical Physics*, vol. 19, no. 5, pp. 3506–3522, 2017.

[141] F. A. Perras and M. Pruski, “Linear-scaling ab initio simulations of spin diffusion in rotating solids,” *The Journal of Chemical Physics*, vol. 151, no. 3, p. 034110, 2019.

[142] F. A. Perras, M. Raju, S. L. Carnahan, D. Akbarian, A. C. Van Duin, A. J. Rossini, and M. Pruski, “Full-scale ab initio simulation of magic-angle-spinning dynamic nuclear polarization,” *The Journal of Physical Chemistry Letters*, vol. 11, no. 14, pp. 5655–5660, 2020.

[143] F. A. Perras, S. L. Carnahan, W.-S. Lo, C. J. Ward, J. Yu, W. Huang, and A. J. Rossini, "Hybrid quantum-classical simulations of magic angle spinning dynamic nuclear polarization in very large spin systems," *The Journal of Chemical Physics*, vol. 156, no. 12, p. 124112, 2022.

[144] E. Weber, H. Vezin, J. Kempf, G. Bodenhausen, D. Abergel, and D. Kurzbach, "Anisotropic longitudinal electronic relaxation affects dnp at cryogenic temperatures," *Physical Chemistry Chemical Physics*, vol. 19, no. 24, pp. 16 087–16 094, 2017.

[145] M. Borghini, "Spin-temperature model of nuclear dynamic polarization using free radicals," *Physical Review Letters*, vol. 20, no. 9, p. 419, 1968.

[146] S. Jannin, A. Comment, and J. Van der Klink, "Dynamic nuclear polarization by thermal mixing under partial saturation," *Applied Magnetic Resonance*, vol. 43, no. 1, pp. 59–68, 2012.

[147] O. Leifson and C. Jeffries, "Dynamic polarization of nuclei by electron-nuclear dipolar coupling in crystals," *Physical Review*, vol. 122, no. 6, p. 1781, 1961.

[148] C. Jeffries, "On nuclear relaxation in dilute paramagnetic crystals," *Proceedings of the Physical Society (1958-1967)*, vol. 88, no. 1, p. 257, 1966.

[149] D. Jardón-Álvarez, T. Malka, J. van Tol, Y. Feldman, R. Carmieli, and M. Leskes, "Monitoring electron spin fluctuations with paramagnetic relaxation enhancement," *Journal of Magnetic Resonance*, vol. 336, p. 107143, 2022.

[150] S. Chandrasekhar, "Stochastic problems in physics and astronomy," pp. 1–89, 1943.

[151] E. Genies, A. Boyle, M. Lapkowski, and C. Tsintavis, "Polyaniline: A historical survey," *Synthetic metals*, vol. 36, no. 2, pp. 139–182, 1990.

[152] S. Mishra, A. Kumar, M. Venkatesan, L. Pigani, L. Pasquali, and C. Fontanesi, "Exchange interactions drive supramolecular chiral induction in polyaniline," *Small Methods*, vol. 4, no. 10, p. 2000617, 2020.

[153] R. Naaman, Y. Paltiel, and D. H. Waldeck, "Chiral molecules and the electron spin," *Nature Reviews Chemistry*, vol. 3, no. 4, pp. 250–260, 2019.

[154] W. Li and M. Wan, "Porous polyaniline films with high conductivity," *Synthetic metals*, vol. 92, no. 2, pp. 121–126, 1998.

[155] X.-H. Li, L. Dai, Y. Liu, X.-J. Chen, W. Yan, L.-P. Jiang, and J.-J. Zhu, "Ionic-liquid-doped polyaniline inverse opals: Preparation, characterization, and application for the electrochemical impedance immunoassay of hepatitis b surface antigen," *Advanced Functional Materials*, vol. 19, no. 19, pp. 3120–3128, 2009.

[156] S. Fujiwara, N. Matsumoto, K. Nishimura, N. Kimizuka, K. Tateishi, T. Uesaka, and N. Yanai, "Triplet dynamic nuclear polarization of guest molecules through induced fit in a flexible metal–organic framework," *Angewandte Chemie*, vol. 134, no. 9, p. e202115792, 2022.

[157] Y. Li, A. Equbal, T. Tabassum, and S. Han, "1h thermal mixing dynamic nuclear polarization with bdpa as polarizing agents," *The Journal of Physical Chemistry Letters*, vol. 11, no. 21, pp. 9195–9202, 2020.

[158] A. Equbal, Y. Li, T. Tabassum, and S. Han, “Crossover from a solid effect to thermal mixing 1h dynamic nuclear polarization with trityl-ox063,” *The Journal of Physical Chemistry Letters*, vol. 11, no. 9, pp. 3718–3723, 2020.

[159] A. A. Kuzhelev, D. Dai, V. Denysenkov, and T. F. Prisner, “Solid-like dynamic nuclear polarization observed in the fluid phase of lipid bilayers at 9.4 t,” *Journal of the American Chemical Society*, vol. 144, no. 3, pp. 1164–1168, 2022.

[160] V. Krinichnyi, S. Chemerisov, and Y. S. Lebedev, “Epr and charge-transport studies of polyaniline,” *Physical Review B*, vol. 55, no. 24, p. 16233, 1997.

[161] N. Bloembergen, “On the interaction of nuclear spins in a crystalline lattice,” *Physica*, vol. 15, no. 3-4, pp. 386–426, 1949.

[162] J. Korringa, “Nuclear magnetic relaxation and resonnance line shift in metals,” *Physica*, vol. 16, no. 7-8, pp. 601–610, 1950.

[163] A. Anderson and A. Redfield, “Nuclear spin-lattice relaxation in metals,” *Physical Review*, vol. 116, no. 3, p. 583, 1959.

[164] J. R. Owers-Bradley, A. J. Horsewill, D. T. Peat, K. S. Goh, and D. G. Gadian, “High polarization of nuclear spins mediated by nanoparticles at millikelvin temperatures,” *Physical Chemistry Chemical Physics*, vol. 15, no. 25, pp. 10 413–10 417, 2013.

[165] M. L. Hirsch, N. Kalechofsky, A. Belzer, M. Rosay, and J. G. Kempf, “Brute-force hyperpolarization for nmr and mri,” *Journal of the American Chemical Society*, vol. 137, no. 26, pp. 8428–8434, 2015.

[166] G. Khutsishvili, “Polarization of the nuclei of ferromagnetic atoms,” *SOVIET PHYSICS JETP-USSR*, vol. 2, no. 4, pp. 744–744, 1956.

[167] L. Lumata, Z. Kovacs, A. D. Sherry, C. Malloy, S. Hill, J. Van Tol, L. Yu, L. Song, and M. E. Merritt, “Electron spin resonance studies of trityl ox063 at a concentration optimal for dnp,” *Physical Chemistry Chemical Physics*, vol. 15, no. 24, pp. 9800–9807, 2013.

[168] T. A. Siaw, A. Leavesley, A. Lund, I. Kaminker, and S. Han, “A versatile and modular quasi optics-based 200 ghz dual dynamic nuclear polarization and electron paramagnetic resonance instrument,” *Journal of Magnetic Resonance*, vol. 264, pp. 131–153, 2016.

[169] A. Feintuch, D. Shimon, Y. Hovav, D. Banerjee, I. Kaminker, Y. Lipkin, K. Zibzener, B. Epel, S. Vega, and D. Goldfarb, “A dynamic nuclear polarization spectrometer at 95 ghz/144 mhz with epr and nmr excitation and detection capabilities,” *Journal of Magnetic Resonance*, vol. 209, no. 2, pp. 136–141, 2011.

[170] J. Granwehr, J. Leggett, and W. Köckenberger, “A low-cost implementation of epr detection in a dissolution dnp setup,” *Journal of Magnetic Resonance*, vol. 187, no. 2, pp. 266–276, 2007.

[171] J. H. Ardenkjær-Larsen, S. Macholl, and H. Johannesson, “Dynamic nuclear polarization with trityls at 1.2 k,” *Applied Magnetic Resonance*, vol. 34, no. 3, pp. 509–522, 2008.

[172] H. Jóhannesson, S. Macholl, and J. H. Ardenkjaer-Larsen, “Dynamic nuclear polarization of [1-13c] pyruvic acid at 4.6 tesla,” *Journal of Magnetic Resonance*, vol. 197, no. 2, pp. 167–175, 2009.

[173] W. Blumberg, “Nuclear spin-lattice relaxation caused by paramagnetic impurities,” *Physical Review*, vol. 119, no. 1, p. 79, 1960.

[174] G. Khutsishvili, “Spin diffusion and magnetic relaxation of nuclei,” *Sov. Phys. JETP*, vol. 15, p. 909, 1962.

[175] H. Rorschach Jr, “Nuclear relaxation in solids by diffusion to paramagnetic impurities,” *Physica*, vol. 30, no. 1, pp. 38–48, 1964.

[176] C. Ramanathan, “Dynamic nuclear polarization and spin diffusion in nonconducting solids,” *Applied Magnetic Resonance*, vol. 34, pp. 409–421, 2008. [Online]. Available: http://link.springer.com/10.1007/s00723-008-0123-7https://link.springer.com/article/10.1007/s00723-008-0123-7

[177] A. Chessari, S. F. Cousin, S. Jannin, and Q. Stern, “The role of electron polarization on nuclear spin diffusion,” *arXiv preprint arXiv:2206.14771*, 2022.

[178] I. Waller, “Über die magnetisierung von paramagnetischen kristallen in wechselfeldern,” *Zeitschrift für Physik*, vol. 79, no. 5, pp. 370–388, 1932.

[179] P. De Gennes, “Sur la relaxation nucleaire dans les cristaux ioniques,” *Journal of Physics and Chemistry of Solids*, vol. 7, no. 4, pp. 345–350, 1958.

[180] G. Khutsishvili, *Proc. Inst. Phys. Acad. Sci. Georgia (U.S.S.R.)*, vol. 4, p. 5, 1956.

[181] M. Goldman, “Impurity-controlled nuclear relaxation,” *Physical Review*, vol. 138, no. 6A, p. A1675, 1965.

[182] G. Khutsishvili, “Spin diffusion, magnetic relaxation, and dynamic polarization of nuclei,” *Soviet Phys. JETP*, vol. 16, no. 6, pp. 1540–1543, 1963.

[183] I. Lowe and D. Tse, “Nuclear spin-lattice relaxation via paramagnetic centers,” *Physical Review*, vol. 166, no. 2, p. 279, 1968.

[184] E. Fukushima and E. A. Uehling, “Nuclear-spin-diffusion relaxation to a finite density of paramagnetic impurity ions,” *Physical Review*, vol. 173, no. 2, p. 366, 1968.

[185] O. Leifson and E. Vogel, “Observation of the influence of electron-pair spin flips on nuclear thermal relaxation,” *Physical Review B*, vol. 2, no. 11, p. 4626, 1970.

[186] G. Khutsishvili, “Diffusion and relaxation of nuclear spins in crystals containing paramagnetic impurities,” in *Progress in Low Temperature Physics.* Elsevier, 1970, vol. 6, pp. 375–404.

[187] L. Buishvili, G. Khutsishvili, and M. Zviadadze, “Nuclear relaxation and nmr saturation in a crystal with a magnetic impurity,” *physica status solidi (b)*, vol. 48, no. 2, pp. 851–861, 1971.

[188] L. Buishvili and M. Zviadadze, “On the quasithermodynamic theory of magnetic relaxation,” *Physica*, vol. 59, no. 4, pp. 697–706, 1972.

[189] Y. Hovav, A. Feintuch, and S. Vega, “Theoretical aspects of dynamic nuclear polarization in the solid state–the solid effect,” *Journal of Magnetic Resonance*, vol. 207, no. 2, pp. 176–189, 2010.

[190] ——, “Dynamic nuclear polarization assisted spin diffusion for the solid effect case,” *The Journal of chemical physics*, vol. 134, no. 7, p. 074509, 2011.

[191] J. Ramakrishna and F. Robinson, “A transient effect in dynamic nuclear polarization,” *Proceedings of the Physical Society (1958-1967)*, vol. 87, no. 4, p. 945, 1966.

[192] J. Ramakrishna, “A note on the anisotropy of spin diffusion barrier,” *Proceedings of the Physical Society (1958-1967)*, vol. 89, no. 2, p. 473, 1966.

[193] D. Tse and S. Hartmann, “Nuclear spin-lattice relaxation via paramagnetic centers without spin diffusion,” *Physical Review Letters*, vol. 21, no. 8, p. 511, 1968.

[194] L. Buishvili, M. Zviadadze, and B. Mikaberidze, “Nuclear cross-relaxation induced by a paramagnetic impurity,” *Sov. Phys. J. Exp. Theor. Phys*, vol. 69, pp. 1077–1079, 1975.

[195] K. K. Sabirov, “Nuclear flip-flop transitions induced by paramagnetic impurities,” *physica status solidi (b)*, vol. 91, no. 2, pp. 735–739, 1979.

[196] V. Atsarkin and V. Demidov, “Nuclear magnetic relaxation and spin diffusion in the local fields of paramagnetic centers,” *Zh. Eksp. Teor. Fiz*, vol. 79, pp. 1438–1450, 1980.

[197] J. Wolfe, “Direct observation of a nuclear spin diffusion barrier,” *Physical Review Letters*, vol. 31, no. 15, p. 907, 1973.

[198] A. King, J. Wolfe, and R. Ballard, “Nmr of nuclei near a paramagnetic impurity in crystals,” *Physical Review Letters*, vol. 28, no. 17, p. 1099, 1972.

[199] K. O. Tan, M. Mardini, C. Yang, J. H. Ardenkjær-Larsen, and R. G. Griffin, “Three-spin solid effect and the spin diffusion barrier in amorphous solids,” *Science advances*, vol. 5, no. 7, p. eaax2743, 2019.

[200] D. Pagliero, P. R. Zangara, J. Henshaw, A. Ajoy, R. H. Acosta, J. A. Reimer, A. Pines, and C. A. Meriles, “Optically pumped spin polarization as a probe of many-body thermalization,” *Science advances*, vol. 6, no. 18, p. eaaz6986, 2020.

[201] S. K. Jain, C.-J. Yu, C. B. Wilson, T. Tabassum, D. E. Freedman, and S. Han, “Dynamic nuclear polarization with vanadium (iv) metal centers,” *Chem*, vol. 7, no. 2, pp. 421–435, 2021.

[202] N. Wili, J. H. Ardenkjær-Larsen, and G. Jeschke, “Reverse dynamic nuclear polarisation for indirect detection of nuclear spins close to unpaired electrons,” *Magnetic Resonance Discussions*, pp. 1–12, 2022.

[203] A. Karabanov, D. Wiśniewski, I. Lesanovsky, and W. Köckenberger, “Dynamic nuclear polarization as kinetically constrained diffusion,” *Physical review letters*, vol. 115, no. 2, p. 020404, 2015.

[204] C. Wittig, “The landau- zener formula,” *The Journal of Physical Chemistry B*, vol. 109, no. 17, pp. 8428–8430, 2005.

[205] A. A. Smith, B. Corzilius, A. B. Barnes, T. Maly, and R. G. Griffin, “Solid effect dynamic nuclear polarization and polarization pathways,” *The Journal of Chemical Physics*, vol. 136, no. 1, p. 01B602, 2012.

[206] J. J. Wittmann, M. Eckardt, W. Harneit, and B. Corzilius, “Electron-driven spin diffusion supports crossing the diffusion barrier in mas dnp,” *Physical Chemistry Chemical Physics*, vol. 20, no. 16, pp. 11 418–11 429, 2018.

[207] N. A. Prisco, A. C. Pinon, L. Emsley, and B. F. Chmelka, "Scaling analyses for hyperpolarization transfer across a spin-diffusion barrier and into bulk solid media," *Physical Chemistry Chemical Physics*, vol. 23, no. 2, pp. 1006–1020, 2021.

[208] M. M. Hoffmann, S. Bothe, T. Gutmann, F.-F. Hartmann, M. Reggelin, and G. Buntkowsky, "Directly vs indirectly enhanced 13c in dynamic nuclear polarization magic angle spinning nmr experiments of nonionic surfactant systems," *The Journal of Physical Chemistry C*, vol. 121, no. 4, pp. 2418–2427, 2017.

[209] M. Roos, P. Micke, K. Saalwächter, and G. Hempel, "Moderate mas enhances local 1h spin exchange and spin diffusion," *Journal of Magnetic Resonance*, vol. 260, pp. 28–37, 2015.

[210] F. Mentink-Vigier, S. Paul, D. Lee, A. Feintuch, S. Hediger, S. Vega, and G. De Paëpe, "Nuclear depolarization and absolute sensitivity in magic-angle spinning cross effect dynamic nuclear polarization," *Physical Chemistry Chemical Physics*, vol. 17, no. 34, pp. 21 824–21 836, 2015.

[211] J. Dolinšek, P. Cereghetti, and R. Kind, "Phonon-assisted spin diffusion in solids," *Journal of Magnetic Resonance*, vol. 146, no. 2, pp. 335–344, 2000.

[212] G. Lindblad, "On the generators of quantum dynamical semigroups," *Communications in Mathematical Physics*, vol. 48, no. 2, pp. 119–130, 1976.

[213] V. Gorini, "Completely positive dynamical semigroups of n-level systems," *Journal of Mathematical Physics*, vol. 17, no. 5, p. 821, 1976. [Online]. Available: https://doi.org/10.1063/1.522979

[214] C. Bengs and M. H. Levitt, "A master equation for spin systems far from equilibrium," *Journal of Magnetic Resonance*, vol. 310, p. 106645, 2020.

[215] M. P. Silveri, J. A. Tuorila, E. V. Thuneberg, and G. S. Paraoanu, "Quantum systems under frequency modulation," *Reports on Progress in Physics*, vol. 80, no. 5, 2017.

[216] J. Li, M. P. Silveri, K. S. Kumar, J. M. Pirkkalainen, A. Vepsäläinen, W. C. Chien, J. Tuorila, M. A. Sillanpää, P. J. Hakonen, E. V. Thuneberg, and G. S. Paraoanu, "Motional averaging in a superconducting qubit," *Nature Communications*, vol. 4, pp. 1–6, 2013.

[217] K. Wódkiewicz, B. W. Shore, and J. H. Eberly, "Noise in strong laser-atom interactions: Frequency fluctuations and nonexponential correlations," *Phys. Rev. A*, vol. 30, pp. 2390–2398, Nov 1984. [Online]. Available: https://link.aps.org/doi/10.1103/PhysRevA.30.2390

[218] D. Suter and R. Ernst, "Spin diffusion in resolved solid-state nmr spectra," *Physical Review B*, vol. 32, no. 9, p. 5608, 1985.

[219] M. Ernst and B. H. Meier, "Spin diffusion in solids," *Studies in Physical and Theoretical Chemistry*, vol. 84, pp. 83–122, 1998.

[220] N. Benetis, J. Kowalewski, L. Nordenskiöld, H. Wennerström, and P.-O. Westlund, "Nuclear spin relaxation in paramagnetic systems: The slow motion problem for electron spin relaxation," *Molecular Physics*, vol. 48, no. 2, pp. 329–346, 1983.

[221] B. Meier, J.-N. Dumez, G. Stevanato, J. T. Hill-Cousins, S. S. Roy, P. Hakansson, S. Mamone, R. C. Brown, G. Pileio, and M. H. Levitt, "Long-lived nuclear spin states in methyl groups and quantum-rotor-induced polarization," *Journal of the American Chemical Society*, vol. 135, no. 50, pp. 18 746–18 749, 2013.

[222] M. Ceillier, O. Cala, T. El Daraï, S. F. Cousin, Q. Stern, S. Guibert, S. J. Elliott, A. Bornet, B. Vuichoud, J. Milani *et al.*, "An automated system for fast transfer and injection of hyperpolarized solutions," *Journal of Magnetic Resonance Open*, vol. 8, p. 100017, 2021.

[223] R. Picazo-Frutos, Q. Stern, J. W. Blanchard, O. Cala, M. Ceillier, S. F. Cousin, J. Eills, S. J. Elliott, S. Jannin, and D. Budker, "Zero-to ultralow-field nuclear magnetic resonance enhanced with dissolution dynamic nuclear polarization," *Analytical Chemistry*, 2022.

[224] A. C. Pinon, A. Capozzi, and J. H. Ardenkjær-Larsen, "Hyperpolarization via dissolution dynamic nuclear polarization: new technological and methodological advances," *Magnetic Resonance Materials in Physics, Biology and Medicine*, vol. 34, no. 1, pp. 5–23, 2021.

[225] T. Harris, C. Bretschneider, and L. Frydman, "Dissolution dnp nmr with solvent mixtures: Substrate concentration and radical extraction," *Journal of Magnetic Resonance*, vol. 211, no. 1, pp. 96–100, 2011.

[226] J. Granwehr, R. Panek, J. Leggett, and W. Köckenberger, "Quantifying the transfer and settling in nmr experiments with sample shuttling," *The Journal of chemical physics*, vol. 132, no. 24, p. 244507, 2010.

[227] J. H. Ardenkjaer-Larsen, A. M. Leach, N. Clarke, J. Urbahn, D. Anderson, and T. W. Skloss, "Dynamic nuclear polarization polarizer for sterile use intent," *NMR in biomedicine*, vol. 24, no. 8, pp. 927–932, 2011.

[228] L. M. Epasto, K. Che, F. Kozak, A. Selimovic, P. Kadeřávek, and D. Kurzbach, "Toward protein nmr at physiological concentrations by hyperpolarized water—finding and mapping uncharted conformational spaces," *Science Advances*, vol. 8, no. 31, p. eabq5179, 2022.

[229] M. H. Lerche, M. Karlsson, J. H. Ardenkjær-Larsen, and P. R. Jensen, "Targeted metabolomics with quantitative dissolution dynamic nuclear polarization," in *NMR-Based Metabolomics*. Springer, 2019, pp. 385–393.

[230] A. Dey, B. Charrier, K. Lemaître, V. Ribay, D. Eshchenko, M. Schnell, R. Melzi, Q. Stern, S. F. Cousin, J. G. Kempf *et al.*, "Fine optimization of a dissolution-dnp experimental setting for 13 c nmr of metabolic samples," *Magnetic Resonance Discussions*, pp. 1–27, 2022.

[231] S. Bowen and C. Hilty, "Rapid sample injection for hyperpolarized nmr spectroscopy," *Physical Chemistry Chemical Physics*, vol. 12, no. 22, pp. 5766–5770, 2010.

[232] L. Frydman and D. Blazina, "Ultrafast two-dimensional nuclear magnetic resonance spectroscopy of hyperpolarized solutions," *Nature physics*, vol. 3, no. 6, pp. 415–419, 2007.

[233] M. Negroni, D. Guarin, K. Che, L. M. Epasto, E. Turhan, A. Selimović, F. Kozak, S. Cousin, D. Abergel, G. Bodenhausen *et al.*, "Inversion of hyperpolarized 13c nmr signals through cross-correlated cross-relaxation in dissolution dnp experiments," *The Journal of Physical Chemistry B*, 2022.

[234] P. Miéville, S. Jannin, and G. Bodenhausen, "Relaxometry of insensitive nuclei: optimizing dissolution dynamic nuclear polarization," *Journal of Magnetic Resonance*, vol. 210, no. 1, pp. 137–140, 2011.

[235] A. S. Kiryutin, B. A. Rodin, A. V. Yurkovskaya, K. L. Ivanov, D. Kurzbach, S. Jannin, D. Guarin, D. Abergel, and G. Bodenhausen, "Transport of hyperpolarized samples in dissolution-dnp experiments," *Physical Chemistry Chemical Physics*, vol. 21, no. 25, pp. 13 696–13 705, 2019.

[236] B. Vuichoud, A. Bornet, F. De Nanteuil, J. Milani, E. Canet, X. Ji, P. Miéville, E. Weber, D. Kurzbach, A. Flamm *et al.*, “Filterable agents for hyperpolarization of water, metabolites, and proteins,” *Chemistry–A European Journal*, vol. 22, no. 41, pp. 14 696–14 700, 2016.

[237] P. Miéville, P. Ahuja, R. Sarkar, S. Jannin, P. R. Vasos, S. Gerber-Lemaire, M. Mishkovsky, A. Comment, R. Gruetter, O. Ouari *et al.*, “Scavenging free radicals to preserve enhancement and extend relaxation times in NMR using dynamic nuclear polarization,” *Angewandte Chemie International Edition*, vol. 49, no. 35, pp. 6182–6185, 2010.

[238] B. Melton, V. Pollak, T. Mayes, and B. L. Willis, “Condition for sudden passage in the earth’s-field nmr technique,” *Journal of Magnetic Resonance, Series A*, vol. 117, no. 2, pp. 164–170, 1995.

[239] K. Kouřil, M. Gramberg, M. Jurkutat, H. Kouřilová, and B. Meier, “A cryogen-free, semi-automated apparatus for bullet-dynamic nuclear polarization with improved resolution,” *Magnetic Resonance*, vol. 2, no. 2, pp. 815–825, 2021.

[240] A. Yurkovskaya and G. Bodenhausen, “In memoriam konstantin l’vovich ivanov,” *Magnetic Resonance*, vol. 2, no. 1, pp. 341–342, 2021.

[241] M. Goldman, H. Jóhannesson, O. Axelsson, and M. Karlsson, “Hyperpolarization of 13c through order transfer from parahydrogen: a new contrast agent for mri,” *Magnetic resonance imaging*, vol. 23, no. 2, pp. 153–157, 2005.

[242] E. Cavallari, C. Carrera, T. Boi, S. Aime, and F. Reineri, “Effects of magnetic field cycle on the polarization transfer from parahydrogen to heteronuclei through long-range j-couplings,” *The Journal of Physical Chemistry B*, vol. 119, no. 31, pp. 10 035–10 041, 2015.

[243] E. Cavallari, C. Carrera, and F. Reineri, “Parahydrogen hyperpolarized substrates for molecular imaging studies,” *Israel Journal of Chemistry*, vol. 57, no. 9, pp. 833–842, 2017.

[244] B. A. Rodin, K. F. Sheberstov, A. S. Kiryutin, J. T. Hill-Cousins, L. J. Brown, R. C. Brown, B. Jamain, H. Zimmermann, R. Z. Sagdeev, A. V. Yurkovskaya *et al.*, “Constant-adiabaticity radiofrequency pulses for generating long-lived singlet spin states in nmr,” *The Journal of chemical physics*, vol. 150, no. 6, p. 064201, 2019.

[245] L. D. Landau, “Zur theorie der energieubertragung ii,” *Z. Sowjetunion*, vol. 2, pp. 46–51, 1932.

[246] C. Zener, “Non-adiabatic crossing of energy levels,” *Proceedings of the Royal Society of London. Series A, Containing Papers of a Mathematical and Physical Character*, vol. 137, no. 833, pp. 696–702, 1932.

[247] M. P. Ledbetter, C. W. Crawford, A. Pines, D. E. Wemmer, S. Knappe, J. Kitching, and D. Budker, “Optical detection of nmr j-spectra at zero magnetic field,” *Journal of Magnetic Resonance*, vol. 199, pp. 25–29, 2009.

[248] R. W. Adams, J. A. Aguilar, K. D. Atkinson, M. J. Cowley, P. I. Elliott, S. B. Duckett, G. G. Green, I. G. Khazal, J. López-Serrano, and D. C. Williamson, “Reversible interactions with para-hydrogen enhance NMR sensitivity by polarization transfer,” *Science*, vol. 323, no. 5922, pp. 1708–1711, 2009.

[249] M. P. Augustine, A. Wong-Foy, J. L. Yarger, M. Tomaselli, A. Pines, D. M. TonThat, and J. Clarke, “Low field magnetic resonance images of polarized noble gases obtained with a dc superconducting quantum interference device,” *Applied physics letters*, vol. 72, no. 15, pp. 1908–1910, 1998.

[250] V. Yashchuk, J. Granwehr, D. Kimball, S. Rochester, A. Trabesinger, J. Urban, D. Budker, and A. Pines, "Hyperpolarized xenon nuclear spins detected by optical atomic magnetometry," *Physical review letters*, vol. 93, no. 16, p. 160801, 2004.

[251] R. Jiménez-Martínez, D. J. Kennedy, M. Rosenbluh, E. A. Donley, S. Knappe, S. J. Seltzer, H. L. Ring, V. S. Bajaj, and J. Kitching, "Optical hyperpolarization and NMR detection of 129 Xe on a microfluidic chip," *Nature communications*, vol. 5, no. 1, pp. 1–6, 2014.

[252] D. J. Kennedy, S. J. Seltzer, R. Jiménez-Martínez, H. L. Ring, N. S. Malecek, S. Knappe, E. A. Donley, J. Kitching, V. S. Bajaj, and A. Pines, "An optimized microfabricated platform for the optical generation and detection of hyperpolarized 129 Xe," *Scientific reports*, vol. 7, no. 1, pp. 1–10, 2017.

[253] M. Jiang, R. P. Frutos, T. Wu, J. W. Blanchard, X. Peng, and D. Budker, "Magnetic gradiometer for the detection of zero-to ultralow-field nuclear magnetic resonance," *Physical Review Applied*, vol. 11, no. 2, p. 024005, 2019.

[254] D. Budker and M. Romalis, "Optical magnetometry," *Nature physics*, vol. 3, no. 4, pp. 227–234, 2007.

[255] D. Budker, D. Kimball, S. Rochester, V. Yashchuk, and M. Zolotorev, "Sensitive magnetometry based on nonlinear magneto-optical rotation," *Physical Review A*, vol. 62, no. 4, p. 043403, 2000.

[256] H. J. Bernstein, J. A. Pople, and W. Schneider, "The analysis of nuclear magnetic resonance spectra: I. systems of two and three nuclei," *Canadian Journal of Chemistry*, vol. 35, no. 1, pp. 67–83, 1957.

[257] M. Emondts, M. P. Ledbetter, S. Pustelny, T. Theis, B. Patton, J. W. Blanchard, M. C. Butler, D. Budker, and A. Pines, "Long-lived heteronuclear spin-singlet states in liquids at a zero magnetic field," *Physical review letters*, vol. 112, no. 7, p. 077601, 2014.

[258] J. Zhu, E. Ye, V. Terskikh, and G. Wu, "Experimental verification of the theory of nuclear quadrupole relaxation in liquids over the entire range of molecular tumbling motion," *The Journal of Physical Chemistry Letters*, vol. 2, no. 9, pp. 1020–1023, 2011.

[259] M. C. Tayler and L. F. Gladden, "Scalar relaxation of NMR transitions at ultralow magnetic field," *Journal of Magnetic Resonance*, vol. 298, pp. 101–106, 2019.

[260] D. Gajan, A. Bornet, B. Vuichoud, J. Milani, R. Melzi, H. A. Van Kalkeren, L. Veyre, C. Thieuleux, M. P. Conley, W. R. Grüning *et al.*, "Hybrid polarizing solids for pure hyperpolarized liquids through dissolution dynamic nuclear polarization," *Proceedings of the National Academy of Sciences*, vol. 111, no. 41, pp. 14 693–14 697, 2014.

[261] M. Leutzsch, A. J. Sederman, L. F. Gladden, and M. D. Mantle, "In situ reaction monitoring in heterogeneous catalysts by a benchtop NMR spectrometer," *Magnetic resonance imaging*, vol. 56, pp. 138–143, 2019.

[262] P. A. Boeg, J. Ø. Duus, J. H. Ardenkjær-Larsen, M. Karlsson, and S. Mossin, "Real-time detection of intermediates in rhodium-catalyzed hydrogenation of alkynes and alkenes by dissolution dnp," *The Journal of Physical Chemistry C*, vol. 123, no. 15, pp. 9949–9956, 2019.